
ALMA MATER STUDIORUM - UNIVERSITÀ DI BOLOGNA

DOTTORATO DI RICERCA IN ASTRONOMIA

Ciclo XXII

Settore Scientifico-Disciplinare di afferenza: *FIS/05*

**PROCEDURES
OF QUALITY CONTROL AND DATA ANALYSIS
OF MULTI-SITE GROUND-BASED OBSERVATIONS
FOR THE ABSOLUTE FLUX CALIBRATION OF GAIA**

Presentata da: Silvia MARINONI

Coordinatore Dottorato:
Prof. Lauro MOSCARDINI

Relatore:
Prof. Bruno MARANO

Co-Relatori:
Dott. Elena PANCINO
Dott. Giuseppe ALTAVILLA

Esame Finale anno 2011

1	Introduction	7
2	Gaia: taking the galactic census	11
2.1	Gaia’s scientific goals and capabilities	12
2.1.1	Galactic Structure, Formation and Evolution	12
2.1.2	Stellar Astrophysics and rare stellar types	13
2.1.3	Solar System studies	18
2.1.4	Extra-solar Planets	20
2.1.5	Observations of Quasars and AGN	21
2.1.6	Microlensing	22
2.1.7	Fundamental Physics	22
2.1.8	Distance and Ages Scale in the Universe	23
2.2	Mission timeline and data release	23
2.3	Launch and Operations	25
2.4	Gaia Scanning Law	27
2.5	Spacecraft overview	29
2.6	Payload and telescopes overview	30
2.6.1	Radiation damage	33
2.6.2	The Gaia Focal Plane	34
2.7	Object Detection, Sampling and Windowing	36
2.8	Astrometry	38
2.9	Spectro-Photometry	42
2.10	Radial Velocity Spectrometer	44
2.11	Gaia Data Treatment: the DPAC	46
2.11.1	The Italian contribution	48
2.11.2	CU5: Photometric Processing	48
3	Spectro-Photometric calibration	53
3.1	Classical Spectro-Photometric Calibration	54
3.1.1	Atmospheric Extinction: the Bouguer’s Law	54
3.1.2	Instrument Response and Calibration	57
3.2	Gaia Spectro-Photometric System: a challenge	60
3.3	The Gaia Calibration Philosophy	61
3.4	The Absolute Flux Calibration of Gaia data	66
3.4.1	Spectroscopic Calibration Model: the concept	67

CONTENTS

3.4.2	Inversion of the Dispersion Matrix	70
3.4.3	Diagonalization of the dispersion matrix	70
3.4.4	Integrated Photometry Calibration Model	74
3.4.5	RVS spectra absolute calibration	78
4	The Gaia Grid of SPSS	79
4.1	Classes of SPSS for Gaia	81
4.1.1	SPSS Pillars	82
4.1.2	Primary SPSS: selection criteria and Candidates	84
4.1.3	Secondary SPSS: selection criteria and Candidates	97
4.2	Observation Strategy and Campaigns	113
4.2.1	Main Campaign description	113
4.2.2	Constancy Monitoring Campaign description	114
4.2.3	Observation Protocols	115
4.3	Observing Facilities	116
4.4	Survey Status	122
5	The Instrument Familiarization Plan	127
5.1	CCD Performance Tests: Shutter effects	128
5.1.1	Shutter delay	129
5.1.2	2D exposure time variation	131
5.1.3	Lamp Stability	132
5.2	CCD Performance Tests: CCD linearity	133
5.2.1	Classical method	135
5.2.2	Stello method	137
5.3	CCD performance tests results	139
5.4	Calibration Frames Monitoring	141
5.4.1	Masterbias Monitoring	141
5.4.2	Photometric Masterflat Monitoring	141
5.4.3	Spectroscopic Masterflat Monitoring	143
5.4.4	Masterdark Monitoring	143
5.4.5	Wavelength Lamp Flexures	149
5.5	Calibration Frames Monitoring results	152
5.6	Instrument Tests: 2 nd Order Contamination	155
5.7	Instrument Tests: Polarization	164
5.7.1	Possible sources of polarization	164
5.7.2	Possible effects of polarization	166

5.7.3	An experiment with DOLoRes	169
5.8	Photometricity and Extinction	171
6	The Pre-reduction Protocol for photometric observations	175
6.1	Imaging Pre-reduction procedures	176
6.2	Bias Frames	177
6.2.1	Single frame Quality Assessment	179
6.2.2	Masterbias production and Quality Assessment	182
6.3	Dark Frames	187
6.3.1	Masterdark Quality Assessment	187
6.4	Flat Fielding	189
6.4.1	Single frame Quality Assessment	189
6.4.2	Masterflat Production and Quality Assessment	190
6.5	Bad Pixel Mask	197
6.6	Fringing	198
6.7	2-d Imaging Pre-reductions	200
7	Quality Control on SPSS Photometric Frames and Photometric Catalogues Production	201
7.1	SExtractor	202
7.2	The Quality Control strategy	204
7.3	The <i>Star Level</i> QC	205
7.3.1	Step <i>a</i> : SExtractor FLAGS	205
7.3.2	Step <i>b</i> : Signal to Noise Ratio	208
7.3.3	Step <i>c</i> : Seeing and focus	208
7.3.4	Step <i>d</i> : Bad pixels	209
7.4	The <i>Frame Level</i> QC	209
7.5	The <i>Series Level</i> QC	211
7.6	QC results and logging	211
7.6.1	Run pages Reduction Logs Tables	215
7.6.2	Higher level logging: the Primary and Secondary observations tables	215
7.6.3	The individual SPSS page	217
8	Short-term Constancy Monitoring of SPSS candidates	219
8.1	SPSS light curve production	219
8.2	Analysis of light curves	222

CONTENTS

8.2.1	Time series and light curve QC	222
8.2.2	Constancy Criteria	223
9	Future prospects and scientific outcome	231
9.1	Scientific implications	232
9.1.1	White dwarfs atmosphere and compact pulsators	232
9.1.2	Other kinds of variables	234
9.2	Variable SPSS examples	238
9.2.1	SPSS 034	239
9.2.2	SPSS 172	243
10	Conclusions	249
10.1	Gaia mission calibration	250
10.2	SPSS survey scientific output	252
A	Wiki-Bo pages and Data Archives	253
A.1	Wiki-Bo pages	253
A.1.1	Short-term monitoring light curves page	255
A.2	Archiving SPSS raw and reduced data	257
A.2.1	The raw data archive	257
A.2.2	The reduced data archive	259
A.2.3	Downloading data	260
A.2.4	Uploading data	261
	Bibliography	264

1

Introduction

The Gaia space mission is a major project for the European astronomical community. The Gaia satellite will perform a 5 year long all-sky scanning survey that will provide exquisitely accurate astrometry (> 100 times better than Hipparcos) and photometry for one billion of Galactic stars down to $V \simeq 20$, and radial velocity for several millions of stars to $V \leq 17$ (Chapter 2). The data coming from Gaia will significantly improve our understanding in many astrophysical fields. It will provide detailed information on stellar evolution and star formation in our Galaxy. It will clarify the origin and formation history of our Galaxy. The Gaia results will precisely identify relics of tidally-disrupted accretion debris, probe the distribution of dark matter, establish the luminosity function for pre-main sequence stars, detect and categorize rapid evolutionary stellar phases, place unprecedented constraints on the age, internal structure and evolution of all stellar types, establish a rigorous distance scale framework throughout the Galaxy and beyond, and classify star formation and kinematical and dynamical behaviour within the Local Group of galaxies. Gaia will pinpoint exotic objects in colossal and almost unimaginable numbers: many thousands of extra-solar planets will be discovered and their detailed orbits and masses determined; tens of thousands of brown dwarfs and white dwarfs will be identified; tens of thousands of extragalactic supernovae will be discovered; Solar System studies will receive a massive impetus through the detection of many tens of thousands of new minor planets; near-Earth objects, inner Trojans and even new trans-Neptunian objects, including Plutinos, may be discovered.

As challenging as it is, the processing and analysis of the huge data-flow incoming from Gaia is the subject of thorough study and preparatory work by the DPAC (Data Processing and Analysis Consortium), in charge of all aspects of the Gaia data reduction. This PhD Thesis was carried out in the framework of the DPAC, within the team based in Bologna. The task of the Bologna team is to define the calibration

model (Chapter 3) and to build a grid of spectro-photometric standard stars (SPSS) suitable for the absolute flux calibration of the Gaia G-band photometry and the BP/RP spectrophotometry (Chapter 4). Such a flux calibration can be performed by repeatedly observing each SPSS during the life-time of the Gaia mission and by comparing the observed Gaia spectra to the spectra obtained by our ground-based observations.

To reach this goal our team started a vast spectro-photometric observational effort, involving six different ground-based facilities around the globe. Observations started in the second half of 2006, comprising at present 45 accepted proposals. We have been awarded, at the time of writing, a total of $\simeq 300$ observing nights, at the rate of $\simeq 36$ per semester. The number of estimated nights to survey completion, calculated by projecting the actual SPSS observation rate (including lost time for weather or technical reasons) on the number of SPSS still to observe, is about 95. If the projection is accurate, our survey will have a final size of $\simeq 400$ nights, comparable to the forthcoming ESO Public Survey in terms of observing time, and was carried out by a team of only 3–5 FTE per year. The Gaia SPSS grid ($\simeq 200$ stars) will represent an unprecedented catalogue of spectrophotometric standard stars, characterized by high precision and accuracy, full sky coverage and with stars spanning a wide range of spectral types. Most of our SPSS are WDs and hot subdwarfs, the remaining are dwarf/giant stars covering different spectral types, including cool stars of late spectral type up to M. For comparison, CALSPEC, containing the composite stellar spectra which are the fundamental flux standards for HST calibrations, consists of about 60 stars: our SPSS grid will be more than three times larger, and it will be about twice the Stritzinger et al. (2005) catalogue.

Due to both the different observing sites involved and the huge amount of frames expected ($\simeq 100\,000$), it is essential to maintain the maximum homogeneity in data quality, acquisition and treatment, and a particular care has to be used to test the capabilities of each telescope/instrument combination (through the “instrument familiarization plan”), to devise methods to keep under control, and eventually to correct for, the typical instrumental effects that can affect the high precision required for the Gaia SPSS grid (a few % with respect to Vega).

I contributed to the ground-based survey of Gaia SPSS in many respects: with the observations (Chapter 4), the instrument familiarization plan (Chapter 5, and Marini et al. 2011b), the data reduction and analysis activities (both photometry and spectroscopy), and to the maintenance of the data archives (Appendix A). However, the field I was personally responsible for was photometry and in particular relative

photometry for the production of short-term light curves (Chapter 8, and Marinoni et al. 2011d). In this context I defined and tested a semi-automated pipeline which allows for the pre-reduction of imaging SPSS data (Chapter 6, and Marinoni et al. 2011a) and the production of aperture photometry catalogues ready to be used for further analysis (Chapter 7, and Marinoni et al. 2011c). A series of semi-automated quality control (QC) criteria are included in the pipeline at various levels, from pre-reduction, to aperture photometry, to light curves production and analysis.

2

Gaia: taking the galactic census

Gaia is a cornerstone mission of the ESA Space Program, presently scheduled for launch in 2013. The Gaia satellite will perform an all-sky survey to obtain positions, parallaxes and proper motions to μas precision for the about 10^9 point-like sources on the sky. Expected accuracies are in the 7-25 μas range down to 15-th mag and sub-mas accuracies down to a limiting magnitude of $V \simeq 20$. The astrometric data are complemented by low-resolution spectrophotometric data in the 330-1050 nm wavelength range and, for the brighter stars ($V < 17$), by radial velocity measurements in the spectral region around the calcium triplet at a resolution of about 10000.

The expected end-of-mission astrometric accuracies are almost 100 times better than the HIPPARCOS dataset (see Perryman et al. 1997). This exquisite precision will allow a full and detailed reconstruction of the 3-d spatial structure and 3-d velocity field of the Milky Way galaxy within $\simeq 10$ kpc from the Sun. This will provide answers to long-standing questions about the origin and evolution of our Galaxy, from a quantitative census of its stellar populations, to detailed characterization of its substructures as, for instance, tidal stream in the Halo (Ibata & Gibson 2007) and to the distribution of dark matter.

The accurate 3-d motion of stellar systems and more distant Galactic satellites (as the Magellanic Clouds for example) will be also obtained by averaging the proper motions of many thousands of member stars: this will provide an unprecedented leverage to constrain the mass distribution of the Galaxy and/or non-standard theories of gravitation.

Gaia will determine direct geometric distances to almost any kind of standard candle currently used for distance determination, setting the whole cosmological distance scale on an extremely firm base.

As challenging as it is, the processing and analysis of the huge data-flow incoming

from Gaia is the subject of thorough study and preparatory work by the *Data Processing and Analysis Consortium* (DPAC), in charge of all aspects of the Gaia data reduction. The Consortium comprises more than 400 scientists from 25 European Institutes.

Gaia is usually described as a self-calibrating mission, but it also needs *external* data to fix the zeropoint of the magnitude system and radial velocities, and to calibrate the classification/parametrization algorithms. All these additional data are termed *auxiliary data* and will have to be available, at least in part, *three months before launch*. While part of the auxiliary data already exist and must be only compiled from archives, this is not always true for several components. To this aim, a coordinated program of ground-based observations is being organized by a dedicated inter-CU committee (GBOG), that promotes synergies and avoids duplications of efforts.

2.1 Gaia's scientific goals and capabilities

Gaia will measure the positions, distances, space motions and many astrophysical parameters (T_{eff} , $logg$, $E(B - V)$, metallicity etc.) of some billion stars in our Galaxy and beyond. For many years, the state of the art in celestial cartography has been the Schmidt surveys of Palomar and ESO, and their digitized counterparts. Gaia will provide the detailed 3-d distributions and space motions of all these stars, complete to 20-th magnitude. The measurement precision, reaching a few μas , will be unprecedented: some millions of stars will be measured with a distance accuracy of better than 1%, and some 100 millions or more better than 10%. This will allow our Galaxy to be mapped, for the first time, in three dimensions.

Gaia's resulting scientific harvest is of almost inconceivable extent and implication in a huge range of scientific disciplines:

2.1.1 Galactic Structure, Formation and Evolution

The primary objective of the Gaia mission is to survey the Milky Way, gathering data that will allow us to study the composition and evolution of our Galaxy, as well as advancing galaxy studies in general. Understanding our Galaxy requires measurements of distances and space motions for large and unbiased samples of stars of different mass, age, metallicity and evolutionary stage. Gaia's global survey of the entire sky down to 20-th magnitude is the ideal (and only) approach to define and measure such sample. The huge number of stars, the impressive astrometric

accuracy and the faint limiting magnitude of Gaia will quantify our understanding of the structure and motions of stars within the bulge, the spiral arms, the disc, and the outer halo, and will revolutionise dynamical studies of our Galaxy.

Galactic-evolution studies require the determination of the ages of relatively young object in the Galactic disc, mainly open clusters and main-sequence A-F stars with ages ranging from several millions to a few billion years. By providing accurate data for a large number of A-F stars, Gaia will drastically reduce the impact of the distance uncertainty on the age estimates for single stars. Gaia will also provide clean sequences in the HR diagram for many open clusters containing hundreds to thousands of members.

The position of the ZAMS in the HR diagram depends critically on the chemical composition of stars. The large sample of non-evolved, low-mass stars with determined metallicities and accurate positions in the HR diagram, that will be constituted from Gaia observations of K-M dwarfs, will be a key tool for interpreting the helium abundance and the chemical evolution of the Galaxy.

The determination of the age of the oldest objects in the Galaxy (Population II) provides a lower limit to the age of the Universe. This can be used to constrain cosmological models and parameters. Currently, the best estimate for the age of the oldest stars is based on the absolute magnitude of the main-sequence turn-off in globular clusters, and is affected by the uncertainty on the cluster distances. With its precise measurements, Gaia will improve the age estimate of the oldest star.

Gaia will also provide detailed information on stellar evolution and star-formation history in our Galaxy, describing the temporal evolution of the star-formation rate and the cumulative numbers of stars formed in the bulge, inner disc, solar neighbourhood, outer disc and halo of the Milky Way. The star-formation history defines the luminosity evolution of the Galaxy directly. In combination with the relevant chemical abundance distributions, the accretion history of gas may be derived. Together with kinematics, the merger history of smaller stellar systems can be defined. The determination of the relative rates of formation and/or accumulation of the stellar populations in a large spiral, typical of those galaxies which dominate the luminosity in the Universe, will provide, for the first time, the possibility to test galaxy-formation models in a quantitative manner.

2.1.2 Stellar Astrophysics and rare stellar types

Gaia will provide distances of astonishing accuracy to all types of stars in all stellar populations, even those in the most rapid evolutionary phases, which are very

sparsely represented in the solar neighbourhood. With the determination of extinction/reddening, luminosities and metallicities through the use of photometry and spectroscopy, the resulting extensive and high-accuracy data will stimulate a revolution in the study of stellar formation and evolution. All parts of the HR diagram will be comprehensively calibrated by the results from Gaia, including all phases of stellar evolution, a wide range of masses, many types of variables and binary systems, and all standard distance indicators.

- **Stellar structure and evolution.** The study of stellar structure and evolution provides fundamental informations on the properties of matter under extreme physical conditions as well as on the evolution of galaxies and cosmology. The further progress required in stellar modelling (for example on atmospheric models, transport processes of matter, angular momentum and magnetic fields, microscopic physics etc.) need more numerous samples of rare objects, including distant stars and stars undergoing rapid evolutionary phases, an increased number of common objects with high-quality data and a census over all stellar populations. Gaia will return luminosities, surface temperatures, abundances, masses, and determinations of the interstellar extinction for all these types of stars, helping in addressing discrepancies between the observations and the predictions of standard stellar models.
- **Binary Systems.** As a result of its aperture size, Gaia will resolve all binaries with separations above some 20 mas, which have a moderate magnitude difference between their components. Many such systems exist and these will form the bulk of the “Gaia Binary Catalogue”. Gaia will study resolved binaries in a variety of stellar populations: nearby star-forming regions, open clusters and associations, as well as field binaries of varying ages. Gaia’s high precision parallaxes and proper motions will also enable identification of the very widest binaries amongst the individually observed stars. Gaia will detect the majority of the estimated 10 million binaries (down to magnitude 20) closer than 250 parsec to the Sun. This huge sample can be used to investigate age groups, variability and possible evolutionary trends of the binary frequency at different orbital periods.

One of Gaia’s strengths is its extreme sensitivity to non-linear proper-motions. Large fractions of the astrometric binaries with periods in the range 0.03-30 yr will be recognized immediately. If the period of such systems is below 7–8 yr, it will be possible to determine a photocentric orbit. For systems up to 15-th

magnitude radial-velocity observations will define large numbers of shorter-period binaries. At the shortest periods, Gaia will photometrically observe millions of eclipsing binaries, mostly too faint for radial-velocity observations. At longer periods, binary systems with a period of about 100 yr will be hard to detect with Gaia.

- **Variability of stars.** Gaia will provide multi-epoch, multi-color photometry and high-quality broad-band photometric measurements made in the astrometric field. The combined photometric data will have the precision necessary to detect different variable phenomena and to describe nearly all types of variability. The photometric data will allow a global description of stellar stability and variability across the Hertzsprung-Russell diagram and will permit the identification of the physical processes causing variability. Expected numbers of variable objects are difficult to predict, but invariably large. Considering the conservative estimates given by Eyer & Cuypers (2000), we expect about 18 million of variable stars in total (including 5 million of “classic” periodic variable, about 3 million of eclipsing binaries, 300 000 stars with rotation-induced variability, 2 000-8 000 Cepheids, 6 000-240 000 δ Scuti variables, 70 000 RR Lyrae stars and about 250 000 Miras and SV variables.).

Precise physical and orbital parameters of eclipsing binaries will be derived for about 10 000 systems (Zwitter et al. 2003). The pulsating stars sample observed by Gaia will include key distance calibrators such as Cepheids, RR Lyrae stars, and long-period variables, for which present samples are incomplete already at magnitudes as bright as 10. A complete sample of objects will allow determination of the frequency of peculiar objects, and will accurately calibrate period-luminosity relationships across a wide range of stellar parameters (i.e. mass, age and metallicity). Variability on short (seconds) to long (of order of 5 years) time scales will be determined.

In addition to stellar variability, other transient phenomena, not necessarily of stellar origin, will also be present in the Gaia data: supernovae (estimated at $\sim 21\,000$, see Belokurov & Evans 2003), microlensing events (though astrometry will be able to detect more events, about 1,300 stars will have perturbed photometry; see Belokurov & Evans 2002), and planetary transits (5 000-30 000 detectable transits are expected, see Robichon 2002). Finally, non-stellar variable objects will be observed, including gamma-ray bursts, quasars, active galactic nuclei, and small bodies in the solar system.

- **White Dwarfs.** The mechanical structure of white dwarfs is supported by the pressure of the gas of degenerate electrons, whereas the partially degenerate outer layers control the flow of energy. Precise spectro-photometric data, like those that Gaia will provide, will introduce tight constraints on the models. In particular, Gaia will allow the mass-radius relationship to be tested. By comparing theoretical models with the observed properties of white dwarfs in binary systems, Gaia will be able to constrain the relation between the mass of the star on the main sequence and the mass of the resulting white dwarf. Gaia will also provide precise informations on the physical mechanisms (crystallization, phase separation, etc.) operating during the cooling process. Given their long cooling time scales, white dwarfs have been used as a tool for extracting information about the past history of our Galaxy. The large number of white dwarfs that Gaia will observe will allow us to determine, with unprecedented accuracy, the age of the local neighborhood and the star-formation history of the Galaxy. Furthermore, Gaia will be able to distinguish among the thin- and thick-disc white-dwarf populations and, in this way, it will be able to provide fundamental insight into the Galactic history. Gaia will also probe the structure and dynamics of the Galaxy and provide new clues about the halo white-dwarf population and its contribution to the mass budget of our Galaxy.

Finally, new constraints on the (hypothetical) rate of change of the gravitational constant G will be derived by comparing the measured average cooling rates of white dwarfs. More specifically, Gaia will largely reduce the observational errors in the determination of the disc white-dwarf luminosity function. Since the white-dwarf luminosity function measures the average rate of cooling of white dwarfs, and since this rate depends crucially on the rate of change of G , the Gaia observations will strongly constrain its rate of change.

- **Brown Dwarfs.** In observing the whole sky down to 20-th magnitude, Gaia will detect and observe a large number of isolated brown dwarfs in the solar neighbourhood. Structural models show that brown dwarfs cool and fade rapidly after formation, so the distance out to which Gaia can detect them is a function of their mass and age. Gaia should see Pleiades-age (~ 100 Myr) brown dwarfs out to around 400 pc, and younger brown dwarfs (such as those in the Orion Nebula Cluster, 1-3 Myr) out to about 1 kpc. This volume encompasses numerous young clusters and star-forming regions, and Gaia will be able to measure accurate properties for young brown dwarfs located in it

(Baraffe et al. 2002). For example, for an $I = 20$ mag brown dwarf at 200 pc, Gaia will obtain a distance accuracy of about 4% and transverse velocities to around 0.2 Km/s.

One of the main contributions of Gaia to substellar astrophysics will be a detailed spatial and kinematic map of brown dwarfs in clusters of known metallicity (determined from Gaia parallaxes of higher-mass stars), permitting a comprehensive study of mass segregation and ejection of brown dwarfs. These are key ingredients to understanding the formation mechanism of substellar mass objects, whether it be via cloud fragmentation and gravitational collapse, premature ejection from an accreting envelope, or some other mechanism.

Brown dwarfs will be identified primarily from their absolute luminosities, obtained from the precise Gaia parallaxes, as well as from the on-board multi-band photometry. The latter will provide physical parameters of brown dwarfs (in particular effective temperature, but perhaps also metallicity and the nature of cloud coverage). As brown dwarfs will be found in clusters of a range of ages, a significant contribution of Gaia will be an accurate observational determination of their cooling curves. The photometry and absolute magnitudes will furthermore help in the detection of spatially and astrometrically unresolved brown-dwarfs binaries. From this information, we will be able to determine the substellar mass function and the 3-d spatial and age distribution of brown dwarfs, thus establishing their formation history in the context of the Galaxy.

Predictions of the number of brown dwarfs which Gaia will detect depend sensitively on their cooling function and their distribution. Rough estimates based on current knowledge are of the order of 50 000 over a wide range of masses and ages.

- **Supernovae.** Gaia is an ideal instrument to detect nearby supernovae (i.e. within a few hundred Mpc). Gaia will provide a huge dataset of high-quality local type-Ia supernovae in which any deviations from “standard candles” can be analysed. As the dataset is so large, there will likely also be a good number of relatively rare phenomena, such as sub-luminous and type Ib/c supernovae. Gaia will record data of more than 20 000¹ supernovae during the five-year mis-

¹The number of detected supernovae may change according to different observing parameters (as the scanning law) and changes in the expected instrument performances. More recent estimates of the detectable supernovae (type Ia and core collapse) predict $\sim 6\,000$ objects over the five years mission lifetime.

sion lifetime (more than 14 000 type Ia, more than 1 000 type Ib/c and more than 5 000 type II, see Belokurov & Evans 2003). These supernovae will span a redshift range up to $z \sim 0.14$.

Supernova rates will be found as a function of galaxy type, as well as extinction and position in the host galaxy. Amongst other applications, there may be about 26 supernovae each year for which detection of gravitational waves should be possible and about 180 supernovae each year for which detection of gamma-rays should be possible. Gaia's astrometry will provide the supernova position to better than mas precision, offering opportunities for the identification of progenitors in nearby galaxies and for studying the spatial distribution of supernovae of different types in galaxies.

2.1.3 Solar System studies

While tracking stars with its telescopes, Gaia will also observe solar system objects by the thousands, primarily asteroids of the main belt circling the Sun between the orbits of Mars and Jupiter, but also inner-Trojans and even trans-Neptunian objects.

- **NEOs.** With its ability to detect faint and fast-moving objects, it is expected that Gaia will also detect several thousand Near-Earth-Objects (NEOs), which are thought to be comets and asteroids that have been nudged by the gravitational attraction of nearby planets into orbits that allow them to enter the Earth's neighbourhood. Due to its vantage point of observation at the Lagrange point L2 and its ability to observe down to an angular distance of 45 degrees from the Sun, Gaia will be ideally situated to probe the asteroid blind spot between the Sun and Earth and to discover small bodies orbiting the Sun inside the Earth's orbit, a region virtually unreachable from the Earth. In the course of its all-sky survey, Gaia will also observe the sky far from the ecliptic, where ground-based surveys of minor planets are predominantly active, an instance very favorable to the discovery of objects roaming the solar system on exotic orbits. Gaia will accurately measure the positions and velocities of asteroids over the five years of the mission, leading to a determination of their orbits with an unprecedented precision. Orbital parameters are essential to compute well in advance when and where a stellar occultation by a small body will be observable. Such events yield a wealth of information on the sizes and shapes, and when the masses are known, on the densities of these objects. Orbits are also a key element in identifying members of "orbital families" sharing

a common origin. Beyond astrometry, Gaia's multi-epoch photometric data will reveal the surface properties of minor planets providing information on how much light is reflected in a particular color. A refined classification of the population of minor bodies will emerge from the Gaia database, revealing the kinship between asteroids, NEOs and meteorites. In addition, the variation of the physical parameters with the distance to the Sun will also be studied.

- **Trojans.** Uniquely among the minor planets, the so-called Jupiter Trojans are made up of small bodies librating around the stable L4 and L5 Lagrangian points of the Sun-Jupiter system, on orbits thought to be stable over the age of the solar system. A few Mars and Neptune Trojans are also known to exist, whereas no results have been obtained from searches for Trojans of other planets. There are many unanswered key questions related to the peculiar locations and orbital properties of Trojans, and Gaia may cast some light on their origin (did they accrete from planetary grains in the same region where they are found or were they trapped there in the early stages of formation of the solar system?) and classification (can Trojans be simply considered as a sub-class of the objects that we collectively call "asteroids", or should we consider them as a separate category of bodies, somehow intermediate between main-belt asteroids and trans-Neptunians objects with distinctive physical properties?). The composition of Trojans constitutes a serious constraint for any study of the original gradient in composition of the planetesimals in the early phase of the solar system. A comparison of their spectral-reflectance properties with those of other classes of minor bodies is an important task and clearly this is an area where Gaia will contribute significantly. Precise astrometric measurements will produce significant improvements in the accuracy of the derived orbits of these objects, leading to the refinement of the statistics of the distribution of orbital elements. The systematic and homogeneous survey of the spectrophotometric properties of Trojans will make it possible to investigate the spectral diversity among Trojans, and to detect possible systematic differences in surface reflectance between the two clouds. Moreover, Gaia's photometric data is expected to produce reliable estimates of rotation periods, spin axis orientation, and overall shapes for a statistically significant sample of the whole population.
- **TNOs and Centaurs.** Beyond the orbit of Neptune, another group of minor bodies is clustered in the Edgeworth-Kuiper Belt: due to their large distance to the Sun and Earth, trans-Neptunians objects (TNOs) and Centaurs (objects

with perihelia between the orbits of Jupiter and Neptune) are faint. Very few of them will be visible by Gaia: currently, only 65 objects are known to be brighter than 20-th magnitude (the limit of completeness of Gaia) and 138 are brighter than magnitude 21 (10%-level of detection efficiency). So Gaia should detect a few tens of object at most. Most of these should be Centaurs or Scattered Disk Objects (semi-major axis > 50 AU and pericenter distance within gravitational reach of Neptune) on their way to the Centaurs region. Despite this small number, Gaia will provide a valuable contribution to the study of the outer solar system. First of all, it will be the first and only instrument that will survey the whole sky down to magnitude 20, allowing detection of any bright object of the solar system that is currently in front of the Milky Way, or at very high inclination. All ground-based observations have limited detection efficiency in the direction of the Milky Way because of stellar confusion. Existence or not of these bright objects will give fundamental clues on the formation mechanism of the Edgeworth-Kuiper Belt and the outer solar system. For the largest Centaurs which will be cruising at 10 to 30 AU from Gaia, it should be possible to resolve them, providing the only direct measurement of the size of these objects, and hence of their albedo, besides Pluto. Among the ~ 50 objects detected by Gaia, a handful should be binary systems. With the astrometric accuracy of Gaia, it will be possible to detect this binarity, and even to determine the orbits, providing a direct measurement of the mass of these objects. This sample will be a noticeable fraction of masses known at that time, allowing an estimate of the volume bulk density.

2.1.4 Extra-solar Planets

The size of the stellar sample out to 150-200 pc to be investigated for planets (comprising hundreds of thousands of objects) constitutes the most significant contribution that Gaia will provide to the science of extra-solar planets. Indeed, the results derived from Gaia's μas -precision astrometric measurements will help to decisively improve our understanding of orbital parameters and actual mass distributions. Gaia will thus provide important data to constrain theoretical models of formation, migration and dynamical evolution of planetary systems.

Within 200 pc from the Sun, and limiting counts to bright solar-type main-sequence stars (i.e. stars brighter than 13-th magnitude and with spectral types earlier than K5), about 3×10^5 objects are predicted to exist: Gaia will be able to discover thousands of planets around these stars, and will accurately measure the orbital

characteristics and actual masses for a significant fraction of the detected systems. Simulations indicate that Gaia will detect all existing Jupiter-mass planets within 50 pc and with periods between 1.5 and 9 years. Employing a standard Galaxy model and planetary frequencies from recent radial velocity surveys, studies predict somewhere around 10 000 detections of Jupiter-mass planets, depending on the details of the detection or orbital distribution hypothesis.

The frequency of multiple-planet systems, and their preferred orbital spacing and geometry, is not currently known. Star counts predict $\sim 13\,000$ stars up to 60 pc: Gaia, with its high-precision astrometric surveys of the solar neighbourhood, will observe each of them, searching for planetary systems composed of massive planets in a wide range of possible orbits, making precise measurements of their orbital elements, and establishing quasi-complanarity (or non-complanarity) for detected systems with favorable configurations.

2.1.5 Observations of Quasars and AGN

Gaia will provide astrometric and photometric observations for about 5×10^5 quasars (QSOs) down to 20-th magnitude over the whole sky, 5 times more than the number expected from the Sloan Digital Sky Survey. The Gaia data set will constitute the first all-sky survey of optically-selected active galactic nuclei (AGN) and QSOs. AGN and QSOs are of prime importance in establishing the relativistic reference frame, one of the scientific objectives of the Gaia mission. Gaia's QSO sample will have a profound impact on studies of the large-scale structure of the Universe. Their spectroscopy will allow the gas content in distant galactic haloes and in intervening intergalactic clouds to be probed. In addition, about 2000 QSOs in the final sample are expected to be lensed by a foreground galaxy, and 50% of these should directly be identified as multiply-imaged objects thanks to Gaia's reconstructed sky-mapper images. This number is an order of magnitude larger than the number of known lensed QSOs. The number and properties of lensed QSOs in a complete sample contain information on the nature of distant lensing galaxies and on the geometry of the Universe. Thus, Gaia also offers the prospect of constraining the values of cosmological parameters.

Since QSOs only represent 0.05% of the objects detected by Gaia, it is crucial to discriminate them from the much more numerous stars. The precision of Gaia's astrometric measurements allows to recognize QSOs from their lack of proper motion and parallax, and the photometric data collected during the 5-year mission lifetime can detect their variability.

2.1.6 Microlensing

Gaia can observe gravitational microlensing by measuring the photometric amplification of a background source star at epochs when it is coincidentally aligned with a foreground lens. The all-sky averaged photometric optical depth associated with such an alignment is $\sim 5 \times 10^{-7}$, hence there will be $\sim 7\,500$ photometric microlensing events during the Gaia's 5-year mission lifetime, most of which will have only a few data points because of the poor sampling. If photometry is combined with the measurements of the centroid of the two images of a microlensed source, then complete information about the distance and the mass of the lens can be obtained. One of the major scientific contribution of microlensing studies with Gaia will be the determination of the mass function in the solar neighborhood. Microlensing is the only known technique which can measure the masses of objects irrespective of whether they happen to be components of a binary system or emit electromagnetic radiation.

2.1.7 Fundamental Physics

With highly accurate positional measurements like those of Gaia, the minute effects of relativistic light bending caused by the Sun, planets and larger moons of our solar system must be taken into account. For example, photons detected by Gaia are bent during the last hours of their long journey, while traversing the solar system, under the influence of the gravitational fields of the Sun, planets, moon, asteroids, etc. The amount of this post-Newtonian light deflection depends on the mass of the perturbing objects, their distance to the observer (Gaia) and the angular separation at which the photons pass the objects. In the context of Gaia, correcting for solar-system light bending is critical because its astrometric measurements will be affected to a significant extent ($\sim 1\text{--}10 \mu\text{as}$) by all solar system bodies with radii larger than ~ 624 km (for Jupiter and Saturn, the quadrupole contribution of their gravitational fields should also be taken into account). Gaia's sophisticated data reduction will require accurate inclusion of these effects. Gaia's sensitivity also provides the opportunity to test General Relativity more stringently and in new observational domains, via the observation of the gravitational light bending and the perihelion precession of minor planets in the Solar System. At the level of accuracy expected from Gaia, even more subtle effects will start to become apparent, such as the quadrupole components of the gravitational fields of the Sun and the planets (Perryman et al. 1997), and the "frame-dragging" effects of their motions and rotations (see, e.g., Soffel 1989).

2.1.8 Distance and Ages Scale in the Universe

Gaia will have a major impact upon our knowledge of the distance scale in the Universe by providing accurate distances and physical parameters for all types of observable primary distance indicators in the Milky Way and in the closest galaxies of the Local Group. It will generate a complete sampling of these indicators versus the corrections due to metal, oxygen, or helium contents, color, population, age, and so on. In particular, Gaia will extensively observe many Galactic open and globular clusters and countless Cepheids and RR Lyraes, thus providing solid calibrations for cluster-sequence fitting and period-luminosity relations.

Major efforts have been made during the past decade to observe distance indicators in external galaxies (for example, the Hubble Space Telescope key project). Nowadays, the dominant contribution to the uncertainty on these distances, and hence on the most important cosmological parameter describing the Universe (the Hubble constant) is the uncertainty in the distance to the Large Magellanic Cloud (LMC). Gaia will provide a firm foundation to the sequence of steps leading to the determination of distances of far-away galaxies and, as a consequence, to the determination of the Hubble constant by measuring individual trigonometric distances to the Cepheids and brightest stars of the LMC. Moreover, Gaia will establish a first check of the universality of the period-luminosity relationship for pulsating variables, with direct distances of all Galactic and LMC Cepheids and with mean Gaia distances for Cepheids in the closest galaxies of the Local Group.

Moreover, Gaia will touch a second crucial parameter for the description and understanding of the Universe: its age. The accurate determination of the distances of the oldest objects in the Galaxy, namely subdwarf stars and globular clusters, combined with a fit to theoretical models of stellar evolution, will lead to a precise estimation of their ages. These age estimates naturally provide a lower limit to the age of the Universe.

2.2 Mission timeline and data release

The first ideas for Gaia began circulating in the early 1990's, culminating in a proposal for a cornerstone mission within ESA's science programme submitted in 1993, a workshop in Cambridge in June 1995 to discuss possibilities and, following a 2-year Concept & Technology Study Phase, the selection of the Gaia mission by the ESA Science Programme Committee in 2000.

The results of the Concept & Technology Study indicated that a launch in 2009-10

Gaia: taking the galactic census

was feasible, and that a period of technological development would be required in advance of the detailed design and construction phase, in order to gain full confidence in the required technology. This technology phase was scheduled to run between 2002-04.

Gaia was originally foreseen to be launched by Ariane 5, but a further industrial study was carried out in early 2002 to assess accommodation within the smaller (and cheaper) Soyuz launcher. The studies were completed, a workable design with only small accuracy degradation was identified, and the Gaia mission was reconfirmed within the ESA science programme in mid-2002.

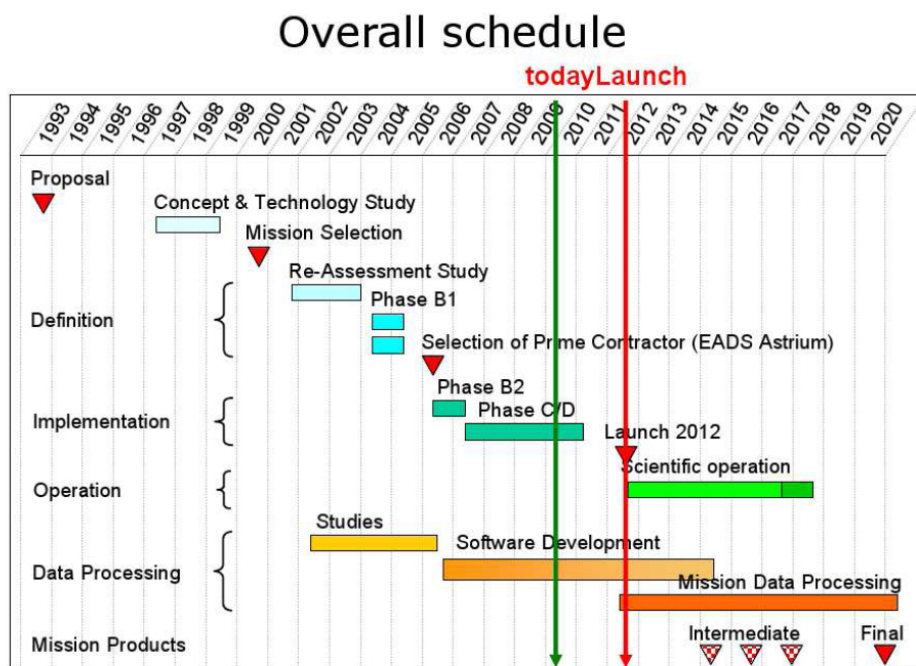


Figure 2.1: The figure shows the overall Gaia mission timeline. At the present time, the launch has been deferred and it is foreseen in March 2013. Image credit: ESA.

A series of industrial technology studies ran between 2002-05, in parallel with many further feasibility and assessment studies by European scientists involved in the Gaia programme. The data simulation chains, prototype analysis algorithms, and a prototype reduction system were studied during this period. With reasonable confidence in the critical hardware (detectors, optics, etc.) and the critical scientific elements,

ESA issued a competitive call for the industrial phase in mid-2005. In early 2006, the contract for Phases B2/C/D was agreed between ESA and the industrial prime contractor, EADS Astrium SAS.

A final phase of detailed design lasted until early 2007. In parallel, the scientific community began its preparatory phase for handling the huge amounts of data that will flow from the satellite after launch.

We are presently in technical development phase C/D, and the hardware is being built, tested and assembled. The software development is presently producing and testing pipelines with the aim of delivering to the astrophysical community a full catalogue and dataset ready for scientific investigation.

Operations and observations will extend for 5(+1) years², during which period the data analysis will be ongoing.

A final phase of 2-3 years will be required to tie up the data analysis in advance of data release to the scientific community. Apart from the end-of-mission final data release, foreseen around 2020, some intermediate data releases are foreseen. In particular, there should be one first intermediate release covering either the first 6 months or the first year of operation, followed by a second and possibly a third intermediate release, that are presently being discussed. The data analysis will proceed in parallel with observations, the major pipelines re-processing all the data every 6 months, with secondary cycle pipelines (dedicated to specific tasks) operating on different timescales. In particular, verified science alerts, based on unexpected variability in flux and/or radial velocity, are expected to be released within 24 hours from detection, after an initial period of testing and fine-tuning of the detection algorithms.

2.3 Launch and Operations

Gaia will be launched by a Soyuz-Fregat launch vehicle (consisting of the latest evolution of the Soyuz rocket, Fregat upper stage and an enhanced ST fairing to accommodate extended payloads) from the European Spaceport in Kourou, French Guiana.

Gaia will operate in the vicinity of the second Lagrange point (L2), approximately 1.5 million km from the Earth, along the Sun-Earth line in the direction opposite

²If, after careful evaluation, the scientific output of the mission will benefit from an extension of the operation period, the satellite should be able to gather data from one more year, remaining within the Earth eclipse (see Section 2.3).

to the Sun. The region around L2 is a gravitational saddle point, where spacecrafts can be maintained at roughly constant distance from the Earth for several years by small and cheap manoeuvres.

Around L2 there is a circular zone of radius $\simeq 13\,000$ km where the Sun is always eclipsed by the Earth. Here the solar panels of a spacecraft would be unable to generate sufficient power since they would not receive enough sunlight. In addition, even entering this region for a few minutes would generate a detrimental thermal shock in the spacecraft. Therefore, Gaia will be placed in a large Lissajous orbit ($\simeq 300\,000$ km) around L2 to ensure that it stays away from the eclipse zone for at least six years. The constant pull exerted by the Sun and the Earth will cause Gaia to swing around L2 on a nearly periodic circuit and six months will be needed to complete a full cycle (see Fig.2.2).

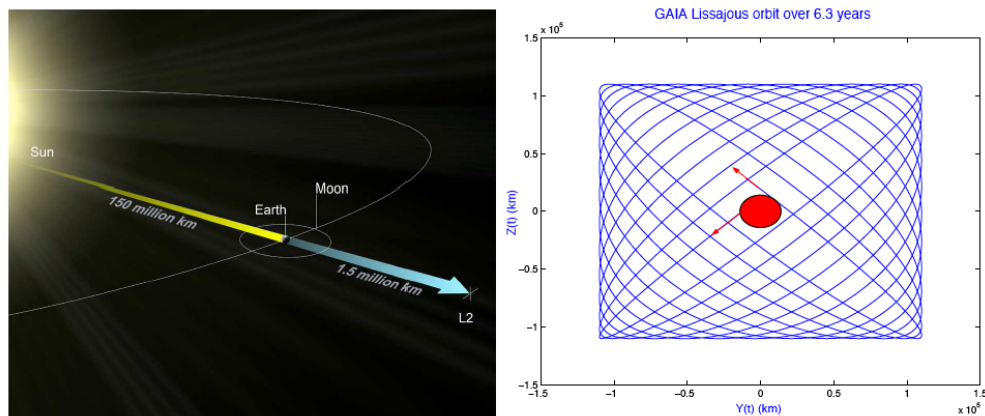


Figure 2.2: The *left panel* show a schematic view of the L2 point. The *Right Panel* shows an example of a Lissajous orbit projected on the plane perpendicular to the Earth-L2 line, as seen from the Earth. The initial conditions are chosen such that the orbit wanders outside the Earth shadow (red circle at the center) until the occurrence of the next eclipse more than six years later. Image credit: ESA.

The selection of the orbit arises from a trade-off between communication, operation, cost, thermal and radiation environment and accessibility with current rockets. Around L2 one benefits from a virtually unchanging environment with very stable thermal conditions, an essential asset for the success of the mission. The optics are

so sensitive to minute changes of temperature that a variation of less than one thousandth of a degree over a few hours would disturb the alignment of the mirrors and degrade the quality of the images.

Gaia will first be launched into low-Earth orbit and then injected into a smooth transfer orbit for a quiet trip of about one month to its final Lissajous orbit around L2, where the observation will commence for a mission lasting at least 5 years. After separation from the launcher, solar array deployment, spin rate and axis control will be performed autonomously by the spacecraft.

Mission operations will be carried out by ESOC (Germany). These will comprise spacecraft operations (mission planning, spacecraft monitoring and control, and all orbit and attitude determination and control) as well as scientific instrument operations (functional quality control and collection of the science telemetry). Two ground stations will receive the compressed Gaia data during the 5 years of operation: Cebros (Spain) and New Norcia (Australia). The data will then be transmitted to the main data-centers throughout Europe to allow for data processing.

2.4 Gaia Scanning Law

During its 5-year operational lifetime, the satellite will continuously spin around its axis, with a constant speed of 60 arcsec/sec. As a result, over a period of 6 hours, the two astrometric fields of view will scan across all objects located along the great circle perpendicular to the spin axis (see Fig.2.3, left panel). As a result of the basic angle of 106.5° separating the astrometric fields of view on the sky (Fig. 2.5), objects will transit the second field of view with a delay of 106.5 minutes compared to the first field. Gaia's spin axis does not point to a fixed direction in space but is carefully controlled so as to precess slowly on the sky. As a result, the great circle that is mapped out by the two fields of view every 6 hours changes slowly with time, allowing repeated full sky coverage over the mission lifetime.

The "scanning law" prescribes how the satellite's spin axis evolves with time during the mission. The optimum scanning law maximizes the angle ξ between the Sun and the spin axis at all times³ and maximizes the uniformity of the sky coverage after 5 years of operation. Thermal stability and power requirements, however, limit ξ to about 45° . The best strategy for Gaia is to let the spin axis precess around the

³This requirement results from the fact that the parallactic displacement of transiting stars is proportional to $\sin\xi$: a higher value of ξ thus leads to larger measurable parallaxes and higher end-of-mission astrometric accuracies.

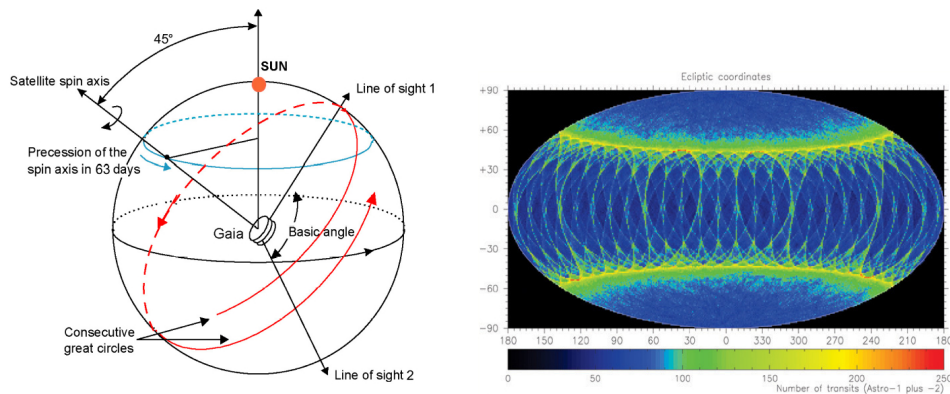


Figure 2.3: *Left panel:* graphical representation of the Gaia scanning law (see text). *Right panel:* mapping of the sky coverage, i.e., number of Gaia passages on the sky, in ecliptic coordinates. Image credit: ESA.

solar direction with a fixed angle of 45° . This combination of a spinning satellite, scanning the sky along great circles and a precession of the spin axis is referred to as *revolving scanning*, and was successfully adopted during the Hipparcos mission. The actual speed of precession of the spin axis on the sky should be small enough that consecutive great-circle scans overlap sufficiently, and large enough that all stars on the sky transit the astrometric fields sufficiently often. The above requirements have been worked out in detail for Gaia, leading to an optimum nominal scanning law. For a spin rate of 60 arcsec/sec and a solar aspect angle of 45° , the precession speed is such that 5 years of operation correspond to 29 revolutions of the spin axis around the solar direction; the precessional period thus equals 63 days.

On average, every sky region will be scanned 70–80 times, with regions lying at $\pm 45^\circ$ from the Ecliptic Poles being scanned on average more often than other locations. Each of the Gaia targets will be therefore scanned (within differently inclined great circles) from a minimum of approximately 10 times to a maximum of 250 times (see Fig.2.3, right panel). Only point-like sources will be observed, and in some regions of the sky, like Baade’s window, ω Centauri or other globular clusters, the star density of the two combined fields of view will be of the order of 750 000 or more per square degrees, exceeding the storage capabilities of the on-board processors, so Gaia will not study in detail these dense areas.

2.5 Spacecraft overview

The Gaia spacecraft (Fig. 2.4) provides all necessary support to the payload instrumentation. Generally, the spacecraft subsystems follow well-established spacecraft engineering approaches, although specific innovative features are needed for Gaia, for example for the mechanical and thermal configuration, and for the telecommunication subsystem.

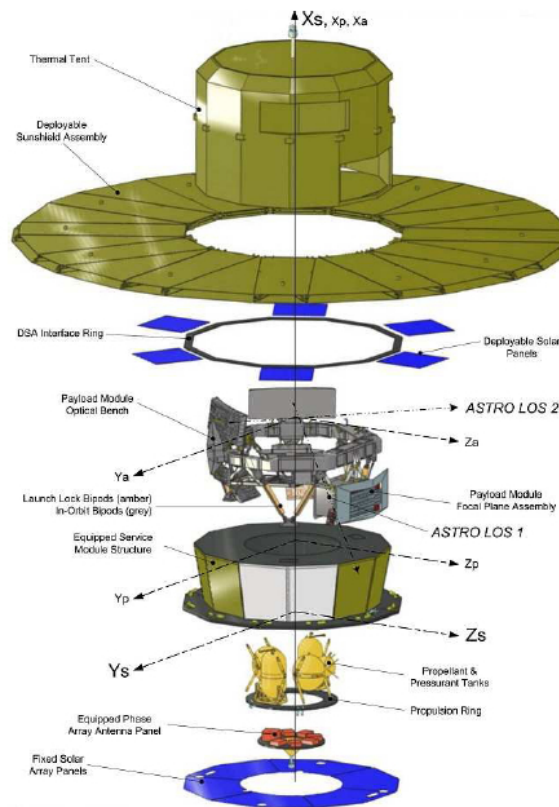


Figure 2.4: A schematic view of the adopted design of the Gaia spacecraft. Image courtesy of EADS Astrium.

- *Mechanical design:* The main structure, of hexagonal conical shape to avoid turning shadows on the sunshield, is an aluminium structure with carbon-fibre reinforced plastic (CFRP) walls, and a central tube supporting the propellant tanks. The deployable solar array is made of six panels (CFRP structure back-insulated with multi-layer insulation, and shape-memory alloy hinges)

and completed with a sunshield made of multi-layer insulation sheets with Kevlar cables for deployment post launch.

- *Thermal control:* the very high stability thermal control is achieved through optical solar reflector material, multilayer insulation sheets on the outer faces of the service module, and a black painted cavity with a heat pipe network.
- *Propulsion and attitude control:* after injection into its L2 transfer orbit, a chemical bi-propellant propulsion system is used for the transfer phase (attitude acquisition, spin control, mid-course corrections, L2 orbit injection, and safe mode). One redundant set of cold-gas thrusters will control the operational orbit and spin motion once at L2. Three Sun acquisition sensors plus one gyroscope provide spin-axis stabilisation during the transfer phase, with one large field of view star sensor plus use of the main instrument sky mappers for the 3-axis controlled operational phase.
- *Payload data handling:* dedicated processing electronics are provided for the computationally intensive tasks of on-board object detection, attitude determination, window allocation, data compression, and temporary storage (a solid state memory of around 600 Gb). The typical (continuous) payload data rate is about 1 Mbps.
- *Power and electrical subsystem:* the required solar-array area is split into a number of deployable and fixed panels, with GaAs (gallium arsenide) cells on a CFRP structure. A lithium-ion battery is used for launch and early-orbit operation.
- *Communications:* telemetry and telecommand employs X-band up- and down-links with a few kbps capacity and an omni-directional coverage. The science telemetry X-band down-link has 4-8 Mbps capacity which is used during each ground station visibility period (of about 8 hours per day), based on a set of electronically-scanned phased array antennae accommodated on the service module panels.

2.6 Payload and telescopes overview

The spacecraft and payload configuration was re-optimised by the industrial teams in their Phase B2/C/D proposal in response to the mission requirements document issued by the ESA project team in 2005. As a result, from early 2006, the final Gaia

payload looks somewhat different from the previous design, although all functionality is preserved.

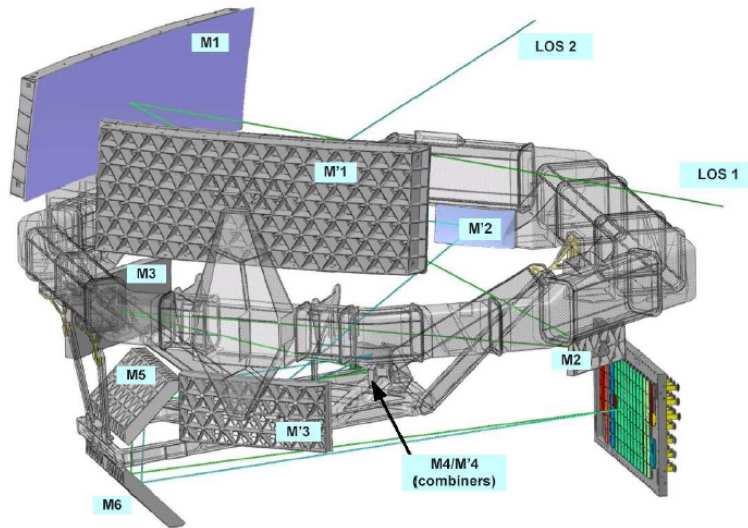


Figure 2.5: Schematic view of the dual telescope system: light from each line-of-sight (LOS) is reflected by a series of mirrors (M1-M4, M1'-M4'); followed by M5-M6) to the common focal plane. Image credit: EADS Astrium

The previous design had two separated telescopes, with one comprising the two astrometric viewing directions with a combined focal plane with broad-band photometric filters; the other comprising the medium-band photometry and radial velocity spectrometer. The new Gaia payload combines all functions into a single telescope structure. The photometric measurement concept has also been substantially revised: in place of a series of broad- and medium-band filters, two dispersive prisms now provide full spectral coverage over the entire optical wavelength.

The new (post-2006) payload concept is now characterised as follows (Fig.2.5):

- a dual telescope, with a common structure and common focal plane. Each telescope is based on a three-mirror anastigmatic design with three flat-folding mirrors, the two viewing directions are separated by a 106.5° basic angle. The two telescopes have rectangular entrance pupils ($1.45 \times 0.5 \text{ m}^2$) and large focal lengths (35 m). A CCD pixel size of $10 \mu\text{m}$ in the along-scan direction

has been selected. With the 35 m focal length, corresponding to a plate scale of $170 \mu\text{m}/\text{arcsec}$, this allows a 6-pixel sampling of the diffraction image along scan. The field of view of both telescopes is unvignetted and covers 0.45 deg^2 per telescope. The across-scan height of 0.7° is sufficient to avoid gaps in the sky coverage resulting from the slow continuous precession of the spin axis;

- the optical system is compact, with an optical-bench diameter of about 3 m, and is housed within a mechanical structure adapted to the Soyuz-Fregat launcher fairing. The optical design allows high-quality imaging, both in terms of wave-front errors (WFEs) and (optical) distortion. The total, effective RMS WFE over the astrometric field of view, including optical design, manufacturing and integration, alignment, and cool-down, is 46 nm. The total, effective RMS distortion over the astrometric field of view, including payload optical design, manufacturing and integration, and in-orbit WFE compensation, is $1.3 \mu\text{m}$ (0.13 pixel) over a single CCD transit. The latter value is acceptable in terms of causing only limited along-scan blurring of star images during a CCD crossing. Although the optical design is fully reflective, based on mirrors only, diffraction effects with residual aberrations induce systematic chromatic shifts of the diffraction images and thus of the measured star positions. This effect, usually neglected in optical systems, is critical for Gaia. The overall system design is such that these systematic chromatic displacements, which can amount to $500 \mu\text{as}$ or more, will need to be calibrated as part of the on-ground data analysis using the colour information provided by the photometry of each observed object.
- the common focal plane is shared by all instruments, with the astrometric and photometric fields all having the same angular scale;
- the same type of CCD (pixel size and format) is used for all three instruments. A total of 106 CCDs and accompanying video chains are used, with a pixel size of $10 \mu\text{m}$ along scan and $30 \mu\text{m}$ across scan, TDI (time-delayed integration) mode operation, and an integration time of $\sim 4.4 \text{ s}$ per CCD.
- the use of silicon-carbide ultra-stable material for the mirrors and telescope structure, providing low mass, isotropy, thermo-elastic stability, and stability in moving from ground to space. Basic angle stability requirements are largely met with passive thermal control, and a highly robust basic angle measurement system is in place to measure any variation down to $0.5 \mu\text{as}$ per 5-minute

interval;

- the radial velocity spectrometer is an integral field spectrograph with a resolving power of 11 500. It uses a grating plate and an afocal field-corrector lens located close to the focal plane;

These primary instruments are supported by the opto-mechanical-thermal assembly comprising:

- the single structural torus supporting all mirrors and focal planes;
- a deployable sunshield to avoid direct Sun illumination and rotating shadows on the payload module, combined with the solar array assembly;
- control of the heat injection from the service module into the payload module, and control of the focal plane assembly power dissipation in order to provide an ultra-stable internal thermal environment;
- an alignment mechanism on the secondary mirror for each astrometric instrument, with micron-level positional accuracy to correct for telescope aberration and mirror misalignment at the beginning of the mission.

2.6.1 Radiation damage

When operating electronic equipment in space, one of the most important considerations is always the energetic particle radiation environment. For Gaia, which will operate at L2, this environment will be particularly critical because the large astrometric focal plane (carrying 106 CCD detectors) will be very difficult to shield. Radiation damage to the CCDs will degrade their performance and hence the overall performance of Gaia.

There are three main sources of damaging particles:

- *Galactic Cosmic Rays*: very high energy particles (typically hundreds of MeV) trapped in the galactic magnetic field. These are mainly generated by supernovae and are just passing through our Solar System. The rate observed varies between about 4–8 particles per cm² per second, depending upon the phase of the solar cycle and they comprise approximately 90% protons, 9% He ions and 1% heavier ions. It is not possible to shield effectively against galactic cosmic rays because their energy is high enough to penetrate many centimeters of shielding.

- *Solar Particles*: particles ejected directly from the Sun. The solar particle flux varies from essentially zero during solar quiet times to thousands of particles per cm^2 per second during periods of high solar activity. Like galactic cosmic rays, solar particles are predominantly protons and helium ions. However, the peak energy of the solar proton spectrum is several orders of magnitude lower than that of the galactic cosmic ray spectrum, so that shielding can be effective in reducing the dose to sensitive components.
- *Trapped particle environment*: these are protons and electrons trapped in the Earth's magnetic field to form the "radiation belts". This environment is not relevant for Gaia which will be situated at L2.

During solar-quiet observing periods, there will always be a particle flux of between 4 and 8 galactic cosmic rays per cm^2 per second passing through the Gaia CCDs. These background particle events will affect Gaia astrometric observation essentially in two ways. First of all, particle events which can be incorrectly identified as sources, could erroneously be assigned windows, tracked across the focal plane and transmitted to the ground. This is clearly a waste of resources and a reliable on-board rejection algorithm is required. On the other hand, particle events detected in a CCD, close to a source Point Spread Function (PSF) will introduce PSF distortion and hence centroiding errors. These errors need to be quantified and mitigation techniques assessed.

2.6.2 The Gaia Focal Plane

The Gaia focal plane will be the largest ever developed, with 106 CCDs, a total of almost 1 Gigapixels and physical dimensions of about $0.5 \text{ m} \times 1 \text{ m}$.

Given the concept of Gaia as a scanning instrument, the payload focal plane assembly (FPA) is designed around a mosaic of CCD chips operating in TDI (time-delayed integration) mode. All CCDs have the same format, are derived from e2v Technologies design and are large-area, back-illuminated, full-frame devices. A schematic view of the CCD characteristics is reported in Table 2.1. During nominal operations, the satellite spin rate, and thus the speed with which objects traverse the focal plane, is continuously synchronized with the fixed TDI period of the CCDs. As a result, stars cross the focal plane at a constant speed (60 arcsec s^{-1}) and star images are progressively built up as objects cross the CCDs. At the end of each CCD crossing, the generated charge packets are transferred to the serial register for read out and, subsequently, pass through digital processing, temporary on-board storage, and

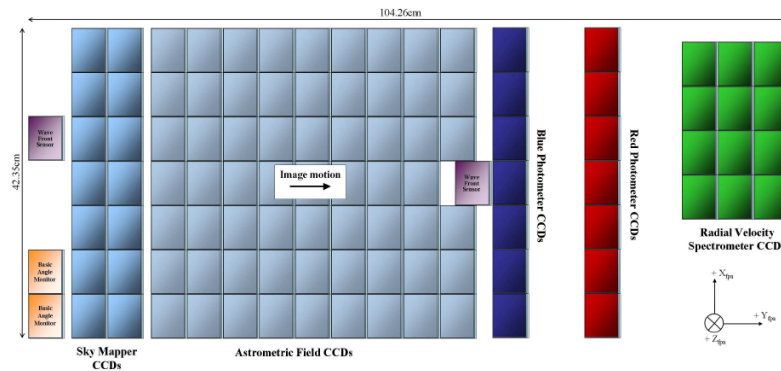


Figure 2.6: The Gaia focal plane. The viewing directions of both telescopes are superimposed on this common focal plane which features 7 CCD rows, 17 CCD strips and 106 large-format CCDs. Star images cross the focal plane from the left at a constant speed of 60 arcsec/sec. Image courtesy of ESA - A. Short.

transmission to the ground.

The 106 detectors are distributed over the focal plane as shown in Fig.2.6. A wave-front sensor (WFS) and two basic-angle monitors (BAM) are used to measure the optical quality of each telescope and to monitor fluctuations in the basic angle, respectively. The objects enter the focal plane from the left and cross one CCD in 4 seconds. The first two columns, the Sky Mappers (SM1 or SM2), perform the on-board detection of point-like sources, each of the two columns being able to see only one of the two lines of sight. After the objects are identified and selected, small windows are assigned which follow them in the Astrometric Field CCDs (62 detectors), where white light (or G-band) images are obtained (Section 2.8). Immediately following the Astrometric Field, two additional columns of CCDs (14 detectors) gather light from two slitless prism spectrographs, the Blue (Spectro)Photometer (BP) and the Red one (RP), which produce dispersed images (Section 2.9). Finally, objects transit on the Radial Velocity Spectrometer (RVS) CCDs (12 detectors) to produce higher resolution spectra around the Calcium Triplet (CaT) region (Section 2.10).

The detailed design of the focal plane is the result of many, often competing, requirements. For example, the FPA-mosaic dimension has been selected to be large enough to offer a large field of view, and thus a sufficiently large observing time for each object, to meet the end-of-mission scientific performance requirements, while keeping the total number of CCDs manageable in the light of manufacturing, testing, integration, power requirements, thermal-stability characteristics, launch schedule, cost,

Table 2.1: Gaia CCD characteristics

	pixel size along scan	$10\mu\text{m}$
	pixel size across scan	$30\mu\text{m}$
	nr. of pixels along scan	4500
	nr of pixels across scan	1966
	TDI lines per CCD	4500
	Operational temperature	$-115\text{ }^\circ\text{C}$

and so on. Similarly, the chosen (along-scan) CCD pixel size is small enough to offer sufficient spatial resolution to allow extraction of the centroid position of diffraction images with adequate precision, yet large enough to be feasible with currently available CCD technology in terms of quantum efficiency, modulation-transfer function, noise characteristics at the required read-out rates and manufacturing yield, etc. The number of TDI lines per CCD has been chosen large enough to yield sufficient signal-to-noise for faint stars at the CCD-transit level, yet small enough to avoid performance degradation due to “image smearing” caused by attitude disturbances, scanning-law effects, distortions, radiation-damage driven charge trapping and de-trapping and so on.

2.7 Object Detection, Sampling and Windowing

Gaia’s main goal is to provide an astrometric catalogue of objects complete down to magnitude 20. Since similar catalogues in the Gaia photometric passband (G) and with the Gaia spatial resolution do not exist, Gaia, unlike Hipparcos, can not operate based on the principle of a pre-compiled input catalogue. For this reason, the Sky Mapper CCDs have to perform an *autonomous on-board object detection*. This kind of operation has two associated advantages:

1. on-board detection allows “special objects” such as supernovae and NEOs to

2.7 Object Detection, Sampling and Windowing

be naturally detected and observed

2. on-board detection allows object selection and object windowing, significantly limiting the number of CCD pixels which have to be read (hence improving CCD noise performances) and the amount of data which have to be transmitted to the ground

Developing a suitable detection algorithm is subject to many trade-offs between scientific requirements (reliable discrimination between stars, double stars, extended non-stellar objects, blended stars, saturated stars, and prompt-particle events such as cosmic rays or solar protons; functional over the magnitude range 6-20; stable under the peculiarities of the real sky, and so on) and operational constraints (operation compliant with real-time constraints; on-board processing architecture and on-board processing power, and so on). Then, the detection algorithm has an impact on the Gaia scientific return: the number and nature of the sources observed and the completeness of the Gaia Catalogue (and any selection biases) will depend on the detailed characteristics of the detection algorithm.

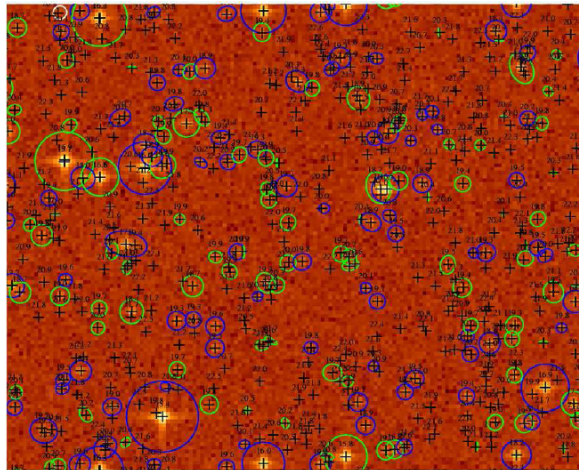


Figure 2.7: Simulation, based on HST data, of Baade's Window observed by one Gaia's Sky Mapper. A Sky Mapper sample is composed by 2×2 binned pixels. Black crosses indicate all stars up to magnitude 23. Detections are shown with blue and green ellipses, corresponding to objects classified as single and multiple stars respectively. Image courtesy of ESA -C. Babusiaux.

The most recent prototype algorithm, which is based on a thresholding philosophy, accounts for saturated stars, does not generate false detections on stellar diffraction spikes, and it is able to detect close double stars allowing for a correct window assignment to cover both components. In a field of average stellar density, a 99% detection completeness for single stars is obtained at magnitude 20, with less than one false detection per million sample. Baade’s Window is the challenging archetype of a large-scale high-density field which has to be managed in real time. Fig.2.7 shows a 13×32 arcsec² image simulated with the GIBIS Gaia Simulator (developed by Carine Babusiaux and colleagues) and based on a list of stars extracted from a high-resolution HST image. A detection rate of 86% at magnitude 20 without false detection is achieved: the incompleteness is mainly due to faint companions close to brighter primaries.

Given real-time processing constraints, limits on the acceptable CCD read-out noise and the limited telemetry bandwidth, not all CCD pixels data can be read and subsequently transmitted to the ground. A limited number of “windows”, regions of interest around objects, are therefore observed in the focal plane, thus effectively removing the “empty space between the stars” from the data stream. The object detection and confirmation tasks have to be accompanied by a selection step in order to decide which sources are tracked on in the remaining CCDs and how these objects are observed. The sample and window sizes for the different CCD strips and magnitude intervals were chosen to give an optimal astrometric, photometric and spectroscopic result for all stars, taking into account the resolution of the star images, the smearing of these images in the across-scan direction due to the continuous precession of the spin axis, the scientific interest (in double stars, for example), and the (variable) sky background. In order to optimize the signal-to-noise ratio of measurements, pixels that are read from the CCDs are generally binned on-chip in the across-scan direction to form samples. Normally, no on-chip (hardware) binning takes place in the along-scan direction in order to preserve the full angular resolution of the images.

2.8 Astrometry

The Astrometric Field CCDs will provide G-band images, i.e. white light images where the passband is defined by the telescope optics transmission and the CCD sensitivity, with a very broad combined passband ranging from 330 to 1050 nm and peaking around 500–600 nm (see Fig.2.8, left panel).

The main objective of Gaia’s astrometric data reduction system is the construction of core mission products: the five standard astrometric parameters, position (α , δ), parallax (π) and proper motion (μ_α , μ_δ) for all observed objects. The properties of Gaia’s optical and detector system are such that for stars brighter than $G \sim 12$ mag photon noise is negligible. The expected end-of-mission accuracy for these stars will be better than $10 \mu\text{as}$. For magnitudes between 12 and 20, photon noise determines the line-spread-function centroiding accuracies, and the expected end-of-mission astrometric accuracies are $20\text{--}25 \mu\text{as}$ for $G=15$ stars, and a few hundred μas at 20-th magnitude. At a given magnitude, astrometric accuracy also depends on apparent star color (i.e. intrinsic star color combined with interstellar reddening) through, for example, the wavelength-dependent properties of the modulation transfer function (the “image quality”), the quantum efficiency of the CCDs and the transmission of the optics. Generally, redder stars have smaller astrometric errors, as shown in Fig.2.9, produced using the Gaia Astrometric Accuracy Tool (GAAT⁴).

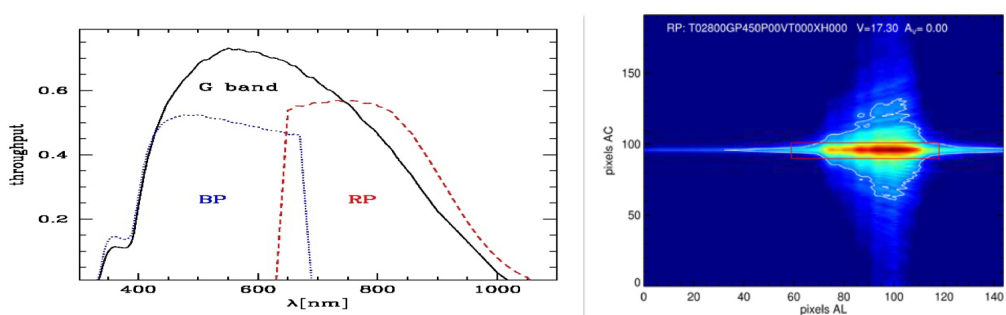


Figure 2.8: *Left panel:* the passband of the G-band, BP and RP. *Right panel:* a simulated RP dispersed image, with a red rectangle marling the window assigned for compression and ground telemetry. Image courtesy of ESA.

To reach these end-of-mission precisions, the average 70-80 observations per target gathered during the 5-years mission duration will have to be combined into a single, global and self-consistent manner. The ~ 40 Gb of daily telemetry data coming from the satellite are first processed by the Initial Data Treatment (IDT) which

⁴GAAT has been developed by the Gaia Project Scientist Support Team in order to carefully assess the impact of various design alternatives on the scientific value of the mission product, to optimize instrument parameters such as the mirror coating reflectivity, and to safeguard the mission objectives in general.

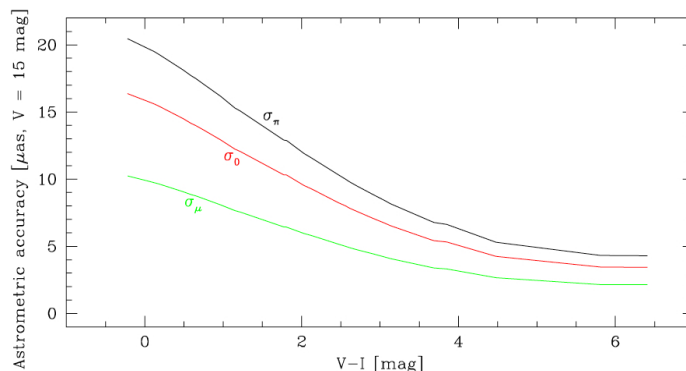


Figure 2.9: Results from the GAAT astrometric accuracy tool: predicted sky-averaged end-of-mission astrometric accuracies, at $V=15$ mag, and as a function of $V-I$ color index (black: parallaxes π in μas ; red: positions in μas ; green: proper motions μ in $\mu\text{as/yr}$). Image courtesy of ESA.

determines the image parameters and centroids. A second main task, the so-called “cross-matching”, links observation data to celestial objects. These outputs of IDT form the main input to the One Day Astrometric Solution (ODAS). ODAS produces from one day’s worth of data estimates for source positions, satellite attitude and calibration parameters at the level of sub-milli-arcsec accuracy. The results of the daily processing of IDT and ODAS are then written to the Main Database.

The next step, representing the Gaia’s core data processing module, is the Astrometric Global Iterative Solution (AGIS) system. AGIS processes together the satellite’s attitude and calibration parameters with the source parameters (treating them as unknowns) and tries to find the best global match in a least-square sense between all measurement data and an observational model (which is formulated in terms of these unknowns). Numerically this is done through an iterative adjustment of the parameters from a starting point to an approximation to the sought solution of the least-square problem. The system is considered converged and iterations are stopped if the adjustments become sufficiently small. At this point the results are written back to the Main Database. The fact that attitude and calibration parameters are optimized together with the source parameters in the same scheme is a necessity, since they cannot be determined to the required level of μas accuracy in any other way. This aspect of the astrometric data reduction is the reason why Gaia is sometimes referred to as a *self calibrating* mission. A schematic overview of Gaia’s astrometric data reduction system is shown in Fig.2.10.

Only stars that are flagged as single and non-variable (expected to be around 500 millions) will take part in such a “primary” AGIS cycle. For the remaining objects only provisional values will be computed by AGIS in a subsequent “secondary” cycle which only optimizes source parameters using the attitude and calibration solutions produced in the preceding primary cycle. Dedicated pipelines for specific kinds of objects (asteroids, slightly extended objects, binary and multiple systems, variable objects and so on) are being put in place to extract the best possible precision.

Unlike IDT and ODAS which run daily, AGIS is executed only about every 6 months, reprocessing all the acquired data, and therefore on an ever increasing data volume. Owing to the large data volume (100 Tb) that Gaia will produce and to the iterative nature of the processing, the computing challenges are formidable: the AGIS processing alone is estimated to require some 10^{21} FLOPs which translates to runtimes of months on the baselined 10 FLOP/s local computing system at ESAC (ESA’s European Space Astronomy Centre, in Spain near Madrid).

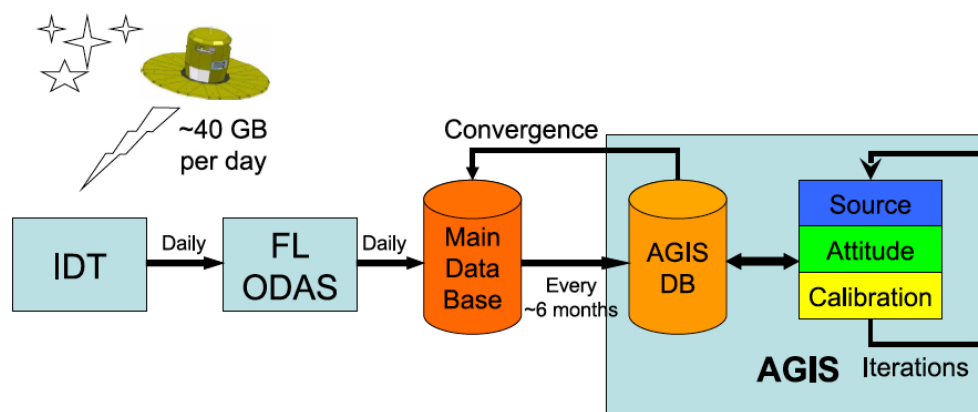


Figure 2.10: Simplified schematic overview of Gaia’s astrometric data reduction system. The main processing modules are IDT, FL-ODAS and AGIS which will iteratively generate the final astrometric mission products. Image courtesy of ESA.

2.9 Spectro-Photometry

If Gaia's astrometric measurements would be unsupported by appropriate diagnostic data, the final catalogue would contain immense numbers of positions and velocities of objects whose astrophysical nature would otherwise be unknown. With such limited data, the key objective of the mission (the study of the structure and history of the Milky Way) could not be met. Therefore, Gaia has been equipped with a photometric instrument with the goal of measuring the spectral energy distributions of all objects. These measurements can be used to derive astrophysical characteristics of all objects, such as effective temperature, gravity, mass, age and chemical composition (in the case of stars), and are indispensable in providing the basic tools for classifying stars across the entire HR diagram, as well as in identifying specific and peculiar objects.

The primary aim of the photometric instrument is mission critical to meet the astrometric performance requirements because the measured centroid positions must be corrected for systematic chromatic shifts induced by the optical system. This effect is usually neglected in optical systems, but was relevant for Hipparcos and becomes even more critical for Gaia. The chromatic image displacement depends on the position in the field and on the spectral energy distribution of the star, but not on its magnitude. For this reason, the knowledge of the spectral energy distribution of each observed target in the wavelength range covered by the CCDs of the main astrometric field is of fundamental importance, and the photometric instrument also covers this requirement.

Gaia's photometric system is based on a dispersive-prism approach such that the incoming light is not focussed in a PSF-like spot but dispersed along the scan direction in a low-resolution spectrum. The instrument consists of two low-resolution fused-silica prisms dispersing all the light entering the field of view. One disperser (BP) operates in the wavelength range 330-680 nm; the other (RP) covers the wavelength range 640-1050 nm (see Fig. 2.8). Both prisms have appropriate broad-band filters for blocking unwanted light.

The two dedicated CCD stripes cover the full height of the AF and use the SM function for detection and confirmation. Therefore, all objects that are imaged in the AF are also imaged in the BP and RP (Fig. 2.11). This means that astrophysical informations will not be limited to stars but will also be available for quasars, solar system objects and many other celestial bodies.

The resolution is a function of wavelength as a result of the natural dispersion curve

of fused silica; the dispersion is higher at short wavelengths, and ranges from 4 to 32 nm/pixel for BP and from 7 to 15 nm/pixel for RP. The spectral resolution $R=\lambda/\Delta\lambda$ ranges from 20 to 100 approximately. The variation across-scan direction does not exceed $\pm 9\%$ for BP and $\pm 4\%$ for RP. Both dispersers have been designed in such a way that BP and RP spectra have similar size (on the order of 45 pixel along scan). Window extensions meant to measure the sky background have been implemented.

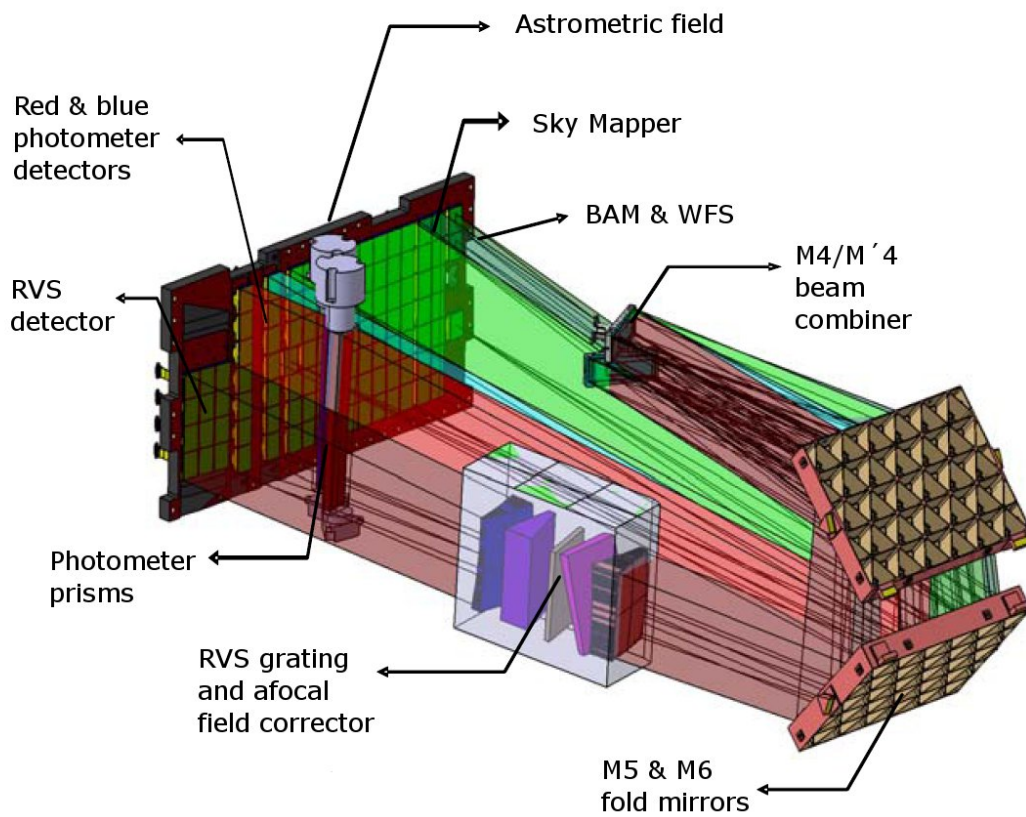


Figure 2.11: Schematic view of the Gaia instruments and the focal plane, with the path of light marked. Image courtesy of EADS Astrium.

2.10 Radial Velocity Spectrometer

The primary objective of the Gaia's Radial Velocity Spectrometer (RVS) instrument is the acquisition of radial velocities which, combined with positions, proper motions and parallaxes will provide the means to decipher the kinematical state and dynamical history of our Galaxy .

The RVS will provide the radial velocities of 100-150 million stars up to 17-th magnitude with precisions ranging from 10-15 km/s at the faint end to 1 km/s or better at the bright end. The RVS instrument is a near-infrared (847-874 nm), medium-resolution ($R = \lambda/\Delta\lambda \sim 11500$), integral-field spectrograph dispersing all the light entering the field of view. As seen in Fig.2.11, the RVS instrument is integrated with the astrometric and photometric instruments and telescopes, and the RVS CCDs are located on the Gaia focal plane (Fig.2.6). RVS uses the (astrometric) Sky Mapper function for object detection and confirmation. Objects will be selected for RVS observation based on measurements made slightly earlier in the Red Photometer. Light from objects coming from the two viewing directions of the two telescopes is superimposed on the RVS CCDs. The spectral dispersion of objects in the field of view is made by means of an optical module, physically located between the last telescope mirror (M6) and the focal plane. This module contains a grating plate, a filter plate, and four fused-silica lenses which correct the main aberrations of the off-axis field of the telescope. The spectral dispersion is oriented in the along-scan direction and a dedicated passband filter limits the throughput of the RVS to the desired wavelength range.

The RVS-part of the Gaia focal plane contains 3 CCD strips and 4 CCD rows. On the sky, the RVS CCD rows are aligned with the astrometric and photometric CCD rows. All RVS CCDs are operated in TDI mode. RVS spectra will be binned on-chip in the across-scan direction apart for bright stars, for which single-pixel-resolution window will be used.

On average, 40 transits will be collected for each object during the 5-year lifetime of Gaia, since the RVS does not cover the whole width of the Gaia AF (see Fig.2.6). In total, we expect to obtain some 5 billion spectra (single transit) for the brightest stars. The analysis of this huge dataset will be complicated, not only because of the sheer data volume, but also because the spectroscopic data analysis relies on the multi-epoch astrometric and photometric data. As a consequence, the extraction of radial velocities, astrophysical parameters, chemical abundances, rotational velocities and interstellar reddening from RVS observations will be performed in a

fully automated mode. Radial velocities will be obtained by cross-correlating observed spectra with either a template or a mask. An initial estimate of the source parameters derived from the astrometric and photometric data will be used to select the most appropriate template or mask. For stars brighter than ~ 15 -th magnitude, it will be possible to derive radial velocities from single-transit spectra whereas for fainter stars (down to ~ 17 -th magnitude) accurate summation of the ~ 40 single-transit spectra collected during the mission will allow the determination of mean radial velocities.

The multi-epoch radial-velocity informations provided by RVS will be ideally suited for identification and characterization of double and multiple systems. In particular, Gaia will provide masses and radii accurate to a few per cent for thousands of eclipsing binaries. The RVS will also monitor the radial motions of the outer layers of pulsating stars. It will provide pulsation curves for RR Lyrae stars, Cepheids, and Miras up to ~ 14 -th magnitude. Radial velocities will also be used to correct the astrometric data of nearby, fast-moving stars for the effects of “perspective acceleration”.

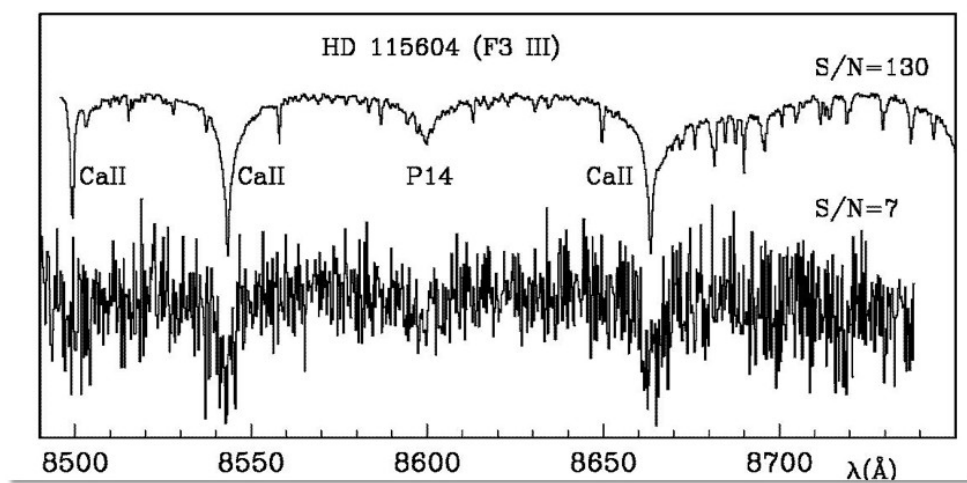


Figure 2.12: Simulated RVS end-of-mission spectra for the extreme case of one single transit (bottom spectrum) and of 250 transits (top spectrum). Image courtesy of ESA

The RVS covered wavelength range (847–874 nm, see Fig.2.12) is a rich domain, centered on the infrared calcium triplet and containing several atomic lines of var-

ious species. It will not only provide radial velocities, but also many stellar and interstellar diagnostics. It has been selected to coincide with the energy distribution peaks of G and K type stars, which are the most abundant targets. For these late-type stars, the RVS wavelength range displays, besides numerous weak lines due to Fe, Si and Mg, three strong ionized Ca lines (at around 849.8, 854.2, and 855.2 nm): this triplet allows for radial velocities to be derived even at modest signal-to-noise ratios. In early-type stars, RVS spectra may contain also weak CaII, HeI, HeII and NI, although they will be dominated by the Paschen lines. The RVS data will effectively complement the astrometric and photometric observations of Gaia's targets, improving object classification. For stellar objects, it will also contribute to the derivation of atmospheric parameters, in particular effective temperature, surface gravity, and individual abundances of key elements such as Fe, Ca, Mg, Si for millions of stars down to $G \simeq 12$, bringing major improvements in our knowledge of the chemical history and the enrichment processes of the Galaxy. Information on many facets of stellar physics will be extracted from the spectroscopic observations, for example, stellar rotation, chromospheric activity, and mass loss. Also, Diffuse Interstellar Bands (DIB) around 862 nm will enable the derivation of a 3-d map of interstellar reddening.

2.11 Gaia Data Treatment: the DPAC

ESA will take care of the satellite design, build and testing phases, of launch and operation, and of the data telemetry to the ground, managing the ESAC datacenter in Madrid (Spain).

The data treatment and analysis are instead a responsibility of the European scientific community. In 2006, the announcement of opportunity opened by ESA was successfully answered by the *Data processing and Analysis Consortium* (DPAC), a consortium that is presently counting more than 400 scientist in Europe (and outside) and more than 25 scientific institutions.

The DPAC should assure preparation of the data analysis algorithms to reduce the astrometric, photometric, and spectroscopic data within a coherent and integrated processing framework; on the other hand the DPAC is responsible for the generation and supply of simulated data to support the design, development and testing of the entire data processing system; the design, development, procurement and operation of all aspects of the hardware and software processing environment necessary to

process the mission data and finally the design and operation of the Gaia database. The DPAC executive body (DPACE) oversees the DPAC activities, and the work has been organized among a few *Coordination Units* (CU) each of them being responsible of a key aspect of the data treatment:

- **CU1. System Architecture** (manager: O' Mullane), dealing with all aspects of hardware and software, and coordinating the framework for software development and data management.
- **CU2. Data Simulations** (manager: Luri), in charge of the simulations of various stage of data products, necessary for software development and testing.
- **CU3. Core Processing** (manager: Bastian), developing the main pipelines such as IDT, AGIS and astrometry processing in general.
- **CU4. Object Processing** (managers: Pourbaix/Tanga), for the processing of objects that require special treatment such as minor bodies of the Solar System, for example.
- **CU5. Photometric Processing** (manager: van Leeuwen), dedicated to the BP, RP and M_G processing and calibrations, including image reconstruction, background treatment and crowding treatment, among others.
- **CU6. Spectroscopic Processing** (managers: Katz/Cropper), dedicated to RVS processing and radial velocity determination.
- **CU7. Variability Processing** (managers: Eyer/Evans/Dubath), dedicated to processing, classification and parametrization of variable objects.
- **CU8. Astrophysical Parameters** (managers: Bailer-Jones/Thevenin), developing object classification software and, for each object class, software for the determination of astrophysical parameters.
- **CU9. Catalogue Production and Access** (to be activated in the near future), responsible for the production of astrophysical catalogues and for the publication of Gaia data to the scientific community.

CUs may be sub-divided into smaller groups called *Development Units* (DU) and in charge of one or more work packages, and are flanked by a few working groups (WG) that deal with aspects that are either transversal among the various CUs (such as the GBOG, coordinating the ground-based observations for the external calibration

of Gaia) or of general interest (such as the Radiation Task Force, serving as the interface between DPAC and the industry in all matters related to CCD radiation tests).

2.11.1 The Italian contribution

Italian efforts for the preparation of Gaia, and the participation to the DPAC, are regulated by an INAF-ASI agreement with ESA. A coordination group (P.I. M. Lattanzi) manages the funding and activities, and contains representatives of the main Italian institutes involved in DPAC activities. In total, approximately 60 Italian scientists work in the DPAC, for a total of 36 FTE, who are involved in almost all of the CUs activities outlined in Section 2.11.

To summarize the main contributions, I firstly mention the most numerous group, involved in CU3 and also CU2 activities (INAF- OATO, University of Torino, Politecnico of Torino, University of Padova), dealing mainly with astrometry and fundamental physics. There is also a large group involved in CU5 (INAF-OABO, University of Bologna, INAF- ROMA, INAF-OATE, University of Roma, INAF-OAPD) that is responsible for all aspects of the external flux calibration of Gaia photometry and for other aspects of photometric processing such as crowding issues and image reconstruction. Finally, Italian scientists are also involved in CU7 (INAF-OACT, INAF-OABO, INAF-OANA) working on algorithms for the classification and parametrization of particular kinds of variable objects (mainly stellar pulsators), and in CU8 (INAF-OAPD, University of Padova, INAF-OANA, INAF-OACT) dealing mainly with spectral libraries for the classification and parametrization of stellar sources. Apart from these four main groups, there are also smaller groups or individuals that are DPAC active members on other topics.

All in all, Italy is one of the major DPAC contributors, both in terms of funding and in terms of FTE and responsibilities.

2.11.2 CU5: Photometric Processing

CU5 is responsible for the design, development, testing and implementation of the software for the photometric data processing, related calibrations and related shell tasks. The activities of CU5 are distributed over five management and technical support DUs (DU01 to DU05), and 9 development DUs (DU10 to DU18).

In the context of CU5, my work has been (and actually is) carried out in the framework of DU13 which, together with DU14, is dedicated to the external calibration of

Gaia spectrophotometric data.

In particular, the activities of DU14 are:

1. definition of the external (absolute) photometric calibration model for the G -band, G_{BP} and G_{RP} integrated photometry, and for the BP/RP spectra;
2. estimation/determination of the G, BP, RP filter transmission curves;
3. estimation/determination of the wavelength calibration as derived from the absolute flux calibration process of the mean BP/RP spectra;
4. LSF estimation/determination for BP/RP;
5. definition and development of the application software of the external flux calibration model.

I am involved in the activities of DU13, which can be roughly summarized as:

1. selection of a suitable number of SpectroPhotometric Standard Stars (SPSS), with magnitude and spectral-type range as required by DU14 model;
2. assessment of needed ground-based observations for all the selected SPSS;
3. acquisition and reduction of those observations, through the definition of precise protocols;
4. preparation of the data for the application in the CU5 pipeline.

A more detailed description of DU13 and DU14 general activities can be found in Chapters 3 and 4, respectively. My personal contribution within DU13 is presented in this thesis, from Chapter 5 to Chapter 10.

In van Leeuwen (2010), all the activities carried out by the various DUs within CU5 are defined. In brief, the 9 CU5 development DUs are in charge of:

- **Pre-processing of spectrophotometric Gaia data**, covered by DU10 (PSF/LSF and CCD calibrations) and DU11 (BP/RP extraction and initial data treatment). DU10 is in charge of creating the background solutions (incorporating CCD bias, charge release background and sky background) in order to perform the CCD one-day calibrations. Radiation damage mitigation via the application of a suitable charge distortion model will allow the CCD health monitoring and the analysis of radiation damage parameters and trends. The PSF/LSF

calibration process shall be driven, via analytical models, by the availability of suitable calibration sources. DU11 will provide the extraction of BP/RP spectra and integrated BP/RP fluxes for “normal” sources, bright (saturated) sources and complex or multiple systems, incorporating in the spectral extraction algorithm the background determination and the management of radiation damage effects, CCD bias non-uniformity effects and serial register CTI effects.

- **Internal calibrations**, covered by DU12 (internal calibration model) and DU16 (selections of internal reference sources). The main task of DU12 is to provide the internal calibration model, derived from a set of “well-behaved” transits of internal reference sources, selected by DU16, in order to report all observations to a “reference” instrument.
- **External flux calibrations**, covered by DU13 (ground-based observations) and DU14 (external calibration processing), see Chapters 3 and 4.
- **Application of Photometric Calibration**, covered by DU15. The activities of DU15 include the application of the internal and external calibration models to G-band photometry, BP and RP integrated fluxes and to the BP/RP spectra, the accumulation of epoch photometry (including the collection of data per source in terms of statistical parameters and their analysis) and BP/RP spectra, and the preparation of data release to the main data base hosted at ESAC.
- **Ancillary processes**, covered by DU17 (science alerts) and DU18, (source environment analysis). The activities of DU17 include the definition, development, test and implementation of methods to provide rapid detection of large flux anomalies, to classify these anomalies and to select candidates for suitable science alerts (i.e., to filter out likely spurious events and to identify common and less interesting variability effects in order to ensure that only high grade rare events trigger genuine alerts). The aim of DU18 is to produce an inventory of the sky immediately surrounding each source⁵ observed by Gaia. During the 5 year mission lifetime of Gaia, the content of these small sky regions are not static but change due to the proper motions and parallaxes of the various sources. This implies that the real meaning of “source environment analysis”

⁵The immediate neighborhood of a source has a diameter of 4.7" and 1.1" for the sky mappers (SM) and the astrometric field (AF), respectively

is to produce a model of the region of sky under consideration which includes at least the position, flux, proper motion, and parallax of each source.

3

Spectro-Photometric calibration

As explained by Bessell (2005), the purpose of the absolute spectro-photometry calibration is to place the measurements onto a standard physical flux scale by removal of the absorption by the Earth's atmosphere and calibration of the sensitivity of the photometric or spectroscopic equipment at different wavebands. For mainly historical reasons, but also for good practical reasons, astronomical photometric observations are calibrated through the use of networks of constant brightness stars rather than laboratory based calibration lamps of constant temperature. This means that, in order to determine the absolute spectral energy distribution of the observed objects, we have to compare their spectra with spectrophotometric standard star spectra. The ingredients of absolute calibration are therefore:

1. the data, i.e. observed magnitudes in various bands or spectra
2. the knowledge of (and correction from) the atmospheric absorption (obviously not needed for space observations)
3. the knowledge of the instrument response
4. the use of constant brightness standard stars as calibrators

These basic principles are common to the absolute calibration of any spectro-photometric system. What makes Gaia special with respect to the classical systems is the complexity of its instrument response (see below).

3.1 Classical Spectro-Photometric Calibration

A spectro-photometric system is defined by the relations:

$$m_i = ZP_p - 2.5 \log \int f(\lambda) T_i(\lambda) d\lambda \quad (3.1)$$

and

$$s(\lambda) = ZP_s [f(\lambda) T(\lambda)] \quad (3.2)$$

where:

- m_i is the observed magnitude in the i filter band
- $f(\lambda)$ is the stellar spectral energy distribution (SED) in photons $s^{-1} m^{-2} nm^{-1}$
- $T_i(\lambda)$ is the instrument response function over the i filter band
- $T(\lambda)$ is the overall instrument response function
- $s(\lambda)$ is the observed spectrum
- ZP_p and ZP_s are the respective zero points defined by a standard star (e.g., an unreddened A0V star, generally Vega).

In particular, $T(\lambda)$ includes several factors:

- the collecting area of the telescope primary mirror (entrance pupil area)
- the telescope (mirrors) transmission and optical characteristics
- the camera optics and the detector CCD quantum efficiency (QE)
- the filter-coating transmission
- the dispersing elements transmission (in spectrographs).

3.1.1 Atmospheric Extinction: the Bouguer's Law

Every object observed through the terrestrial atmosphere is affected by extinction and the longer the path length the starlight traverses through the atmosphere, the more it is dimmed. Extinction is a property of the atmosphere and it varies with location and altitude, but it is always composed by two components: absorption (light is absorbed) and scattering (light is deviated).

Three different sources originate scattering:

3.1 Classical Spectro-Photometric Calibration

- molecules (Rayleigh scattering), which are particles much smaller than the wavelength of the light. Their effect has a strong wavelength dependence proportional to λ^{-4} (this means that the extinction is stronger in blue light than in red, so the effect is a “reddening” of the observed object). The Rayleigh scattering also varies linearly with airmass. The airmass can be approximated as $\simeq \sec(z)$, where z is the angular distance from the zenith. This approximation is tolerable for zenith angles up to 60° , where the error is $\simeq 25\%$, but the error increases to $\simeq 10\%$ at $z=85^\circ$ (see Jurado Vargas et al. 2000 and references therein)¹
- aerosols, which are tiny particles of solid or liquid suspended in the air. Since the aerosol particles are usually bigger than the wavelength of light, there is no (or weak) dependence on wavelength;
- large dust particles scattering is to some extent wavelength independent (gray extinction).

More precisely, the total extinction is a combination of Rayleigh and aerosol scattering, ozone bands and telluric lines (due to O_2 , H_2O) absorption (see Fig. 3.1).

Atmospheric extinction is given by Bouguer’s law:

$$m_\lambda = m_{\lambda_0} + k_\lambda X \quad (3.3)$$

where:

- m_λ is the apparent magnitude of the observed star (at wavelength λ) including extinction wavelength-dependent effects and zero point;
- m_{λ_0} is the true stellar magnitude (at wavelength λ), as would be observed from outside the Earth’s atmosphere;
- k_λ is the extinction coefficient (at wavelength λ) expressed in magnitude/airmass;

¹In his classical work, Hardie (1959) gives a polynomial formula for calculating the airmass X from the zenith distance z . In his review, Young (1974) discussed airmass calculations and suggested a simpler formula, which takes into account not only the curvature, but also the refraction of the atmosphere: $X = \sec(z)\{1 - 0.0012[(\sec z)^2 - 1]\}$, which is valid up to $\sec z = 4$ and good to better than 1%.

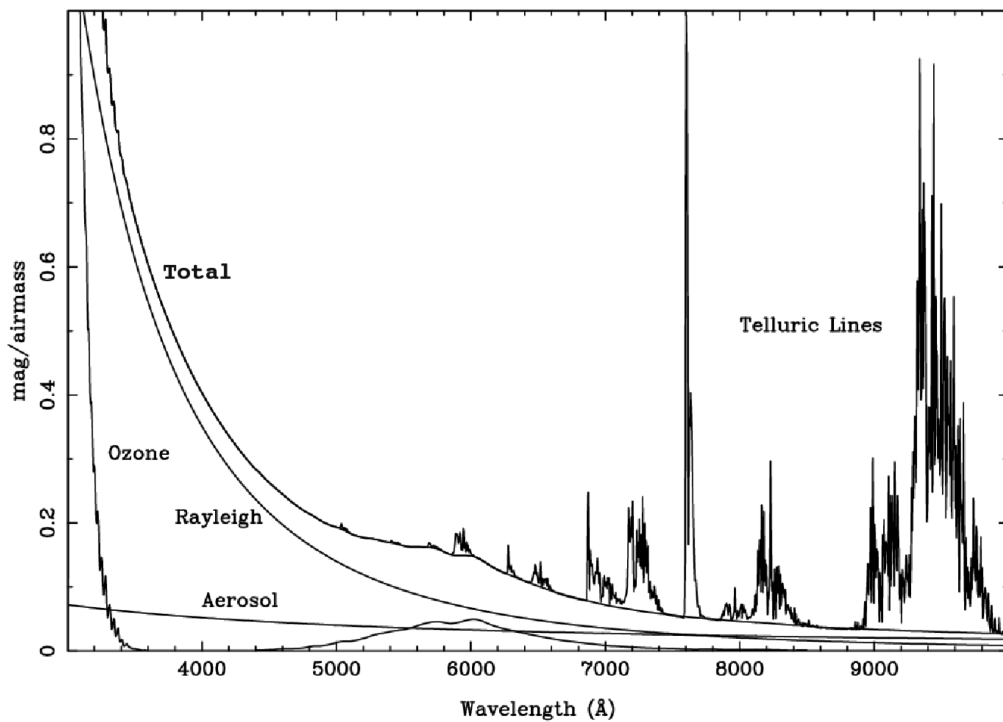


Figure 3.1: Simulation of a typical extinction by Earth's Atmosphere (magnitude/airmass versus wavelength), showing the relative contributions of Rayleigh and aerosol scattering, ozone and telluric line absorption. Figure adapted from Smalley et al. (2007).

- X is the airmass, representing the path length that light from celestial objects takes through the Earth's atmosphere relative to the length at the zenith: by definition, a source at the zenith has $X=1$.

According to equation 3.3, the extinction coefficient represents the difference in magnitude between the brightness of the star as observed at the zenith and the brightness that would be observed from outside the Earth's atmosphere.

Bouguer's law shows a linear behavior in the magnitude versus the air mass traversed by stellar light. However, it must be noted that this linearity only applies strictly to monochromatic magnitudes m_λ . For real observations in which a narrow-band or broad-band filter is used (for example U, B, V, R, I filters), the width of the passband

3.1 Classical Spectro-Photometric Calibration

complicates the classical Bouguer's formula: in this case k'_λ , a second order extinction correction term including parameters related to the spectral energy distribution of the observed star, must be incorporated in the equation. In this case equation 3.3 becomes:

$$m_i = m_{i,0} + k_i X + k'_{i,j} (m_{i,0} - m_{j,0}) X \quad (3.4)$$

where $k'_{i,j}$ is the second-order extinction coefficient in units of magnitudes per airmass per $(m_{i,0} - m_{j,0})$ color.

The second order extinction correction accounts for the effective wavelengths λ_{eff} shift :

$$\lambda_{eff} = \frac{\int \lambda F_\lambda S_\lambda d\lambda}{\int F_\lambda S_\lambda d\lambda} \quad (3.5)$$

where F_λ is the spectral energy distribution (SED) and S_λ is the system response. This λ_{eff} shift is due to different spectral energy distribution (i.e. different color $m_{i,0} - m_{j,0}$) of different stars. In other words, because λ_{eff} can be interpreted as the passband average wavelength, and because it is different for different SEDs, the corresponding extinction coefficient will be different, even if used to correct measurements obtained with the same broad band filter (even more: different stars observed at the same airmass with the same filter are affected by a different amount of extinction). Second order extinction correction has a bigger impact observing objects of extreme colors, and/or observing with bandpasses in which the extinction coefficient varies rapidly within the bandpass (e.g., the near-UV, see Fig. 3.1), since a small shift in the effective wavelength implies a significantly different extinction coefficient. The extinction coefficient can be determined by making multiple observations of a star spanning a suitable airmass range, large enough to get good leverage on the fit and to bracket the airmasses of all the scientific targets to be observed.

3.1.2 Instrument Response and Calibration

Calibrating spectro-photometric data obtained from the usual type of ground-based observations (broad-band imaging, spectroscopy) is not a trivial task, but the procedures are well known (see, for example, Bessell 1999) and several scientists have developed sets of standard stars appropriated for the more than 200 photometric system known, and for spectroscopic observations.

3.1.2.1 Photometry

The instrumental magnitudes, even when corrected for the extinction in the atmosphere, are still specific to our telescope and detector. To convert our magnitudes to a standard system we must derive calibration equations which relate them to the standard system. These equations can be derived through the observations of standard stars with known standard magnitudes and colors. Generally, the calibration equations are in the form:

$$M_i = m_{i,0} + ZP_{ij} + \alpha_{ij}^i(m_i - m_j) \quad (3.6)$$

where:

- M_i is the calibrated magnitude of a standard star (tabulated) in a chosen photometric band;
- $m_{i,0}$ is the extinction corrected instrumental magnitude of the same star in the same (or sufficiently similar) band;
- α_{ij}^i is the color term referred to a certain band (i) for the color ($m_i - m_j$);
- ZP_{ij} is the zeropoint constant.

The color term is mainly due to differences in the wavelength response (filter pass-band) between the system used and the standard one. However, the difference between our system and the standard system should be (and generally is) sufficiently small ($< \pm 0.05$ mag). If this is not the case, a second order color term is needed to take into account for the difference between the filter used and the standard filter defining the system, and eq. 3.6 becomes:

$$M_i = m_{i,0} + ZP_{ij} + \alpha_{ij}^i(m_i - m_j) + \beta_{ij}^i(m_i - m_j)^2 \quad (3.7)$$

where $\beta_{ij}^i(m_i - m_j)^2$ is the second order correction mentioned before.

Using our own observations of standard stars, which standard magnitude and colors we take from a catalog (e.g., Landolt 1992 for the Johnson–Cousins system), we can derive calibration equations which relate our instrumental colors to the standard colors by applying a linear regression.

In principle, only one red and blue standard stars are needed to solve for the calibration equation but, in practice, a few blue and red standard star are used in order to increase the accuracy and reliability of the solution.

3.1.2.2 Spectroscopy

For the spectra, usually the instrumental effect on the observed spectral energy distribution (SED) is parametrized as:

$$S_o(\lambda) = R(\lambda)S_t(\lambda) \quad (3.8)$$

where the observed spectra, $S_o(\lambda)$ is the result of the convolution of the “true” SED, $S_t(\lambda)$, with all the instrumental effects (optic trasmissivity, CCD quantum efficiency, ad so on), as shown in Fig.3.2. The instrumental effects are empirically determined in the form of a *response curve* $R(\lambda)$, through the use of spectrophotometric standard stars. The instrument response curve $R(\lambda)$ is obtained by comparing the observed spectrum of a spectrophotometric standard star with the corresponding tabulated absolute (“true”) flux values. The flux calibration of any observed spectrum, that recovers both the true shape and the physical zeropoint of the SED², is therefore given by:

$$S_c(\lambda) = S_t(\lambda)/R(\lambda) \quad (3.9)$$

where S_c is the calibrated spectrum.

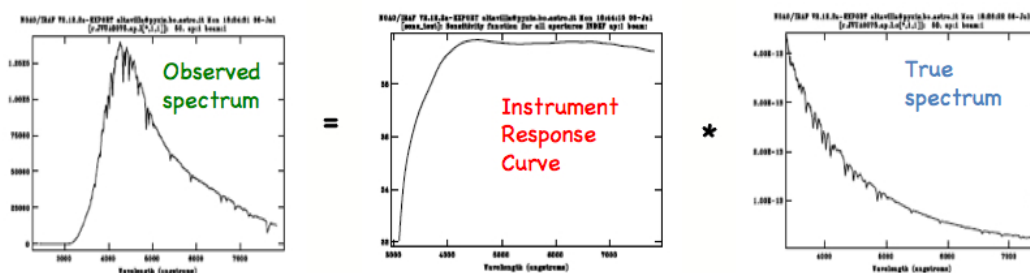


Figure 3.2: The observed spectrum of HZ44 (*left panel*) at TNG is the result of convolution of the instrument response curve $S(\lambda)$ for the DOLoRes spectrograph (*middle panel*) with the calibrated SED (the “true” SED, *right panel*).

²If the observing conditions are photometric.

3.2 Gaia Spectro-Photometric System: a challenge

Gaia's spectrophotometry (see Chapter 2) consists of integrated G-band fluxes from unfiltered light measured in the Astrometric Field CCDs, and low-resolution prism spectra from the blue (BP) and red (RP) spectro-photometers. The integrated flux of the BP and RP spectra yields G_{BP} and G_{RP} magnitudes as two broad passband. Because of its optical design and operation mode, Gaia's spectro-photometric system is much more complicated to calibrate than any of the classical ones. The most difficult Gaia data to calibrate are the BP and RP spectra because, in the case of Gaia, several instrumental effects (much more complex than those usually encountered) redistribute the light along the SED of the observed objects. The calibration of BP and RP data requires a new approach to the derivation of the calibration model (see Section 3.4.1) and to the SPSS needed to perform the actual calibration (see Chapter 4).

The large focal plane with its large number of CCDs makes it so that different observations of the same star will be generally on different CCDs, with different quantum efficiencies. Also, each CCD is in a different position, with different optical distortions, optics transmissivity and so on. Therefore, each wavelength and each position across the focal plane has its (sometimes very different) PSF (point spread function). The time delay integration (TDI) and continuous reading mode, combined with the need of compressing the data before on-ground transmission, make it necessary to translate the full PSF into a linear (compressed into 1D) LSF (line spread function), which of course adds complication into the picture. In addition, the PSF/LSF itself is generally larger than one Gaia pixel in the BP/RP spectra, introducing a large LSF smearing effect, i.e., the spread of photons with one particular wavelength into a large range of wavelengths.

In-flight instrument monitoring is foreseen, but never comparable to the full characterization that will be performed before launch, so the real instrument, at a certain observation time, will be different from the theoretical one assumed initially, and this difference will change with time. One of the most important factors in the time variation of the instrument model is due to the radiation damage (see Section 2.6.1) and the resulting Charge Transfer Inefficiencies (CTI). It has particular impact onto the BP and RP dispersed images because the objects travel along the BP and RP CCD strips in a direction that is parallel to the spectral dispersion (wavelength coordinate). Radiation damage causes traps that subtract photons from each passing object at a position corresponding to a certain wavelength. Slow traps release the

trapped charges once the object is already passed, while fast traps can release the charges within the same object, but at a different wavelength. Given the low resolution, one pixel can cover as much as 15–20 nm (depending on the wavelength) and therefore the net effect of radiation damage can be to alter significantly the SED of some spectra. There are several ways to reduce the effects of radiation-induced charge trapping and possible solutions are under testing. For example, incorporating a supplementary buried channel into the CCD design causes electrons to be transported through the CCD in a narrow stream so that they encounter fewer empty traps. Another option is to operate at low temperatures so that traps stay filled for longer, once a trap contains an electron it cannot trap another. An operating temperature of -115°C is about optimum and this has been selected as the operating temperature for Gaia CCDs. Unfortunately, most traps will still release electrons after a few seconds so a charge injection structure is incorporated to periodically re-fill them. In addition, different transits for the same object will be affected differently by CTI effects, allowing for a certain degree of correction through average or median spectra. However, it is never possible to eliminate all trapping because real traps are invariably complex, comprising several different energy levels with different de-trapping time constants.

3.3 The Gaia Calibration Philosophy

The basic assumption underlying the current BP/RP data processing scheme (which is the main task of CU5 – photometric processing)³ is that there are three clearly separated processes:

1. *Pre-processing* of the raw dispersed images received from IDT. This step consist of extracting “clean” BP/RP spectra from the raw data and includes the bias subtraction, removal of the sky background and the disentangling of the overlapping spectra in crowded regions (more details can be found in Brown et al. 2008). This is the task of the CU5 developments units DU10 (PSF/LSF and CCD calibrations) and DU11 (BP/RP extraction and initial data treatment).
2. *Internal Calibration* of the pre-processed BP/RP spectra, monitoring the variations in response curve across the focal plane (at the FoV, CCD and column

³See Chapter 2, Section 2.11 for further information on the CU tasks within the DPAC. In particular, information about CU5 development units can be found in Section 2.11.2.

levels and considering activation of gates⁴) and the variations with time, to produce an internally consistent flux scale valid for bright and faint sources of all types. This step takes care of modeling the relation between different observations of a given source, aiming to refer all observations to an ideal and “reference instrument” model, on the same instrumental flux and wavelength scales. The internal calibration takes care of, for example, response, dispersion curve, and PSF variations, along scan (AL) and across scan (AC) geometry. As a result all transits for each source will be averaged to produce one single BP and RP spectrum for each object, with its integrated instrumental magnitudes: M_G , M_{BP} and M_{RP} . Only for specific classes of objects, epoch spectra and magnitudes will be released, with variable stars as an obvious example. After the internal calibration, only the mean absolute response, and the wavelength scale and zeropoint remain to be determined (details can be found in Fabricius et al. 2009 and reference therein). The internal calibration is the main task of DU12 (internal calibration model) and DU16 (selections of internal reference sources).

3. *External Calibration* of the internally calibrated spectra. This last step takes care of determining the mean absolute response of Gaia’s photometers and of the wavelength scale and wavelength zeropoint. This is achieved through a set of standard stars for which high quality spectrophotometry is being collected from the ground (more details can be found in Bellazzini et al. 2006, Montegriffo et al. 2007 and in Section 3.4). This is the task of DU13 (ground-based observations) and DU14 (external calibration processing).

In this paradigm, the pre-processing, the internal and external flux and wavelength calibrations are treated as three entirely separated and consecutive pieces of the CU5 photometric pipeline (see Fig. 3.3), with independent calibration models.

Following more detailed studies of the BP/RP data processing it became clear that the three processes mentioned above are not necessarily so independent:

- The disentangling of the flux of overlapping dispersed images in the pre-processing step can only be done accurately if the dispersed images in the focal plane

⁴Gaia will observe objects over a very wide range of apparent magnitude and the CCDs must therefore be capable of handling a wide dynamic signal range. In order to observe all objects as efficiently as possible, the CCD quantum efficiency has been optimized and a number of features have been incorporated in the CCD design in order to cope with bright stars. These include a large full-well capacity, an anti-blooming drain, and 12 TDI *gates* which effectively reduce the integration time for bright objects.

can be precisely predicted starting from “template spectra” (see Brown et al. 2008 and Giuffrida et al. 2008a,b). The templates can be synthetic or observed SEDs (in the initial phases of the mission) or accurate internally calibrated spectra. The transformation from template to predicted images requires the application of the internal calibration (or instrument) model. Because the templates and the instrument model improve as the internal calibration progresses the crowded field treatment will have to be redone on a regular basis in order to take advantage of the latest template and instrument information.

- The presence of CTI (both in the image section and in the serial register), non-linear response and saturation, reinforces the need to repeat the crowded field treatment when the calibration model (which now includes a charge distortion step) improves.
- The BP/RP end products for CU5 were foreseen to be spectra that will be as close as possible to the actually observed dispersed (and AC-summed) images. That is, the effects of the (mean) PSF, (mean) response curve and (mean) dispersion curve would not be removed. However, over the past year ideas were discussed to include in the external calibration process a means to remove the mean instrument from the spectra and thus to produce spectra on a more physical scale of absolute flux versus wavelength (Montegriffo 2009a and Montegriffo & Bellazzini 2009b,c). Thus the external calibration will partly take care of what was originally one of the internal calibration tasks, i.e., determining a mean instrumental model, and at the same time producing the wavelength calibration.

For these reasons, a *forwarding* model approach seems to be needed in the BP/RP data processing. Forward modeling is also a natural option for dealing with the complications of deriving epoch BP/RP spectra (for variable stars) and for dealing with solar system objects and multiple sources (i.e., those not resolved by AF). Fig. 3.4 shows the characteristics of the forwarding model as proposed during the CU5 meeting in Leiden (May 2010). It is important to note that in the forwarding model there is still a clear separation between the *internal calibration* process (upper half of the diagram shown in Fig.3.4 down to the production of “mean spectra”) and the *external calibration* (lower part of the diagram shown in Fig.3.4), even if some characteristics of the external calibration model should be used for the forward modeling step in the baseline approach, as propose by Montegriffo during the CU5 Meeting in Leiden (Montegriffo et al. 2011, in preparation).

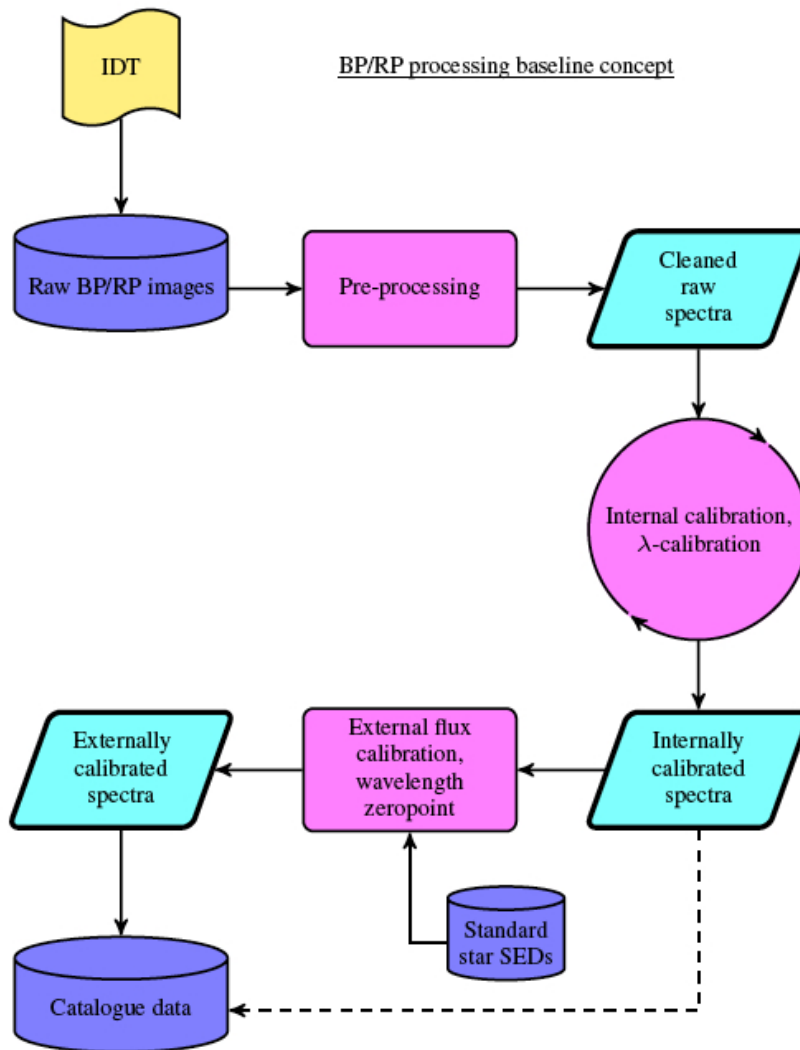


Figure 3.3: Schematic overview of the baseline BP/RP data processing chain. The dashed line indicates that in 2006/2007, when the processing chain was developed, it was not clear whether the internally calibrated spectra would end up in the main database. Figure adapted from Brown et al. (2010).

Presently, a so-called *full forwarding model* (Carrasco et al. 2011, in preparation) is being considered, in order to maximize the precision of the global calibration procedure, using the same calibration model for both the internal and external calibration.

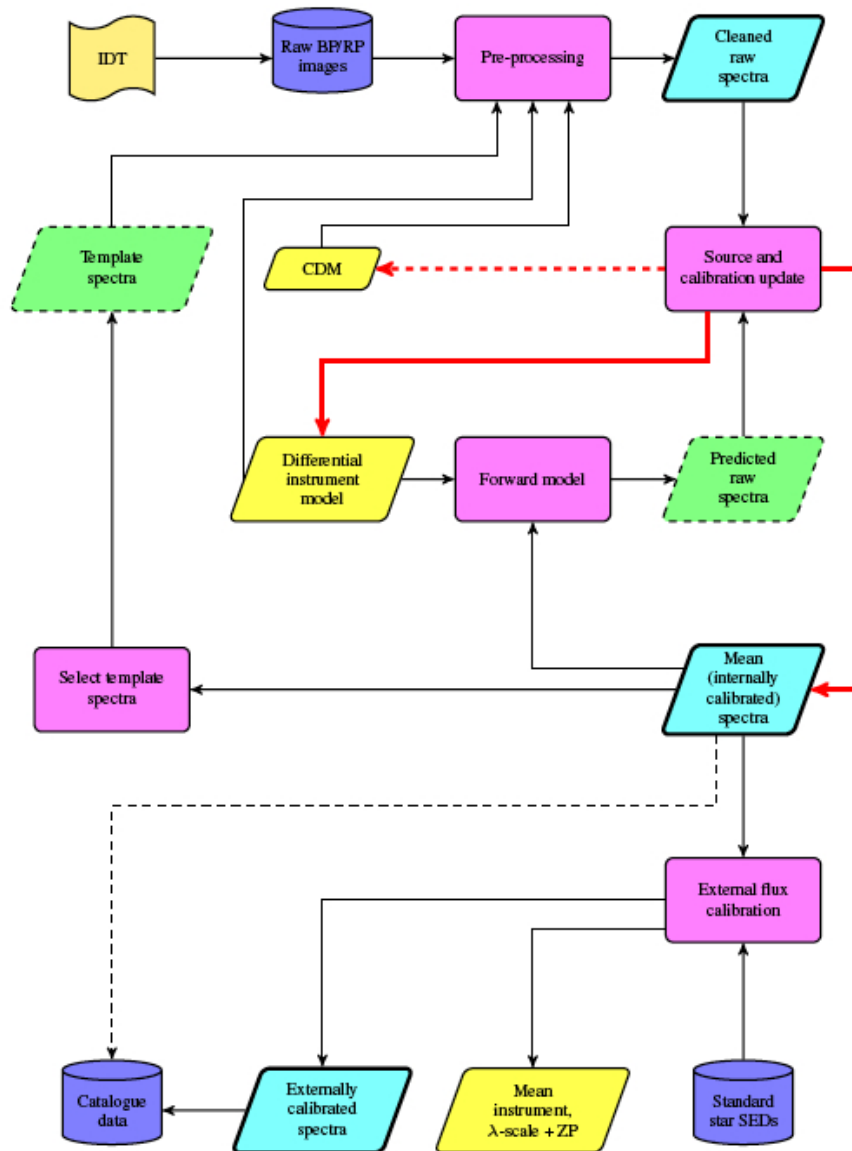


Figure 3.4: Schematic overview of the baseline BP/RP data processing concept as it stood in May 2010. The forward modeling step in the internal calibration loop has been made more explicit: it is where the mean spectra are turned into predicted (cleaned) raw spectra for a given field of view and location in the focal plane assembly. The comparison between predicted and observed raw spectra then leads to updates of the instrument model (calibration update) or of the mean spectra (source update). The thick red lines emphasize the central role of the *updates* process. Figure adapted from Brown et al. 2010.

3.4 The Absolute Flux Calibration of Gaia data

In the following scheme we consider the external calibration as an independent step of the CU5 pipeline. It will receive:

- internal calibrated mean G-band magnitudes or epoch G-band magnitudes in case of particular objects (as, for example, variable stars);
- internal calibrated mean or epoch spectra and integrated G_{BP} and G_{RP} magnitudes.

The derived photometry will be essential not only to properly classify stars, estimate the interstellar extinction and determine astrophysical characteristics of all objects, but also to compute the correction for systematic chromatic effects in order to correct the measured centroids position of stars in the AF. This correction is of fundamental importance to achieve the planned astrometric performances (Busonero et al. 2006). While the internal (relative) calibration, to report all observations to an internally consistent flux scale with an high degree of accuracy will be performed using a large number of constant stars (*internal standards*) selected during the mission itself and observed repeatedly in different parts of the focal plane on time scales varying from hours to months (up to the mission lifetime of 5 years), the final conversion of internally-calibrated data into physical units requires to be tie to an external absolute flux scale by means of few hundreds of Spectro-Photometric Standard Stars (SPSS) with precise and accurate absolute calibrated spectra.

The external calibration cannot be performed as usual by creating a response curve with one single SPSS because this single response curve would strongly depend on the spectral shape of the SPSS. This is due to the effect on the spectral shape of the LSF (Line Spread Function, i.e., the one-dimensional version of the PSF – Point Spread Function), which is different for every wavelength and for every position on the focal plane. The calibration model concept by Montegriffo et al. (2007) foresees the convolution of the SPSS ground based flux tables with the (appropriate) theoretical LSF. This way, for a given position on the focal plane, the response curves built from SPSS of different spectral types differ now by no more than 1%. Additional small residuals (of a few %) are expected, due to the difference between the theoretical LSF computed before launch and the actual LSF. To avoid spoiling the precision reached with the internal calibration (a few %), the uncertainty has to be beaten down by at least one order of magnitude, by averaging together a few hundreds of response curves. Therefore, we selected $\simeq 200$ candidate SPSS (see Chapter 4). No

such large and homogeneous grid of SPSS exists in the literature, at present.

3.4.1 Spectroscopic Calibration Model: the concept

The objective of the external absolute calibration process is to transform an observed spectrum S_o into the best approximation of the corresponding true spectrum S_t , in physical units (see also Section 3.1).

The formation of a spectrum on the detector of a Gaia photometer can be conveniently described as the matricial product of a matrix \mathcal{D} with the source spectrum S_t (expressed in photons $\text{s}^{-1}\text{m}^{-2}\text{nm}^{-1}$):

$$S_o = \mathcal{D} \times S_t \quad (3.10)$$

The element (i, j) of the matrix \mathcal{D} , also called *dispersion matrix*, is defined by:

$$\mathcal{D}_{i,j} = (D \cdot H) T_0(\lambda_j) \rho(\lambda_j) T_p(\lambda_j) T_f(\lambda_j) Q(\lambda_j) L_{\lambda_j}[\kappa_i - \kappa_p(\lambda_j)] \Delta\lambda_j \quad (3.11)$$

where:

- $(D \cdot H)$ is the area of the telescope primary mirror (entrance pupil area),
- $T_0(\lambda)$ is the telescope (mirrors) transmittance,
- $\rho(\lambda)$ is the reflectivity attenuation due to mirrors molecular contamination and rugosity,
- $T_p(\lambda)$ is the prism (fused silica) transmittance,
- $T_f(\lambda)$ is the prism filter coating transmittance,
- $Q(\lambda)$ is the quantum efficiency for BP/RP CCDs,
- κ_j is the AL pixel coordinate,
- $\kappa_p(\lambda_j)$ is the dispersion function,
- L_{λ_j} is the monochromatic effective LSF at wavelength λ_j , integrated over the pixel κ_j ; the LSF is computed by integrating the corresponding monochromatic effective PSF in the AC direction inside a window centered on the PSF.

The Dispersion Matrix \mathcal{D} is an $n \times m$ matrix where n is the resolution of the observed spectrum, m is the resolution of the true spectrum. If $\Delta\lambda_j$ is small enough (~ 1 nm), eq. 3.10 represents a good approximation of the continuous formula which describes the formation of dispersed images given by Brown (2007).

The elements of \mathcal{D} can be determined if S_o and S_t are known, i.e., using a well defined set of SPSS observed by Gaia, which also have well known SED, derived from ground-based observations. Equation 3.10 reveals the linear nature of the image formation process of the photometers, suggesting the possibility that the problem can be inverted: once \mathcal{D} is properly determined, each mean, internally calibrated BP/RP spectrum (S_o) can be corrected into a flux-calibrated spectrum (S_t) by solving the system of linear equations expressed by:

$$S_t = \mathcal{D}^{-1} \times S_o \quad (3.12)$$

Fig. 3.5 shows examples of the dispersion matrices, illustrating how the incoming photons are distributed over the instrument samples depending on their wavelength. The main advantage of the inversion of \mathcal{D} to calibrate BP/RP spectra is that \mathcal{D} contains the actual effects of LSF smearing, even if the real shape of the LSF is not perfectly known a priori, therefore enabling their removal from the calibrating spectra. More than that, each column of the matrix contains an empirical determination of the effective monochromatic LSF: basically each column of the matrix describes how photons at a given wavelength from the incoming spectrum are distributed on the detector. From a complementary point of view, each row in \mathcal{D} represents the effective passband corresponding to each Gaia pixel (including the full effect of LSF smearing), in the sense that it describes the relative contributions from different wavelengths to the flux at a given position in the observed spectrum. By definition, the Dispersion Matrix \mathcal{D} contains also the actual dispersion function, which can be seen in Fig. 3.5 as the curved structure close to the diagonal of the matrix.

The derivation of a calibrated spectrum consists in attributing the correct physical flux to any given wavelength (and/or wavelength bin), hence flux and wavelength calibrations are fully interwoven⁵. The Dispersion Matrix \mathcal{D} is a good example of this entanglement: as it transforms observed spectra into calibrated spectra it *must*

⁵The common perception of the spectro-photometric calibration process focuses the attention mostly on obtaining correct fluxes, because the wavelength calibration of ordinary long-slit spectra is (generally) straightforward. This is clearly not the case for the Gaia low-resolution slitless BP/RP spectra.

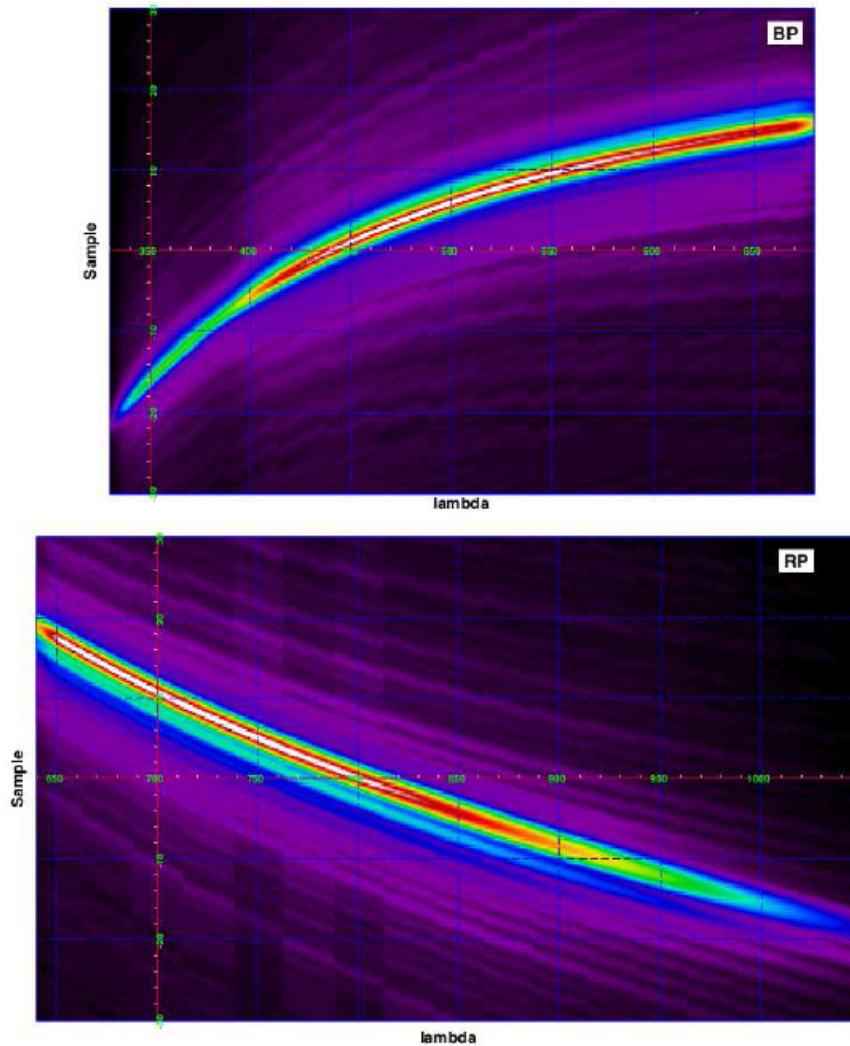


Figure 3.5: Dispersion matrix for BP (top) and RP (bottom) instruments for FoV 1 and CCD row number 4: each column of the matrices represents a LSF centred on the dispersion function at the corresponding wavelength, while the profile of the rows reveals the shape of the photometric band corresponding to each pixel. Figure adapted from Montegriffo 2009a.

provide simultaneously both flux and wavelength calibration. The needed information comes from the SPSS template spectra that are wavelength-calibrated with good accuracy ($\simeq \pm 1\text{\AA}$) and have a much higher spectral resolution than BP/RP spectra (typically 4–5 times higher).

3.4.2 Inversion of the Dispersion Matrix

The main problem with the above approach owes to \mathcal{D} being a rectangular matrix, because the Gaia observed spectra have a smaller number of samples (pixels) than the SPSS spectra used to build their calibration model (wavelength sampling), and therefore the number of unknowns is too high compared to the number of equations. The number of equations is fixed by the number of observed Gaia samples which is expected to be 180 (60 samples \times 3, the oversampling factor of the accumulated spectra, see Montegriffo 2009a). On the other hand, considering a sampling step of 1 nm for true spectra, we can roughly expect at least a number of unknowns of about 350 for BP and 410 for RP (the number comes from the spectrum length of the two instruments).

To circumvent the problem of inverting a rectangular matrix, we must find a method to reduce the dimensionality of \mathcal{D} , reducing the dimensionality of high resolution ground-based SPSS spectra. This can be done by applying *smoothers*: a few different strategies have been considered such a Gaussian smoothing with variable width Gaussians (Montegriffo, 2010, private communication), a smooth through rectangular functions corresponding to the Gaia pixels (Montegriffo et al. 2011), and by performing spline polynomial fitting of the SPSS SED (Montegriffo 2009a). A new approach using B-splines is under implementation.

Whatever method is chosen to smooth the SPSS ground-based spectra, it allows for the construction of a square dispersion matrix called *effective dispersion matrix*, \mathcal{D}_e , and we can write:

$$S_o \simeq \mathcal{D} \times S_t \simeq \mathcal{D}_e \times S_{smooth} \quad (3.13)$$

where $S_{smooth} = \mathcal{K}_s \times S_t$, and \mathcal{K}_s represent the smoother applied to the ground-based calibrated spectrum S_t . However, we can still have degeneracies in the solution of the Effective Dispersion Matrix, so \mathcal{D}_e can still be non-diagonal (see Fig. 3.6).

3.4.3 Diagonalization of the dispersion matrix

One reason why the Dispersion Matrix is non-diagonal, is that the SPSS adopted set can never be an orthogonal set of independent calibrators: stars are all similar to each other, they have all a black-body-like continuum with some features (absorption and

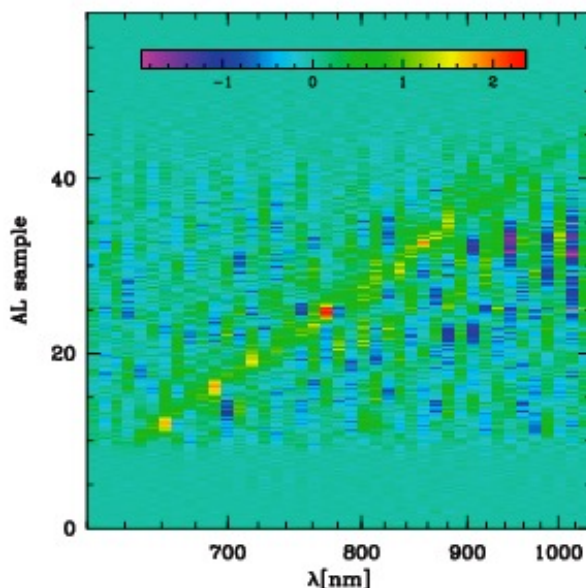


Figure 3.6: Example of a degenerate effective dispersion matrix \mathcal{D}_e , where the diagonal is drowned into noise-like patterns due to non independent set of SPSS used to construct it. Figure by courtesy of P. Montegriffo.

emission lines or bands). As a result, if a dispersion matrix is built with white dwarfs and hot subdwarfs (the ideal calibrators in the classic spectroscopic observations), it will be able to calibrate properly only objects with similar spectra: relatively smooth, with some absorption lines in the blue part of the spectrum. It can totally fail when calibrating red stars with big absorption bands by molecules, or stars with emission features.

An example of the effect of degeneracies is shown in Fig. 3.7, where two different dispersion matrices are used to calibrate the same set of simulated Gaia observations. In the first case (left panel of Fig. 3.7), a dispersion matrix is built using only white dwarfs and hot subdwarfs, with a minority of solar type stars, and it can clearly be seen that red stars with deep absorption bands are calibrated with an error of 0.15 mag at least, failing the specified requirements (1-3% with respect to Vega). In the second case (right panel of Fig. 3.7), a small sample of ten red stars with deep absorption bands are included in the SPSS set used to build a second dispersion matrix. The second dispersion matrix is able to calibrate all red stars with absorption features to better than 1%, exceeding the requirements.

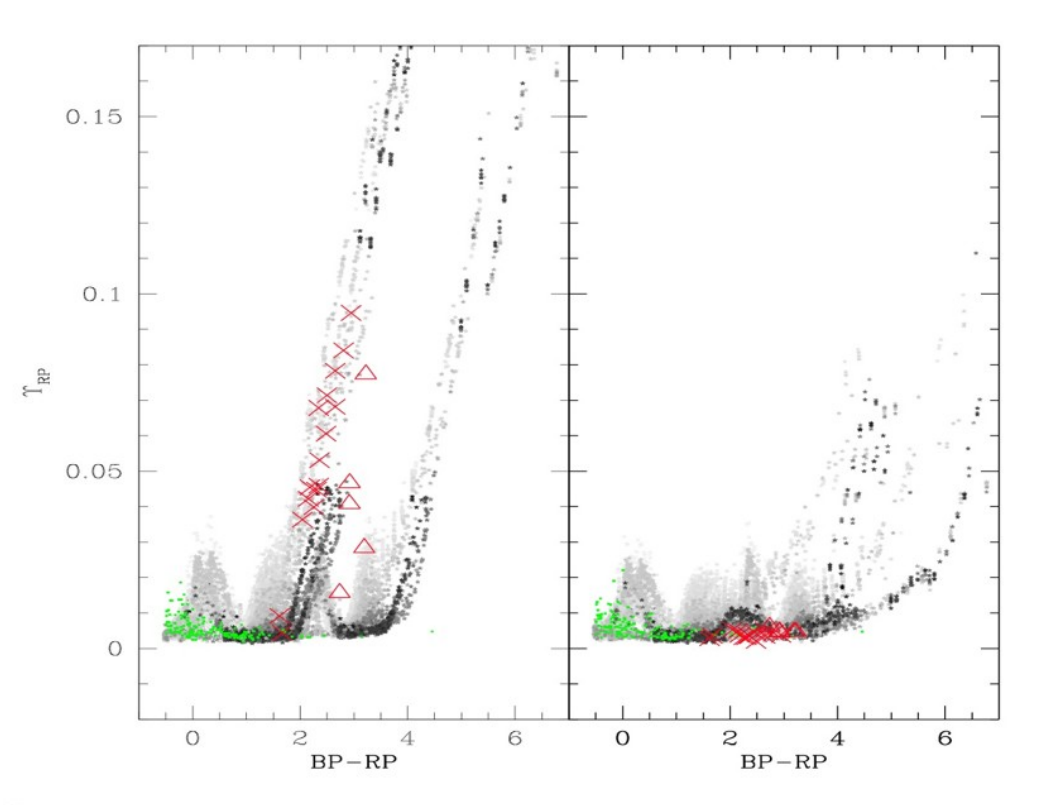


Figure 3.7: On both panels, grey dots are simulated spectra of different metallicity and reddening (this explains the parallel sequences). Green dots are white dwarfs and hot subdwarfs, while red symbols are different types of red stars with significant absorption features (i.e., molecular bands). Abscissae represent the BP–RP color, ordinates are the difference between the “known” magnitude of the used SEDs and the “calibrated” ones obtained by applying a dispersion matrix. *Left panel:* all points are calibrated with a matrix built with hot spectral types only (green dots). The reddest stars are calibrated with an error of 0.15 mag or more. *Right panel:* all points are calibrated with a matrix determined using also ten red SPSS with absorption features (red symbols). All stars with SEDs similar to the ten red stars ($2 \text{ mag} < \text{BP-RP} < 4 \text{ mag}$) are calibrated with an error of less than 1%. Figure extracted from Pancino (2010b).

This example shows the importance of spectral features in the SPSS set used in construction of the Dispersion Matrix. Hot stars have prominent absorption lines in the blue, but no features in the red. The addition of a few red stars with absorption bands “trains” the matrix in the calibration of stars with features in the red (effectively reducing degeneracy). Similarly, problems are encountered in the calibration of emission line objects (peculiar hot stars and quasars, for example). But it is quite difficult to include these objects into the SPSS set since they are often variable. Even if several types of objects are included when determining the Dispersion Matrix, other effects can have a large impact on the degeneracy. For this reason, the accurate choice of the SPSS set is crucial, but does not solve the problem of degeneracy once and for all.

To further reduce degeneracy of the effective dispersion matrix \mathcal{D}_e , we can use other constraints such as the fact that we know most aspects of the instrument from pre-launch characterization. These include the quantum efficiency of the CCDs, the optical layout and transmissivity, the nominal LSF at various positions along the focal plane and at different wavelengths, the nominal dispersion function and its variation along the focal plane. The slow change of these with time can also be monitored to a certain extent, and included in the modelization. We can therefore separate the Dispersion Matrix in a part that is theoretically modeled assuming an instrument model⁶ based on pre-launch instrument description and on its (partially reconstructed) variation with time (the *nominal dispersion matrix*, \mathcal{D}_n), and in a part that is completely unknown, which can be considered as a *correction matrix* \mathcal{K} , made of the residual corrections after the nominal model is taken into account (Montegriffo et al. 2011):

$$\mathcal{D}_e = \mathcal{K} \times \mathcal{D}_n \tag{3.14}$$

The nominal dispersion matrix will be clean: diagonal and non-degenerate.

The correction matrix \mathcal{K} has the role to absorb all residual systematic errors produced by differences between the real instrument and the nominal one: in particular it should compensate for differences with the real dispersion relation and with real LSFs. If the nominal instrument model were the exact one, the correction matrix would be the identity matrix. For a nominal instrument model reasonably close to the real one we can assume the correction matrix being a “band diagonal” matrix

⁶Which is an a priori knowledge of the BP/RP dispersion relations and of the monochromatic effective LSFs as a function of wavelength.

(i.e., with values different from zero only in a few neighbours of the main diagonal). Using the eq. 3.14, the calibration model expressed by eq. 3.13 becomes:

$$S_o \simeq \mathcal{D}_e \times S_{smooth} = \mathcal{K} \times \mathcal{D}_n \times S_{smooth} \quad (3.15)$$

and the matrices involved can be easily inverted to calibrate all Gaia observations since they are all square and almost completely diagonal (see Fig.3.8)

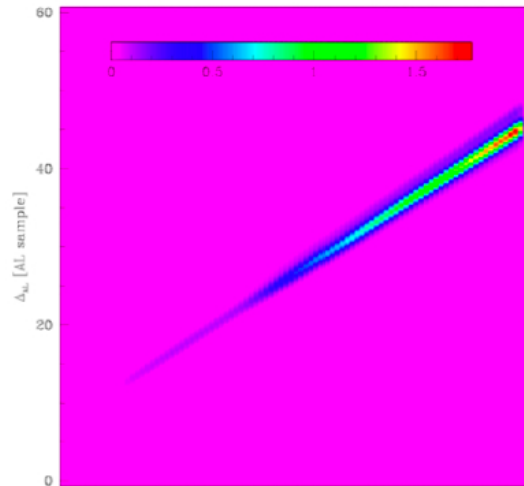


Figure 3.8: Example of a nearly diagonal dispersion matrix, obtained with an appropriate SPSS set and with the use of both the nominal dispersion matrix \mathcal{D}_n and the correction matrix \mathcal{K} to further reduce degeneracy. Figure by courtesy of P. Montegriffo.

3.4.4 Integrated Photometry Calibration Model

In a preliminary study, Ragaini et al. (2009a,b) adopt a classical approach for the absolute calibration of integrated M_G , M_{BP} and M_{RP} magnitudes. G-band fluxes and the integrated fluxes of the BP and RP spectra can be considered as equivalent to three wide photometric passband (G, BP, RP, see Fig.3.9).

The same grid of SPSS that we are assembling for the calibration of the BP and RP spectra shall be used as calibrators for the G, BP, RP photometric system. The reference calibrated magnitudes of the SPSS (M_G , M_{BP} and M_{RP}) are obtained through synthetic photometry, i.e. by convolution of their SED with the nominal profile of the three corresponding bands, as defined by the best of our pre-launch

knowledge of the system response curve. The difference between the *calibrated* values M_G , M_{BP} and M_{RP} and the corresponding *observed* values of the SPSS magnitudes (denoted as m_g , m_{BP} , m_{RP}) will provide the observational constraints for the model which will transform instrumental into calibrated magnitudes.

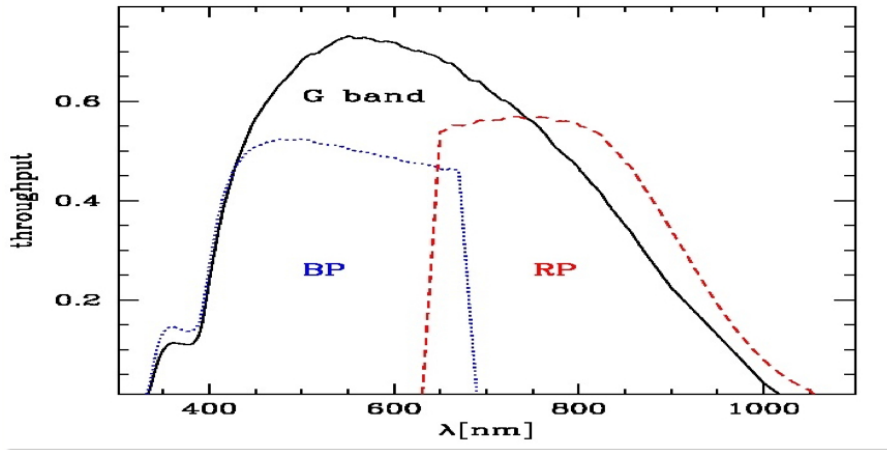


Figure 3.9: G, BP and RP passbands

The (M_G , M_{BP} and M_{RP}) Gaia magnitude system is defined as:

$$M_i = -2.5 \log \frac{\int F_o(\lambda)R(\lambda) d\lambda}{\int F_t(\lambda)R(\lambda) d\lambda} \quad (3.16)$$

where:

- $F_o(\lambda)$ is the star photon flux distribution in photons $s^{-1} m^{-2} nm^{-1}$,
- $F_f(\lambda)$ is the photon flux distribution of some reference spectrum which defines the magnitude system,
- $R(\lambda)$ is the response function for each instrument:
 - $R_G(\lambda)$ is built by multiplying together the telescope (mirrors) transmittance, the reflectivity attenuation due to mirrors molecular contamination and rugosity, and the quantum efficiency (QE) of the "mean" CCD
 - $R_{BP}(\lambda)$ and $R_{RP}(\lambda)$, for the BP and RP passbands, include additional terms: the transmissivity of the prism (fused silica) and the prism filter-coatings transmittance.

We expect that the internal accumulated flux should provide an instrumental magnitude that can be expressed as:

$$m_i = -2.5 \log \int F_o(\lambda) A R(\lambda) d\lambda - \varepsilon \quad (3.17)$$

where the observable spectrum $F_o(\lambda)$ is multiplied by the telescope pupil area A and by the response function $R(\lambda)$ to model the response of the mirrors and the detectors.

The term ε takes into account some further effects: first of all, it contains the aperture correction factor, as fluxes are integrated over a finite window (flux loss). In addition, it accounts for the fact that the true instrumental response can be somehow different from the assumed one⁷. Equations 3.16 and 3.17 suggest a simple form for the calibration model:

$$M_i = m_i + zp_i + \varepsilon_i \quad (3.18)$$

where

$$zp = 2.5 \log \int F_t(\lambda) R(\lambda) d\lambda + 2.5 \log A \quad (3.19)$$

In this contest the term ε was modeled using just one parameter: the *observed* color ($m_{BP} - m_{RP}$). After careful simulations (see Ragaini et al. 2009b), this kind of model was abandoned, since differences of just a few % between the nominal and the actual response curves prevent the achievement of millimag accuracies over the whole range of colors spanned by realistic celestial sources.

For this reason, a new approach, based on the same general principles adopted for the calibration of BP and RP spectra, was instead adopted (Ragaini et al. 2011, in preparation). If we consider that an integrated magnitude M is the convolution of the spectral energy distribution S_t with the effective passband B , we can derive the *true* filter passband response curve B_t using the SPSS SED (from ground-based observations):

$$M_i = S_t \times B_{t,i} \quad (3.20)$$

⁷As the actual Gaia observations will not be perfectly reproduced by the synthetic band profiles which define the system, it is expected that the model parameters will have some dependence on the intrinsic shape of the spectrum of any given source. These kind of effects should be taken into account by the calibration model.

where:

- M_i is the m -dimension vector of observed integrated flux values in the i photometric band ($i=G/BP/RP$ and m =number of SPSS),
- S_t is a rectangular matrix of n columns (the wavelength samples) and m row (the number of SPSS),
- $B_{t,i}$ is the n -dimension vector containing the i filter band true response sampled in n data points corresponding to the wavelength bins.

To solve the system expressed by eq. 3.20, the dimensionality needs to be decreased to $n \leq m$, so a smoothing procedure is applied also in this case to both S_t and filter curves $B_{t,i}$, similarly to what done in the case of BP and RP spectra. We can slit $B_{t,i}$ in two components as well: a known basic filter shape given by the *nominal* instrument model $B_{n,i}$ (stored in the Parameter Database⁸), and an unknown modification of the initial filter shape expressed by a *correction* vector K' , which defines the residual differences between the nominal (from $B_{n,i}$) and the observed (from $B_{t,i}$) SPSS data. With this assumption, eq. 3.20 becomes:

$$M_i = S_{smooth} \times K' \times B_{n,i} \quad (3.21)$$

With this kind of treatment, K' can be derived by least square fitting these residual differences, and hence the true instrument response curve $B_{t,i}$ can be derived, allowing to calibrate all Gaia integrated magnitude data.

Test and simulations indicate that calibration equations in the form of:

$$M_i = m_i + ZP_i \quad (3.22)$$

can be obtained (in magnitude units) for the G/BP/RP bands, where the color dependence is negligible and the possible flux loss is recovered by the zero point ZP (see Ragaini et al. 2011, in preparation).

⁸The actual spectral shape is known before launch, but might be slowly vary with time due to several causes, the most important one being the CCDs quantum efficiency decrease due to radiation damage.

3.4.5 RVS spectra absolute calibration

The possibility of calibrating in flux the RVS spectra as well has been so far considered a secondary problem, since both radial velocities and astrophysical parameters can be derived in most cases without the need of an absolute flux scale attached to the spectra. However, Allende Prieto (2008) has shown that a proper spectrophotometric calibration of the RVS spectra may be useful in order to determine atmospheric parameters of observed stars with the highest-possible precision. A preliminary study by Trager (2010) shows that, in principle, the ground-based SPSS grid presently under construction for the absolute flux calibration of BP/RP spectrophotometry and G-band imaging (see Chapter 4) could be sufficiently sampled also to ensure the absolute flux calibration of RVS spectra.

We expect the topic to be further explored by CU6 (dedicated to RVS processing and radial velocity determination) in the near future.

4

The Gaia Grid of SPSS

The task of CU5-DU13, in which I am involved, is to build a grid of spectrophotometric standard stars (SPSS) suitable for the flux calibration of the Gaia G-band photometry and the BP/RP spectrophotometry. Such a flux calibration can be performed by repeatedly observing each SPSS during the life-time of the Gaia mission (5+1 years) and by comparing the observed Gaia spectra (S_o) to the spectra obtained by our ground-based observations (S_t) in order to derive the Gaia's instrument responses (see Montegriffo & Bellazzini 2009b). As shown in Section 3.4 and 3.4.1, the Gaia SPSS grid had to be chosen with great care in order to build the best possible dispersion matrix, because the final results of the absolute calibration strongly depend on both the total number and the spectral type range covered by SPSS.

The Gaia SPSS (or, better, their reference flux tables S_t) should conform the general requirements reported in the *Software Requirements Specification* document (van Leeuwen 2010):

1. resolution $R=\lambda/\Delta\lambda \simeq 1000$, i.e., they should oversample the Gaia BP/RP resolution by a factor of 4-5 at least;
2. wavelength coverage consistent with the Gaia BP/RP coverage: 330–1050 nm;
3. typical uncertainty on the absolute flux scale, with respect to the assumed calibration of Vega, of a few % excluding small troubled areas in the spectral range covered (telluric bands residuals, extreme red and blue edges) where it can be somewhat worse.

The total number of SPSS in the Gaia grid should be $\simeq 200$ stars, including a variety of spectral types (see Chapter 3).

Table 4.1: Existing sets of spectrophotometric standard stars

Reference	$\Delta\lambda(\text{\AA})$	Nr stars	Nr ($V \geq 10$)	Notes
Stone & Baldwin 1983	3200-8280	18	18	F, G, WDs
Gunn & Stryker 1983	3130-10800	175	14	all spectral types, (a)
Oke & Gunn 1983	3080-12000	4	0	hot stars, $V=8.0-9.7$
Filippenko & Greenstein 1984	3300-11000	5	5	sdG, WDs
Pickles 1985	3600-10000	200	?	all spectral types, (a,b)
Massey et al. 1988	3200-8100	25	23	sd's, WDs, (c)
Massey & Gronwall 1990	to 10000	11		
Oke 1990	3200-9200	25	22	Hot stars
Turnshak et al. 1990	1100-9200	23	17	Hot stars, (d,e)
Glushneva et al. 1992	3200-7600	238	?	secondary standards, (f)
Hannay et al. 1994	3300-10400	29	16	F, G, hot stars, (g)
Hickson & Mulrooney 1998	2500-9200	21	21	$V \sim 15$, $\delta \sim +33^\circ$
Bessell 1999	3300-10500	33	22	sd's, WDs,
Stritzinger et al. 2005	3050-11000	102	20	Landolt stars

(a) many late type stars, lime-rich: for population synthesis.

(b) see also Pickles (1998): 131 stars, 1150–10620 \AA .

(c) 14 new stars.

(d) see also Bohlin (1996): 13 of 17 faint stars in Oke's list.

(e) Oke's absolute magnitudes are systematically brighter by 0.04 mag.

(f) for 99 stars also 6000-10800 \AA .

(g) see also Hannay et al. (1992); new observations of stars from Taylor (1984), Stone (1977), Stone & Baldwin (1983).

(h) essentially Hannay et al. (1994) plus 4 other stars form Oke (1990). Telluric features subtracted

Several spectro-photometric standard stars libraries are already available in the literature (Oke 1990; Hamuy et al. 1992, 1994; Bohlin et al. 1995, to cite the most commonly used, see also Table 4.1 for a representative, even if not exhaustive list). Anyway, the material already available is not as homogeneous as required because of different spectral ranges covered, different spectral sampling, different data treatment (as the extinction correction and telluric lines removal, if any¹), and different zero-point (due to the different revisions of the Vega magnitudes).

It is therefore necessary to build the Gaia SPSS grid with *new, dedicated* observations.

4.1 Classes of SPSS for Gaia

The assembly of the whole SPSS grid involves three classes of SPSS:

- The *Pillars* are three DA White Dwarfs (WDs) already used as fundamental flux standards for the Hubble Space Telescope (HST) calibrations and directly calibrated on Vega (Bohlin et al. 1995, Bohlin 1996, see CALSPEC² and references therein). The use of these stars as spectrophotometric standards to calibrate the Gaia *Primary SPSS* will ensure the homogeneity of the flux scale of the whole grid.
- The *Primary SPSS* are 45 bright, well known spectro-photometric standards whose spectra are already in the CALSPEC flux scale or can be tied to this scale with dedicated ground-based observations. The *Primary SPSS* were selected from the best existing datasets (such as CALSPEC, Oke 1990, Hamuy et al. 1992, 1994, and Stritzinger et al. 2005), and are calibrated by means of the *Pillars* mentioned above. They constitute the *ground-based calibrators* of the *actual* Gaia standards (that we call *Secondary SPSS*). For these reasons the Primary SPSS are well distributed in the sky to allow observability from any observing site all year round.
- The *Secondary SPSS* are the *actual* members of the Gaia SPSS Grid. The main observational campaign aimed at the establishment of the Grid (see Section 4.2.1) will obtain whole range 330–1050 nm spectra of selected candidates.

¹As an example, the fluxes given by Hamuy et al. (1994), calculated through 50 Å bandpasses at continuous steps of 50 Å, include telluric features and the author himself stresses that the contaminated bandpasses are *particularly inaccurate* and that fluxes very close to strong absorptions can not be trusted because of the feature broadening, due to the low resolution (11–16 Å) of the observations.

²<http://www.stsci.edu/hst/observatory/cdbs/calspec.html>

These spectra will be calibrated using the *Primary SPSS*. The Gaia data of these *Secondary SPSS* will be used to derive accurate response curves for the G-band and BP/RP spectrophotometry.

4.1.1 SPSS Pillars

Three³ DA WDs, G 191–B2B, GD 71 and GD 153 (described in Bohlin et al. 1995, shown in Table 4.2), that already represent the basis of the Hubble Space Telescope (HST) calibration, will constitute also the core of our calibration.

The flux calibrated spectra of these stars, available in the CALSPEC database, are tied to the revised Vega flux by Bohlin & Gilliland (2004) and Bohlin (2007)⁴. The

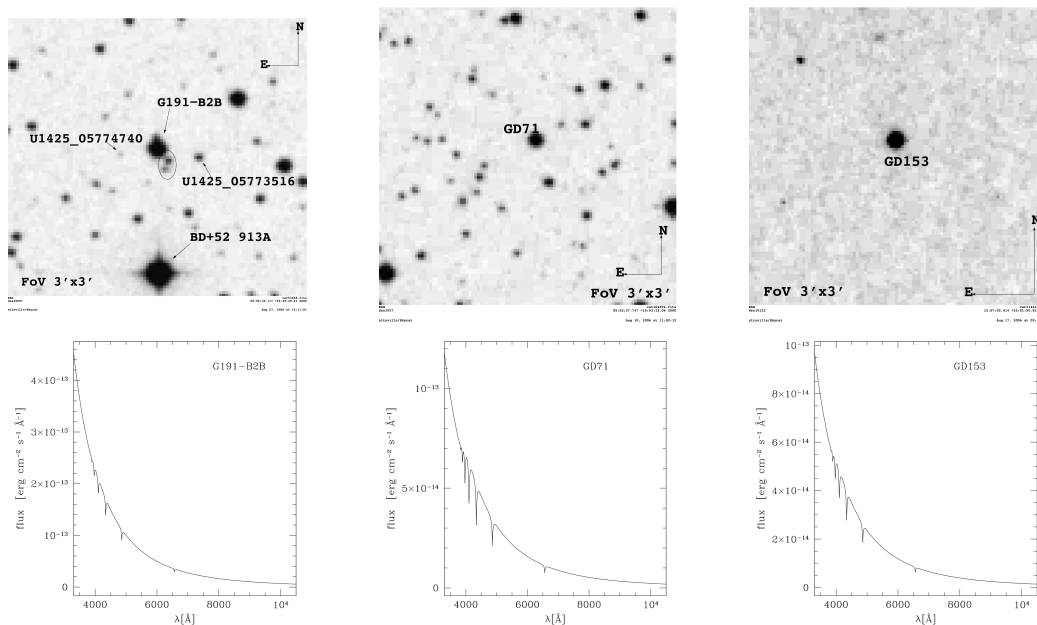


Figure 4.1: *Upper panels*: $3' \times 3'$ images. Faint unknown stars very close to the SPSS may be marked with a circle. North and East as shown in the figure. *Bottom Panels*: Pillar spectra.

³HZ 43 – a hot, hydrogen-rich (DA) WD listed in Bohlin et al. (1995) as a *pillar* – was excluded from our list because it is member of a binary system, together with a dMe star (Dupuis et al. 1998) $\sim 3''$ away, which is brighter longward of $\simeq 700$ nm (Bohlin et al. 2001) and makes it useless as a ground-based calibrator.

⁴The new composite flux table of Vega is available at: ftp://ftp.stsci.edu/cdbs/current/_calspec/alpha_lyr_stis_003.fits.

Table 4.2: Pillars

Star name	ID	R.A. ($hh\ mm\ ss$)	Dec. ($o\ \prime\ ''$)	B	V	Spectral type	Proper motion (mas/yr)	Parallax (mas)	Parallax error [error]	T_{eff} K	$\log g$ dex	notes	
fundamental standard stars													
G191-B2B	001	05 05 30.612	+52 49 51.945	11.455	11.781	DA0	6.46 -90.70	[3.15 2.00 64]	A	14.53 [3.09]	A	61193 7.492	WD c,l
GD71	002	05 52 27.627	+15 53 13.37	12.780	13.032	DA1	85 -174	[- - -]	C	12 [-]	D	32747 7.683	WD c
GD153	003	12 57 02.333	+22 01 52.52	13.065	13.346	DA1	-46 -204	[- - -]	C	-	-	38686 7.662	WD c

ID: identification number for internal use.

A..E: quality flag: A=best quality, E=worst quality, ~ = unknown quality.

c: spectrum available in CALSPEC

l: additional photometric data available in Landolt & Uomoto (2007).

T_{eff} & $\log g$ for Bohlin et al. (1995) WD models.

flux calibration of these three stars is based on the comparison of WD model atmospheres with spectra obtained with the Faint Object Spectrograph (FOS) aboard HST. These hydrogen WDs cover the temperature range $32000 \leq T_{eff} \leq 61000$ K and the FOS spectrophotometry agrees with the model fluxes to within 2% over the whole UV-visible range. In addition, the simulated B and V magnitudes of the data agree to better than 1% with Landolt photometry⁵ (Landolt & Uomoto 2007). In particular these model⁶ flux distributions are normalized to the absolute flux of Vega of $3.46 \times 10^{-9} \text{erg cm}^{-2} \text{s}^{-1} \text{\AA}^{-1}$ at 5556 Å.

A spectrum of each Pillar (within the Gaia spectral range) and the corresponding finding chart (Digitized Sky Version I, ESO) is shown in Fig.4.1.

4.1.2 Primary SPSS: selection criteria and Candidates

In order to obtain a homogeneous and accurate ($\sim 1\%$ internal, $\sim 3\%$ absolute) dataset directly tied to the Vega revised calibration by Bohlin & Gilliland (2004) and Bohlin (2007), and covering the Gaia spectral range, we decided to select a set of already well known SPSS to be observed and reduced in a self-consistent and homogeneous way by means of dedicated ground based observations, to be used as the Gaia grid ground-based calibrators.

The selection criteria for Primary SPSS, derived from the general requirements described in van Leeuwen (2010) can be summarized as follows:

- Primary SPSS spectra should be as featureless as possible.
- Primary SPSS shall be validated against variability.
- Primary SPSS should have already been used as a spectrophotometric standard and, possibly, with a well referenced flux calibrated spectra over a wavelength range comparable to that covered by Gaia BP/RP (330–1050 nm).
- Primary SPSS should be isolated enough to avoid contamination from nearby stars.
- The magnitude of each Primary SPSS should be sufficiently bright to provide high signal to noise spectra ($S/N \sim 100$ per pixel over most of the wavelength range), with reasonable exposure times when observed with 2–4 m class ground-based telescopes.

⁵<http://www.eso.org/sci/observing/tools/standards/spectra/wdstandards.html>

⁶Hubeny NLTE models, Hubeny & Lanz (1995). See also Bohlin (2007) and references therein

- Primary SPSS shall cover a suitable range of RA and Dec to ensure all-year-round ground-based observations from both hemispheres. A small subsample of Primaries should have equatorial location to permit inter-run comparisons and checks between different telescopes/sites from both Northern and Southern observatories.

We selected CALSPEC as the main source of Primary SPSS. This library contains about 50 SEDs (including Vega) which are the fundamental flux standards for the Hubble Space Telescope (HST) calibrations.

About half (25+3 *Pillars*) of the objects listed in CALSPEC fulfill our requirements. In order to get a more complete sky distribution we expanded our sample with SPSS selected from other sources, such as Oke (1990), Hamuy et al. (1992, 1994), the STELIB3.1 archive⁷, the Indo-U.S. Library of Coudé Feed Stellar Spectra⁸.

A few stars observable from both the Northern and Southern hemispheres were selected from Stritzinger et al. (2005) (equatorial Landolt standard stars⁹). For a subsample of twelve stars additional photometric data were available in Landolt & Uomoto (2007).

A list of the 45 Primary SPSS Candidates is shown in Table 4.3, and more details can be found in Altavilla et al. (2008).

The coordinates, B and V magnitudes and spectral types were mainly retrieved from the SIMBAD¹⁰ astronomical database and references therein. In particular RA and Dec are ICRS¹¹ 2000.0 equatorial coordinates (mainly by Perryman et al. 1997, but they can have heterogeneous sources and different precision). Proper motions and parallaxes (mainly from Perryman et al. 1997) are also listed, when available. SIMBAD B and V magnitudes come from heterogeneous sources and can differ from the values listed in other catalogues. When available, photometry by Landolt & Uomoto (2007) is preferred, otherwise we selected magnitude estimates according to their precision and concordance between different authors. T_{eff} and $\log g$ have been retrieved from the literature. When multiple estimates were available, we selected a representative value, and we did the same for the spectral type. A large fraction of

⁷http://www.ast.obs-mip.fr/users/leborgne/stelib/fits_files.html

⁸<http://www.noao.edu/cflib/V1/IRAF/>

⁹spectra available in <http://csp1.lco.cl/~mhamuy/SPECSTDS>, see Stritzinger et al. (2005), but this URL seems out of date. Altavilla wrote to the author, and we are waiting for an answer.

¹⁰<http://simbad.u-strasbg.fr/>

¹¹From 1 January 1998, the International Celestial Reference System (ICRS) replaced the FK5 system (Fricke et al. 1988), as decided by the International Astronomical Union (IAU) in the 23rd General Assembly in August 1997.

the sample (at least 13 stars) is made of high proper motion stars. 28 stars out of 48 are listed in CALSPEC. Our aim here is not to present an exhaustive scanning of literature data, but to give a reliable characterization of Primary SPSS. For a more complete and up-to-date listing of the astrophysical parameters and corresponding sources see the Wiki-Bo pages¹² where each SPSS is linked to a detailed card.

Fig. 4.2 shows the distribution on the sky and the magnitude range of the candidate Primary SPSS: stars are equally distributed in the two hemispheres, with about one half of our sample (26 stars out of 48) in the Northern hemisphere; also the right ascension coverage is quite complete and homogeneous. Their magnitude range is $8.76 \leq V \leq 14.11$, but about 70% of them have $V < 13.0$. The $B - V$ color range is $-0.34 \leq B - V \leq 0.63$. As shown in Table 4.3, 14 out of 48 stars are WDs (18 according to SIMBAD – but for some stars there are discordant data in literature) but there are also several hot subdwarfs, O,B,A stars and cold stars down to the K spectral type.

A spectrum of each Primary SPSS (within the Gaia spectral range) and the corresponding finding chart (Digitized Sky Version I, ESO) is shown from Fig. 4.3 to Fig. 4.10.

It is important to remember that stars that have long been used as spectro-photometric standards can be characterized by discordant values in literature data. Usually magnitudes and/or spectral types are slightly refined in the most recent studies, but sometimes there are significant differences. As an example, the old magnitudes of HZ 44 ($B=11.18$, $V=11.3$) reported in SIMBAD differ by ~ 0.4 mag from the new values by Landolt & Uomoto (2007) ($B=11.382$, $V=11.673$).

This strengthens the importance of an ad-hoc ground-based spectrophotometric observational program in order to homogenize the data.

¹²http://yoda.bo.astro.it/wiki/index.php/Primary_Observations_Table The password is available upon request. Please, contact Elena Pancino (mail: elena.pancino@oabo.inaf.it).

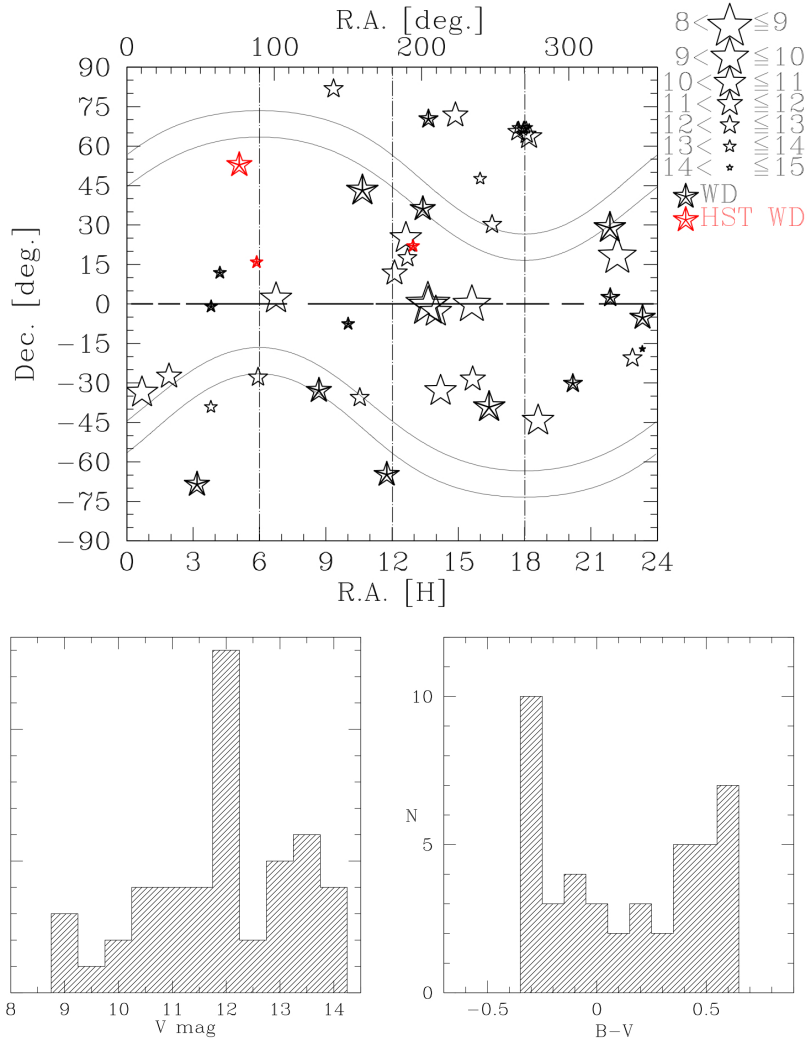


Figure 4.2: Spatial distribution (*top panel*), magnitude coverage (*left bottom panel*) and color coverage (*right bottom panel*) of the candidate *Primary SPSS*. The stripes corresponding to the ecliptic latitude $40 < |\delta| < 50$ are shown in the top panel. Stars falling into these two regions will be observed more than ~ 150 times during the whole mission. The only stars falling in these stripes are: LTT 3218, LTT 3864, HZ 44. The HST WDs marked with red stars are, from left to right, G 19–B2B, GD 71, GD 153.

Table 4.3: Primary SPSS candidates.

Star name	ID R.A. (J2000) <i>hh mm ss</i>	Dec. (J2000) ° ' "	B	V	Spectral type	Proper motion (mas/yr) [error ellipse]	Parallax (mas) [error]	T_{eff} K	$\log g$ dex	notes
EG21	005 03 10.31.0229	-68 36 03.389	11.418	11.379	DA3	41.87 -104.14 [1.86 1.47 178]	A 98.50 [1.46]	A 16181	8.06	WD-
GDD50	006 03 48.50.20	-00 58 31.2	13.787	14.063	DA2	64 -161 [~~~~] D	-	43102	9.09	WD c
HZ2	007 04 12.43.55	+11 51 49.0	13.787	13.877	DA3	48 -86 [~~~~] D	64 [~] D	20790	7.81	WD c,1
LTT3218	008 08 41.32.56	-32 56 34.9	12.071	11.846	DA	-984 1262 [100 100 45] C	108 [7] D	-	-	WD, high p.m.-
LTT2415	009 05 56.24.7416	-27 51 32.349	12.600	12.201	sdG	236.31 -155.90 [2.42 2.24 164] A	-2.46 [2.95] A	-	-	high p.m.-
GDI108	010 10 00.47	-07 33 30	13.342	13.580	sdB	-	-	27760	5.60	(WD) c
Feige34	011 10 39.36.7400	+43 06 09.252	10.838	11.181	DO	13.63 -25.13 [2.54 1.77 104] A	2.74 [3.03] A	-	-	WD c,1
LTT4364	012 11 45.42.9205	-64 50 29.459	11.691	11.497	DQ6	2665.25 -346.19 [2.00 1.88 62] A	216.40 [2.11] A	-	-	WD, high p.m.-
Feige66	013 12 37.23.5169	+25 03 59.874	10.220	10.509	sdO	2.72 -26.71 [1.81 1.34 99] A	5.11 [1.74] A	-	-	in cluster Mel111 c,1
HZ44	014 13 23.35.2581	+36 07 59.514	11.382	11.673	sdO(B2)	-61.60 -3.10 [3.10 1.70 0] B	-	-	-	(WD) c,1
GRW+705824	015 13 38.50.4743	+70 17 07.619	12.682	12.773	DA3	-403.80 -26.17 [3.28 2.99 141] A	40.33 [2.89] A	20230	8.05	WD, high p.m. c,1
EG274	016 16 23.33.8367	-39 13 46.163	10.885	11.029	DA2	75.52 0.05 [2.62 1.62 107] A	78.04 [2.40] A	24800	8.10	WD-
LTT7987	017 20 10.56.8453	-30 13 06.639	12.269	12.206	DA4	-345.60 -250.49 [4.53 2.42 62] A	65.06 [3.85] A	-	-	WD, high p.m.-
BD+28 4211	018 21 51.11.0222	+28 51 50.364	10.168	10.509	Op	-34.41 -57.85 [1.70 1.47 50] A	9.63 [1.71] A	82000	6.20	(WD) c,1
G93-48	019 21 52.25.3835	+02 23 19.556	12.731	12.739	DA3	23.00 -302.98 [5.77 2.84 73] A	39.84 [4.47] A	17653	7.994	WD, high p.m. c
BD+17 4708	020 22 11.31.3737	+18 05 34.174	9.907	9.464	sdF8	511.55 59.92 [1.64 1.25 70] A	8.43 [1.42] A	-	-	high p.m. c,1
LTT9239	021 22 52.41.032	-20 35 32.89	12.673	12.065	F(sdG)	80 -309 [3 3 90] C	-	-	-	high p.m.-
LTT9491	022 23 19.35.44	-17 05 28.4	14.132	14.111	DB3	270 0 [50 40 90] C	-	-	-	WD c,1
Feige110	023 23 19.58.3977	-05 09 56.207	11.527	11.832	sdOB	-11.45 -4.93 [4.38 2.97 87] A	5.59 [3.34] A	42300	5.95	(WD) c,1
HILT600	024 06 45.13.3706	+02 08 14.697	10.620	10.441	B1V	1.20 -3.30 [1.80 1.70 0] B	-	-	-	-
AGK+81266	025 09 21.19.1801	+81 43 27.642	11.596	11.936	sdO	-10.15 -50.14 [1.93 1.53 58] A	2.27 [1.84] A	-	-	c,1
Feige56	026 12 06.47.2343	+11 40 12.643	10.934	11.057	A0V	-8.45 -8.10 [2.46 1.31 103] A	0.87 [2.39] A	-	-	-
Feige67	027 12 41.51.7912	+17 31 19.752	11.479	11.822	sdO	-5.62 -37.08 [2.82 1.73 132] A	2.46 [2.71] A	-	-	c,1
sa105-663	028 13 37.30.3369	-00 13 17.368	9.102	8.760	A8	4.65 5.68 [1.09 0.60 115] A	5.91 [1.16] A	-	-	Landolt-
sa105-448	029 13 37.47.0728	-00 37 33.021	9.437	9.192	A3	-20.90 -20.30 [2.80 1.80 0] B	-	-	-	Landolt-
HD121968	030 13 58.51.1664	-02 54 52.322	10.047	10.236	B1V	1.66 17.20 [2.13 0.90 130] A	-0.87 [1.68] A	-	-	Landolt-
sa107-544	031 14 11.46.3242	-33 03 14.304	10.840	10.441	A0	-7.10 6.40 [2.50 1.90 90] B	-	-	-	-
LTT 6248	032 15 36.48.0952	-00 15 07.112	9.438	9.037	A5	-2.10 21.70 [3.10 2.40 0] B	-	-	-	Landolt-
1740346	033 15 38.59.660	-28 35 36.87	12.288	11.798	A	-233 -175 [3 3 71] C	-	-	-	-
1743045	034 17 40.34.68	+65 27 14.8	12.9	12.36	A5V	-	-	-	-	A star c
1805292	035 17 43.04.48	+66 55 01.6	13.7	13.13	A5V	-	-	-	-	A star c
	036 18 05.29.28	+64 27 52.0	12.5	12.06	A1V	-	-	-	-	A star c

Table 4.3: Primary SPSS candidates -continued

Star name	ID	R.A. (J2000) <i>hh mm ss</i>	Dec. (J2000) <i>o ' "</i>	B	V	Spectral type	Proper motion (mas/yr) [error ellipse]	Parallaxes (mas) [error]	T_{eff} K	$\log g$ dex	notes
						cold stars					
1812095	037	18 12 09.57	+63 29 42.3	11.9	11.8	A2V	-	-	-	-	A star c
LT1377	038	00 41 30.4732	-33 37 32.017	11.696	11.219	K(F)	-348.13 -249.40 [1.95 1.47 70]	A 50.29 [1.93]	A	-	high p.m. -
LT11020	039	01 54 50.273	-27 28 35.74	12.061	11.510	G	312 -234 [2 2 128]	C	-	-	high p.m. -
LT11788	040	03 48 22.67	-39 08 37.2	13.611	13.145	F	250 -210 [80 30 90]	C	-	-	high p.m. -
LT13864	041	10 32 13.604	-35 37 41.80	12.651	12.167	F	-263 -8 [2 2 0]	C	-	-	high p.m. -
P041C	042	14 51 58.19	+71 43 17.3	12.616	12.005	GOV	-	-	5828	-	Solar analog c
P177D	043	15 59 13.59	+47 36 41.8	13.963	13.356	GOV	-	-	5831	-	Solar analog c
P330E	044	16 31 33.85	+30 08 47.1	13.521	12.917	GOV	-	-	5822	-	Solar analog c
KF08T3	045	17 55 16.23	+66 10 11.7	14.3	13.5	K0.5III	-	-	-	-	K giant c
KF06T1	046	17 57 58.49	+66 52 29.4	14.5	13.52	K1.5III	-	-	-	-	K giant c
KF06T2	047	17 58 37.99	+66 46 52.2	15.1	13.8	K1.5III	-	-	-	-	K giant c
KF01T5	048	18 04 03.8	+66 55 43	-	13.56	K1III	-	-	-	-	K giant c
LT17379	049	18 36 25.9455	-44 18 36.937	10.826	10.219	G0	-172.03 -161.48 [2.19 1.42 108]	A 6.38 [1.94]	A	-	high p.m. -

ID: identification number for internal use

● = WD & sd stars ; ● = O,B,A stars ; ● = cold stars

A...E: quality flag: A=best quality, E=worst quality, ~ = unknown quality.

c: spectrum available in CALSPEC

i: additional photometric data available in Landolt & Uomoto (2007).

Landolt - Landolt (1983), Stritzinger et al. (2005).

GD108 - labelled as WD in SIMBAD, but classified as sdB in the same web page. Classified as sdO

HZ44 - labelled as WD in SIMBAD, but classified as B2 in the same web page. Classified as sdB in Kawka et al. (2007).

GRW + 705824, EG274, LTT7987, LTT3218 - Warning, these stars have been removed from the Nearby Supernova Factory Spectroscopy

Standards list^a "Due to broad lines".

EG274 (WD 1620-391) has a dG2 companion at 432" (Farihi et al. 2005).

BD + 17 4708 - listed in Bessell (1999), as a low-resolution smooth spectrum star suitable for telluric line elimination; fundamental primary star in the SLOAN photometric system.

Feige110 - labelled as WD in SIMBAD, but classified as sdOB by Heber et al. (1984). Listed in Bessell (1999), as a near-blackbody spectrum star.

BD + 28 4211 - a binary with a separation of roughly 3 arcsec. The secondary is quite red^b. It may be used to calibrate in the blue.

Since precise photometry by Landolt & Uomoto (2007) is available, we have not rejected this star, but it must be used with caution; labelled as WD in SIMBAD, but classified as Op in the same web page and in Oke (1990); sdOp in Stone (1977).

^a<http://snfactory.lbl.gov/snf/snf-specstars.html>

^bfrom http://www2.keck.hawaii.edu/inst/lris/stone_stds_1977.html

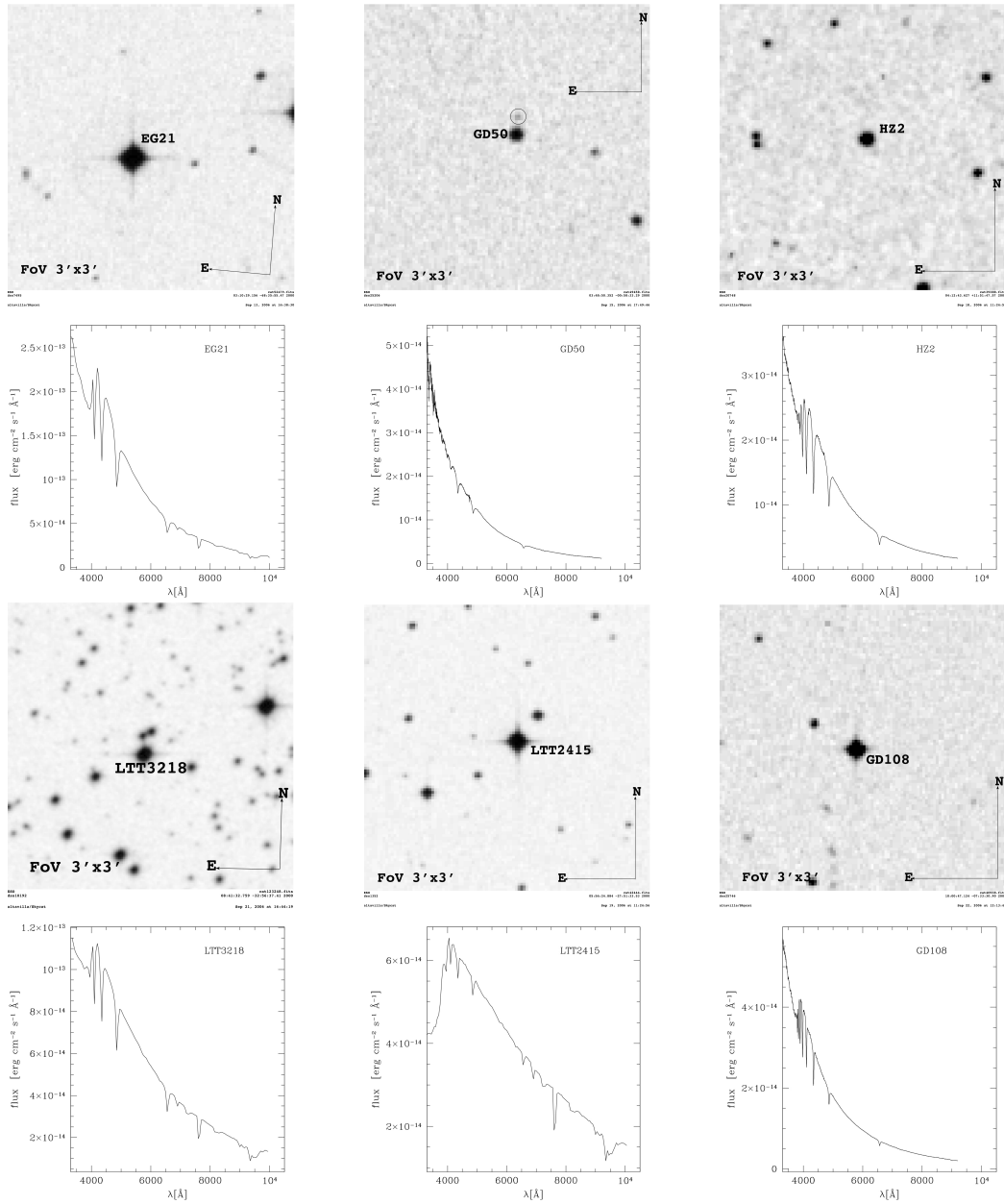


Figure 4.3: Primary SPSS $3' \times 3'$ image thumbnails and spectra. Faint unknown stars very close to the SPSS flux are marked with a circle. North and East are shown in each figure.

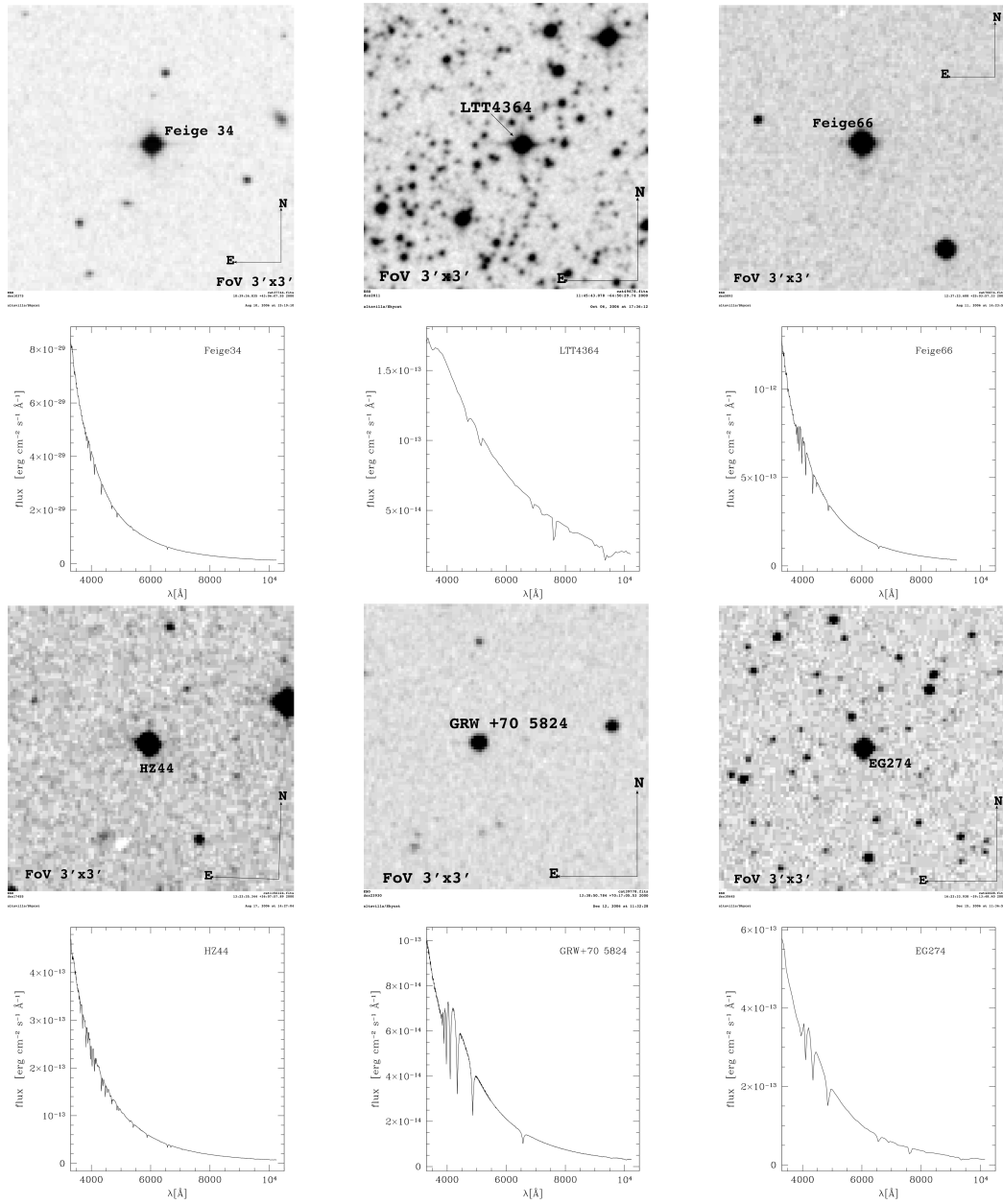


Figure 4.4: Primary SPSS $3' \times 3'$ image thumbnails and spectra. Faint unknown stars very close to the SPSS are marked with a circle. North and East are shown in each figure.

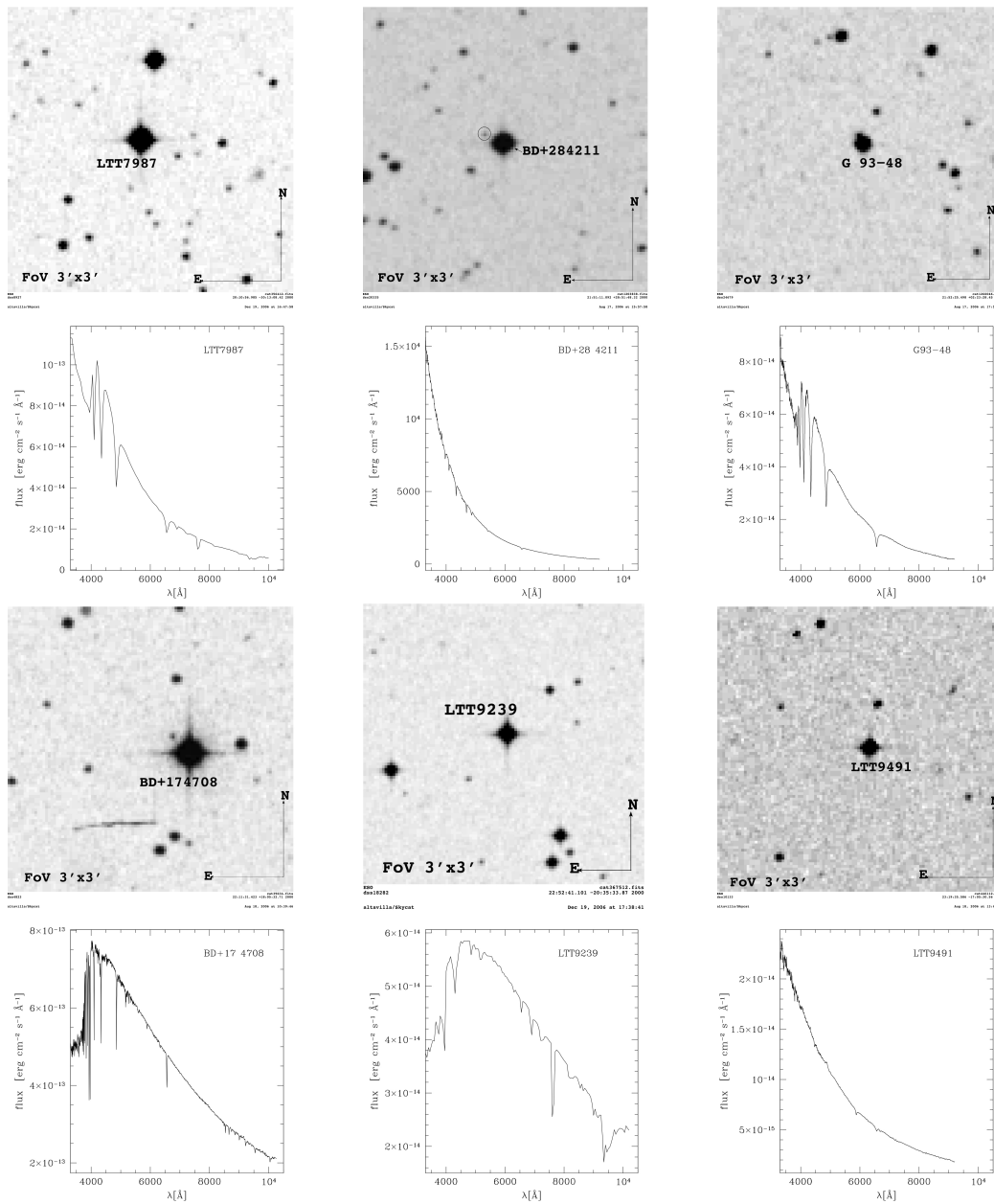


Figure 4.5: Primary SPSS $3' \times 3'$ image thumbnails and spectra. Faint unknown stars very close to the SPSS are marked with a circle. North and East are shown in each figure.

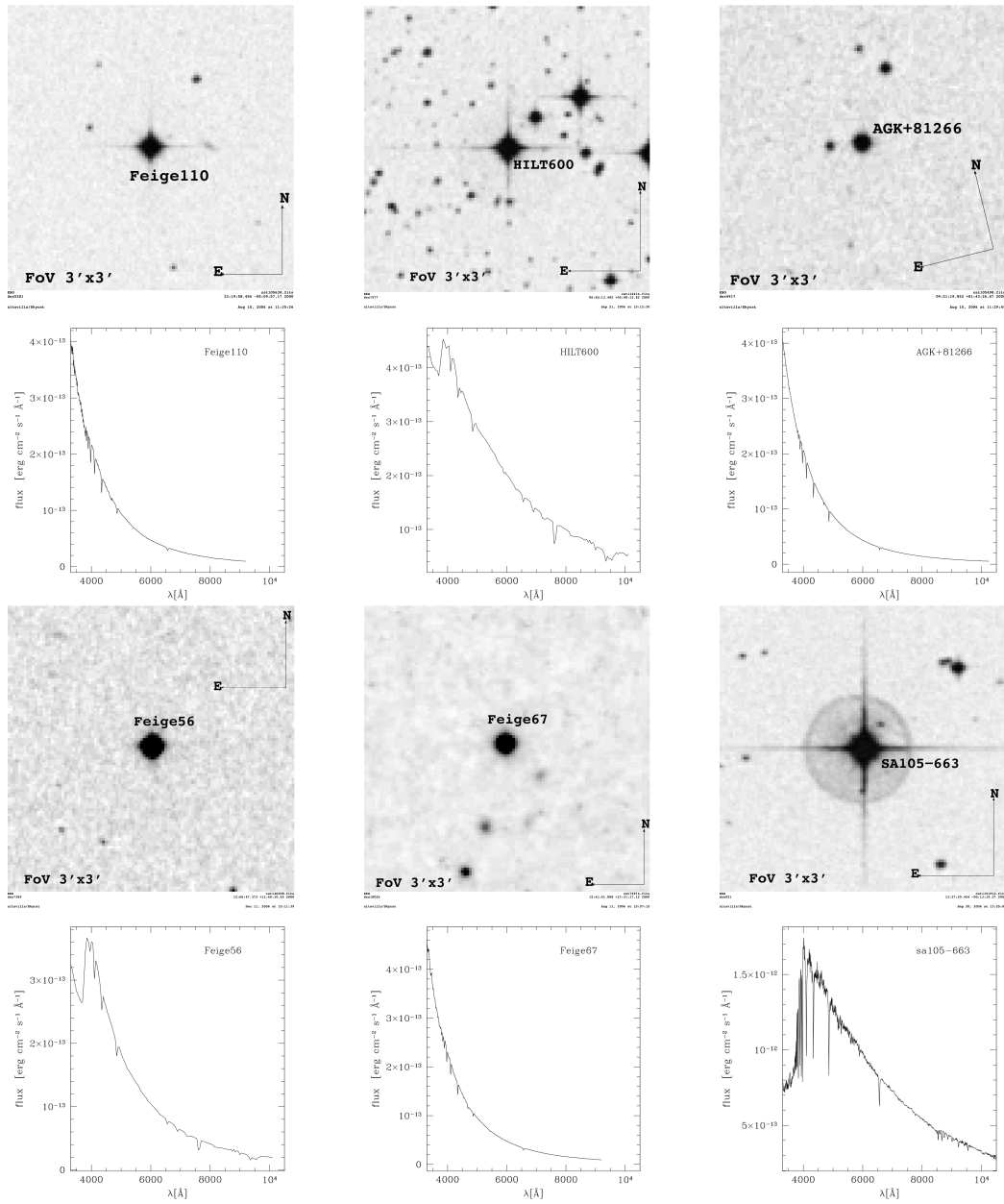


Figure 4.6: Primary SPSS $3' \times 3'$ image thumbnails and spectra. Faint unknown stars very close to the SPSS are marked with a circle. North and East are shown in each figure.

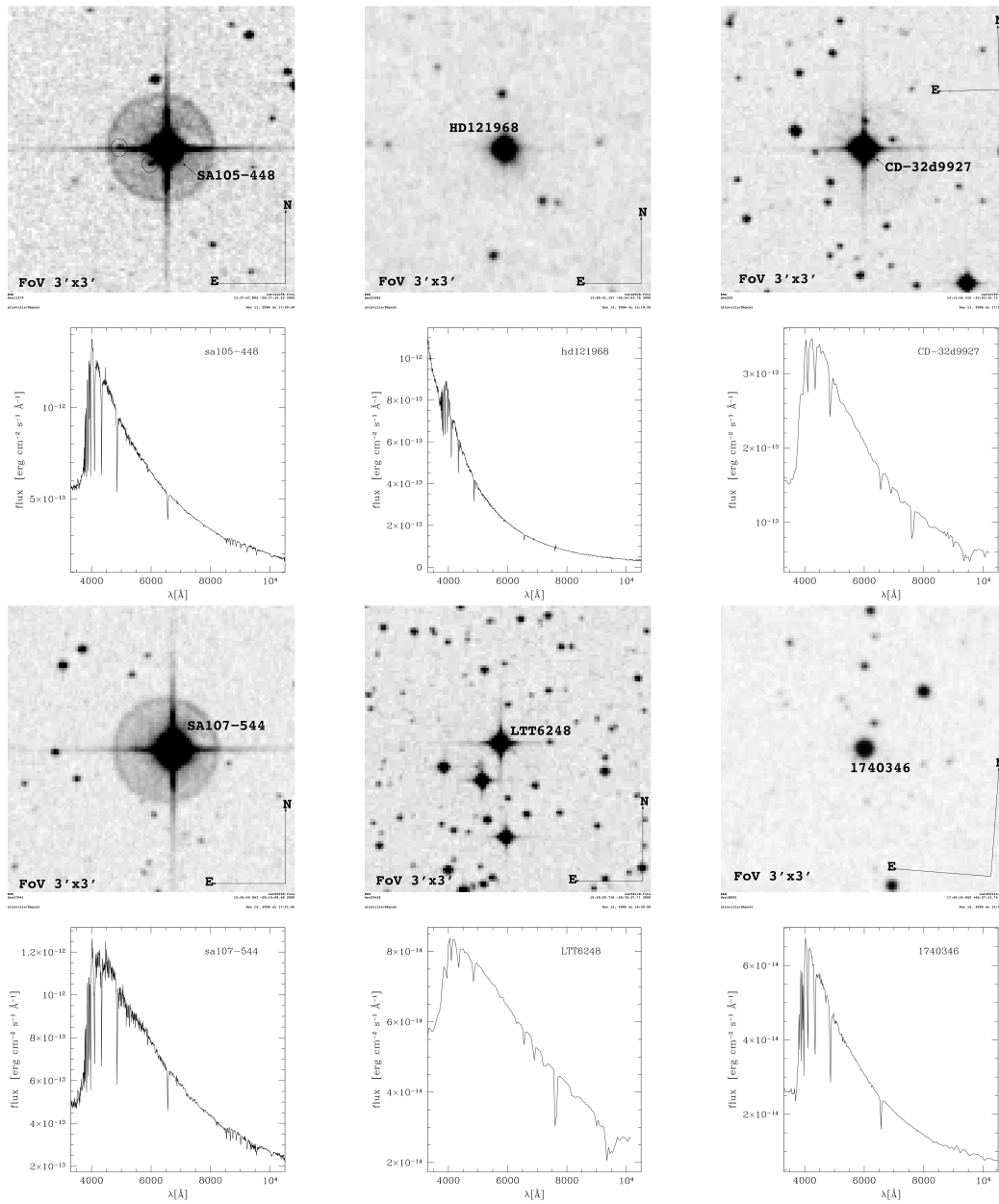


Figure 4.7: Primary SPSS $3' \times 3'$ image thumbnails and spectra. Faint unknown stars very close to the SPSS are marked with a circle. North and East are shown in each figure.

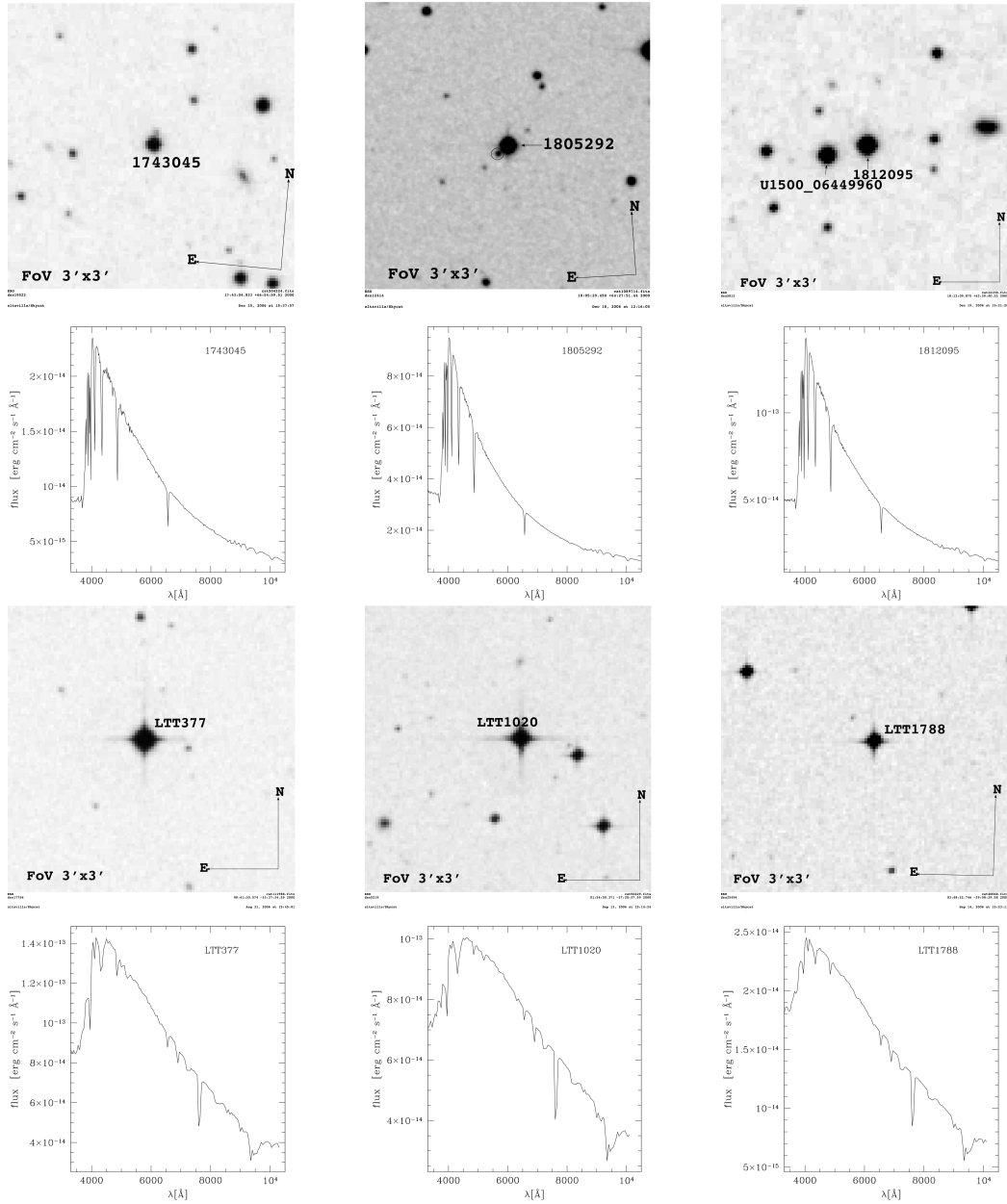


Figure 4.8: Primary SPSS $3' \times 3'$ image thumbnails and spectra. Faint unknown stars very close to the SPSS are marked with a circle. North and East are shown in each figure.

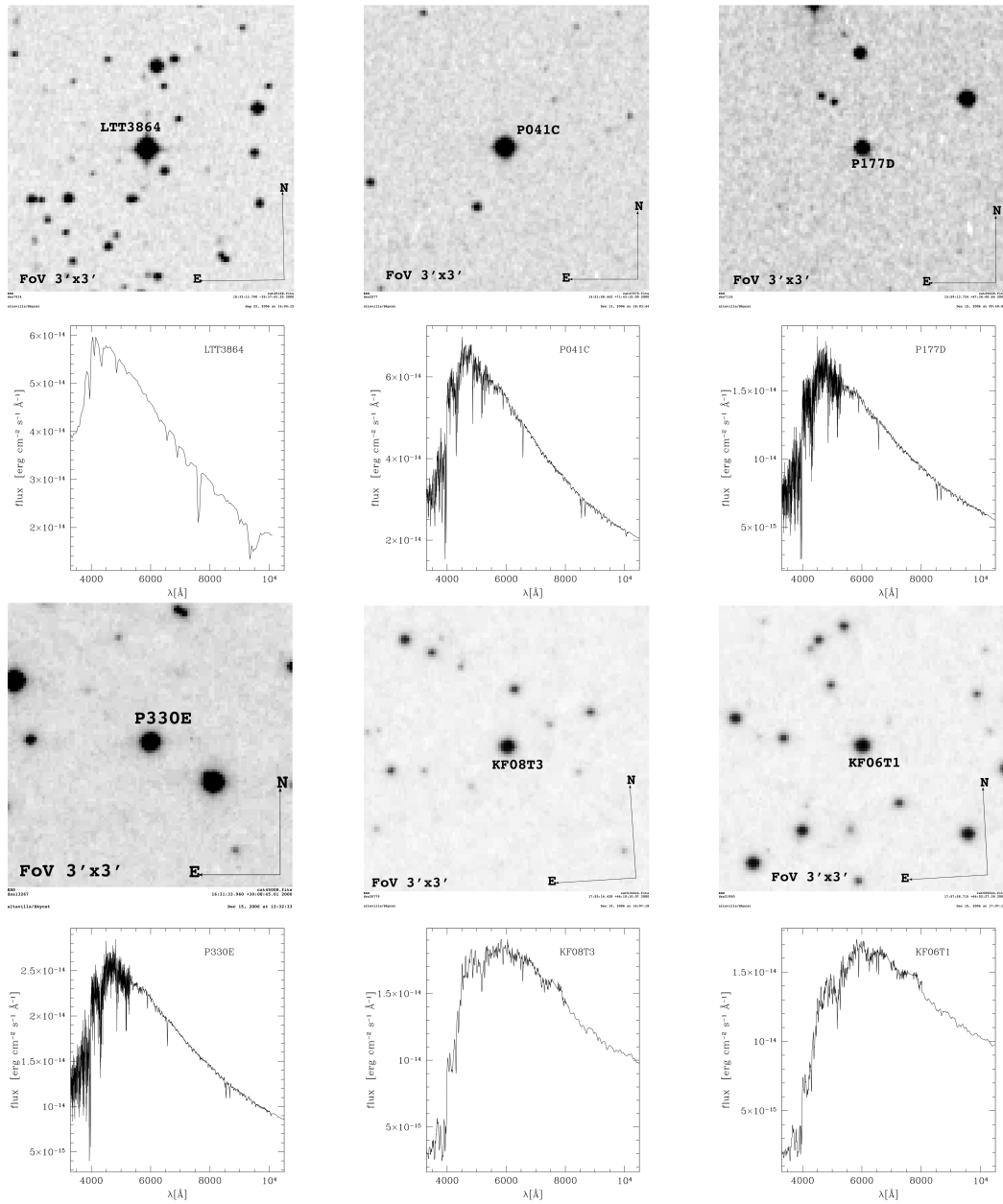


Figure 4.9: Primary SPSS $3' \times 3'$ image thumbnails and spectra. Faint unknown stars very close to the SPSS are marked with a circle. North and East are shown in each figure.

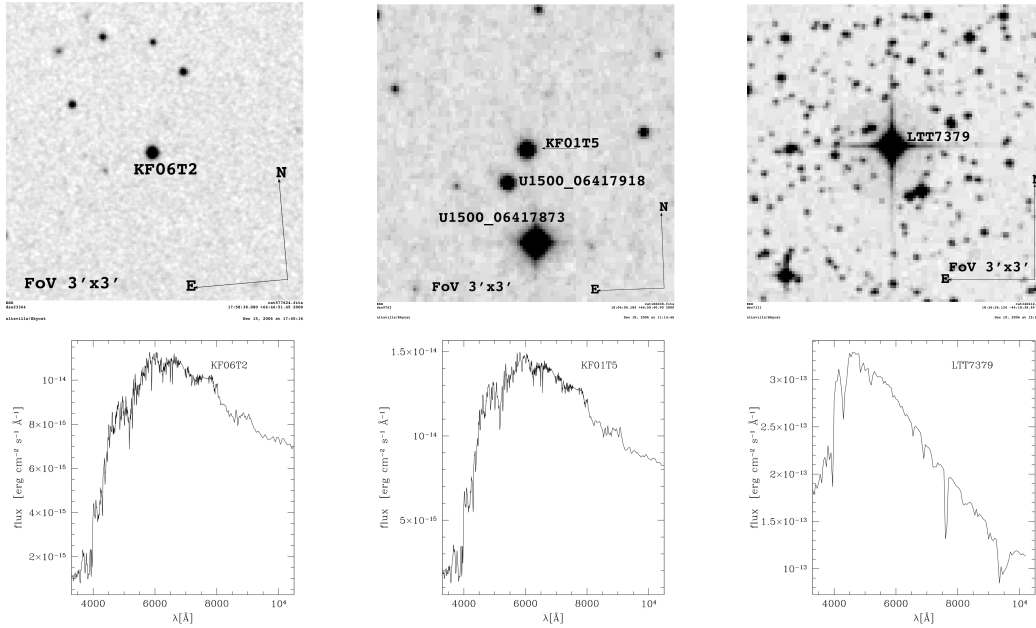


Figure 4.10: Primary SPSS $3' \times 3'$ image thumbnails and spectra. Faint unknown stars very close to the SPSS are marked with a circle. North and East are shown in each figure.

4.1.3 Secondary SPSS: selection criteria and Candidates

The *Secondary SPSS* will constitute the actual Gaia SPSS grid. These SPSS should meet the following requirements (van Leeuwen 2010):

- Secondary SPSS must have available flux-calibrated spectra ($R \sim 200-1000$) on a homogeneous scale, with wavelength coverage from 330 nm to 1050 nm. The typical uncertainty on the absolute flux scale, with respect to the assumed calibration of Vega (see Bohlin & Gilliland 2004; Bohlin 2007), shall be of a few %, excluding small troubled sections in the spectral range (e.g., telluric absorptions band, extreme blue and red edges) where it can be somewhat worse.
- The magnitude range is $V \sim 9-15$, to provide high signal to noise spectra ($S/N \sim 100$ per pixel over most of the wavelength range), with reasonable exposure times when observed with 2–4m class ground-based telescopes.

- Secondary SPSS magnitude and sky location grant a resulting S/N~100 per sample over most of the wavelength range when observed by Gaia (i.e., taking into account the expected number of useful and clean transit to the end of mission, Carrasco et al. 2006, 2007).
- Secondary SPSS shall be validated against variability.
- Secondary SPSS cover a wide range of spectral types and spectral shapes, as needed to ensure the best possible calibration of all kinds of objects observed by Gaia (see also Chapter 3).

Of course, all *Primary SPSS* that fulfill the *Secondary SPSS* requirements will be included in the actual Gaia grid, as well. We estimated that we need approximately 200 SPSS to statistically ensure the desired calibration accuracy (see Section 3.4). The selection criteria of the *Secondary SPSS* are quite similar to the ones used to select the Primary SPSS (see Section 4.1.2, and Table 4.4) and are derived from the general requirements described in van Leeuwen (2010), but with a few differences, as shown in Table 4.4 (and explained below). The Primary SPSS, mainly used as ground-based spectro-photometric standard stars, range over a more limited spectral type interval, i.e., most of all are hot subdwarfs and white dwarfs with few exceptions. Their spectra show less features than other stars and this allows a better determination of the overall instruments response, hence of the flux calibration, from ground-based telescopes. The initial Secondary SPSS candidate list was populated mainly with hot, featureless stars, at least initially. Following the indications of the latest calibration model (Montegriffo & Bellazzini 2009b), we started however to implement a significant number of red and cold stars (from Zechmeister et al. 2009 and Jenkins et al. 2009) in our Secondary SPSS sample. The Secondary SPSS candidate list may still be adjusted according to the development and testing of the calibration model by CU5-DU14.

One obvious and fundamental requirement for an SPSS is that its magnitude is constant (see Section 4.2.2). The Secondary SPSS are *new* spectro-photometric standard star candidates, hence, unlike Primary SPSS, no literature flux tables are required *a priori*. Nevertheless the literature was scanned to collect all the information easily available to select suitable targets, as reported in Table 4.5 (see Altavilla et al. 2010 for more details). A complete and updated list of the secondary SPSS sources is available in the Wiki-Bo¹³ page. This list presently contains 48 references to litera-

¹³http://yoda.bo.astro.it/wiki/index.php/SPSS_Secondary_Sources, restricted access, please contact elena.pancino@oabo.inaf.it for the guest access credentials

Table 4.4: SPSS selection criteria

<i>Primary SPSS</i>	<i>Secondary SPSS</i>
Spectral energy distribution (SED)	
as featureless as possible.	covering a wide range of spectral types.
Constant luminosity	
not variable within ~ 0.01 mag in the optical range.	not variable within ~ 0.01 mag in the optical range.
Literature data	
the stars should have already been used as spectrophotometric standard.	the stars can be new spectrophotometric standards without literature data or/and SEDs.
SNR: Magnitude range & transits	
$V \sim 9 - 15$, i.e: not too bright to avoid saturation but sufficiently bright to provide high signal to noise spectra ($SNR \geq 100$) over most of the wavelength range also with reasonable exposure times with 2-4m class telescopes	$V \sim 10 - 15$, i.e.: not too bright to avoid saturation and number of expected end-of-mission transits high enough to provide $SNR \geq 100$ over most of the wavelength range when observed by Gaia.
Location	
isolated enough to avoid contamination from nearby stars; covering a suitable range of right ascension and declination to ensure all-year-round ground-based observations from both hemispheres.	isolated enough to avoid contamination from nearby stars from both fields of view when observed by Gaia; a subsample close to the EPs to facilitate the initial instruments calibration.

ture papers.

Additional, special members of the Secondary SPSS candidates are:

- a few selected SPSS around the Ecliptic Poles (3 close to the North Pole, 6 close to the South Pole), two regions of the sky that will be repeatedly observed by Gaia in the first two weeks after reaching its orbit in L2, for calibration purposes;
- a few SDSS stars that were observed in the SEGUE sample (Yanny et al. 2009), since the SEGUE sample has the potential of being extremely useful in the Gaia flux calibration (Bellazzini et al. 2010);
- a few well known SPSS, which are among the targets of the ACCESS mission (Kaiser et al. 2010), dedicated to the absolute flux measurement of a few stars

besides Vega. Actually, some of these stars were also included in the Primary SPSS list.

Fig. 4.11 shows the distribution on the sky and the V magnitude range of our present candidate Secondary SPSS. Stars are preferentially distributed in the Northern hemisphere, where about two third of our sample are located, reflecting the source catalogues distribution. The Secondary SPSS V magnitude range is $8.9 < V < 15.3$, and about 42% of the star has $V < 13.0$. The B–V color range is $-0.5 < B-V < 1.7$ ¹⁴. As noticed above, the Secondary SPSS accepted candidates are listed in Table 4.5. Coordinates, magnitudes (B, V), spectral type, expected end-of-mission transits and astrophysical parameters (T_{eff} , $\log g$, [Fe/H]) from the literature are listed in the table. For a more complete and updated listing of the candidate secondary SPSS and their characteristics is available in the Wiki-Bo¹⁵ page where each target is linked to a specific page with more detailed information, finding charts, astrophysical parameters and observation status. The SPSS candidates rejected so far (for variability, crowding or other reasons) are listed in Table. 4.7.

¹⁴ID 208 and ID 234, both DA WD, have unrealistic blue colors: $B-V=-0.90$ and $B-V=-0.96$ respectively, due to their uncertain magnitudes.

¹⁵http://yoda.bo.astro.it/wiki/index.php/Secondary_Observations_Table

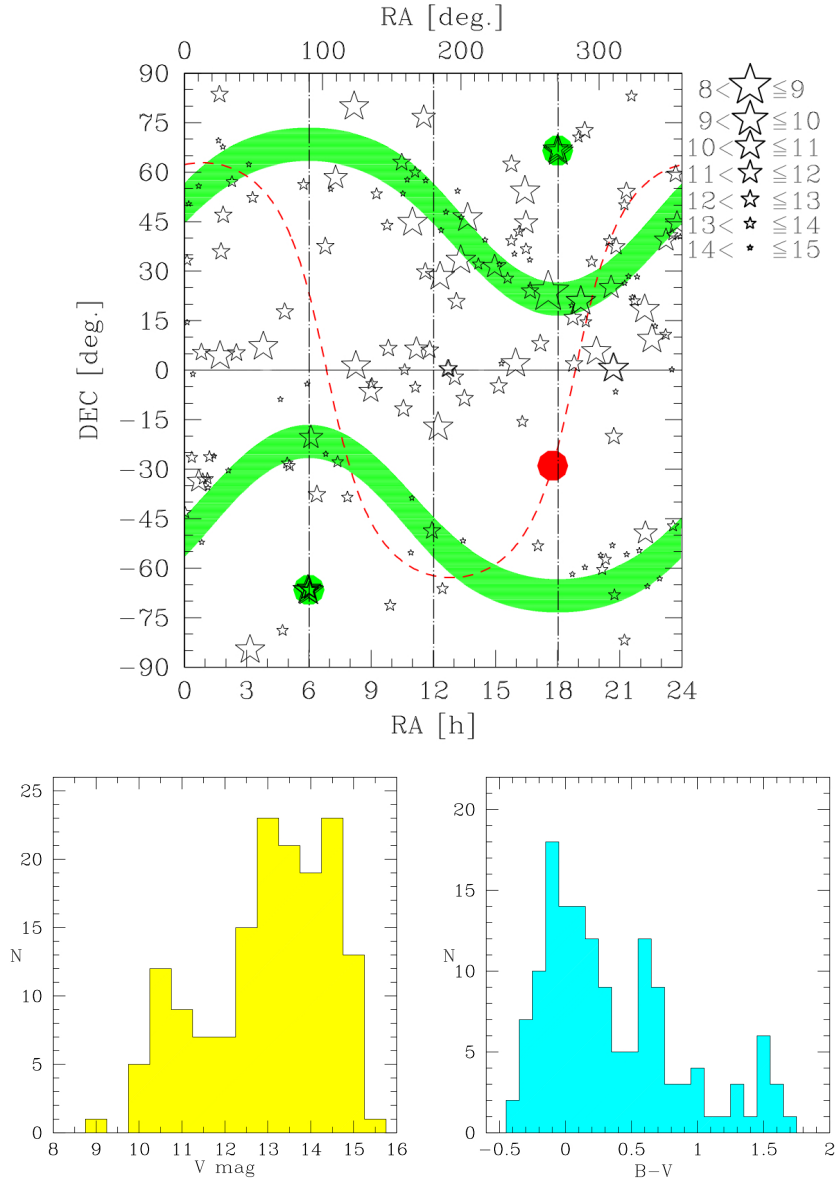


Figure 4.11: Spatial distribution (*top panel*), magnitude coverage (*left bottom panel*) and color coverage (*right bottom panel*) of the candidate *Secondary SPSS*. The stripes corresponding to the ecliptic latitude $40 < |\delta| < 50$ are marked in green in the top panel. Stars falling into these two regions will be observed more than ~ 150 times during the whole mission. The green circles marks the North and South Ecliptic Poles. The red dashed line shows the Galactic plane and the red filled circle the Galactic center.

Table 4.5: Secondary SPSS list

ID	Name	RA (J2000) <i>hh mm ss</i>	DEC (J2000) <i>° ' "</i>	B	V	Sp. Type	Tr.	$T_{eff}/\log g/[Fe/H]$ & Notes
101	WD0046+051	00 49 09.90	+05 23 19.01	12.92	12.36	DZ7-8	61	$T_{eff} \sim 6500$ K (Bergeron et al. 2001; Dufour et al. 2005)
102	WD0134+833	01 41 31.00	+83 35 00.00	13.0	999	DA2/3	76	$T_{eff} \sim 18600$ K (Bergeron et al. 1992; Lajoie & Bergeron 2007)
103	G72-34	01 46 03.76	+35 54 48.60	13.84	12.98	-	66	$T_{eff}/\log g/[Fe/H]=4750/4.5/-2.0$; not RV var. (Latham et al. 2002)
104	WD0148+467	01 52 02.96	+47 00 06.67	12.50	12.44	DA3.5	88	High Proper Motion Star $T_{eff} \sim 13700$ (Bergeron et al. 1992; Lajoie & Bergeron 2007); not RV var. (Maxted et al. 2000)
105	WD0227+050	02 30 16.62	+05 15 50.69	12.745	12.799	DA2/3	57	$T_{eff} \sim 18900$ (Bergeron et al. 1992; Lajoie & Bergeron 2007) Landolt phot. std. (Landolt 1992, (Feige 22))
106	WD0316-849	03 09 59.89	-84 43 21.14	11.6	10.50	DA1	72	magnetic WD: to be rejected?
109	WD0604-203	06 06 13.39	-20 21 07.30	11.75	11.80	He-Bsd	113	$T_{eff}/\log g/[Fe/H]=19800/4.55$ (Yennes et al. 2007) recently discovered as Albus 1 (Caballero & Solano 2007); He-B subdwarf (previously WD/sd)
110	WD0621-376	06 23 12.20	-37 41 29.00	11.76	12.09	DA1	78	$T_{eff} \sim 59000$ K (Kawka webpage)
112	WD0644+375	06 47 37.99	+37 30 57.09	12.00	12.0	DAn	66	Spinning Star, $T_{eff} \sim 21000$ K (Bergeron et al. 1992)
113	WD0713+584	07 17 36.26	+58 24 20.51	12.00	11.91	DA	97	$T_{eff} \sim 13400$ (Kepler & Nelan 1993); no cold comp. (Farhi et al. 2005)
114	G251-54	08 11 06.24	+79 54 29.56	10.57	10.07	G0	81	$T_{eff}/\log g/[Fe/H]=6000/4.0/-1.5$, not RV var. (Latham et al. 2002) [Fe/H]=-2.34 (Zhang & Zhao 2005)
115	G114-25	08 59 03.37	-06 23 46.19	12.51	11.92	F7	63	CPM pair sep. 110" (Zapatero Osorio & Martin 2004, Tab.2)
116	G43-5	09 49 51.58	+06 36 35.50	13.18	12.52	K:	57	$T_{eff}/\log g/[Fe/H]=5500/4.5/-2.5$, not RV var. (Latham et al. 2002)
118	G236-30	10 28 48.39	+62 59 44.90	13.49	12.85	-	90	$T_{eff}/\log g/[Fe/H]=5500/4.5/-2.5$ (Latham et al. 2002) SBI: $P = 617d$ (?), $sep. = 18.7''$ (Zapatero Osorio & Martín 2004)
119	WD1031-114	10 33 42.76	-11 41 38.35	12.82	13.00	DA2	66	$T_{eff} \sim 27000$ K (Lajoie & Bergeron 2007); not RV var. (Maxted et al. 2000)
120	G146-76	10 59 57.48	+44 46 43.70	12.20	10.49	-	89	$T_{eff}/\log g/[Fe/H]=6000/4.0/-1.0$, not RV var. (Latham et al. 2002) [Fe/H]=-1.64 (Zhang & Zhao 2005) if bin. sep. > 25" (Zapatero Osorio & Martin 2004)

Table 4.5: Secondary SPSS list - continued

ID	Name	RA <small>hh mm ss</small>	DEC (J2000) <small>o , ' , ''</small>	B	V	Sp. Type	Tr.	$T_{eff}/\log g/[Fe/H]$ & Notes
121	WD1105-048	11 07 59.95	-05 09 25.90	13.094	13.059	DA3	61	DA+dM3 at about 280" (Farihi et al. 2005); WD possibly magnetic (Jordan et al. 2007); (Landolt 1992, (G163-050))
122	G10-4	11 11 00.00	+06 25 11.50	12.13	11.41	sd:G3	55	$T_{eff}/\log g/[Fe/H]=5000/4.5/-2.5$, not RV var. (Latham et al. 2002) wide bin., <i>sep.</i> = 16" (Zapatero Osorio & Martín 2004)
123	G254-24	11 32 23.31	+76 39 18.03	12.18	11.53	-	75	$T_{eff}/\log g/[Fe/H]=5250/4.5/-2.0$, not RV var. (Latham et al. 2002) if bin. <i>sep.</i> > 25" (Zapatero Osorio & Martín 2004)
124	WD1134+300	11 37 05.10	+29 47 58.34	12.41	12.49	DA2	63	$T_{eff} \sim 21500$ K (Bergeron et al. 1992; Lajoie & Bergeron 2007) Phot. Landolt & Uomoto 07, opt. phot. (?), (GDI40))
125	G10-54	11 49 48.18	+06 08 51.70	13.18	12.58	-	57	$T_{eff}/\log g/[Fe/H]=5250/4.5/-2.0$, not RV var. (Latham et al. 2002)
127	WD1153-484	11 56 11.43	-48 40 03.30	12.65	12.86	DA2/sdB	107	$T_{eff}/\log g=30800/5.15$ (Kawka et al. 2007)
129	WD1211-169	12 14 10.53	-17 14 20.19	11.20	10.23	DAH	63	magnetic WD (McCook & Sion 1999; Anselowitz et al. 1999)
130	G14-24	13 02 01.58	-02 05 21.80	13.53	12.81	DA:	56	$T_{eff}/\log g/[Fe/H]=5250/4.5/-2.0$ (Latham et al. 2002) wide bin., <i>sep.</i> = 16", (Zapatero Osorio & Martín 2004); $\Delta mag(\text{prim./second.}) > 5$ (Zapatero Osorio & Martín 2004); new SDSS WD1259-015, but coords differ, $g=17.19$: not the same
131	WD1327-083	13 30 13.64	-08 34 29.49	12.40	12.31	DA	59	$T_{eff} \sim 14000$ K (Bragaglia et al. 1995, e.g.,) DA+dM4.5, <i>sep.</i> = 503" (Farihi et al. 2005); not variable (Giovannini et al. 1998)
132	G15-10	15 09 46.02	-04 45 06.63	13.00	13.00	G2	60	$T_{eff}/\log g/[Fe/H]=5250/4.5/-2.0$ (Latham et al. 2002) wide bin. uncertain <i>sep.</i> : 20.16" (Zapatero Osorio & Martín 2004) or 677" (Allen et al. 2000)
133	G224-83	15 46 14.66	+62 26 39.40	13.36	12.76	-	67	$T_{eff}/\log g/[Fe/H]=5250/4.5/-2.0$ (Latham et al. 2002) if bin. <i>sep.</i> > 25" (Zapatero Osorio & Martín 2004)
134	G16-20	15 58 18.62	+02 03 06.10	11.41	10.79	-	66	$T_{eff}/\log g/[Fe/H]=6000/4.0/-1.0$ (Latham et al. 2002) if bin. <i>sep.</i> > 25" (Zapatero Osorio & Martín 2004)
135	WD1615-154	16 17 55.25	-15 35 52.40	13.217	13.422	DA2	56	$T_{eff} \sim 29700$ (Bergeron et al. 1992; Bragaglia et al. 1995) $T_{eff} \sim 29700$ (Lajoie & Bergeron 2007) phot. standard (?), (G 153-41))

Table 4.5: Secondary SPSS list - continued

ID	Name	RA (J2000) <i>hh mm ss</i>	DEC (J2000) <i>° ' "</i>	B	V	Sp. Type	Tr.	$T_{eff}/\log g/[Fe/H]$ & Notes
136	G180-58	16 28 16.87	+44 40 38.27	11.97	11.29	G2	73	$T_{eff}/\log g/[Fe/H]=5000/4.5/-2.5$ (Latham et al. 2002) wide bin., <i>sep.</i> $\simeq 22''$ (Zapatero Osorio & Martín 2004)
138	G139-16	17 09 47.00	+08 04 18.00	13.20	12.55	-	82	$\Delta mag(\text{prim}/\text{second}).3.5$ (Zapatero Osorio & Martín 2004)
139	G170-47	17 32 41.62	+23 44 11.63	9.59	8.95	G0	98	wide bin., <i>sep.</i> $\sim 7.5'' - 15''$ (Zapatero Osorio & Martín 2004) $T_{eff}/\log g/[Fe/H]=5750/4.5/-2.0$ (Latham et al. 2002) $T_{eff}/\log g/[Fe/H]=5228/2.94/-2.42$ (Allen et al. 2000) if bin., <i>sep.</i> $> 25''$ (Zapatero Osorio & Martín 2004)
140	G184-20	18 43 52.00	+16 00 36.00	13.29	12.61	-	117	wide bin., <i>separ</i> $5''-20''$ (Zapatero Osorio & Martín 2004)
141	WD1845+019	18 47 37.00	+01 57 30.0	12.73	12.96	DA2	67	candidate DA+dM. <i>sep</i> $3''$ Hoard et al. (2007)
142	WD1918+725	19 18 10.00	+72 37 24.00	12.70	13.00	DA2.4	69	$T_{eff}=29700$ (Bergeron et al. 1992)
144	WD1919+145	19 21 40.00	+14 40 36.00	13.07	13.01	DA3.5	109	$T_{eff}=14520$ (Lajoie & Bergeron 2007)
145	G23-14	19 51 49.61	+05 36 45.84	11.46	10.72	G5	71	$T_{eff}/\log g/[Fe/H]=6000/4.0/-0.5$ (Latham et al. 2002) bin., <i>sep.</i> $\simeq 21''$ (Zapatero Osorio & Martín 2004)
146	WD2032+248	20 34 22.37	+25 04 09.46	11.46	11.52	DA3	123	$T_{eff} \simeq 19500$ (Bergeron et al. 1992; Lajoie & Bergeron 2007); not RV var. (Maxted et al. 2000)
147	G24-25	20 40 16.10	+00 33 19.74	11.13	10.60	G0	64	$T_{eff}/\log g/[Fe/H]=5500/4.5/-2.0$ (Latham et al. 2002)
148	WD2039-202	20 42 34.75	-20 04 35.95	12.27	12.34	DA2/3	59	$T_{eff} \sim 19900$ (Bragaglia et al. 1995; Lajoie & Bergeron 2007); not RV var. (Maxted et al. 2000)
149	WD2047+372	20 49 05.88	+37 28 04.99	13.07	12.93	DA4	86	$T_{eff}=14060$ (Lajoie & Bergeron 2007) Companion, Warning
151	WD2211-495	22 14 11.914	-49 19 27.26	11.3	11.7	DA1	91	$T_{eff} \sim 64000$ (Kawka webpage)
152	G190-15	23 13 38.82	+39 25 02.60	11.67	11.05	F6	162	$T_{eff}/\log g/[Fe/H]=5250/4.5/-2.5$ (Latham et al. 2002) if bin., <i>sep.</i> $> 25''$ (Zapatero Osorio & Martín 2004), high P.M.
153	G241-64	23 41 24.40	+59 24 34.87	13.45	12.70	-	85	$T_{eff}/\log g/[Fe/H]=5000/4.5/-2.0$ (Latham et al. 2002) <i>sep.</i> $= 13'' - 21''$ (Zapatero Osorio & Martín 2004), high P.M.
154	G171-15	23 45 02.71	+44 40 03.60	12.21	11.56	G0	124	$T_{eff}/\log g/[Fe/H]=5250/4.5/-2.0$ (Latham et al. 2002) if bin., <i>sep.</i> $> 25''$ (Zapatero Osorio et al. 2004), high P.M.
155	WD2359-434	00 02 10.75	-43 09 55.6	13.12	13.05	DA5/6	115	$T_{eff} \sim 8700$ (Bragaglia et al. 1995; Lajoie & Bergeron 2007, e.g.); weak magnetic field (Aznar Cuadrado et al. 2004, 4KG)

Table 4.5: *Secondary* SPSS list - continued

ID	Name	RA <i>hh mm ss</i>	DEC <i>(J2000)</i> <i>o ' ''</i>	B	V	Sp. Type	Tr.	$T_{eff}/\log g/[Fe/H]$ & Notes
156	WD0004+330	00 07 32.30	+33 17 27.7	13.53	13.82	DA1	83	$T_{eff} > 46000$ K (Kawka webpage)
158	WD0018-267	00 21 30.7	-26 26 14	-	13.8	DA	71	tentative low-mass companion (Hoard et al. 2007)
159	WD0050-332	00 53 17.43	-32 59 56.5	13.14	13.36	DA1.5	84	$T_{eff} \sim 35000$ K (Kawka webpage)
160	WD0104-331	01 06 45	-32 53 00	13.28	13.57	DA1	92	tentative low-mass companion (Hoard et al. 2007)
161	WD0109-264	01 12 11.66	-26 13 27.7	12.953	13.15	sdB	81	$T_{eff}/\log g = 27700, 5.5$ (Lisker et al. 2005, (as SB 485))
164	WD0214+568	02 17 33.52	+57 06 47.5	13.56	13.68	DA2.5	165	$T_{eff} \sim 21200$ (Bergeron et al. 1992; Lajoie & Bergeron 2007)
165	G174-44	03 17 23.34	+52 17 42.3	14.49	13.75	sdG	92	$T_{eff}/\log g/[Fe/H] = 4750/4.5/-2.0$ (Latham et al. 2002)
167	WD0435-088	04 37 47.42	-08 49 10.7	14.24	14.1	DQ7	82	DQ7 with broad features (see Fig. 7, Dufour et al. 2005); differing mags (McCook & Sion 1999)
168	WD0455-282	04 57 13.9	-28 07 54	999	13.95	DA1	89	$T_{eff} \sim 55-58000$ K (Kawka webpage)
170	WD0501-289	05 03 53.9	-28 55 04	999	13.9	DO	88	$T_{eff} = 68600$ K (Kawka et al. 2007)
171	G191-52	05 44 43.56	+56 15 30.5	14.02	13.26	-	96	$T_{eff}/\log g/[Fe/H] = 5500/4.5/-2.0$ (Latham et al. 2002) Visual companion $\sim 5''$
173	WD0646-253	06 48 55.9	-25 23 57	999	14.5	DA2	96	$T_{eff} \sim 27900$ K (Kawka webpage)
174	G193-26	07 03 26.31	+54 52 05.8	13.5	999	-	84	$T_{eff}/\log g/[Fe/H] = 5500/4.5/-3.0$ (Latham et al. 2002)
175	WD0721-276	07 23 19.8	-27 47 17	13.4	13.5	DA1.4	93	$T_{eff} \sim 36000$ K (Kawka webpage)
177	WD0749-383	07 51 32.579	-38 28 36.41	13.53	13.66	DA	80	in Open Cluster NGC2477 Hartwick et al. (1972)
179	WD0912+536	09 15 56.23	+53 25 24.9	14.09	13.79	DXP7	92	magnetic (McCook & Sion 1999), better avoid
180	WD0943+441	09 46 39.08	+43 54 52.3	13.39	13.29	DA3/4	72	$T_{eff} \sim 13-1400$ K (Liebert et al. 2005; Lajoie & Bergeron 2007) non var. (Giovannini et al. 1998)
181	WD0954-710	09 55 23.6	-71 18 05	13.60	13.48	DA4	75	$T_{eff} = 13900$ K (Bragaglia et al. 1995; Lajoie & Bergeron 2007)
183	WD1104+602	11 07 42.77	+59 58 29.7	13.78	13.80	DA3	89	not RV var. (Maxted et al. 2000)
186	WD1223-659	12 26 42.02	-66 12 18.4	14.37	13.97	DA 7/DF	83	$T_{eff} \sim 18000$ (Bergeron et al. 1992; Lajoie & Bergeron 2007)
191	G167-50	15 35 31.56	+27 51 02.3	14.25	13.50	-	99	$T_{eff} \sim 7700$ K (Kawka webpage) $T_{eff}/\log g/[Fe/H] = 5750/4.5/-1.0$ (Latham et al. 2002) <i>sep.</i> $> 20'' - 25''$ (Zapatero Osorio & Martin 2004)
192	G179-54	15 46 08.26	+39 14 16.4	14.13	13.51	-	78	wide bin, <i>sep</i> 7" (Zapatero Osorio & Martin 2004); avoid?
193	WD1606+422	16 08 22.20	+42 05 43.3	13.91	13.86	DA4	75	probable DD (Bergeron et al. 2001); probable DD (Zuckerman et al. 2003), better avoid?

Table 4.5: Secondary SPSS list - continued

ID	Name	RA (J2000) <i>h m s s</i>	DEC (J2000) <i>° ' "</i>	B	V	Sp. Type	T _r	T _{eff} /log g/[Fe/H] & Notes
194	WD1626+368	16 28 25.00	+36 46 15.8	14.01	13.85	DAZ5	79	T _{eff} =8640 (Bergeron et al. 2001)
196	WD1659-531	17 02 56.34	-53 14 36.2	13.57	13.47	DA4	87	T _{eff} ~14000 K (Kawka webpage)
199	WD1936+327	19 38 28.20	+32 53 19.6	13.46	13.58	DA2.5	86	CPM pair (with HR6314, F7 dwarf, at 113"; SIMBAD)
201	WD2004-605	20 09 05.24	-60 25 41.6	999	13.4	DA1	134	T _{eff} ~20900 K (Bergeron et al. 1992; Lajoie & Bergeron 2007)
202	WD2014-575	20 18 54.9	-57 21 34	13.56	13.73	DA2	92	T _{eff} ~43000 K (Koester et al. 2001)
203	WD2028+390	20 29 56.18	+39 13 32.2	14.2	13.37	DA2	82	in SPY project; UVES high-res in SPY project (Kawka webpage)
204	WD2039-682	20 44 21.47	-68 05 21.3	13.19	13.25	DA3	96	T _{eff} =24630 K (Bergeron et al. 1992) not RV var. (Saffler et al. 1998)
205	WD2111+498	21 12 43.97	+50 06 18.3	12.85	13.09	DA1.3	77	T _{eff} ~16000 K (Kawka webpage)
206	WD2105-820	21 13 15.88	-81 49 10.1	13.77	13.50	DA5	78	T _{eff} =24630 K (Bergeron et al. 1992)
208	WD2122+282	21 25 00.33	+28 26 11.7	13.4	14.3	DA	135	T _{eff} =10200 K (Bergeron et al. 2001)
209	WD2136+828	21 33 43.29	+83 03 32.5	13.0	13.02	DA3	73	T _{eff} ~53000 (Kawka webpage) uncertain mag, it's not so blue
211	WD2140+207	21 42 41.00	+20 59 58.2	13.40	13.27	DQ6	89	T _{eff} ~16800 K (Bergeron et al. 1992; Lajoie & Bergeron 2007) not RV var. (Maxted et al. 2000)
214	WD2329+407	23 31 35.65	+41 01 30.7	13.85	13.82	DA3	156	T _{eff} =8860 K (Bergeron et al. 2001)
215	WD2331-475	23 34 02.19	-47 14 26.6	13.13	13.46	DA1	174	T _{eff} =15900 K (Bergeron et al. 1992)
216	WD0009+501	00 12 14.80	+50 25 21.4	14.6	14.37	DAH7.7	107	T _{eff} ~54000 K (Kawka webpage)
217	WD0038+555	00 41 22.03	+55 50 08.3	14.10	14.0	DQ	100	magnetic WD (McCook & Stion 1999), better avoid?
218	WD0047-524	00 50 03.51	-52 08 15.7	14.157	14.206	DA2/3	82	M4 companion at 11" (SIMBAD: G218-8 + G218-7) T _{eff} ~18500 (Bragaglia et al. 1995; Lajoie & Bergeron 2007), see also Kawka webpage
219	WD0106-358	01 08 20.8	-35 34 43	15.8	999	DA1/2	114	photometry in Landolt & Uomoto (2007)
220	WD0123-262	01 25 24.48	-26 00 44.5	15.34	14.94	DC7	82	T _{eff} ~29-30000 K (Kawka webpage)
221	G245-31	01 38 39.40	+69 38 01.5	15.4	14.50	-	85	DM2 secondary, sep. = 111" (Farhi et al. 2005)
								T _{eff} /log g/[Fe/H]=4750/4.5/-2.5 (Latham et al. 2002) High proper motion, V > 14.5

Table 4.5: Secondary SPSS list - continued

ID	Name	RA (J2000) <i>hh mm ss</i>	DEC (J2000) <i>° ′ ″</i>	B	V	Sp. Type	Tr.	$T_{eff} / \log g / [Fe/H]$ & Notes
223	WD0147+674	01 51 10.16	+67 39 32.2	14.17	14.42	DA2	89	T_{eff} =30700 K (Bergeron et al. 1992) not RV var. (Maxted et al. 2000)
224	WD0302+621	03 06 16.71	+62 22 22.5	15.17	14.95	DA4/6	119	photometrically stable (Gianninas et al. 2006)
230	WD0552-041	05 55 09.53	-04 10 07.1	15.49	14.45	DC10	83	T_{eff} =5060 K (Bergeron et al. 2001)
234	WD1029+537	10 32 10.26	+53 29 36.4	13.5	14.455	DA1	154	T_{eff} =46900 K (Finley et al. 1997) not RV var. (Maxted et al. 2000), uncertain mag, it's not so blue
236	WD1041+580	10 44 45.2	+57 44 38	14.59	999	DA1/2	99	T_{eff} ~30200 K (Bergeron et al. 1992; Lajoie & Bergeron 2007)
237	WD1053-550	10 55 13.63	-55 19 05.9	14.22	14.32	DA4/5	82	T_{eff} =14200 K (Bragaglia et al. 1995)
238	WD1056-384	10 58 20.4	-38 44 51	14.234	14.047	DA2	125	T_{eff} ~27-28000 K (Kawka webpage) UBVRI phot.std. (Landolt & Uomoto 2007)
244	WD1234+481	12 36 45.36	+47 55 23.3	999	14.38	DA1	92	T_{eff} ~51-56000 K (Liebert et al. 2005; Lajoie & Bergeron 2007) and Kawka webpage
246	WD1319+466	13 21 15.09	+46 23 23.7	14.55	14.55	DA3/4	85	T_{eff} ~14600, 13900 (Bergeron et al. 1992; Liebert et al. 2005) $V > 14.5$
247	WD1323-514	13 26 09.56	-51 41 35.8	14.60	14.60	DA3	133	T_{eff} ~18700 (Bragaglia et al. 1995, e.g.)
248	WD1408+323	14 10 26.95	+32 08 35.9	13.96	13.97	DA3	115	T_{eff} ~18300 (Bergeron et al. 1992; Liebert et al. 2005)
250	WD1509+322	15 11 27.63	+32 04 17.9	14.18	14.12	DA3/4	91	T_{eff} =14660 (Bergeron et al. 1992), 13970 (Liebert et al. 2005)
252	WD1553+353	15 55 01.9	+35 13 28	14.64	14.75	DA2	82	T_{eff} ~26000 K (Bergeron et al. 1992; Liebert et al. 2005) $V > 14.5$
254	WD1637+335	16 39 27.823	+33 25 22.30	14.83	14.65	DA5	82	T_{eff} ~10000 K (Bergeron et al. 2001; Liebert et al. 2005) $V > 14.5$, non var. (Giovannini et al. 1998)
259	G184-17	18 40 29.25	+19 36 06.1	15.7	14.10	-	120	$T_{eff} / \log g / [Fe/H]$ =4750/4.5/-2.5 (Latham et al. 2002) bin., sep. ~ 17" - 20" (Zapatero Osorio & Martín 2004), high p.m. $\Delta mag(\text{prim}/\text{second}) > 2.7$ (Zapatero Osorio & Martín 2004) high p.m.
260	WD1837-619	18 42 29.73	-61 51 45.1	14.78	14.67	DC5	122	$V > 14.5$
262	WD1914-598	19 18 44	-59 46 30	14.34	14.39	DA	120	-
264	WD2000-561.1	20 04 24	-56 02 52	-	14.97	DA1	99	in SIMBAD may be WD2000-561A (or WD2000-562, RE J200416-560215)

Table 4.5: Secondary SPSS list - continued

ID	Name	RA (J2000) <i>h m s s</i>	DEC (J2000) <i>° ' "</i>	B	V	Sp. Type	Tr.	$T_{eff}/\log g/[Fe/H]$ & Notes
266	WD2034-532	20 38 16.84	-53 04 25.4	999	14.46	DB4	91	$T_{eff} \simeq 17000$ (Castanheira et al. 2006)
269	WD2111+261	21 13 45.92	+26 21 33.4	14.94	14.69	DA6	179	$T_{eff} = 8120$ K, suspect DD (Bergeron et al. 2001); not RV var. (Maxted et al. 2000)
270	WD2115-560	21 19 36.52	-55 50 14.2	14.54	14.28	DA5/6	117	$T_{eff} = 9950$ K (Bragaglia et al. 1995) and Kawka webpage
271	WD2134+218	21 36 36	+22 04 36	14.42	14.45	DA3	90	$T_{eff} = 18310$ K (Bergeron et al. 1992)
272	WD2147+280	21 49 54.57	+28 16 59.7	14.67	14.68	DB5	117	$T_{eff} = 14000$ K (Wegner & Nelan 1987, called G 188-27)
273	WD2152-548	21 56 21.3	-54 38 24	999	14.44	DA1	123	$T_{eff} = 44500$ K (Barstow et al. 2003)
276	WD2216-657	22 19 48.48	-65 29 18.4	14.56	14.43	DZ5	88	-
279	WD2251-634	22 55 10	-63 10 30	999	14.2	DA	86	-
281	WD2352+401	23 54 56.27	+40 27 29.5	15.28	15.13	DQ6	104	$T_{eff} = 8260$ K (Bergeron et al. 2001) weak C features
285	WD0204-306	02 07 06.37	-30 24 23.1	15.6	999	DA	166	$T_{eff} = 5700$ K DA+dM3, CPM pair(LP883-22/LP883-23)(Silvestri et al. 2001) <i>sep.</i> = 73" (SIMBAD)
300	WD2117+539	21 18 56.27	+54 12 41.25	12.47	12.81	DA	108*	$T_{eff} \sim 14200$ K (Bergeron et al. 1992; Lajoie & Bergeron 2007) wrongly classified as Nova Like Variable RV var. (Saffer et al. 1998) or non-var. (Maxted et al. 2000) star at 8"
301	WD1900+705	19 00 10.25	+70 39 51.24	13.24	13.19	DXP4.5	116*	$T_{eff} = 12070$ (Bergeron et al. 1992); magnetic
303	WD0446-790	04 43 46.47	-78 51 50.4	13.36	13.47	DA2	105*	magnetic fields between 2 and 4 kG citepaznar
304	WD0447+176	04 50 13.52	+17 42 06.20	12.601	12.661	sdO	77*	$T_{eff} \sim 41000$ K (Stroeer et al. 2007, SPY star) Hyades star: Melotte 25 HZ 1
305	WD2309+105	23 12 23.07	+10 47 04.2	12.776	13.094	DA1	89*	$T_{eff} \sim 54-60000$ K (Kawka webpage)
307	WD0859-039	09 02 17.3	-04 07 12	13.36	13.18	DA2	91*	Landolt phot. std. (GD 246) (Landolt 1992, (GD246)) $T_{eff} \sim 23000$ K (Kawka webpage)
308	WD1034+001	10 37 03.79	-00 08 20.3	12.86	13.23	DO	110*	$V = 13.19$, $B - V = -0.168$ (Marsh et al. 1997) photometric standard (Landolt 1992) central star of the largest PN known (Rauch et al. 2004, e.g.)

Table 4.5: Secondary SPSS list - continued

ID	Name	RA (J2000) <i>hh mm ss</i>	DEC (J2000) <i>o ' "</i>	B	V	Sp. Type	Tr.	$T_{eff}/\log g/[Fe/H]$ & Notes
309	2MASSJ17571...	17 57 13.2	+67 03 40.9	11.9	12	A3V	110*	Close to North EP, 2MASSJ17571324+6703409
310	TYC4213-617-1	18 00 02.1	+66 45 55	11.3	10.7	-		Close to North EP
311	BD+661071	18 02 10.9	+66 12 26	10.99	10.6	F5	109*	Close to North EP
313	M5-S1490	15 17 38.64	+02 02 25.6	15.077	14.111	-	97*	red star
314	SA104-428	12 41 41.31	-00 26 25.83	13.58	12.63	-	98*	Landolt (1992), red star
315	SA104-490	12 44 33.46	-00 25 51.7	13.10	12.58	F8:	91*	Landolt (1992), red star
316	sdss13028	16 40 24.19	+24 02 15.00	999	15.254	-	224*	Sloan Digital Sky Survey star
317	sdss15724	20 47 38.18	-6 32 13.20	15.090	14.859	-	71*	Sloan Digital Sky Survey star
318	sdss14276	22 42 04.2	+13 20 28.7	14.525	14.320	-	112*	Sloan Digital Sky Survey star
320	sdss09310	11 38 02.6	+57 29 24.0	15.276	15.006	-	168*	Sloan Digital Sky Survey star
321	sdss00832	23 30 24.9	-00 09 34.9	15.307	15.038	-	112*	Sloan Digital Sky Survey star
322	sdss12720	12 22 41.7	+42 24 43.6	15.250	15.048	-	121*	Sloan Digital Sky Survey star
323	sdss03532	00 24 38.6	-01 11 39.8	15.327	15.063	-	94*	Sloan Digital Sky Survey star
324	sdss09626	14 29 51.1	+39 28 25.3	15.266	15.065	-	154*	Sloan Digital Sky Survey star
325	sdss03932	00 07 52.2	+14 30 24.8	15.412	15.079	-	101*	Sloan Digital Sky Survey star
326	sdss08393	13 10 32.1	+54 18 33.5	15.353	15.082	-	136*	Sloan Digital Sky Survey star
327	G-J70	01 43 20.18	+04 19 17.97	12.48	10.96	M2V	78*	Red star
328	HG7-15	03 48 11.86	+07 08 46.46	12.19	10.85	M1V	70*	Red star
332	G-J2066	08 16 07.98	+01 18 09.26	11.55	10.05	M2V	92*	Red star
333	G-J459.3	12 19 24.09	+28 22 56.51	12.04	10.62	M2V	130*	Red star
334	G-J2097	13 07 07	+20 48 59	14.1	12.54	M1.5V	111*	Red star
335	G-J507.1	13 19 40.12	+33 20 47.49	12.16	10.66	M2V	154*	Red star
336	G-J521	13 39 24.10	+46 11 11.38	11.50	10.26	M2V	145*	Red star
337	G-J570.2	14 57 32.30	+31 23 44.57	12.40	11.08	M2V	219*	Red star
338	G-J625	16 25 24.62	+54 18 14.77	11.80	10.17	M2V	115*	Red star
339	G-J745A	19 07 05.56	+20 53 16.97	12.18	10.84	M2V	203*	Red star
340	G-J745B	19 07 13.20	+20 52 37.26	12.27	10.77	M2V	203*	Red star
341	G-J851	22 11 30.09	+18 25 34.29	11.75	10.29	M2V	118*	Red star
342	G-J863	22 33 02.23	+09 22 40.71	11.89	10.36	M0V	88*	Red star

Table 4.5: *Secondary SPSS list - continued*

ID	Name	RA (J2000) <i>hh mm ss</i>	DEC (J2000) ° ' "	B	V	Sp. Type	Tr.	$T_{eff}/\log g/[Fe/H]$ & Notes
343	sds14511	20 42 42.4	-00 34 03.7	15.374	15.099	-	69*	-
344	HD270422	05 56 47.75	-66 39 4.95	10.92	10.05	G0	102*	Close to South EP (Altmann & Bastian 2009)
345	HD270477	05 59 33.35	-67 01 13.50	10.73	10.28	F8	102*	Close to South EP (Altmann & Bastian 2009)
346	HD271747	05 59 58.63	-66 06 8.86	11.82	11.29	G0	110*	Close to South EP (Altmann & Bastian 2009)
347	HD271759	06 00 41.34	-66 03 13.61	11.0	11.2	A0:	101*	Close to South EP (Altmann & Bastian 2009)
348	HD271783	06 02 11.4	-66 34 58.93	12.63	12.23	F5	100*	Close to South EP (Altmann & Bastian 2009)
349	HIP28618	06 02 27.87	-66 47 28.68	12.20	12.30	B2III	100*	-Close to South EP (Altmann & Bastian 2009)
350	LTT 377	00 41 30.47	-33 37 32.02	11.70	11.22	K	124*	Ex <i>Primary</i> SPSS ID038, see Ap. A.4 in Alavilla et al. (2010)

*: transit computed with the Java classes available in SVN [http://sunstel.asu.cz/~kawka/Mainbase.html](http://gaia.esac.esa.int/dpacsvn/DPAC/CUS/software/DU05/Workshops/W01/Kawka webpage)

Table 4.6: List of discarded *Secondary* SPSS

Nr	Ident	RA(2000)	Dec(2000)	B	V	Sp.Type	Notes
107	WD0426+588	04 31 11.85	+58 58 37.80	12.78	12.45	DC+dM	DC+dM (Holberg et al. 2002)
108	G99-48	05 59 05.98	+04 10 38.70	12.58	11.89	-	double lined spectr. binary, P=352d, asini=152.2e9 m (Goldberg et al. 2002)
111	G109-18	06 40 09.46	+28 27 00.90	12.93	12.07	-	Double lined spectroscopic binary, P~85d (Latham et al. 1988, as G105-50)
117	WD1004+665	10 08 08.00	+66 17 42.00	15.38	14.71	-	V > 14.5, wide binary
126	WD1148-230	11 50 06.2	-23 16 13	14.74	14.84	DA	Coordinates different in McCook & Sion (1999), see Ap. A.2 in Altavilla et al. (2010) SIMBAD: uncertain identification, discordant mag.
128	G123-14	12 13 29.98	+47 10 06.10	13.54	12.91	-	$T_{eff}/\log g/[Fe/H]=5500/4.5/-1.5$, SBI $\alpha \sin i = 205$ Gm (Latham et al. 2002); but sep~25" (Zapatero Osorio & Martin 2004)
137	WD1634-573	16 38 30.00	-57 28 12.00	-	9.75	DO	DOZ1+K0V, sep 3" (Hoard et al. 2007)
143	WD1917-077	19 20 34.93	-07 40 00.05	12.35	12.88	DBQA5	DBQA5 prim.+ dM2.5 second., sep=27.3" (Farhi et al. 2005, as EG131); variable
150	WD2126+734	21 26 57.69	+73 38 44.30	12.89	12.88	DA:	DA+DC, sep 1.4" (Farhi et al. 2005)
157	WD0005+511	00 08 18.4	+51 23 19	13.02	13.32	DA	O VI emitting nebula around (SIMBAD)
162	WD0126+422	01 29 43	+42 28 18	-	14.0	DA	DA+dM4.5, sep=4.7" (Farhi et al. 2005)
163	WD0148+641	01 51 51.052	+64 25 53.88	13.6	14.0	DA:	GJ 3118 B: binary (SIMBAD); primary GJ 3117, sep=12", V=11.51, M2.5
166	WD0347-137	03 50 14.53	-13 35 14.0	15.25	14.91	DA	DA+dM3, sep=0.5" (Farhi et al. 2005)
169	WD0457-103	04 59 50.4524	-10 15 47.970	6.166	5.399	G4V	K0IV + DA binary, bright K0 IV primary (63 Eri)
172	G192-41	06 44 26.33	+50 33 55.4	13.91	13.16	-	Variable Star
176	WD0738-172	07 40 20.79	-17 24 49.1	13.27	12.98	DZ	WD+main-sequence/red dwarf system (Holberg et al. 2002)
178	WD0752-146	07 55 08.954	-14 45 50.96	13.54	13.56	DA	dM6 secondary, spectr.bin. (Farhi et al. 2005)
182	WD1042-690	10 44 10.24	-69 18 18.5	13.05	13.09	DA	dM4.5 secondary, spectr.bin. (Farhi et al. 2005)
184	WD1202+608	12 04 38.58	+60 32 08.4	13.30	13.57	sdO	DD system (e.g. ?, tab. 11)
185	WD1213+528	12 15 44.09	+52 31 01.4	13.0	13.34	DA	EG UMa, DA+dM, sep <4" (Hoard et al. 2007)
187	WD1424+503	14 26 42.7	+50 06 45	14	14	DA:	DA+MVe, close (Hoard et al. 2007)
188	WD1425-811	14 33 07.79	-81 20 14.1	13.0	13.0	DA	ZZ Ceti (McCook & Sion 1999)
189	WD1459+305	15 01 56	+30 22 53	14.28	13.98	DA2	visual double, see PG catalog (close, according to finding chart)
190	G66-59	15 03 49.01	+10 44 23.4	13.85	13.18	-	double lined sp.bin. (Goldberg et al. 2002; ?)
195	WD1645+325	16 47 19.02	+32 28 31.9	13.54	13.65	DB	DBV: the first known pulsating DB (McCook & Sion 1999)
197	WD1824+040	18 27 13.08	+04 03 46.7	14.00	13.98	DA:	DA+DC+DC (McCook & Sion 1999)
198	WD1911+135	19 13 38.68	+13 36 27.3	14.12	14.05	DAn	visual pair, with sep. 17.7". Rejected for crowding, see Ap. A.3 in Altavilla et al. (2010)
200	WD1943+163	19 45 31.77	+16 27 38.8	13.96	13.99	DA	Rejected, crowded field
207	WD2115+339	21 17 08.29	+34 12 27.2	13.30	13.2	-	V* V2027 Cyg : variable (SIMBAD)
210	WD2134+125	21 36 52.98	+12 47 19.3	14.30	13.75	-	PG1159-1iker: Central star of PN (SIMBAD)
212	WD2256+313	22 58 41.00	+31 33 16.0	14.9	13.96	DA	Rejected because much fainter than expected (mag.> 14 - 15).
213	WD2256+249	22 58 47.98	+25 15 45.0	13.72	13.68	DA+	V* MS Peg: variable; DA+dM
222	WD0145-257	01 48 07.89	-25 32 42.3	14.3	-	DA	DA+dM (McCook & Sion 1999; Farhi et al. 2005)
225	WD0331-356	03 33 52	-35 31 19	-	14.8	DA+dM	DA1.6+dM (McCook & Sion 1999)
226	G221-29	04 10 43.16	+74 21 37.1	15.5	14.88	DA:	V > 14.5
227	WD0406+592	04 10 55.08	+59 25 00.6	14.3	14.4	DA:	Close companions, rejected
228	WD0416+701	04 21 27.86	+70 14 19.4	14.85	14.74	DA	DC spectr-secondary (Farhi et al. 2005), also in McCook & Sion (1999)
229	WD0421+740	04 27 36.0	+74 07 06	14.6	14.8	DA	V > 14.5
231	WD0710+741	07 17 09.74	+74 00 40.8	14.91	14.97	DA	dM7, spectr. binary (Farhi et al. 2005), also in McCook & Sion (1999)
232	WD0858-220	09 00 57.20	-22 13 50.3	-	18.37	DC	DC+dM at 4.5" (Hoard et al. 2007), discrepant values for V
233	WD1019+637	10 23 09.07	+63 27 41.6	15.09	14.70	DAs	RV variable (Saffer et al. 1998)
235	WD1033+464	10 36 25.27	+46 08 32.2	13.70	13.15	DA	dM4.5 companion, sep. < 0.5" (Farhi et al. 2005), also in McCook & Sion (1999)
239	WD1121-507	11 24 01.30	-50 59 38.4	14.93	14.86	DA	V > 14.5
240	WD1121+508	11 24 32.16	+50 33 29.3	15.5	-	DA	B > 14.5

Table 4.7: List of discarded *Secondary* SPSS - continued

Nr	Ident	RA(2000)	Dec(2000)	B	V	Sp.Type	Notes
241	WD1132-325	11 34 29.74	-32 49 56.6	17	15	DC	bin. system, KOV stars at <5", ~0 mag brighter, also in McCook & Stion (1999)
242	WD1210+533	12 13 24.62	+53 03 57.5	13.78	14.12	O	Variable peculiar Star (Liebert et al. 2005; Bergeron et al. 1994)
243	WD1232+479	12 34 56.21	+47 37 33.2	14.58	14.52	DA3/4	RV variable (Saffer et al. 1998) or non RV var. (Maxted et al. 2000), $V > 14.5$
245	WD1317+453	13 19 13.72	+45 05 09.8	14.16	14.13	DA	DD system (McCook & Stion 1999)
249	WD1407-475	14 10 39.07	-47 44 39.5	14.24	14.31	DA	RV variable, P~1d (Maxted et al. 2000)
251	WD1550+183	15 52 26.37	+18 10 18.5	14.94	14.83	DA5	$V > 14.5$
253	WD1636+351	16 38 26.32	+35 00 11.8	14.65	14.91	DA	$V > 14.5$
255	WD1655+215	16 57 09.86	+21 26 48.7	14.32	14.08	DA5	V* V749 Her: variable (SIMBAD)
256	WD1709+230	17 11 55.66	+23 01 01.5	14.81	14.90	DBn	$V > 14.5$
257	WD1713+332	17 15 34.86	+33 13 03.9	14.43	14.54	DA	DD system; DA secondary (Farhi et al. 2005)
258	WD1751+106	17 53 32.27	+10 37 23.7	14.53	14.71	-	Central star of PN (McCook & Stion 1999)
261	WD1855+338	18 57 30.18	+33 57 25.8	14.81	14.64	Dan	ZZ Ceti (Bergeron et al. 2001)
263	WD1957+225	19 59 36.34	+22 43 16.1	-	7.5	DA	Planetary Nebula (M27, SIMBAD)
265	WD2010+310	20 12 22.28	+31 13 48.6	14.77	14.85	DXP2	$V > 14.5$, DXH2/DXP2 : magnetic and polarized (Jordan et al. 1998)
267	WD2046+396	20 48 08.3	+39 51 38	14.10	14.43	Daw	Rejected, crowded field
268	WD2058+181	21 01 16.48	+18 20 55.5	15.04	15.03	DA:	Visual companion at 2.8", $V > 14.5$, see Ap. A.3. in Altevilla et al. (2010)
274	WD2154-512	21 57 38.4	-51 00 32	14.93	14.74	DQ	binary, 28" separ., $V > 14.5$
275	WD2205+250	22 07 45.9	+25 20 28	-	14.4	DA:	visual pair, 8".9 separ. Close to a bright star.
277	WD2232-575	22 35 31.06	-57 16 26.6	15.06	14.96	DA	$V > 14.5$
278	WD2248-504	22 51 02.05	-50 11 31.4	15.07	14.96	DA:	$V > 14.5$
280	WD2324+397	23 27 16.04	+40 01 22.0	14.1	-	DO	PG1159-type pulsator (McCook & Stion 1999)
282	WD1038+633	10 41 56.5	+63 07 09	15.49	-	DA	$B \geq 14.5$
283	SDSS J113730.87+460006.2	11 37 31	+46 00 12	15.33	-	sDO	SIMBAD: PG 1134+463 (not binary, see ?) $B > 14.5$
284	SDSS J163930.02+343230.4	16 39 36.4	+34 32 30	-	-	sDB	SIMBAD: PG 1637+346 ?, $V > 14.5?$
286	WD0205-304	02 07 40.74	-30 10 57.9	15.1	-	DA	$B > 14.5$
287	WD0500-156	05 03 08	-15 36.1	-	-	DA..	central star of PN
287	WD0500-156	05 03 08	-15 36 06	-	-	DA	central star of PN Abell 7 (McCook & Stion 1999)
288	WD0658+624	07 03 26.07	+62 22 51.6	15.61	15.55	DA	$V > 14.5$
289	WD0727+600	07 31 21.3	+59 57 37	15.8	-	DO	$B > 14.5$
290	WD1230+417	12 32 26.18	+41 29 19.3	15.68	15.75	DA	$V > 14.5$
291	HZ34	12 55 14.73	+37 32 30.1	15.38	15.66	DA	star 291=star 292 $V > 14.5$
292	WD1253+378	12 55 14.73	+37 32 30.1	15.38	15.66	DA	star 291=star 292 $V > 14.5$
293	WD1616-591	16 20 30	-59 16 00	15.014	14.96	DA5	DA5 ZZ?, seems non var., $V > 14.5$
294	WD1636+160	16 38 40.39	+15 54 16.9	15.74	15.60	DA	DA4/DA5 ZZ?, seems non var., $V > 14.5$
295	WD2018-585	20 22 22.12	-58 22 04.5	15.84	15.55	DC	high prop. motion, $T_{eff}=5200$ K, suspect DD (Bergeron et al. 2001), $V > 14.5$
296	WD2048+263	20 50 20.65	+26 30 40.8	16.53	15.60	DC9	high prop. motion, $T_{eff}=5200$ K, suspect DD (Bergeron et al. 2001), $V > 14.5$
297	SDSS J092830.56+561811.7	09 28 30	+56 18.5	16.05	-	sD	SIMBAD: WD 1035+532 ?, $V > 14.5$
298	SDSS J103854.02+525847.8	10 38 50.5	+52 59 03	15.99	16.34	sDB	SIMBAD: PG 1700+198, $V > 14.5$
299	SDSS J170214.00+194255.1	17 02 14.2	+19 42 56	15.10	-	sd	binary DA1+G2V (McCook & Stion 1999), (Barstow et al. 2001 sep<1")
302	WD0354-368	03 56 30.58	-36 41 19.3	12.8	2.45	DA1+G2V	binary DA1+G2V (McCook & Stion 1999), (Barstow et al. 2001 sep<1")
306	WD2336-079	23 38 51	-07 41 24	13.44	13.26	DA4	ZZ Ceti (Gianninas et al. 2006)
312	G45-20	10 56 28.909	+07 00 53.22	15.541	13.507	M6.5	very red star. Flare star
319	sds14517	20 40 16.6	-00 28 22.8	15.045	14.719	-	Rejected: stars VERY close
329	GJ207.1	05 33 44.79	+01 56 43.43	13.10	11.52	M2.5V	V* V371 Ori - Flare Star : rejected
330	GJ268.3	07 16 19.78	+27 08 32.99	12.40	10.83	M0V	spectroscopic binary
331	GJ3482B	08 08 13.53	+21 06 08.19	12.65	11.20	M2.5V	Very bright star nearby

4.2 Observation Strategy and Campaigns

Our observing campaign is divided in:

- the *Main Campaign*, whose purpose is to produce SEDs on an homogeneous scale (1% internal, \sim 3% absolute accuracy), linked to the *Primary* SPSS and, in turn, to the 3 *Pillars* by Bohlin et al. (1995) and depending on Vega (Bohlin & Gilliland 2004; Bohlin 2007);
- the *Auxiliary Campaign*, dedicated to to monitor candidate SPSS against any kind of variability (intrinsic, e.g., pulsations, or extrinsic, e.g., binarity, since very few of them have systematically been monitored in the literature), and to check for close companions.

4.2.1 Main Campaign description

With regard to the *Main Campaign*, a basic consideration when starting the observations of such a large sample of targets, is that the traditional spectrophotometry techniques require too much observing time: each SPSS should be spectroscopically observed in perfectly photometric conditions, ideally more than once. We therefore chose to split the problem into two parts:

1. spectra are taken in good sky conditions, but not necessarily perfectly photometric; they are relatively calibrated with the help of a Pillar or Primary SPSS thus recovering the correct spectral shape;
2. absolute photometry in the B, V, and R (sometimes I) Johnson-Cousins bands is taken in photometric sky conditions and used to fix the spectral zero point by means of synthetic photometry.

This technique optimizes the use of the observing time. It permits to take advantage of non completely photometric nights (a very common condition) and, in addition, to exploit the characteristics of absolute photometric night points that can be obtained faster than spectra. Obviously, a subset of SPSS candidates will be spectroscopically observed in photometric sky conditions, to check the whole procedure. This strategy, proposed by Bellazzini et al. (2006), together with the pure spectrophotometry technique, was tested in an initial pilot project. The purpose of the pilot project was to define the criteria, parameters, procedures and instruments that are best suited for the Gaia ground-based observing campaign.

4.2.2 Constancy Monitoring Campaign description

As reported in Section 4.1.3, the fundamental requirement for an SPSS is that its magnitude is constant. Except for a few extremely well studied objects, all the other stars in our list need to be accurately monitored for variability, both intrinsic (e.g., pulsations) or extrinsic (i.e., binarity), in particular, whenever the information available in the literature is not enough to rule it out. In fact, even stars used for years as spectro-photometric standards, as the *Primary* SPSS, were found to vary when dedicated studies were performed (see e.g., G24-9, that was found to be an eclipsing binary, Landolt & Uomoto 2007). Stars which are apparently safe may show unexpected variations (e.g. EG131, a featureless DC WD, that showed Δmag of 0.35 ± 0.09 , Aldering, private communication). For these reasons it is mandatory to monitor our SPSS candidates even for unlikely kinds of variability larger than 0.01 mag, i.e. larger than our best expected accuracy for Gaia calibration. In addition to our study, Gaia observations themselves will further check variability, because each of them will be observed tens of times. Hidden, nearby companions may be discovered from space. These stars will simply be eliminated from the SPSS grid, which is built with some redundancy.

Most of our targets are WDs and hot subdwarfs, the remaining are dwarf/giant stars covering different spectral types, including cold stars of very late spectral type. WDs may show variability with (multi)periods from about 1 to 20 minutes and amplitudes from about 1-2% up to 30% of their flux (Sterken & Jaschek 1996). We have tried to exclude stars within the instability strips for DAV, DBV and DOV, but in many cases the existing information is not sufficient (or sufficiently accurate) to decide whether they are safely away from the instability strips. Similar considerations are valid for hot subdwarfs (Kilkenny 2007), which can show variability with (multi)periods from about 2-5 minutes to 1-2 hours. So, series of consecutive one-filter exposures that last for one-two hours will be able to sample even the longest periods, revealing variability down to 0.05-0.01 magnitudes in amplitude, depending on the data quality. Also redder stars are often variable: K stars have shown variability of 5-10% with periods of the order of days to tens of days (Eyer & Grenon 1997); M stars, recently added following simulations of the accuracy reachable for absolute fluxes, can vary, e.g., because of flares.

In addition, binary systems are frequent and eclipsing binaries can be found at all spectral types. Their periods can span a range from a few hours to hundreds of days (most of them having $P \simeq 1-10$ days, Dvorak 2004). Therefore, all our candidate Primary and Secondary SPSS, including the Pillars, will need a monitoring in search

of long-term variability. This will be performed on a three years basis, collecting approximately 4 night points in 3 bands per year. Obviously, in case of clear sky conditions, these observations could also be used to derive absolute photometry.

For all these reasons, we are performing in the *Auxiliary Campaign* repeated and accurate observations of our SPSS candidates, in order to detect variability larger than 0.01 mag (if any). To obtain this goal, relative photometry with respect to field stars is used to monitor the stability of our targets over both short ($\sim 1-2$ hours) and long (~ 3 years) periods. The best seeing multiband images can also be used for companion searches. An example of how good quality dedicated imaging can benefit the validation of the candidates SPSS against close companions is star HZ 43. This star was initially chosen by Bohlin et al. (1995) to be one of the Pillars, and later rejected because of an optical companion lying 3" away, relatively bright in the V band, that made it useless as a standard, at least from the ground.

4.2.3 Observation Protocols

When trying to build our large set of SPSS for calibrating Gaia BP/RP Spectra and G-Band images to a few % in absolute flux, it is essential to maintain the maximum homogeneity in data quality, acquisition and treatment. This is especially true when data come from different observing sites around the globe and are obtained and treated by different persons. The *Observation Protocols* are sets of detailed instructions we have assembled in order to help observers and collaborators that participate in the large effort required. More information can be found in Pancino et al. 2008, 2010a, 2011, in preparation.

For the spectroscopic observations, we acquire wide slit spectra, i.e. spectra acquired with a very large aperture ($\geq 6 \times \text{seeing}$, and for homogeneity we adopted a fixed width equal to 10" or more whenever possible) to collect all the incoming star flux (to obtain actual spectrophotometry), and narrow slit spectra, i.e. spectra acquired with a slit ($\sim 2''$) that is too narrow to collect all the incoming flux, but permits to obtain a better wavelength calibration. To obtain the required accuracy of a few %, we need high S/N spectra ($S/N \sim 100$ for most of the wavelength range), repeatedly observed (3 spectra per grism) to remove cosmic ray hits, and average out the possible residuals of corrections for flat-field. Slit illumination is corrected using spectroscopic skyflat frames. In order to derive the response curve to transform each SPSS spectrum into the CALSPEC scale and to monitor the extinction curve, one Pillar should be chosen as a calibrator for the run, and observed at least three times

for every night with the same strategy adopted for targets (three spectra for each grism should be obtained, at different airmasses). One telluric standard (or an SPSS especially featureless) is observed during the night at different airmasses in order to better correct for telluric lines. In order to obtain a good wavelength calibration, arcs are usually obtained just before or after the spectra of each SPSS, using the same grism and the narrow slit, at the same telescope position. The accurate wavelength calibration of the narrow slit SPSS spectra will be transferred to wide spectra by cross-correlation.

For the photometric observations, night points¹⁶ are taken in three filters (typically B,V,R), with at least three exposures for each filter, ensuring that at least two good comparison stars are present in the field of view. This is of fundamental importance for relative photometry that uses stars in the field of view to derive light curves (see Chapter 8), but remains true also for absolute photometry, because those images should be useful also as relative night points (useful to perform the long-term constancy monitoring). Obviously, night time photometric calibrations, i.e., Landolt Standard fields, are necessary every time absolute photometry is attempted, and 3–4 different standard fields should be observed, each imaged at two different airmasses (possibly covering the whole extent of the night) in three filters (B, V, R) with at least three exposures for each filter, in order to properly monitor the sky conditions during the night. In addition, time series are obtained for each SPSS which needs to be checked against short-term variability. The time series, taken in one filter (typically B or V), should last at least one hour and contain at least 30 exposures. Also for time series, there should be at least two comparison stars in the field.

4.3 Observing Facilities

The ideal instrument for our campaign must provide both spectroscopic and photometric capabilities, offering a suitable set of photometric standard filters and dispersing elements to cover the Gaia spectral range (330–1050 nm). Moreover, the telescopes must cover both the celestial hemispheres since our targets must be distributed all over the sky. The ranking of the available instruments was done according to the following guidelines, listed in order of priority:

1. Availability of instruments for low-resolution spectroscopy ($R \sim 500\text{--}1000$) and

¹⁶One single observation of an SPSS in one night is called a *night point*. When the night is clear and Landolt standard star fields are observed, the *relative* night point becomes an *absolute* night point.

in particular: suitable spectral range coverage (ideal: 330–1050 nm, with no more than 2 instrumental setups to avoid excessive overheads, a few hundred nm of overlap to join the spectra), wide slit ($\geq 10''$) availability.

2. Photometric capabilities, preferably with the same instrument used for spectroscopy and with standard broad band filters (Johnson-Cousins or Bessell, mainly B, V and R).
3. Exposure time per single spectrum as short as possible (2–4 m class telescopes).

Reasonably easy access for European observers, site quality (when available) and geographical location were also taken into account in order to maximize the probability of time allocation and of getting good observing conditions, to cover both the celestial hemispheres and to provide a subsample of SPSS observed from both hemispheres to check for systematics.

Following these guidelines, we have selected six facilities, which we can divide into two main groups:

- telescopes *mainly* devoted to spectroscopic observations (Table 4.8):
 - EFOSC2@NTT – ESO La Silla Observatory, Chile;
 - DOLoRes@TNG – Roque de los Muchachos Observatory, Canary Islands, Spain;
 - CAFOS@CAHA – Calar Alto Observatory, Spain;
- telescopes *mainly* devoted to photometric observations (Table 4.9):
 - LaRuca@SPM – San Pedro Mártir Observatory, Mexico;
 - BFOSC@Cassini – Loiano, Italy;
 - ROSS(REMIR)@REM – La Silla Observatory, Chile;

Tables 4.8 and 4.9 give more details on the adopted telescope/instruments, in particular, the following information is reported:

- **Slit width:** the widths of the adopted slits are reported.
- **Spectral properties and exposure time:** the spectral coverage of the used setup, in terms of total wavelength range and number of sub-ranges, i.e., how many gratings are required to cover the full range. The spectral resolution of each grating is provided. Finally two estimates of the typical exposure time are

given, for different slit widths (1" and 10"). The exposure time is defined as the *total time* to take one spectrum of the source *over the full spectral range*, excluding overheads (separately indicated when available). Exposure times are based on our experience and/or Exposure Time Calculators (ETC) when available¹⁷.

- **Calibration lamp:** when available, the required lamps for the wavelength calibration of the spectra are reported, mainly to give an indication of the time overhead to accomplish a single observation and of the wavelength range actually covered by lines (e.g., we need Ne lamp for blue calibration).
- **Overhead:** the information on the time overhead to perform a complete observation is very useful to evaluate the total amount of observation time. Unfortunately, this information was available a priori only in few cases.
- **Photometry:** all telescopes selected for spectroscopic observations have photometric capabilities too. We managed to select facilities, which can perform both imaging and spectroscopy, just switching from a spectral dispersing element to a filter (this is the case of most focal reducers) to have a more flexible and efficient instrumental setup. The facilities devoted to photometry are instead not required to have spectroscopic capabilities because photometry can be performed also with smaller collecting areas, not suitable for spectroscopy.
- **Filters:** standard photometric filters are preferable (Johnson-Cousins or Bessell).
- **PROS/CONS:** comments are provided under these headings.

¹⁷EFOSC2@NTT ETC:

<http://www.eso.org/observing/etc/bin/gen/form?INS.NAME=EFOSC2+INS.MODE=spectro>,

DOLoRes@TNG ETC: <http://www.tng.iac.es/observing/expcalc/spectro/>;

CAFOS@CAHA2.2m ETC for imaging only:

http://www.caha.es/prada/tcl/script/cafos_im.html.

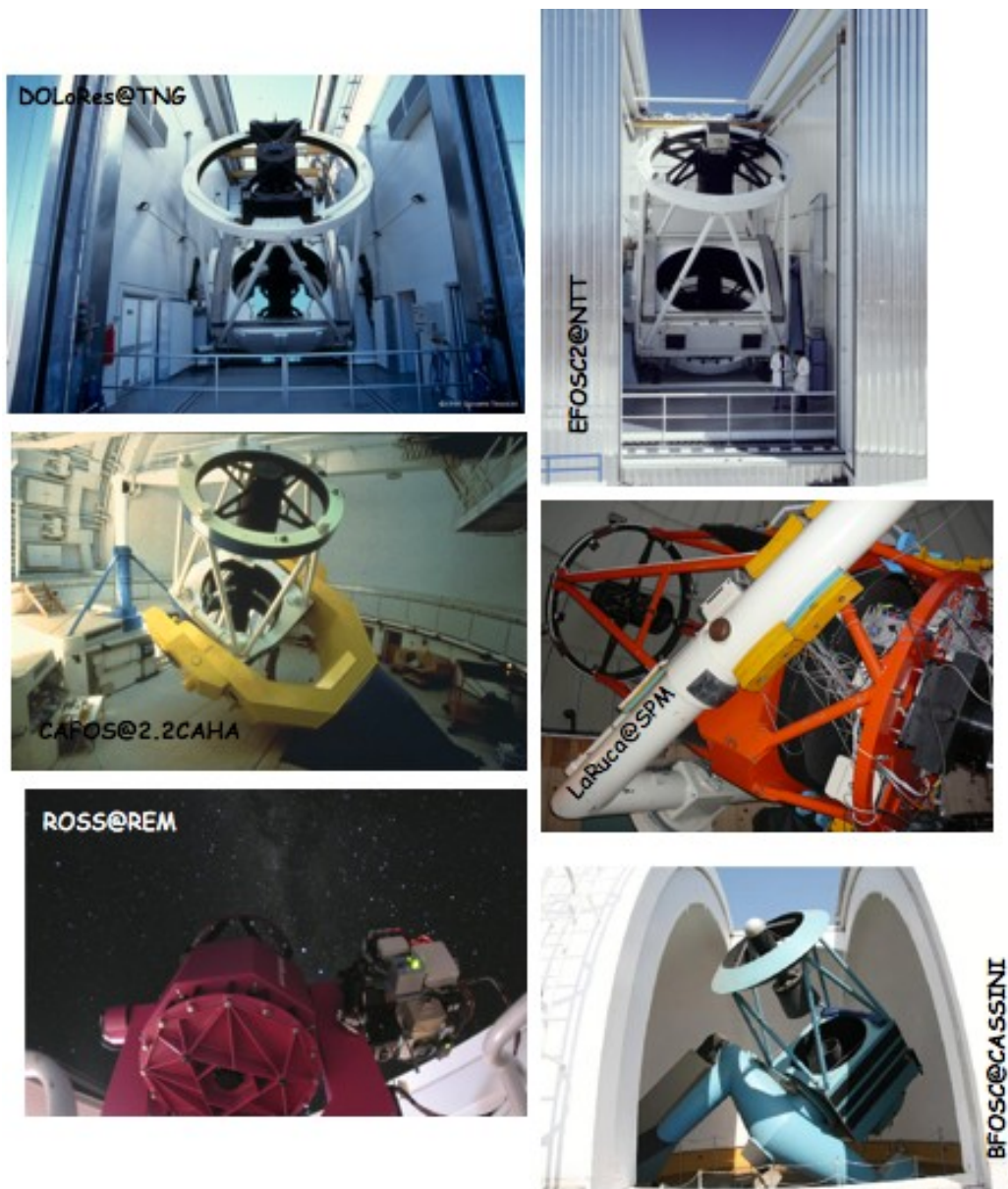


Figure 4.12: Facilities involved in the Gaia SPSS Observing Campaigns.

Table 4.8: Telescopes and instrument setups selected mainly for spectroscopic observations

Telescope	ESO NTT 3.58m	TNG 3.58	CAHA 2.2m
Instrument	EFOSC2, long slit (4:1)	LRS DOLoRes	CAFOs
Location	La Silla, Chile	Roque, Canary Islands, Spain	Calar Alto, Spain
Slit width	1.5"-10"	2"-10"	2"-11.7"
Dispenser, $\Delta\lambda$ (nm), $R(10")$	$G\#11$, 338-752, ~ 300 $G\#16$ 600-1032, ~ 500	LR-B, 300-843, ~ 300 LR-R, 450-1007, ~ 400	B200 320-700, ~ 300 R200 630-1100, ~ 500
$T_{exp}(1"/10" \text{ slit})$	$\sim 7\text{min}$, $\sim 4\text{min}$	$\sim 4\text{min}$, $\sim 3\text{min}$	$\sim 30\text{min}$, $\sim 15\text{min}$
λ calib	He+Ar	Ar+Ne+Hg+Kr. He complementary exposures	Hg+Cd+Ar lamp
Overheads	$\sim 10\text{min}$ point, acquire target & readout $\sim 5\text{min}$ calib. lamp	$\sim 5\text{min}$ star in slit $\sim 1\text{min}$ change of grism/filter $\sim 2\text{hsec}$ readout	
Photometry with same instrument	Yes, 4.1' F0V, 0.12"/px (1x1 binning) 0.24"/px (2x2 binning)	Yes, 8.6' F0V, 0.252"/px	Yes, 16' F0V, 0.53"/px
Filters	$(U)BV R_{Bessel}$	$(U)BV_{Johnson}, R(I) Cousins$	$(U)BV R(I)_{Johnson}$
PROS	<ul style="list-style-type: none"> • Full range coverage at medium R with two exposures • UBVR photom. with the same instrument • The slit can be automatically rotated at any Parallactic Angle on the sky • The used 1x1 binning allows taking imaging of bright stars without saturating. Spectroscopy is done using the fast 2x2 binning • Observing Blocks make the system very efficient 	<ul style="list-style-type: none"> • Full range coverage with two exposures • Reasonable exp. times • UBVR photom. with same instrument 	<ul style="list-style-type: none"> • Full range coverage with two exposures • UBVR photom. with the same instrument
CONS	<ul style="list-style-type: none"> • Internal flats are recommended where accurate removal of fringes at the red wavelengths is required. Arc exposures end of each science exposure are also recommended • Small Field Of View for imaging • The default 2x2 binning is not used in imaging; fast readout but bright stars saturate, the 1x1 binning has a long readout • 2nd Ord. contamination above 717nm 	<ul style="list-style-type: none"> • Possible calibration problems, HgI4358 first useful blue line unless He3888 is acquired. • Fringing at $\lambda > 860$ • Two complementary exposures needed for calibration lamp • Loral chip replaced with E2V4240, new exposure times evaluated • 2nd Ord. contamination above 950nm. 	<ul style="list-style-type: none"> • No on-line ETC • Longish exposure times • Parallactic angle to be computed and set manually
Applications deadlines	Apr.-Sept.: 30 September Oct.-Mar.: 1 April	Feb.-July: Mid October Aug.-Jan.: End of April	Jan. 1-June 30: 15 Sept. July 1-Dec. 31: 15 Mar.

Table 4.9: Telescopes and instrument setups selected mainly for photometric observations

Telescope	SPM 1.5m	Cassini 1.5m	REM 0.6m
Instrument	La Ruca	BFOSC	ROSS(REMIR)
Location	Sierra San Pedro Mártir, Baja California, Mexico	Loiano, Italy	La Silla, Chile
Photometry	4.1' FoV, 0.24" / px	13' × 12.6' FoV, 0.58" / px	9.8' FoV, 0.575" / px
Filters	(U)BVR(I) [*] _{Cousins}	(U)BVR(I) _{Johnson-Kron-Cousin}	VRI [†] , J [‡]
Spectroscopy with the same instrument	NO	YES	NO
Slit width		1.5"-5"	
Disperser, $\Delta\lambda$ [nm], R(5")		G [#] 3, 330-642, ~ 200	
T_{exp} (1"/5" slit)		G [#] 5, 480-980, ~ 300	
λ calib		~ 40min, ~ 30min	
Overheads		HeAr	
PROS	<ul style="list-style-type: none"> • Good location for photometric observations 	<ul style="list-style-type: none"> • Relatively wide Field of View • Availability 	<ul style="list-style-type: none"> • Good location • Robotic telescope
CONS	<ul style="list-style-type: none"> • Small Field Of View • Forbidden zone: $\delta > 59^\circ$ 	<ul style="list-style-type: none"> • Rare photometric conditions 	<ul style="list-style-type: none"> • Sky- concentration to be evaluated
Applications deadlines	Jan. 1-June 30: mid Oct. July 1-Dec.31: mid Apr.	Feb. 1-July 31: beg. of Jan. Aug. 1-Jan. 31: beg. of Jul.	Feb.-July: Mid October Aug.-Jan.: End of April

*<http://haro.astrossp.unam.mx/indexspm.html>† <http://www.rem.inaf.it/ross.html>‡ <http://www.rem.inaf.it/remir.html>

4.4 Survey Status

Observations started in the second half of 2006 with the pilot program (ended in spring 2007). Both the main and the auxiliary campaigns, started in the second half of 2007, are currently ongoing. At present, we obtained 45 accepted proposals.

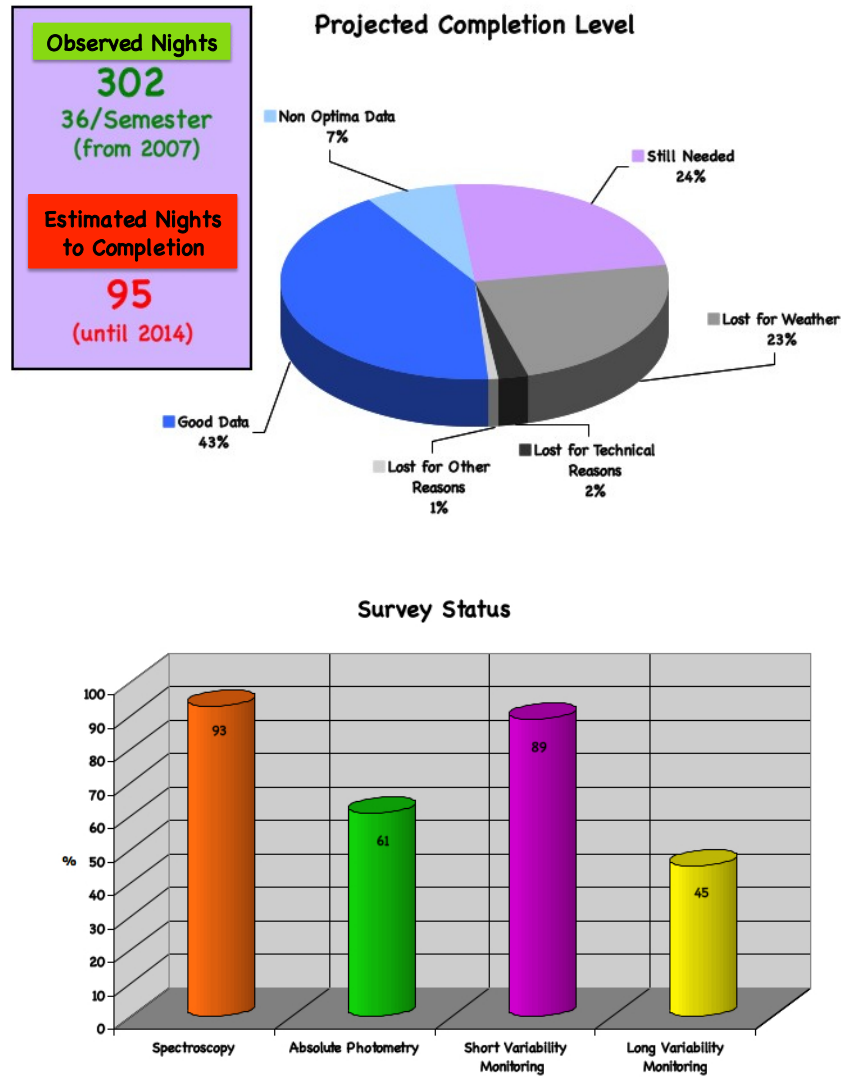


Figure 4.13: Projection Completion (*upper panel*) and Survey Status (*bottom panel*).

We have been awarded, at the time of writing, a total of ~ 300 observing nights, at the rate of ~ 36 per semester. About 50% of this time resulted in at least partially

useful data. The main cause of time losses has been bad weather: about 20% of the observing time was lost for this reason, and only about 2% for technical problems (see Fig. 4.13). The number of estimated nights to survey completion, calculated by projecting the actual SPSS observation rate (including lost time) on the number of SPSS still to observe, is about 95. Obviously, this projection must be considered as a pure indication. If the projection is accurate, our survey will have a size of $\simeq 400$ nights, comparable to the forthcoming ESO Public Survey in terms of observing time, and was carried out by a team of only 3–5 FTE per year.

The survey is now $\simeq 45\%$ complete, with both the spectroscopy observations and the short-variability monitoring campaign almost complete ($\simeq 90\%$). We expect to complete all our observing campaigns around 2013–2014. More precisely, the actual status of both the main and auxiliary campaigns is reported in Fig. 4.14 and Fig. 4.15 respectively.

We expect to complete both the spectroscopy and short-term constancy monitoring observations in 2011–2012. Absolute photometry observations completion need a little more time, and we expect to complete them in 2012–2013. The long-term constancy monitoring requires at least 12 night points acquired in 3 years for each SPSS candidate: for this reason, only $\sim 1\%$ of our stars have been completed already. For most of our candidates (about 69%) the monitoring is ongoing: the survey completion is expected around 2013–2014.

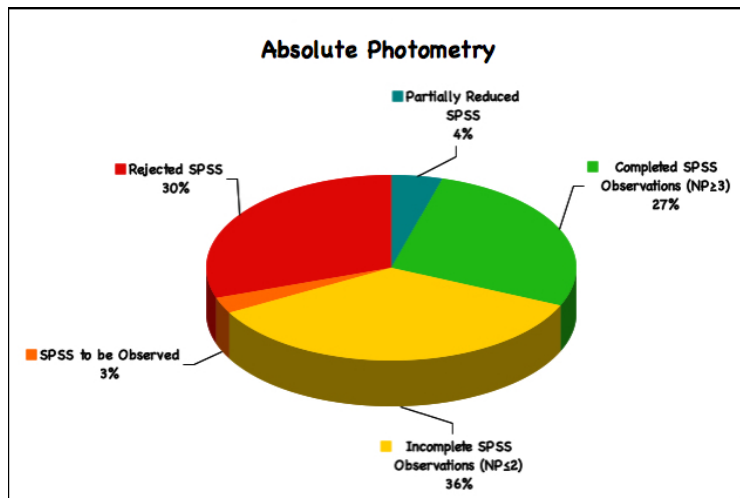
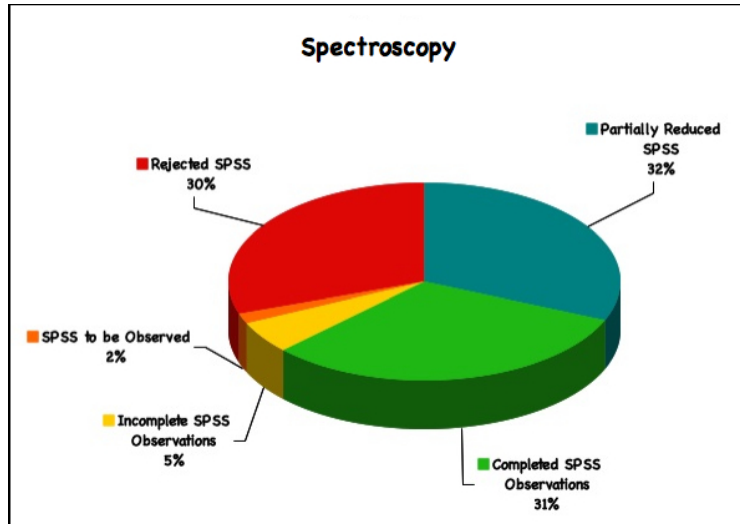


Figure 4.14: Main Campaign status

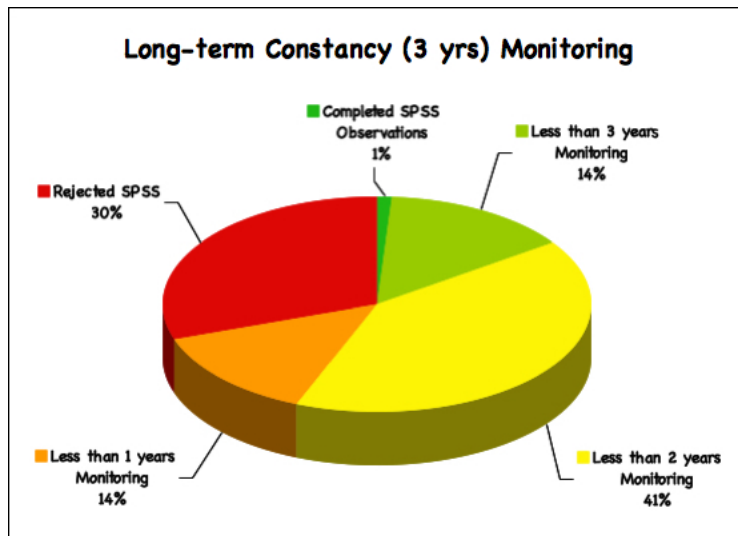
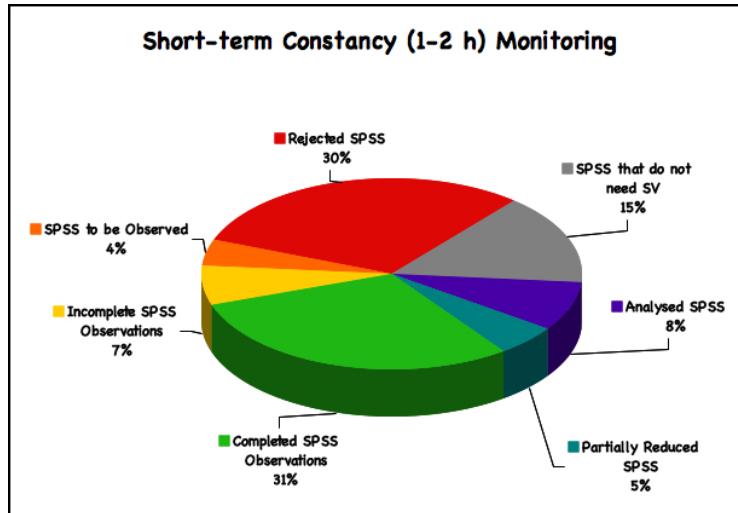


Figure 4.15: Auxiliary Campaign status

5

The Instrument Familiarization Plan

The ground-based observations of SPSS represent an enormous observational effort, that must rely on different telescopes and instruments (see Section 4.3). Therefore, we must ensure the maximum homogeneity, in the observation procedures (see Section 4.2.3), in the data reduction (see Chapter 6) and in the data quality (see Chapter 7).

As a first step, since we are interested in accurate and precise spectrophotometry, it is mandatory to test the capabilities of each telescope/instrument combination and to devise methods to keep under control, and eventually to correct for, all the typical instrumental effects that can affect the high precision required for the Gaia SPSS grid. Four kinds of tests form the so-called *Instrument Familiarization Plan* (IFP):

1. *CCD Performance Tests*: even if most telescope staffs measure regularly their CCD performances, we need to do very high precision photometry and spectroscopy. Therefore we must know the instrument shutter characteristics and the CCD linearity with a very good precision.
2. *Calibration Frames Monitoring*: concerns the stability and reliability of the calibration frames that we use to remove the instrument signature and the lamps to provide the wavelength calibration of our spectra.
3. *Instrument Performance Tests*: are only required for instruments with spectroscopic capabilities, and are aimed to understand and correct for effects like the second order light contamination and polarization added by the mirrors and dispersing elements inside each instrument.
4. *Photometricity and Extinction Monitoring Tests*: aimed at determining zero points and extinction coefficients for all clear nights or nights that were judged photometric by the observers.

The Instrument Familiarization Plan

The Instrument Familiarization Plan is of fundamental importance since its results can affect both the observing and data reduction strategies, as shown in Fig. 5.1. For example, a stability monitoring of calibration frames (over at least one run) is necessary to evaluate if, when appropriate calibrations are missing for one night, those taken in adjacent nights can be safely used to pre-reduce scientific data. This allows to build a *calibration plan* for all the instruments we use. In addition, since we are interested in accurate and precise spectrophotometry, instrumental effects which may affect our measurements, as for example the CCD linearity, must be investigated. The result of the CCD linearity test obviously affects the observing protocols, since it defines the CCD range we can exploit in our observations.

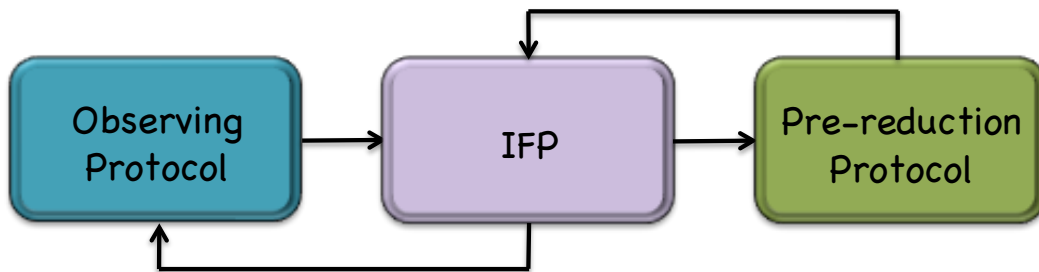


Figure 5.1: Schematic view of how the IFP is related with both the observing and reduction strategies.

The IFP tests were performed on all the instruments involved in our campaigns. I was deeply involved in all the IFP tests activities and, in particular, I lead the *Calibration Frames Monitoring* activities. The results for all our instruments, concerning the first two groups of tests described above, are available in Altavilla et al. (2011) and Marinoni et al. (2011b) respectively, while the other tests are being finalized. In this chapter I will summarize the methodologies used to perform all the IFP tests and I will present some examples of the results.

5.1 CCD Performance Tests: Shutter effects

Due to the finite opening and closing time of shutters, the effective exposure time of an astronomical frame might be slightly different from the settled value or may vary across the CCD.

The offset between the requested exposure time and the effective value is known as the *shutter delay time* or *shutter offset*. It can be measured, for example, by taking

a series of flat fields with increasing exposure time, starting from very short values for which the effect is more relevant. The frames must be trimmed and processed by subtracting overscan and/or bias, as described in Chapter 6. In order to reduce the noise and to get rid of spurious effects, multiple images with the same exposure times are generally taken (usually triplets) and combined. Of course the lamp must be stable or vary slowly enough so that the luminosity drift, monitored with flat fields sequences with constant exposure time, can be corrected as described in Section 5.1.3. The three frames of each triplet are used to build a single median frame for each exposure time and for each set of images with constant exposure time taken to check the lamp stability. Two kinds of tests are performed in order to check for shutter effects:

1. the *shutter delay* tests (Section 5.1.1), which allows to compute the shutter delay time, needed to obtain effective exposure times for a given instrument, and also to define a minimum exposure time for which the shutter delay represents a negligible correction (for our purposes $\leq 1\%$).
2. the *minimum acceptable exposure time* test (Section 5.1.2), important to define the minimum exposure time that can be used when observing with a given instrument/CCD in order to get homogeneously illuminated images (within 1% for our purposes).

5.1.1 Shutter delay

We used two different methods to estimate the shutter delay:

- **Method 1:** the mechanical shutter delay is determined by linear extrapolation at zero ADU of the *linearity curve* (observed counts versus exposure time), thus assuming the response of the CCD is linear over the counts range used for the linear fit, see Fig. 5.2, upper panel. The linear extrapolation crosses the exposure time axis at a value δt which represents the delay to be applied to correct all the exposure times. The correct exposure time can be computed as: $t = t_{exp} + \delta t$. Of course this correction is negligible for very long exposure times but it is important for short ones.
- **Method 2:** the mechanical shutter delay is determined by adjusting the exposure times such that the count rate curve (ADU¹/sec) gives the minimum

¹ADU (Analog-to-Digital Unit) can be converted to photoelectrons through the gain (e^-/ADU).

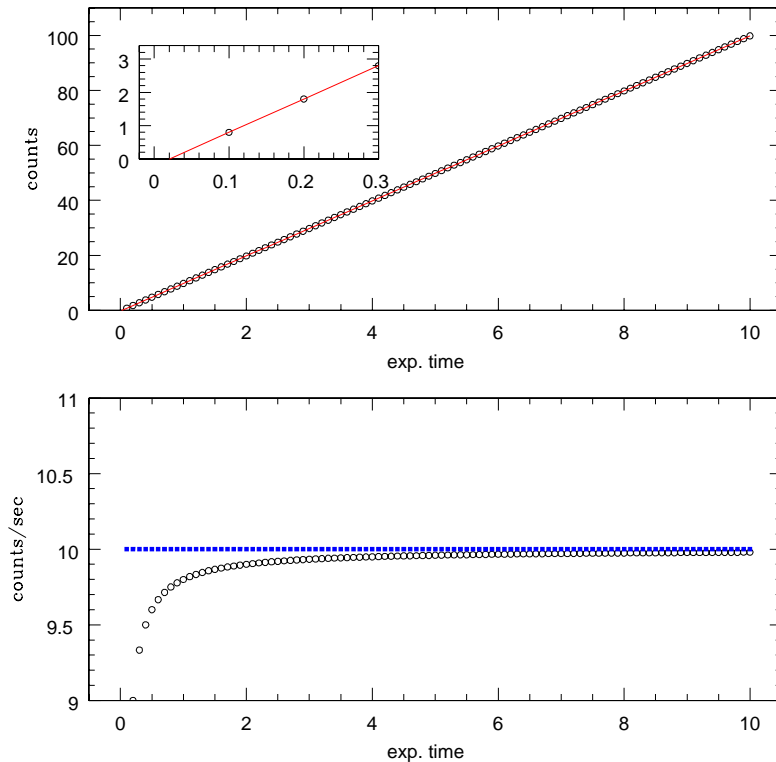


Figure 5.2: In this example, based on fictitious data, the nominal exposure times have been reduced by 0.02 sec. Exposure times are in seconds in both panels. In the *upper panel* the **method 1** is applied to compute the shutter delay. The plot shows how the linear extrapolation (red line) of the counts at zero does not cross the exposure time axis at zero, as expected, but at a time which represents the delay to be applied to correct all the exposure times (in this case $x = 0.02$, as highlighted in the box, corresponding to $\delta t = -0.02$) where the correct exposure time is $t = t_{exp} + \delta t$. The delay time can also be estimated by applying the **method 2**, as shown in the *lower panel*. In an ideal world, the counts/sec should be constant for all exposure times. In practice, there is a deviation at short exposure times (see black circles). We compute the counts/sec with $t + \delta t$ by varying δt in a suitable range (from negative to positive values) until we obtain the most constant distribution as possible (blue squares) (in this case we must apply $\delta t = -0.02$ to flatten the count rate or, in other words, we must minimize the residual from a horizontal line fitting the data for each δt).

residuals from a horizontal straight line fitting all the points (i.e. the count rate is constant for all the exposure times, assuming the response of the CCD is linear over the range used), see Fig. 5.2, lower panel. We can try to compute the count rate curve with $t + \delta t$ by varying δt in a suitable range (from negative to positive values) until we obtain the most constant distribution as possible.

Once known, the shutter delay can be used to correct the exposure times. Usually, it is negligible for long exposure times: a 10 ms shutter offset corresponds to a 1% error in a one second exposure, but the relative effect decreases with longer exposure times².

Because shutter delay effects are usually negligible for long exposure times and because long exposure times usually correspond to high count levels, linearity tests are not much affected by shutter delay: deviations from linearity are usually prominent at high count levels. Vice versa, since deviations from linearity are more evident at high counts, shutter delay test based on relatively short or very short exposure times (usually corresponding to low counts) are not much affected by deviations from linearity. This allows us to perform the two test independently. However, when deviations from linearity are particularly evident, we also applied a linearity correction to the shutter delay tests (and vice versa).

5.1.2 2D exposure time variation

A mechanical shutter can also produce exposure time variations across the CCD. This effect depends on the shutter type and on its quickness: the shutter takes a finite time to travel from fully closed to fully open and vice versa. In short exposures this can produce a significantly non uniform exposure of the CCD. As an example, an iris type shutter can affect short exposure images as shown in Fig. 5.3, where the central part of the frames is exposed for a time longer than at the edges and the iris structure becomes evident. This image is obtained by dividing a flat field acquired with a very short exposure time by a reference one taken with a relatively long exposure time. The ratio is eventually normalized by dividing for its mode. In this case we do not care about the lamp stability, since we are interested only in the two-dimensional structure of the ratio and not in the absolute level of the counts. The structure of the ratio of flat fields with increasing exposure times (starting from

²However, we stress the fact that flat fields acquired with too short exposure times will affect also scientific images taken with relatively long exposure times if they are used in the pre-reduction process.

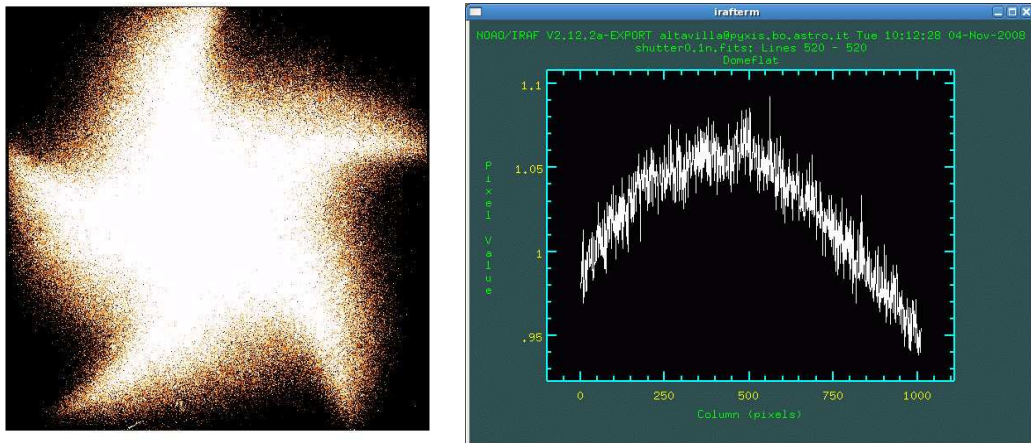


Figure 5.3: *Left panel:* normalized ratio between a 0.1 sec and a 20 sec unfiltered dome flats taken on August 20, 2008 with LaRuca@SPM 1.5m. *Right panel:* counts along a central line of the same frame, variations of $\pm 6\%$ are visible.

very short times) with respect to a flat with a long exposure time (long enough to be reasonable safe from shutter effects) can give an estimate of the *minimum exposure time* for which the CCD illumination is flat enough for our purposes: we look for two-dimensional variations $\leq 1\%$.

It is interesting to note that this effect can be interpreted as a shutter delay varying over the frame. The effect is similar to the pure shutter delay (i.e. the average counts level of a flat field is smaller or larger than expected) but because there is a 2-d gradient, it can not be corrected by simply adding a constant to the exposure time: we should use a two-dimensional map showing $\delta t(x,y)$ to normalize all images to the nominal exposure time. For this reason, while the shutter delay is usually very small, if any ($\delta t \ll 1$ sec), the minimum exposure time given by this test can be much larger, even of the order of a few seconds. For the same reason it must be considered more stringent than the shutter delay test results (see Section 5.3 for results concerning the six instruments we use).

5.1.3 Lamp Stability

The intensity and/or color of the lamps used to acquire dome flat fields for the above tests may vary with time for several reasons. The most common is a thermal drift that may produce an increase or decrease of the intensity with time. Lamp frames with constant exposure times, acquired between images with varying exposure time,

can be used to check the lamp stability and correct the frames taken soon after (or soon before). All monitoring frames should be divided by a frame assumed as reference (for example the first one).

In the ideal case (stable lamp) the result will be constant and equal to 1, in a real case their ratio will vary around 1. If the variations are slow and regular enough, the frames with varying exposure time can be corrected for the drift by dividing them by the ratio frame mentioned above (see Fig. 5.4).

5.2 CCD Performance Tests: CCD linearity

Linearity is a measure of how consistently the CCD responds to different light intensity over its dynamic range. For example, if a 1 second exposure to a stable light source produces 100 ADU, 10 seconds should produce 1000 ADU³, thus increasing linearly with exposure time. CCDs can exhibit non-linearities, typically at either or both low and high signal levels. High quality CCDs show significant deviations ($\geq 1\%$) from linearity only close to saturation, i.e. at high signal levels when the well depth is almost full. Of course CCDs strongly deviate at saturation, when the well depth is full and additional incoming photons do not increase the photoelectrons in a given pixel. Saturation is usually accompanied by blooming, i.e. the additional charge spreads into neighboring pixels, usually along lines or columns depending on the CCDs structure (Fig. 5.5).

With high-performance sensors intended for scientific applications, considerable effort is made to ensure a linear relationship between incident photon level and output signal from the CCD. When observations are restricted to the linear portion of full well capacity⁴, the CCD performs as a detector suitable for accurate spectrophotometric measurements: the better is the linearity, the better is the calibration that can be achieved.

Two methods, based on photometric flat fields or spectroscopic flat fields, can be used to investigate the CCD linearity:

1. the *classical method* maps the CCD dynamic range with a number of points proportional to the number of photometric flat fields acquired, hence a large number of frames is desirable to get a good coverage of the CCD linearity;
2. the *Stello's method* (Stello et al. 2006) maps the whole CCD dynamic range

³Of course the intensity level must be measured on bias (and dark, if needed) corrected images.

⁴The amount of charge that can be accumulated in an individual pixel before saturation

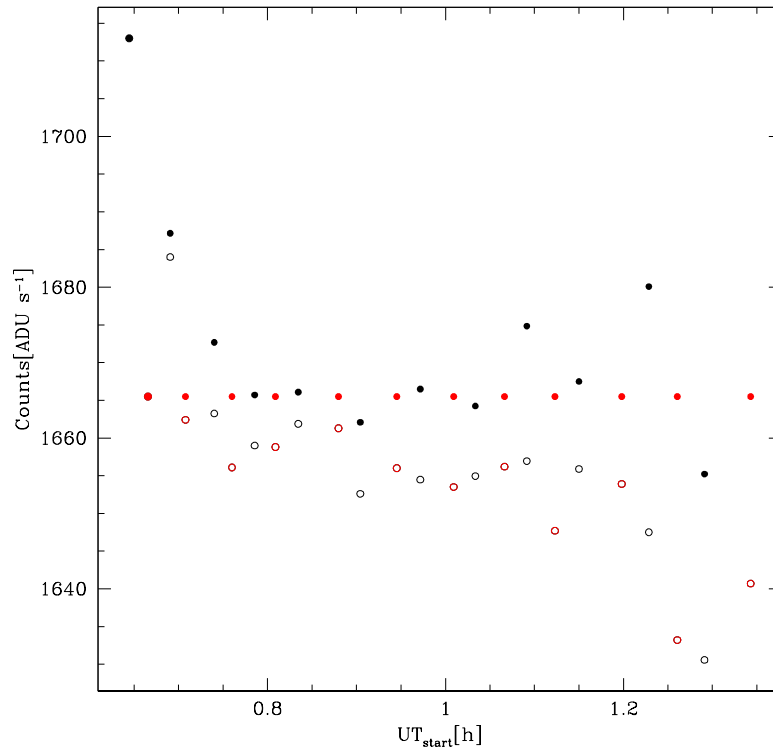


Figure 5.4: Example of real ADU/sec of the flat fields obtained with different exposure times. The red empty dots represent the constant exposure time frames (10 sec) acquired to monitor the lamp (the fixed exposure time allows us to neglect possible shutter or linearity effects). In an ideal case the ADU/sec should not vary with time (in the x axis). The plot shows that the lamp variation is slow: this allows us to perform a good correction of the other frames, using the monitoring frames to scale properly the images. The black empty dots are the ADU/sec of the frames with varying exposure time. The filled dots are the ADU/sec corrected for the lamp variability. As expected the red dots are now aligned. In an ideal case the black dots should be on the same line while in a real case there is some scatter. It is interesting to note, however, that this lamp is quite stable: the variations are of the order of ± 20 counts ($\simeq 1.5\%$), excluding bigger variations corresponding to exposure time shorter than 4 seconds, for which shutter effects become dominant. Data shown in this figure were obtained with LaRuca@SPM during run V-006 (23 August 2008).

with a continuous sampling and it can be performed in principle with two spectroscopic flat fields only⁵.

Both methods allow to define the maximum level (in ADU) for which a given CCD produces a linear response. For our purposes, we look for the intensity range corresponding to a negligible deviation from linearity ($\leq 1\%$).

In both cases flat fields must be trimmed and processed by subtracting overscan and/or bias (and dark, if necessary) as described in Chapter 6. In order to reduce the noise and to get rid of spurious effects, multiple images with the same exposure time are taken (usually triplets) and combined.

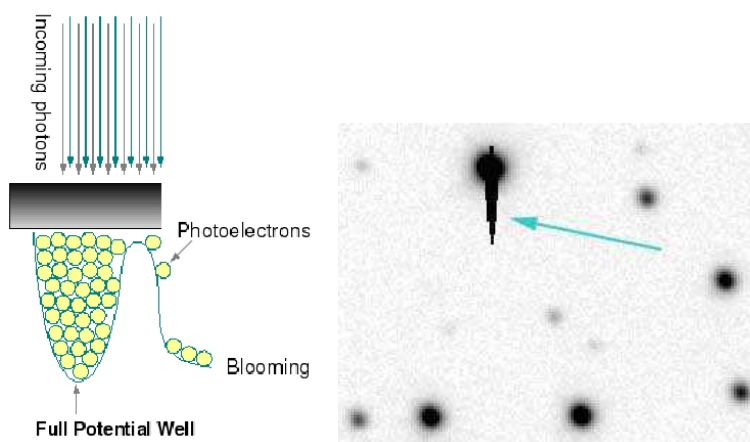


Figure 5.5: *Left panel:* cartoon of the vertical structure of a pixel full well capacity, describing the saturation and blooming effect. *Right panel:* a real example of blooming.

5.2.1 Classical method

The “classical” method for measuring the CCD linearity consists in building a plot with ADU versus exposure time (corrected for shutter delay, if necessary, see Section 5.1). This test requires photometric flat field images with increasing signal (from faint to saturation). This can be simply achieved by taking a sequence of flat fields with increasing exposure time. Since the light source stability is crucial, the sequence must include reference images taken with fixed exposure time, to monitor the lamp stability and to correct for small and slow flux variations as described in Section 5.1.3.

⁵However, the Stello’s method seems very sensitive to the input data and to their treatment.

In the ideal case, CCDs will produce a plot where the ADUs increase linearly with exposure time. In general, the high signal counts close to saturation will deviate from the linear fit of the points in the linear regime, i.e., points related to frames far from saturation and with long enough times to avoid significant shutter effects. The deviation, better visible in a plot showing the residual of the data from the linear fit, will provide a measurement of the non-linearity. In particular we are interested in determining the full well capacity range (in ADU) characterized by deviations from linearity $\leq 1\%$ (see Fig. 5.6).

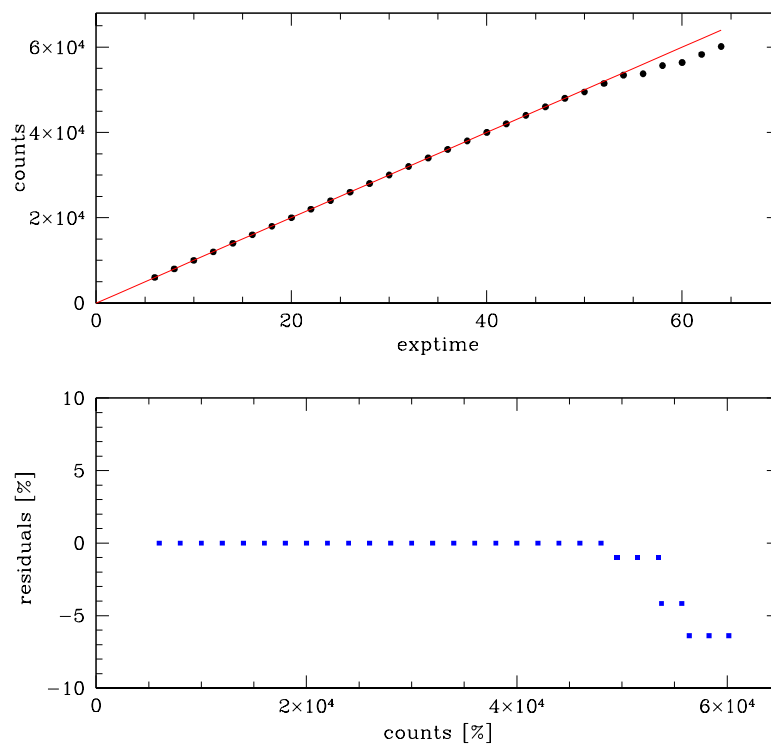


Figure 5.6: In this example, based on fictitious data, the expected counts at high signal have been arbitrarily reduced to simulate a non-linear response. The *upper panel* shows how the linear fit of the points in the linear regime (red line) does not match the simulated points at high signal. The *lower panel* shows the residuals [%] of the points from the expected values: it is clear that the linearity become larger than 1% at 55 000 ADU.

5.2.2 Stello method

A second method for obtaining the linearity profile of the CCD response is the one described by Stello et al. (2006). In this case, the required frames are at least two spectroscopic flats, one reaching the saturation level and the other covering a fainter intensity range. The slit and grism used for the test are not crucial: the important thing is to get spectroscopic flats with a wide intensity range along one direction (column or line). A smooth monotonic variation from the minimum level to the peak is preferred but not mandatory.

All frames must be collapsed to one-dimensional images by averaging them across dispersion⁶ (see Fig. 5.7, upper left panel). As in the “classical” method, lamp luminosity (thermal) drifts must be corrected by scaling the one-dimensional collapsed frames by the ratio between the control frames taken before or after each spectral flat. In this case the ratio of the collapsed control sequence frames may show not only flux but also color variations.

The one-dimensional images, once corrected for lamp drifts if necessary, are used to compute the ratio corresponding to pairs with different exposure times, normalized by their exposure time:

$$R_1(I) = \frac{I_{t_1}/t_1}{I_{t_2}/t_2} \quad (5.1)$$

where I_{t_1} and I_{t_2} are the intensities obtained with exposure times t_1 and t_2 . In an ideal case this ratio should be equal to one. The real case is shown in Fig. 5.7, upper right panel. R_1 was fitted by a polynomial function in order to get rid of the noise, extrapolated to zero ADU and forced to be 1 at 0 ADU level (by multiplying it by a suitable factor), as required by this method.

The so called *gain-ratio curve* R_1 is used as a first estimate of the actual underlying gain curve $G(I)$ to start the following iterative process.

Assuming:

$$G_1(I) = R_1(I) \quad (5.2)$$

we compute a new gain-ratio curve R_2 (for all I) as:

$$R_2(I) = \frac{G_1(I)}{G_1(I * t_2/t_1)} \quad (5.3)$$

⁶This operation can be done with the IRAF task `blkavg`.

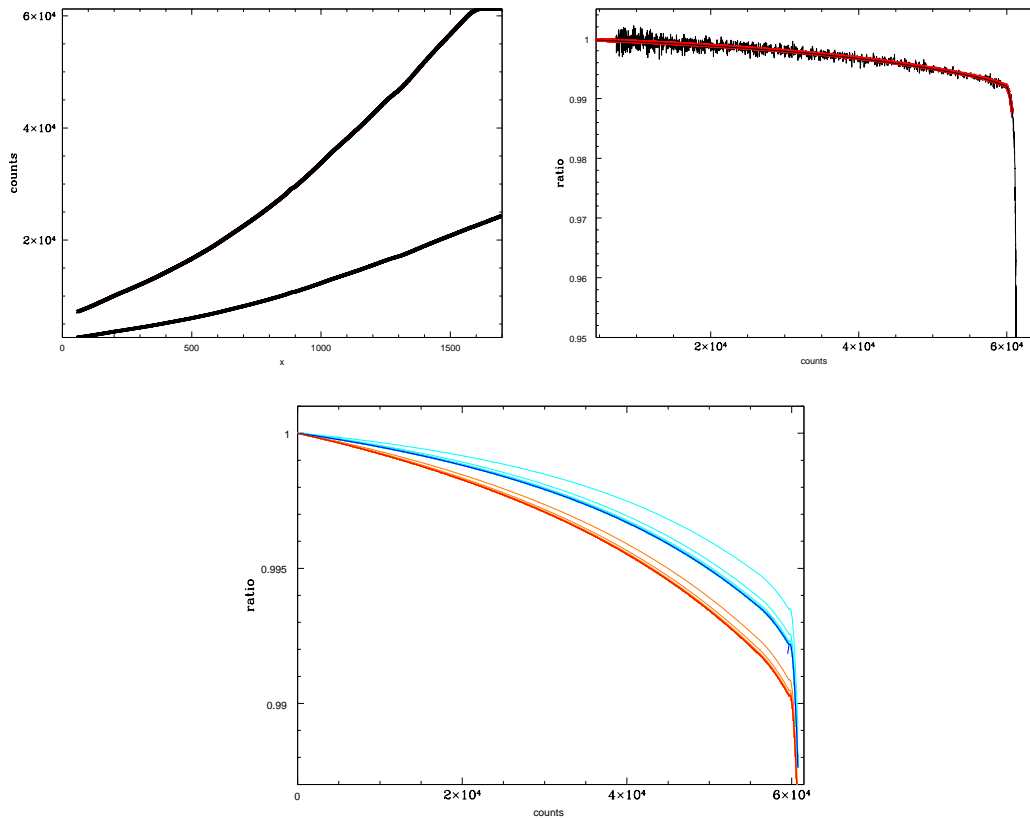


Figure 5.7: *Upper panel:* combined spectroscopic flat fields (collapsed into one-dimension). The saturation limit is reached in the longest exposure image. *Middle panel:* Gain ratio curve (see text). A red line shows the result after replacing the noisy curve with a polynomial fit. The curve has also been extrapolated to intensity zero. Before starting the iterative procedure the resulting curve was multiplied by a suitable factor in order to be 1 at 0 ADU. *Bottom panel:* R_i iteration (cyan line) converges (blue line) on R_1 (in black but hardly seen because matched by the final iterated line) while G_i (orange line) converges on the actual gain curve (in red). The examined CCD is linear well within 1% up to 60 000 ADU, i.e. the detector is quite linear almost up to saturation, when the linearity shows a step drop.

The new estimate for the gain is then corrected by the ratio between R_1 and R_2 according to:

$$G_2(I) = \frac{R_1}{R_2} G_1(I) \quad (5.4)$$

The iterative process is continued:

$$R_i = \frac{G_{i-1}(I)}{G_{i-1}(I * t_2/t_1)} \quad (5.5)$$

$$G_i = R_1/R_i * G_{i-1}. \quad (5.6)$$

until R_i matches R_1 , as shown in Fig. 5.7, bottom panel. The corresponding G_i represents the linearity curve of the CCD.

5.3 CCD performance tests results

We have tested CCD performances on all the instruments we use in our observing campaigns, except for ROSS⁷. Since the beginning of our Campaigns, the original CCD was replaced in three instruments: BFOSC@Cassini, DOLoRes@TNG and, recently, also in LaRuca@SPM. In addition, also the shutter was replaced in BFOSC@Cassini and CAFOS@CAHA. Both the shutter and linearity test were performed on these new shutter and detectors as well⁸. The results for each instrument are extensively reported in Altavilla et al. (2011), and are summarized in Table 5.1. The shutter delay seems to be negligible for relatively long exposure times, except for the old BFOSC shutter ($\delta_t - 0.3$ sec). The longest shutter delay ($\delta_t + 0.028$ sec, LaRuca) is 1% for a 3 seconds exposures, hence can be neglected for longer exposure times. The minimum exposure time to obtain an homogeneous illumination of the CCD varies from negligible (EFOSC2, DOLoRes, CAFOS-new diaphragm) to 5 seconds (BFOSC, LaRuca).

All CCDs have a linear response (deviation within 1%) up to at least 55 000 ADU (EFOSC2, CAFOS) or up to 60 000 ADU (BFOSC, DOLoRes, LaRuca).

⁷The required data to perform both shutter and linearity "classical method" test (i.e. flat field spanning a wide range of exposure time and counts, up to saturation and acquired with a stable illumination) are not easily available with ROSS: flats are automatically acquired on the sky using a fixed exposure time (5 sec), without any control on the resulting levels of the frames. In addition spectroscopy is not allowed ("Stello's method" test can not be performed), and a stable illumination is not available because of light-concentration

⁸At the time of writing, the reduction of data acquired for testing the new Marconi CCD mounted in LaRuca@SPM is ongoing.

Table 5.1: Linearity and shutter effects for the Telescope/Instruments used in the absolute calibration program of the Gaia spectro-photometric data

Telescope Instrument	CCD	Deviation from linearity	Minimum exposure time [sec]	Shutter delay* [sec]
Cassini 1.5m BFOSC	EEV 1300 × 1340B (new)	≤ 1% up to 60000ADU	~ 5	-0.3 before Feb. 2010 negligible afterwards
	EEV 1300 × 1340B (old)	≤ 1% up to 55000ADU		
ESO NTT 3.58m EFOSC2	CCD#40 LORAL/LESSER	≤ 1.2% up to ~ 55000ADU	< 0.1 if any	+0.008 ± 0.003
TNG 3.58m DOLoRes	E2V4240(new)	≤ 1% up to 60000ADU	< 1 if any	-0.011 ± 0.002
CAHA 2.2m CAFOS	SITTE#1d_15	≤ 1% up to ~ 55000ADU	~ 3 before Apr. 2008 < 0.5 after Sep. 2009	-0.017 ± 0.007
REM 0.6m ROSS	Marconi 47-10	n.a.	n.a.	n.a.
SPM 1.5m LaRuca	SITTE#1 Photometrics	≤ 1%	~ 5	+0.028 ± 0.015
	Marconi e2vm E2V-4240	up to 60000ADU		

* to be summed to the nominal exposure time

5.4 Calibration Frames Monitoring

When pre-reducing images and spectra⁹, a quality assurance is performed by defining and measuring a set of Quality Control (QC) parameters¹⁰. These parameters are used both to study the frames stability on a nightly basis, and on timescales longer than a single night. A short-term¹¹ stability monitoring is necessary to evaluate if, when appropriate calibrations are missing for one night, the ones acquired in adjacent nights can be safely used in the pre-reduction process. Together with a long-term¹² stability monitoring, it is also useful to build a *calibration plan* for the instruments used.

The calibration frames monitoring is described in details for all the instruments we use in our Campaigns in Marinoni et al. (2011b).

5.4.1 Masterbias Monitoring

The details of the production of masterbias frames are described in Chapter 6, as well as both the QC parameters evaluation and the short-term monitoring of the level and 2D structure of masterbias frames. In brief, five areas on the surface of each masterbias are defined (one for each corner and one for the center) and the ratio between the median value of each corner and the median value of the center is the QC parameter which allows us to monitor the 2D shape of a masterbias. The stability of the bias level over one run can be checked using the `imstat` task in IRAF. The same parameters can be used to visualize the long-term stability trend over more than one run. An example is shown in Fig. 5.8.

5.4.2 Photometric Masterflat Monitoring

As for bias frames, the production and QC parameters evaluation, as well as the short-term monitoring of masterflat frames (one night and one run), are performed together with the data pre-reduction as described in Chapter 6.

Summarizing, of the three stability tests used to monitor the short-term flat stability and described in detail in Chapter 6, two are of interest for the calibration frame monitoring: the *large scale variability*, which provides information on the “global”

⁹See Marinoni et al. 2011a (summarized in Chapter 6) and Cocozza et al. 2011, for the imaging and spectroscopy pre-reduction protocols, respectively.

¹⁰http://yoda.bo.astro.it/wiki/index.php/IFP_QC_Parameters

¹¹In the present context, *short-term* means at least one run.

¹²In the present context, *long-term* means more than one run.

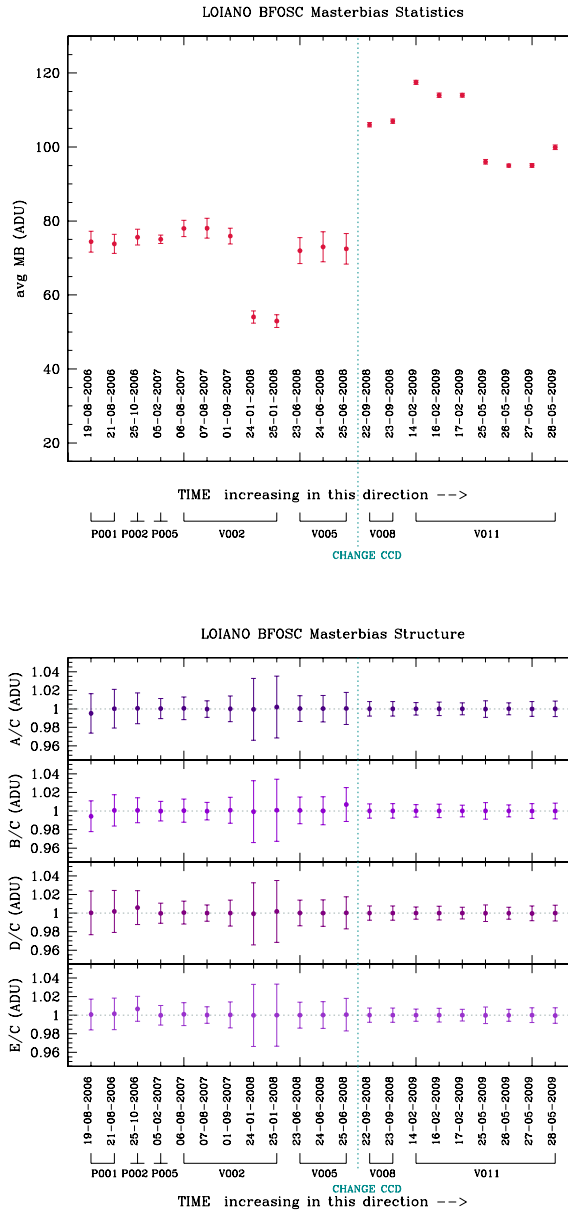


Figure 5.8: Long-time trend monitoring of the bias level (*upper panel*) and two-dimensional structure (*bottom panel*) produced using the data acquired in the first seven runs with BFOSC@Cassini. Between runs V-005 and V-008, a new CCD was mounted : the improvement in data quality is clearly visible in the two-dimensional stability trend plot. Anyway, for both CCDs, the masterbias frames appear to be quite stable in their 2D shape, although not in their level.

variation of the masterflat shape in comparison with a reference flat (assuming the variation uniformly distributed all over the pixels), and the *9 areas* check-plot which provides information on “where” and “how much” is the variation of the flat shape in comparison with a reference flat.

The long-term monitoring of masterflats is not strictly needed, since we generally exclude the possibility to use masterflat frames produced in one run to pre-reduce data acquired during other runs. Therefore, I just show here some examples of long-term large scale variability monitoring performed for some instrument used in photometric mode: the results are reported in Fig. 5.9 and Fig. 5.10

5.4.3 Spectroscopic Masterflat Monitoring

The details of the production of masterflat frames and QC parameters evaluation for spectroscopy is described by Coccozza et al. (2011). When masterflats for all nights of a run are built, their stability can be checked using the spectroscopic version of the *9 areas* check-plot. An example is shown in Fig. 5.11. Because spectroscopic flats are flattened to remove the shape of the lamp spectrum, a long-term monitoring of large-scale variations similar to the one performed on photometric flats is not needed for spectroscopic masterflats.

5.4.4 Masterdark Monitoring

The details of masterdark production and QC parameters evaluation are described in Chapter 6. In brief, the trend of dark counts with exposure time is checked and the extrapolation at zero exposure time is compared with the bias level. The long-term monitoring of masterdark is essential only for ROSS@REM: the CCD is not nitrogen cooled and dark currents become important¹³. This is not the case of all other instruments used in our campaigns: correction for masterdark is not necessary. However a series of dark frames with increasing exposure time are taken each 1-2 years in order to monitor the instrument. I report in Fig. 5.12 and Fig. 5.13 the dark level and the two-dimensional stability trends for the 60 sec and 180 sec masterdarks¹⁴ respectively during the first three REM runs (V-001, V-004 and V-007). Masterdark frames, for both exposure times, are very stable in shape, but the counts level show seasonal changes. Therefore, our pre-reduction protocol foresees

¹³Bias frames are not acquired with ROSS: dark frames already include the bias level and pattern (see Pancino et al. 2010a).

¹⁴From our experience, we found that 180 seconds is a suitable exposure time for most of our targets, while 60 seconds are enough for the brightest targets ($V \leq 10.5$)

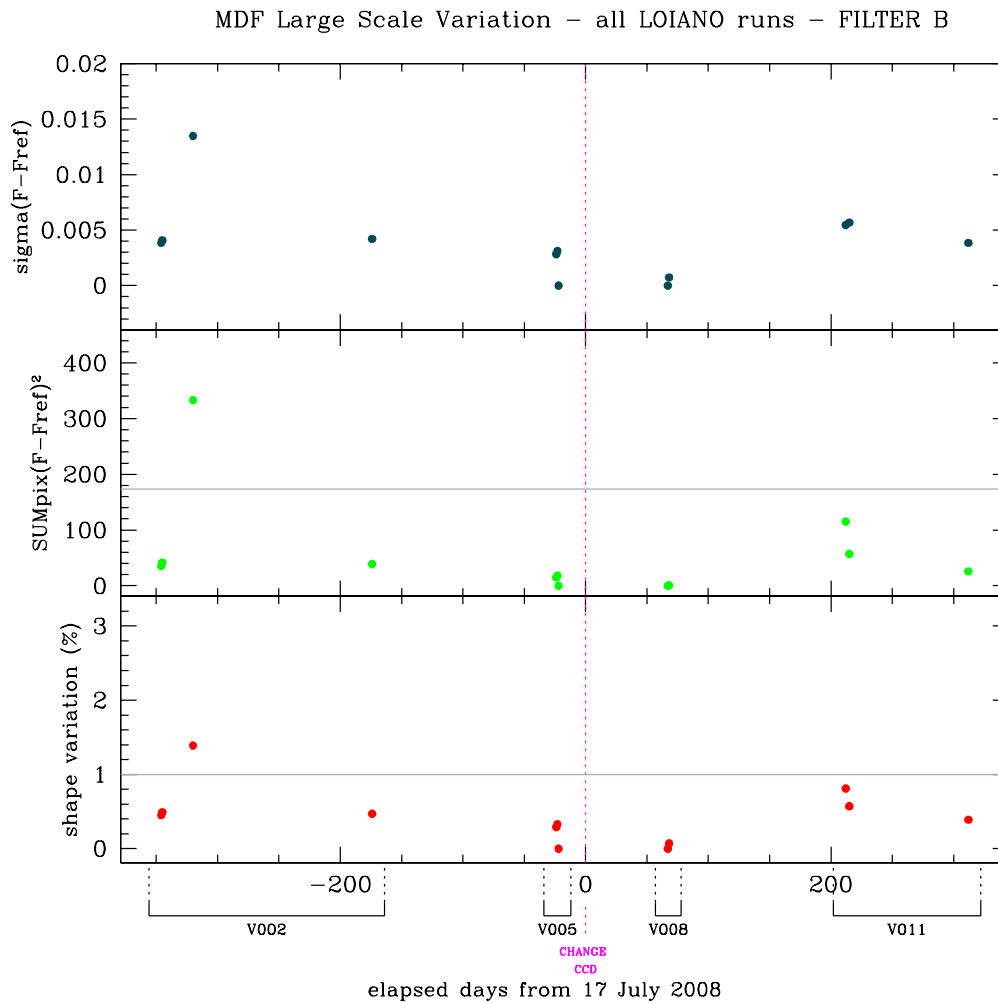


Figure 5.9: Long-time large scale variability test performed on all imaging dome-masterflats produced with the B filter during three consecutive runs in Loiano (BFOSC@Cassini). Due to the CCD change between run V-005 and V-008, two reference frames were chosen: the dome-masterflat of the last night of run V-005 is used as a reference for the old CCD, while that of the first night of run V-008 is the reference for the new CCD. The time-length stability of masterflats is very good for both CCDs, reaching about 300 days.

the use of the closest available masterdark, which is produced monthly by the REM staff.

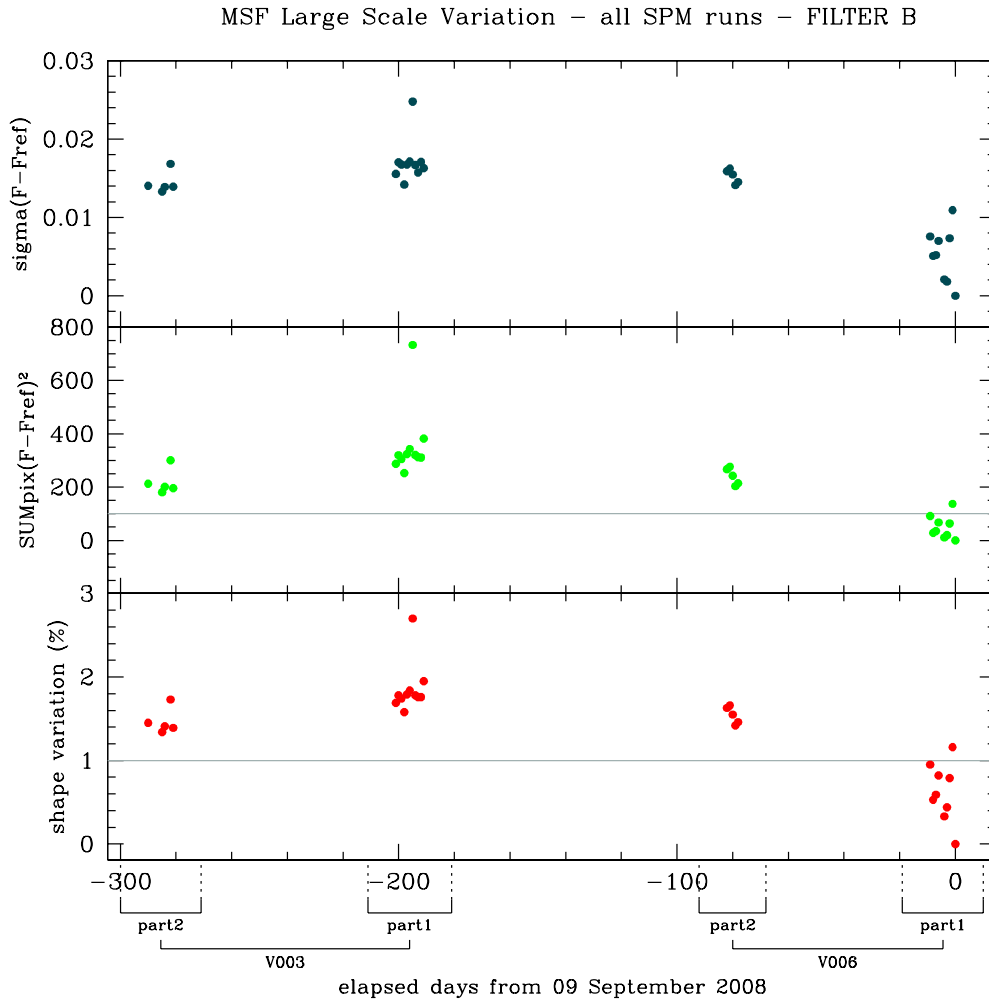


Figure 5.10: Long-time large scale variability test performed on all imaging sky-masterflats produced with the B filter during the first two runs with LaRuca@SPM. The sky-masterflat produced during the last night of run V-006 (09 November 2008) is the reference frame for the test. The inter-run shape variation of the sky-masterflat frames is evident, as well as the night-by-night shape variation between runs V-003 and V-006.

The Instrument Familiarization Plan

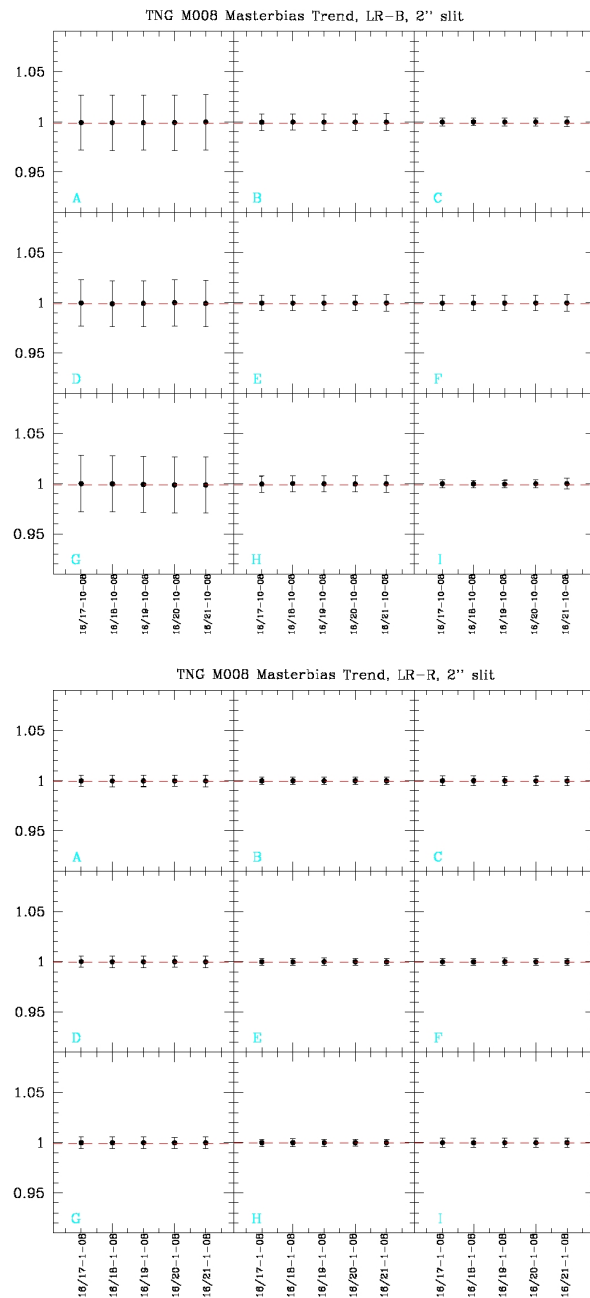


Figure 5.11: Examples of the spectroscopic version of the *9 areas* plot produced for masterflat frames of run M-008@TNG. Grism LR-B and 2" slit are used to obtain data shown in the *upper panel*. In the bluer part of the blue grism (showed in the three left boxes of the plot) the difference in shape between masterflats produced in different night is $\sim 3\text{-}4\%$ in the worst case, due to the low S/N reached in this region. Grism LR-R and 2" slit are used in the *bottom panel*.

5.4 Calibration Frames Monitoring

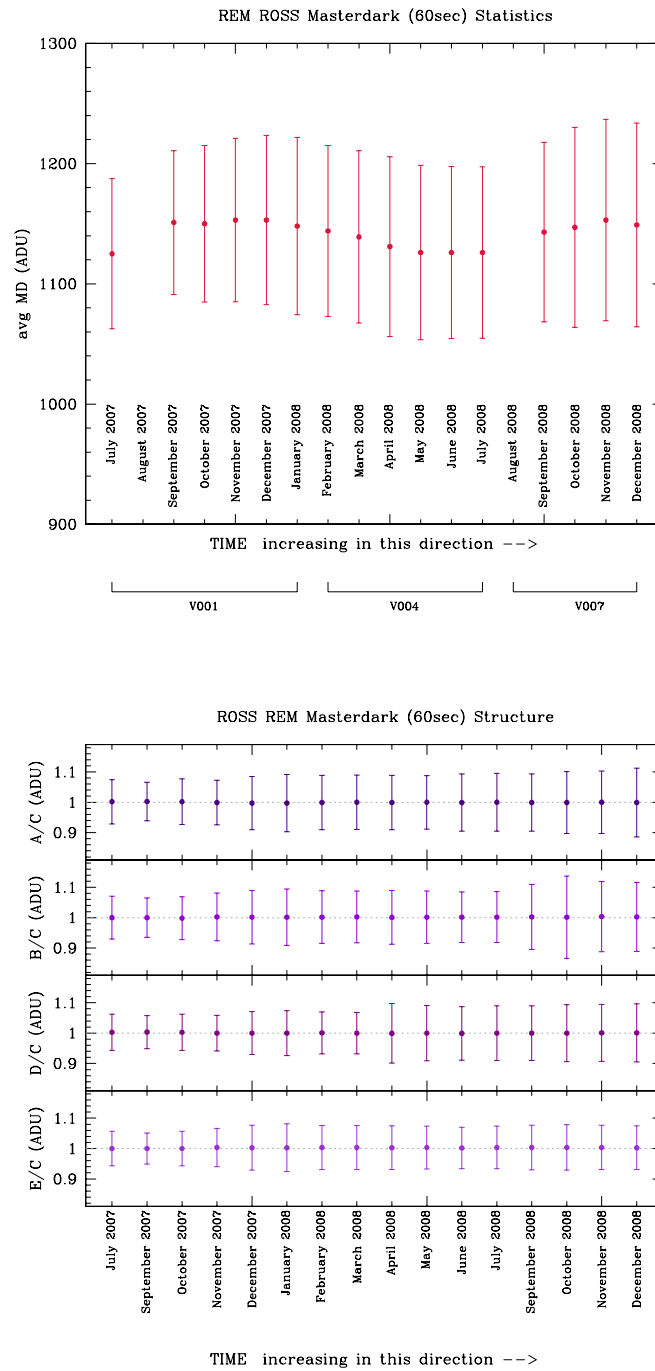


Figure 5.12: Long-time trend of the 60 sec dark level (*upper panel*) and two-dimensional structure (*bottom panel*) produced using data acquired with ROSS@REM in the first three runs.

The Instrument Familiarization Plan

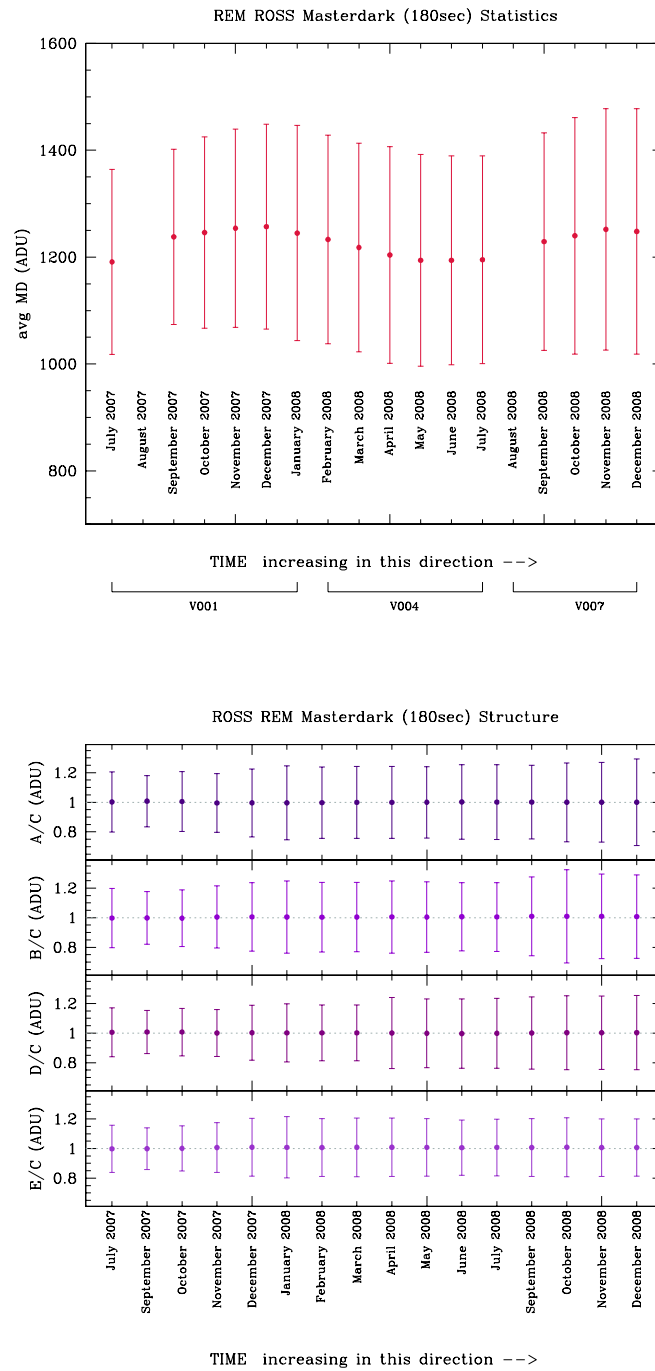


Figure 5.13: Long-time trend of the 180 sec dark level (*upper panel*) and two-dimensional structure (*bottom panel*) produced using data acquired with ROSS@REM in the first three runs.

5.4.5 Wavelength Lamp Flexures

Low resolution spectrographs are usually mounted at the telescope or at the telescope derotator, and they move during observations. At each different position, the varying projection of the gravitational force leads to mechanical distortions, either negligible or important. These mechanical distortions are seen on the wavelength calibration frames, where they produce shifts of the lamp emission lines which can be linear or non-linear in wavelength.

To evaluate mechanical distortions, lamps must be taken at different positions of the telescope. Depending on the instrument/telescope combination, the position can be parametrized with a single angle (the derotator angle), if the instrument is attached to a fixed derotator (as at a Nasmyth focus), or with two different angles, if the instrument is mounted at the telescope. In the simple case, lamp flexures can be measured with one full circle of the derotator angles, by moving the derotator both in the clockwise and anti-clockwise directions, with respect to a reference position, for an ideal total of ~ 70 -140 wavelength lamp exposures (steps of ~ 5 -10 deg).

The choice of the lamp depends on the expected kind of distortion. One lamp with a relatively good wavelength coverage is sufficient if only linear distortions are expected. If, after a first set of measurements, non-linear distortions are suspected, measurements could be repeated with at least two different lamps, to evenly sample the whole spectral range covered by Gaia (350-1050 nm).

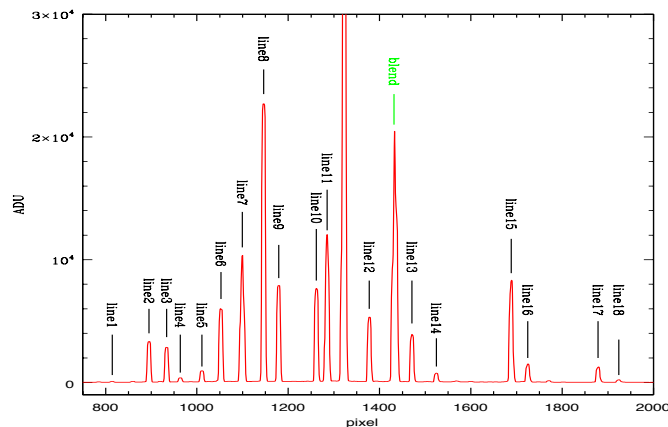


Figure 5.14: Lines used to measure lamp flexures, obtained with Ar lamp, slit 2" and grism LR-R.

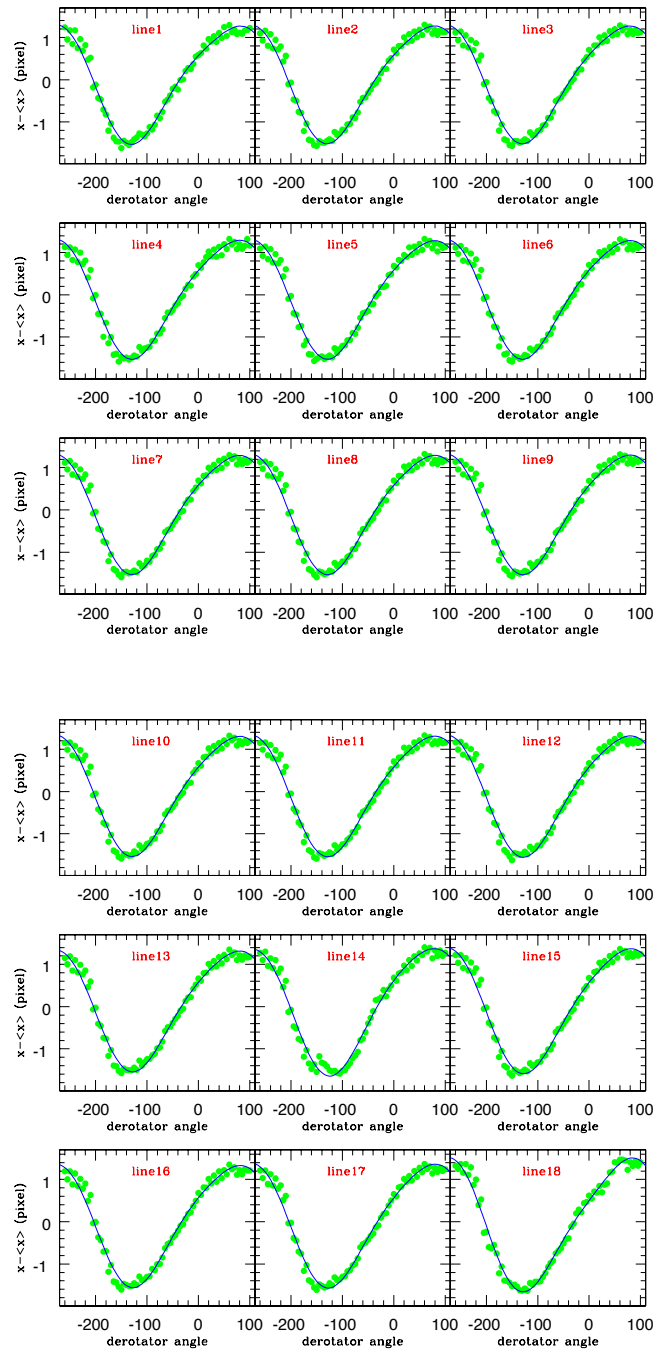


Figure 5.15: Displacement of different lines from their mean position (in pixel) versus derotator angle. Each panel correspond to a different emission line from Fig. 5.14.

This test was performed for DOLoRes@TNG, when it was equipped with three different calibration lamps (He, Ne, Ar) that could not be switched on simultaneously, and the procedure to obtain a high signal-to-noise ratio calibration lamp for each single star was very time consuming (about 20 minutes). The time-consuming problem of acquiring a set of good S/N wavelength calibration arcs for each single observed star could be solved by acquiring the full set of calibration lamps with high S/N during day time, and only one short exposure calibration lamp after each spectrum.

In order to perform this test, I adopted the following configuration: LR-R grism + 2" slit + Ar lamp. Triplets of arc frames were acquired (31 January 2008) at different positions of the derotator, covering a complete derotator circle: from -260 up to +100 degrees in steps of 10 degrees forward, and from +95 up to -255 degrees in steps of 10 degrees backwards. This way, the derotator performed a complete circle in steps of 10 degrees each. The median of the three acquired lamp frames was calculated for each derotator position and corrected for the overscan. The lines used for the test are shown in Fig. 5.14. Lines positions as a function of the derotator angle trends are characterized by a quasi-sinusoidal pattern, as shown in Fig. 5.15. Taking one arc as a reference, we can estimate the shift that we need to apply to each line of all the other arcs to align them to the reference lamp. If the shift is perfectly rigid one would expect to measure, for each derotator position, the same shift in the position of each observed line, with respect to the reference lamp spectrum. In reality, the error on the position of each line, estimated with a gaussian fit, is quite large. For this reason, an average shift was estimated for each lamp by calculating the mean on the shift measured for each line. The reference spectrum obtained during day time can now be properly compared with the calibration spectra (acquired during night time for each observed star), by applying this average shift. The uncertainty resulting from this method is typically larger in the external parts of the spectrum and smaller in the central parts as shown in Fig. 5.16. This is probably due to a small non linearity of the dispersion relation. In any case, this uncertainty is small enough if compared with the error of the wavelength calibration (in particular if a 2" slit is used, as in our case).

As a result of this test, our observing (Pancino et al. 2011) and spectra pre-reduction (Cocozza et al. 2011) protocols foresee the use of one arc observed close to the target during night-time in order to shift (if necessary) the solution found with the calibrations arcs taken in day time.

For all other telescopes, since the measurements needed for the test are too time consuming, we assume that flexures are relevant, and we take high S/N night wave-

length calibration lamps close to each observed object.

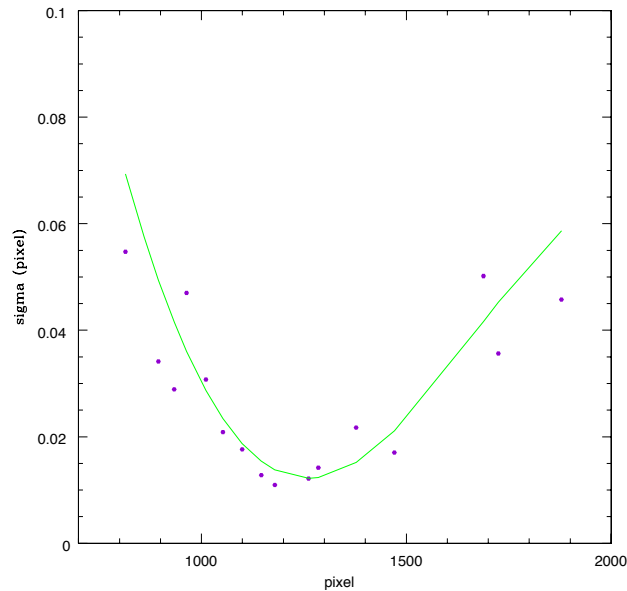


Figure 5.16: Uncertainty in the lines positions measurements (see text).

5.5 Calibration Frames Monitoring results

All the results concerning the calibration frames, for each telescope/instrument configuration, are reported in a dedicated table hosted by Wiki-Bo¹⁵ (see Fig. 5.17). In this table, each active link can be followed to open specific dedicated pages for each kind of calibration frame and for each instrument we used.

The typical stability time scale for each kind of calibration frame is reported in Table 5.2. I also report the calibration plan for each instrument, as derived from IFP tests, which we adopt during our observing Campaigns (see Table 5.3).

¹⁵Wiki-Bo are the internal CU5-DU13 Wiki pages maintained in Bologna, which can be found at: http://yoda.bo.astro.it/wiki/index.php/Main_Page .

The specific section on calibration frames study results is available at:

http://yoda.bo.astro.it/wiki/index.php/IFP_Calibration_Frames_Summary.

5.5 Calibration Frames Monitoring results

SUMMARY						
	BFOSC	CAFOS	DoLoRes	EFOSC2	LaRuca	ROSS
DARK	Short Time Trend at Dark_Lolano NO Long Time Trend	Short Time Trend at Dark_CAHA NO Long Time Trend	Short Time Trend at Dark_TNG NO Long Time Trend	Short Time Trend at Dark_NTT NO Long Time Trend	Short Time Trend at Dark_SPM NO Long Time Trend	Short Time Trend at Dark_REM Long Time Trend at Dark_REM
BIAS	Short Time Trend at Bias_Lolano Long Time Trend at Bias_Lolano	Short Time Trend at Bias_CAHA Long Time Trend at Bias_CAHA	Short Time Trend at Bias_TNG Long Time Trend at Bias_TNG	Short Time Trend at Bias_NTT Long Time Trend at Bias_NTT	Short Time Trend at Bias_SPM Long Time Trend at Bias_SPM	NO BIAS
BAD PIXEL MASK	BPM_Lolano	BPM_CAHA	BPM_TNG	BPM_NTT	BPM_SPM	no BPM
FRINGING MASK	correction not needed	correction not needed	correction not needed	correction not needed	correction not needed	correction not needed
PHOT DOME FLAT	Short Time Trend at Domeflat_Lolano	Short Time Trend at Domeflat_CAHA	NO DOME FLAT	Short Time Trend at Domeflat_NTT	NO DOME FLAT	NO DOME FLAT
PHOT SKY FLAT	Short Time Trend at Skyflat_Lolano	Short Time Trend at Skyflat_CAHA	Short Time Trend at Skyflat_TNG	Short Time Trend at Skyflat_NTT	Short Time Trend at Skyflat_SPM	correction not performed
SPEC LAMP FLAT	NO SPECTRA	Short Time Trend at SpecLampflat_CAHA	Short Time Trend at SpecLampflat_TNG	Short Time Trend at SpecLampflat_EFOSC2	NO SPECTRA	NO SPECTRA

Figure 5.17: Portion of the Calibration Frames IFP summary table.

Table 5.2: Typical Calibration Frames stability time scale

Instrument Telescope	Bias	Photometric Dome Flat	Photometric Sky Flat	Spectroscopic Flat	Dark
BFOSC Cassini 1.5m	1 run	~ 300 days	1 run	n.a.	-
CAFOS CAHA 2.2m	1 run	1 day	1 day	1 day	-
DoLoRes TNG 3.58m	1 day	n.a.	1 run	1 run	-
EFOSC2 NTT 3.58m	1 run for photometry 1 day for spectroscopy	1 run	1 run	1 day	-
LaRuca SPM 1.5m	1 day	n.a.	4-5 day	n.a.	-
ROSS REM 0.6m	n.a.	n.a.	-	n.a.	~1 month

BFOSC@Cassini: 1 run ~ 4 days

CAFOS@CAHA2.2: 1 run ~ 7 days

DoLoRes@TNG: 1 run ~ 5 days

EFOSC2@NTT: 1 run ~ 5 days

LaRuca@SPM1.5: 1 run ~ 10 days

Table 5.3: Calibration Plan

Instrument Telescope	CCD	Bias	Photometric Dome Flat	Photometric Sky Flat	Spectroscopic Flat	Spectroscopic Illumination Flat	Wavelength calib. Lamm	Dark
BFOSC Cassini 1.5m	EEV 1300 × 1340B (old) EEV 1300 × 1340B (new)	daily daily	daily daily	daily daily	-	-	-	once for year once for year
CAFOSS CAHA 2.2m	CCD#40 LORAL/LESSEER	daily	daily	daily	daily	once per run	for each star	yearly
DoLoRes TNG 3.58m	E2V4240(new)	daily	-	daily	daily	once per run	Ar+Ne+Hg+Kr for each star He, Ar+Ne+Hg+Kr in day time	yearly
EFOSC2 NTT 3.58m	SITTE#1d_15	daily	daily	daily	daily + for each star in the red grism	once per run	for each star	yearly
LaRucea SPM 1.5m	SITTE#1 Photometrics Marconi e2vm E2V-4240	daily	-	daily	-	-	-	yearly
ROSS REM 0.6m	Marconi 47-10	-	-	-	-	-	-	daily (*)

(*) : daily dark are acquired by REM team and used to produce monthly Masterdark frames.

5.6 Instrument Tests: 2nd Order Contamination

Low resolution spectrographs and large format CCDs allows for observations of a wide wavelength range ($\sim 3300\text{-}10000\text{\AA}$). If we have a transmission grating as the dispersing element, the grating equation is (Schroeder 2000):

$$\lambda \cdot m = \sigma(\sin\beta - \sin\alpha) \quad (5.7)$$

where:

- m is the order number,
- σ is the distance between the grooves,
- α and β are the angles of incidence and diffraction respectively, measured from the normal to the grating surface.

Equation 5.7 shows that λ_1 at first order ($m = 1$) can overlap with a shorter wavelength λ_2 at second order $m = 2$ if $\lambda_1 = 2 \times \lambda_2$ or, more in general, if:

$$\lambda_{m1} = \frac{m2}{m1} \times \lambda_{m2} \quad (5.8)$$

where $m1$ and $m2$ are different orders.

Different dispersing elements, as grisms, are described by more complicate non-linear equations, but the concept of the order contamination is exactly the same.

Two of the instruments involved in our campaigns suffer from this problem in their low-resolution red grisms:

- the LR-R grism available at DOLoRes@TNG covers the range 4500–1070 \AA and it has a built-in order-blocking filter cutting blueward of $\sim 5000 \text{\AA}$. Nevertheless spectra are affected by second order contamination, which is evident especially in blue stars spectra, starting around 9500 \AA ¹⁶
- the G16 grism available at EFOSC2@NTT covers the range 6015–10320 \AA and, according to the ESO web page¹⁷, spectra are affected by second order contamination at wavelengths longer than 7170 \AA (i.e. $\sim 70\%$ of the wavelength range is contaminated)

¹⁶see <http://www.tng.iac.es/instruments/lrs/>

¹⁷<http://www.eso.org/sci/facilities/lasilla/instruments/efosc/inst/Efosc2Grisms.html>

We adapted the method described by Sánchez-Blázquez et al. (2006) to correct the spectra for this effect. This method requires the observed spectra of a blue and a red star and their flux calibrated spectra (from catalogue or other sources, without second order contamination).

These data are used to compute the response curves C_1 and C_2 for the light issuing from the first and second order respectively which, in turn, are used to flux calibrate and remove the second order contamination from any observed spectrum (no matter the color of the star).

Being b the blue star and r the red star, the observed spectra S_b and S_r can be expressed as:

$$S_b = C_1 T_b + C_2 T_{2b} \quad S_r = C_1 T_r + C_2 T_{2r} \quad (5.9)$$

where T_b and T_r are the tabulated data (true flux calibrated spectra, free from second order contamination) for b and r , respectively, and T_{2b} and T_{2r} are T_b and T_r resampled and shifted to the second-order wavelength range (the mapping function must be determined in advance). C_1 and C_2 represent the instrumental response for the light issuing from the first and second dispersion orders, respectively. Solving the system of equations, we obtain the response curves as:

$$C_2 = \frac{T_b S_r - T_r S_b}{T_{2r} T_b - T_{2b} T_r} \quad (5.10)$$

and

$$C_1 = \frac{S_b - C_2 T_{2b}}{T_b} \quad (5.11)$$

Once the response curves C_1 and C_2 are known, the flux calibrated spectrum blueward of the second order contamination (i.e, from 3350 to 6700 Å in Sánchez-Blázquez et al. 2006) can be obtained as:

$$S'_b(\lambda < 6700) = \frac{S_b}{C_1} \quad (5.12)$$

and after resampling and shifting S'_b by the proper amount (6700 Å in Sánchez-Blázquez et al. 2006 – the resulting spectrum of these operations is called S'_{2b}), we finally obtain the whole calibrated spectrum as:

$$S'_b = \frac{S_b - C_2 S'_{2b}}{C_1} \quad (5.13)$$

The second order correction method described above cannot be directly applied to our data for two reasons:

1. the original method is used to correct observed spectra that cover the whole range of interest ($\sim 3300 - 7500\text{\AA}$) in a single image. In our case we have two different setups (the GR11 and GR16 gratings for EFOSC2@NTT and the LR-B and LR-R gratings for DOLoRes@TNG) which cover the whole optical range;
2. in the original method, the equation of the dispersing element (a grating) is known ($\lambda_{1st\ order} = 2 \times \lambda_{2nd\ order}$), while the equation of the grism (GR16 or LR-R) used in our setup is not known *a priori*.

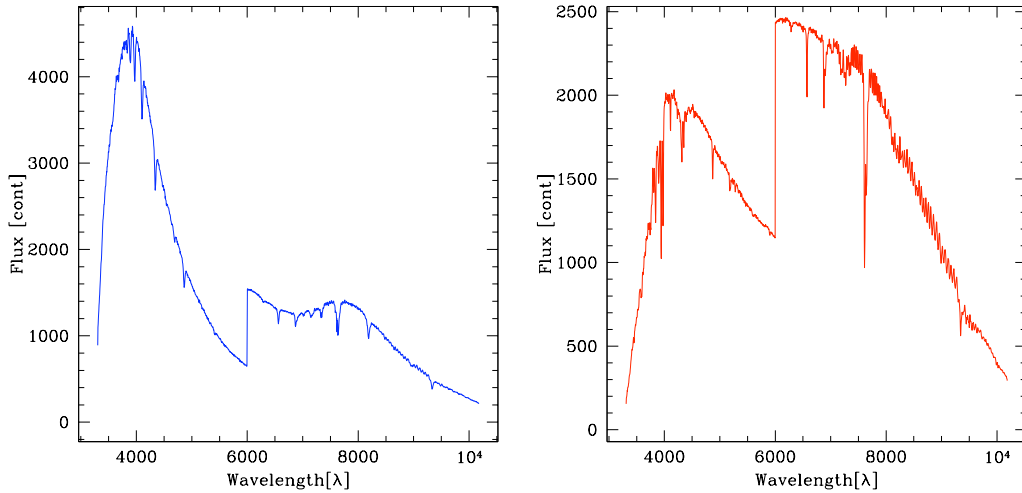


Figure 5.18: Composite observed spectra (GR11+GR16) of Feige 110 (the blue star, or S_b , *left panel*) and LTT 1020 (the red star, or S_r , *right panel*). The red portion of both spectra is affected by second order contamination, but it is much more evident in the blue star, where a “bump” is visible around 7500 \AA .

The Instrument Familiarization Plan

In order to adapt the method to our data we proceeded as follows (for example, for data acquired using EFOSC2@NTT):

1. we joined the GR11 and GR16 spectra of the same star in a single spectrum. We arbitrarily joined them at 6000\AA i.e. before the second order contamination is expected to start. The fact that the counts of the blue and red side do not match, as shown in Fig. 5.18, is not important for the procedure¹⁸. We repeat the procedure for both the blue and the red star: these two new spectra represent S_b and S_r ;
2. we derived the dispersion law analyzing the blue and red spectra of LTT 1020. The absorption lines in the blue spectrum are in fact visible in the red spectrum as well. Fig. 5.19 shows a 2D spectrum of LTT 1020 observed at high zenithal distance, where the first and second order spectra are relatively well separated due to atmospheric dispersion. The comparison of the features of the second order spectrum extracted from the image mentioned above with the blue GR11 spectrum of the same star, allowed us to determine the function which maps the first order into the the second order (see Fig. 5.20).

While the equation of a grating is well known ($\lambda_{1st\ order} = 2 \times \lambda_{2nd\ order}$), grisms dispersion is usually described by a different and more complex relation, as:

$$\lambda_{1st\ order} = a \times \lambda_{2nd\ order} + b \text{ (see Szokoly et al. 2004).}$$

Fig. 5.21 shows a polynomial fit of our data. The fit gives us the following relation:

$$\lambda_{2nd\ order} = -3815 + 3.271\lambda_{1nd\ order} - 0.0001167\lambda_{1nd\ order}^2$$

The “true” flux calibrated spectra T_b and T_r (not affected by second order contamination) were taken from the literature (Feige 110 from CALSPEC and LTT 1020 from Hamuy et al. 1992, 1994). Fig. 5.22 shows the response curves C_2 and C_1 computed according to equations 5.10 and 5.11. C_2 shows that the second order contamination starts at wavelengths shorter than 7170\AA and it seems to affect the whole GR16 spectrum.

The right bottom panel of Fig. 5.23 shows the flux calibrated spectrum of a different star (GD 71, $V = 13.032$, $B - V = -0.252$ Bohlin et al. 1995, observed in a different night and not used to compute C_1 and C_2) with and without second order correction, compared to the CALSPEC spectrum. GD 71 is a blue star showing a clear second

¹⁸But see below for a possible effect on zero-points.

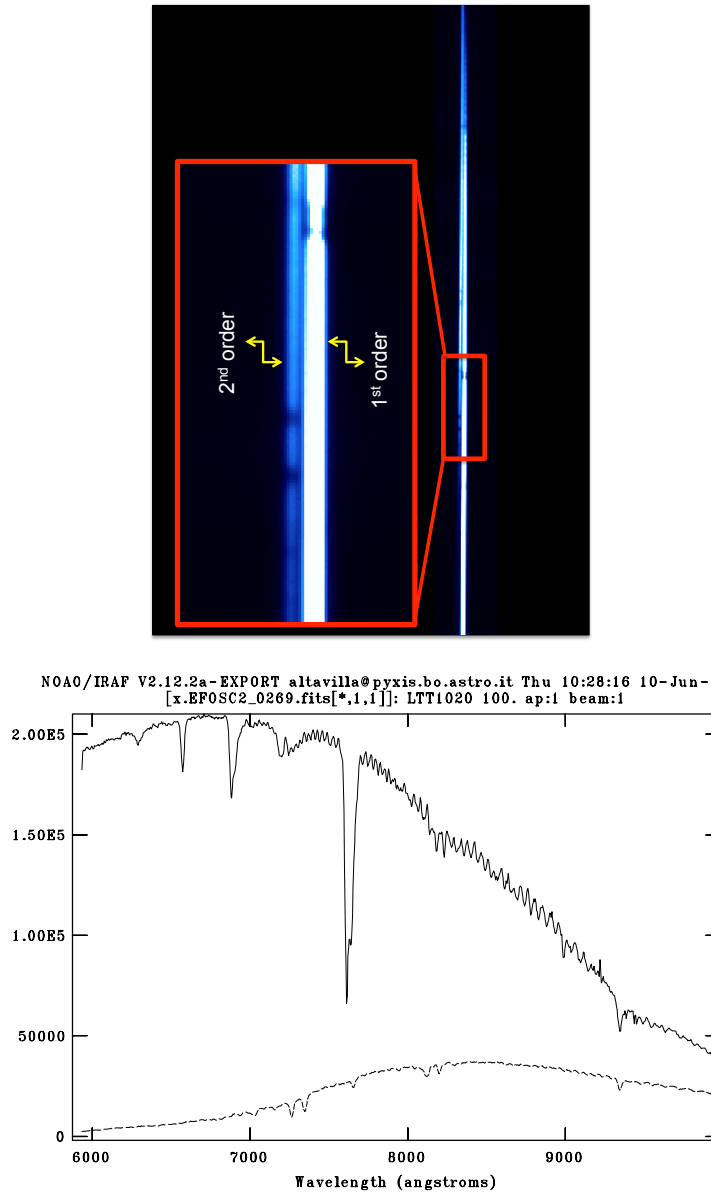


Figure 5.19: *Upper panel:* detail of a GR16, slit 10" spectrum of LTT 1020 observed at airmass ~ 1.92 . Due to the large atmospheric refraction that acts as a cross disperser, the second order spectrum is relatively well separated from the first order spectrum and is evident on the left of the main bright spectrum. *Bottom panel:* one-dimensional extraction of the whole spectrum shown on the left and of the faint second order only (dashed line).

The Instrument Familiarization Plan

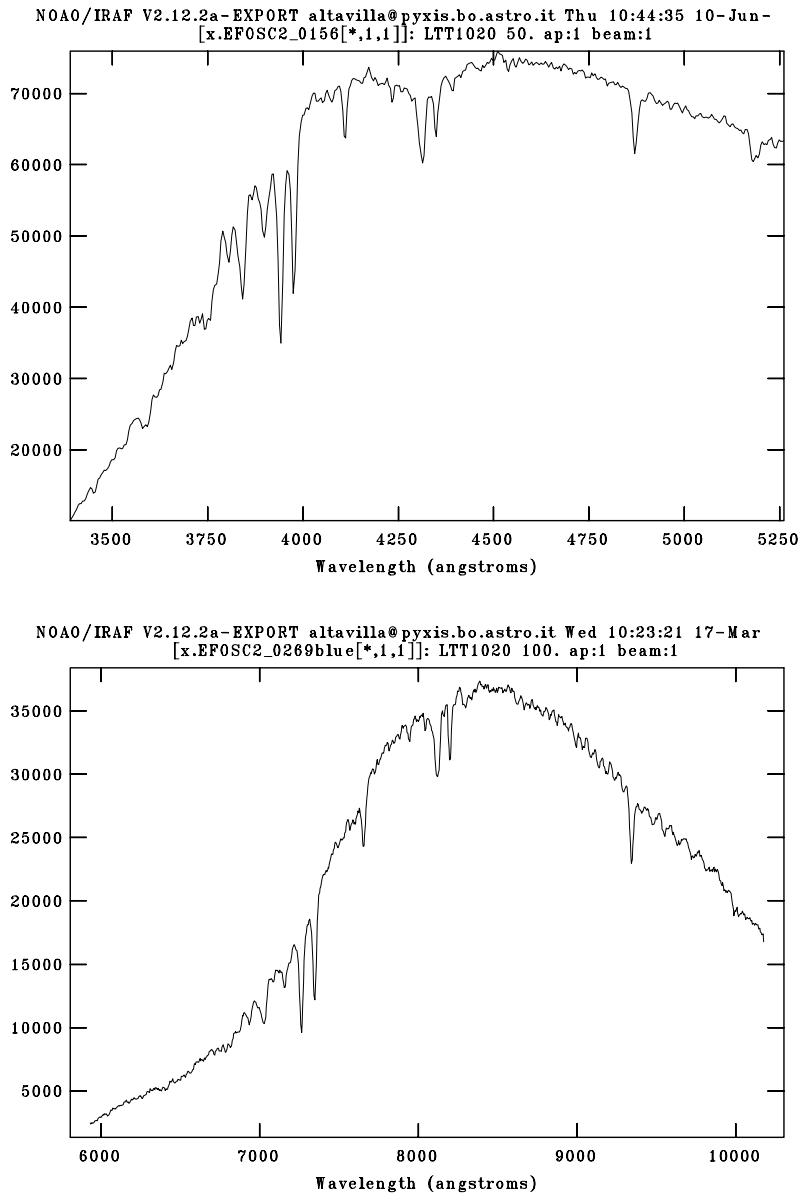


Figure 5.20: *Upper panel:* detail of a GR11, observed spectrum of LTT 1020. *Bottom panel:* second order spectrum extracted from a GR16 spectrum of LTT 1020 observed at high airmass (1.92). Neglecting the overall shape, which is obviously different, it is possible to recognize the absorption lines pattern of the blue wavelength range in the red wavelength range.

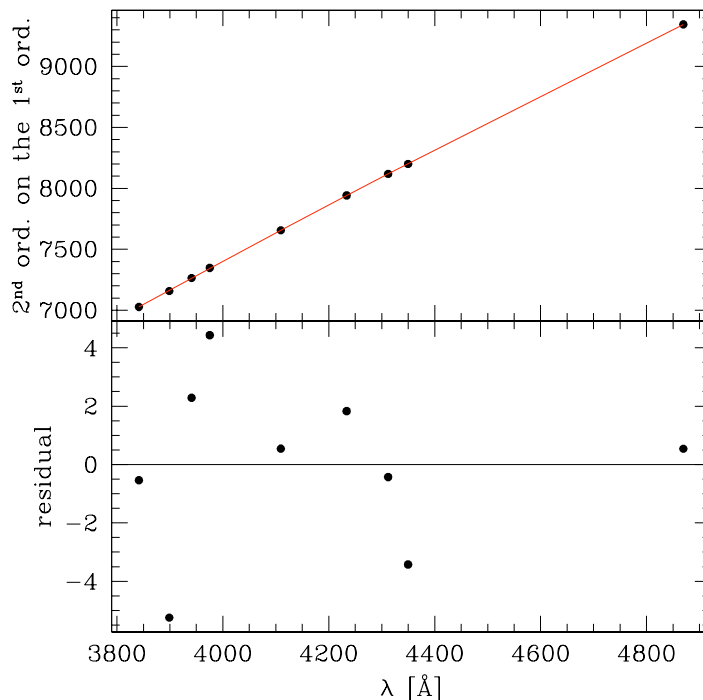


Figure 5.21: Polynomial fit (2nd order) of the relation between first and second order.

order contamination that is roughly corrected with the C_1 and C_2 response curves. The extinction correction assumed in all these tests is the CTIO extinction taken from IRAF (onedstds\$ctioextinct.dat). The result does not change significantly assuming a slightly different function to map the first into the second order, that can be obtained by repeating the measurement of the features shown in Fig. 5.20, or by fitting the relation with a slightly different polynomial.

The results of the test on second order contamination show that the method described by Sánchez-Blázquez et al. (2006) can be adapted to our data even if they were obtained with a different observational setup and strategy (i.e., with gratings as dispersing elements and with two different setups to cover the desired range). Nevertheless, there are some important *caveat*. Because the full wavelength range is not covered with simultaneous images, non photometric conditions can affect the red and the blue spectra and change the “shape” of the combined observed spectrum.

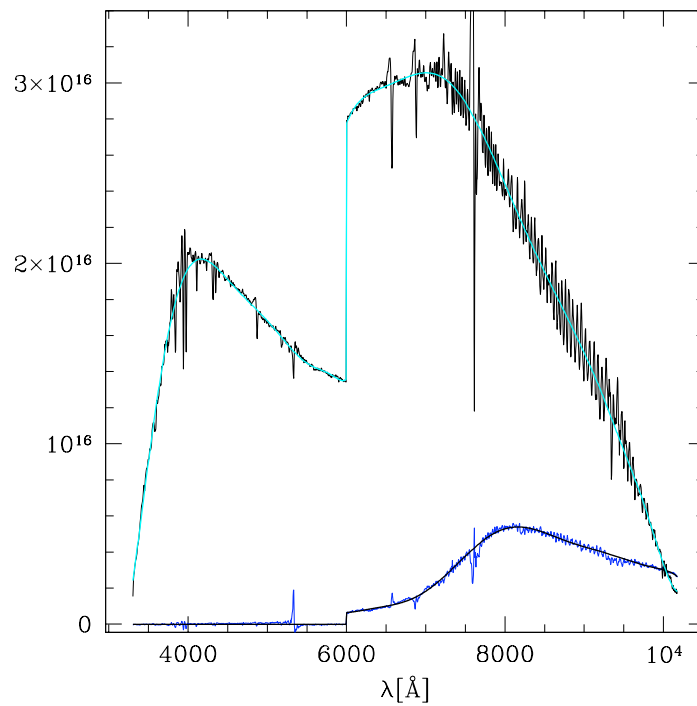


Figure 5.22: C_1 (cyan) and C_2 (blue) response curves. The 6000 \AA discontinuity is the effect of merging the GR11 and GR16 spectra, which are characterized by different zero points and response curves. C_1 and C_2 were fitted with a polynomial to have a smooth trend.

5.6 Instrument Tests: 2nd Order Contamination

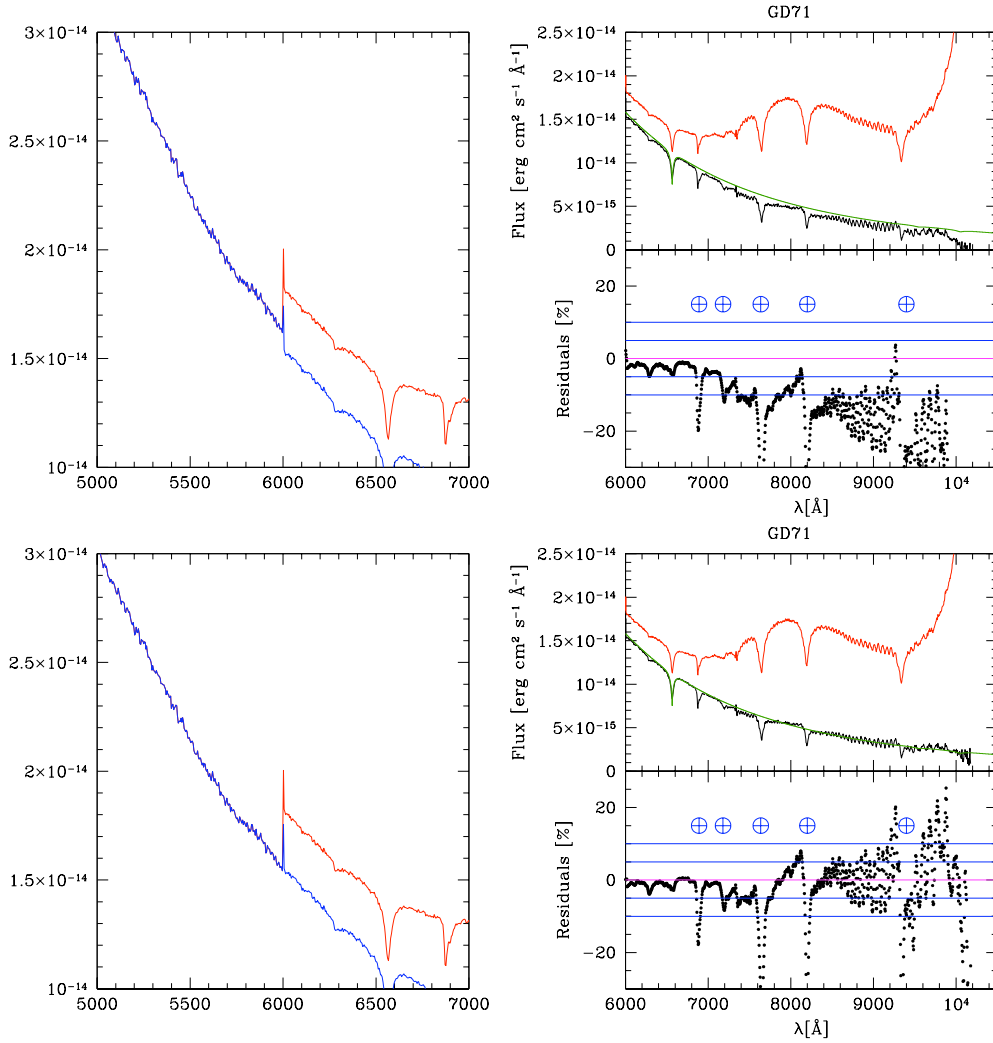


Figure 5.23: *Left panels:* GD71 flux calibrated spectrum (red line: contaminated GR16 spectrum; blue line: GR11 +GR16 spectra, joined at 6000 Å after correction of the second order contamination). *Right panels:* second order contaminated spectrum (red line), corrected spectrum (black line) and CALSPEC spectrum (green line). Residuals of the corrected spectrum with respect to the CALSPEC one are shown (black dots). Telluric lines are marked with \oplus . In the *upper panels* no correction was applied to the exposure times, in the *bottom panels* the exposure time of the GR11 spectrum was scaled (multiplied by a factor 1.05) to match the red spectrum after the second order correction as required if the red spectrum is fainter than expected, for example because of veils, hence overcorrected by the second order contamination correction.

This means that:

- C_1 and C_2 can have wrong zero points;
- the GR11 and GR16 relative fluxes can be wrong, thus affecting the correction even if C_1 and C_2 are correct.

Possible solutions are:

- compute C_1 and C_2 under photometric conditions;
- check the absolute calibration of each GR11 and GR16 while applying the second order correction, i.e., check if the blue and red spectra must be scaled to match and reproduce the correct relative flux (see Fig. 5.23). In this case, while the shape of the spectrum can be recovered, the zero point is not reliable any more and it must be set by comparing synthetic and absolute photometry.

5.7 Instrument Tests: Polarization

Both curved and plane mirrors are known to change to some degree the polarization properties of the incoming light. Their reflectivity may be different for different directions of linear polarization, in a wavelength dependent way (see Breckinridge & Oppenheimer 2004 and references therein). An incoming beam of non-polarized light will be polarized according to this difference of efficiency. This might affect the sensitivity of the whole observing system if the light beam encounters other polarization-sensitive optical elements after reflection. The degree of induced polarization depends on the angle of incidence: the maximum degree of (linear) polarization occurs for an incidence angle which depends on the material, called *polarization angle*. Refractive dispersing elements (grisms, in our case) may also produce some degree of polarization, in principle, and/or have different transmission efficiencies for different polarizations of the incoming light.

5.7.1 Possible sources of polarization

Breckinridge & Oppenheimer (2004) study in detail the polarization properties of reflecting surfaces from the theoretical point of view. They study the behaviour of the percentage difference of reflectivity for light polarized in the directions perpendicular and parallel to the direction of incidence, for different ideal (i.e. perfectly homogeneous) metal coatings and with varying incidence angles. The wavelength range

3 000-11 000 Å is considered. They find that for aluminium coating the maximum absolute difference is 1.6%, and the maximum relative difference along the spectrum is 1%. The properties of silver coating are one order of magnitude better than this; gold is similar to silver for $\lambda \leq 6000$ Å and worse than aluminium for shorter wavelengths. The key point, for our purpose, is that the reflectivity spectrum of the mirrors is different for different directions of linear polarization. Looking at real mirrors in catalogues of commercial and/or professional science-qualified manufacturers, it appears that the differences in reflectivity due to polarization are considered negligible for pure metal coatings, i.e., the response to polarized light is not even mentioned, while in the same catalogues the problem is clearly considered in the case of *protected* metal coatings. For the real cases that we had the opportunity to consider, the difference in reflectivity ranged from 1% to 5%, being relatively grey in shape (to $\sim 1\%$), for incidence angles of 45° .

As for the case of mirrors, we have consulted some catalogues of dispersing prisms and volume phase holographic gratings, looking at commercial and professional quality items. It is manifest from the consulted documentation that one of the objectives of manufacturers is to produce dispersing elements as insensitive to polarization as possible. The result of our brief survey are very similar to those for mirrors: transmission/reflection efficiencies vary by less than 5% across the interesting region of the spectrum in most cases and efficiency variations are “grey” at the $\leq 5\%$ level¹⁹. Another important aspect to be considered arises from the possibility that the incoming star light is *intrinsically* polarized. In such a case, the reflection/transmission of the light beam by a mirror and/or a combination of mirrors and dispersing elements may, in principle, introduce selective light losses. Any polarization induced by the reflection may also produce similar losses in the interaction with other polarization-sensitive optical elements. This seems particularly likely to produce subtle unwanted effects when the reflecting/dispersing elements are rotated in the plane perpendicular to the light path in different ways depending on the telescope pointing. For instance, derotators mounted before spectrographs at Nasmyth foci change the relative position angles between the flat mirror deviating the main light path to the lateral focus and any reflecting/dispersing optical element of the spectrograph. This may lead, for example, to differential efficiency on waves of a given direction of polarization by a grism fed by a flat mirror, to a degree that is dependent on the relative position angles of the elements, that may be different at any pointing. Even if the effect

¹⁹However, it should be noted that there are gratings displaying differences in efficiency as large as 10–30%, in particular in the red part of the spectrum.

were completely wavelength independent, different pointings would lead to different orientations of potentially polarizing optical elements in the plane perpendicular to the beam. The net result would be that the sensitivity of the whole instrumental set-up would depend on the pointing, that is obviously not the same even for the same star observed at different times.

5.7.2 Possible effects of polarization

We can envisage three cases that are exemplified by three different instruments that we have used during our Campaigns:

1. The light beam encounters just one optical element potentially sensitive to polarization, which is the dispersing element (grism) as in the case of CAFOS@CAHA. If the incoming light is not polarized, there is no effect on spectrophotometry. If the incoming light is polarized, there may be a difference in the response depending on the actual orientation of the grism in the plane perpendicular to the direction of the light beam. This orientation will change at any pointing according to the parallactic angle.
2. There is more than one element potentially sensitive to polarization, but their relative orientation in the planes perpendicular to the direction of the incoming beam are fixed, as is the case for the flat mirror feeding the grisms of BFOSC@Cassini. The net result is the same as for the first case above²⁰.
3. There is more than one element potentially sensitive to polarization, and their relative orientation in the planes perpendicular to the direction of the incoming beam changes, depending on the telescope pointing. This is the case of the flat M3 mirror of the TNG that drives the main light path to the Nasmyth focus where it feeds the grism of the DOLoRes spectrograph, mounted on the derotator device. In this case some polarization effect can be induced even on non-polarized incoming light, and the grism may respond slightly differently – in terms of efficiency – to differently polarized light (resulting in a light loss depending on the relative orientation of the two elements).

²⁰It is interesting to note that in the web site: (<http://www.la.eso.org/lasilla/sciops/3p6/efosc/>) of a very similar instrument (EFOSC2@NTT) it is reported, : “Preliminary analysis of instrument polarization shows < 0.1% at field center, and \simeq 0.4% at the edge (07/07/2005)”. This provides a rough quantitative idea of the polarization that must affect BFOSC, as well.

In all considered cases, the light beam encounters a primary and a secondary curved mirror within the telescope: the different set-ups outlined above differ in the number and kind of elements encountered by the light path after reflection by the secondary mirror. Note that as the primary and secondary mirrors are axially symmetric, they should affect the polarization of the incoming light in the same way for any pointing (and are also not expected to introduce any *linear* polarization), hence any effect due to these mirrors should be accounted for by the response function.

The only issue that really matters for our purpose is the amount of variation of sensitivity due to the interaction of a light beam having a reasonable fraction of polarization ($P_\star < 0.10$, i.e. 10%) with an optical element having a reasonable sensitivity to polarization. Let's assume that R_p is the efficiency of an optical element for waves polarized in the direction of incidence (in terms of fraction of reflected/transmitted light to the total amount of incoming light, and R_s is the efficiency for polarization in the perpendicular direction, and be $K = R_p/R_s$ (at a given wavelength). The fractional difference in sensitivity between the case of perfect match between the orientation of the plane of preferential polarization of the light beam and the orientation of the optical element (maximum light loss) and the orientation perpendicular to that (minimum light loss) is:

$$\frac{S}{\Delta S} = \frac{K(0.5 + 0.5P_\star) + (0.5 - 0.5P_\star)}{(0.5 + 0.5P_\star) + K(0.5 - 0.5P_\star)} \quad (5.14)$$

Cases for $R_p - R_s = 5\%$ and $R_p - R_s = 10\%$ are shown in Fig. 5.24. For reasonably high efficiencies and polarizations of the incoming light $\leq 5\%$ the variation of the sensitivity is smaller (by a factor of > 2) than the accuracy we plan to achieve with our spectrophotometry.

Most of our candidate SPSS are relatively bright, nearby and not much extincted white dwarfs. The maximum degree of linear polarization that we can expect in the worst cases is much less than 5%. For typical high efficiency optical elements in the observational set-ups of the type 1 and 2, above, it is very unlikely that polarization can affect the accuracy of spectrophotometry at more than $\simeq 1\%$ level²¹.

²¹While potentially highly polarized sources should be avoided as candidate SPSS (as for instance DP white dwarfs or heavily extincted stars), we stress that there is no observational strategy that can completely avoid the problem.

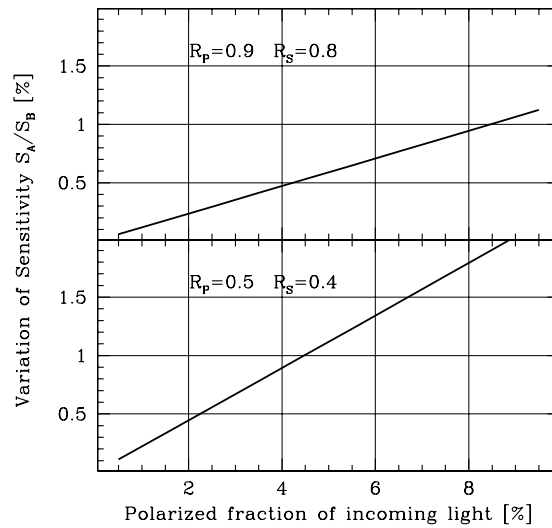
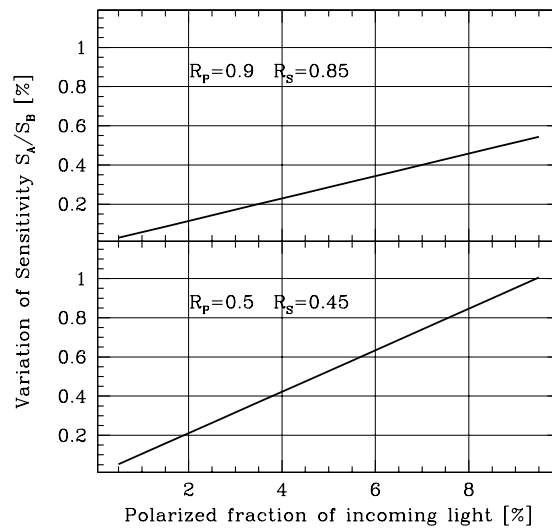


Figure 5.24: Sensitivity variations as a function of the degree of polarization of the incoming light on a polarization sensitive optical element. *Upper panel:* cases in which the efficiency in the two perpendicular direction of polarization differs by 5%. *Bottom panel:* cases in which the efficiency in the two perpendicular direction of polarization differs by 10%.

5.7.3 An experiment with DOLoRes

For case 3, and, in particular, for the case of DOLoRes@TNG, the problem can be studied quantitatively by comparing consecutive spectra of a bright standard²² with different orientation of the spectrograph (i.e., relative orientations of M3 and the grism, in the plane normal to the light beam). The highly polarized star HD 155197²³ was selected to check the combined effect of the source polarization and the internal instrumental polarization at the Nasmyth focus, and its dependency on wavelength. HD 155197 was spectroscopically observed with DOLoRes@TNG, at similar position angles (0, 45, 90 and 135 degrees), with gratings LR-B and LR-R, through the 5" slit, to check the combined effect of the source polarization and the internal instrumental polarization at the Nasmyth focus and its dependency on wavelength. Narrow slit (2") spectra were taken with both gratings at the last position, i.e. 135 deg, and calibration lamps (He for LR-B, Ar for LR-R) were acquired with the same setup at this position.

Star HD 154892²⁴, affected by a low polarization level, was observed with the same instrumental setup used for the highly polarized star, at different position angles (-10, 45, 90 and 135 degrees), to check the effect of the internal instrumental polarization at the Nasmyth focus. The results are shown in Fig. 5.25 and in Fig. 5.26 for the polarized (HD 155197) and non polarized (HD 154892) stars, respectively.

With the exception of two anomalous faint spectra (blue spectrum observed at PA=90°, and red spectrum observed at PA=135°), the spectra of the polarized star observed at different position angles show differences smaller than 1-2%. The polarized star seems to show a slightly different spectral shape in the blue spectrum observed at 135°, but still consistent with the other spectra within 2%. The corresponding red spectrum that has about 1500 Å in common with the blue spectrum, shows a similar slope. The blue spectrum observed at 90° shows a bigger deviation (a few per cent) and it seems peculiar also on the 2D image. On the other hand, the corresponding red spectrum shows a nice flat ratio with respect to the refer-

²²It would be very useful to know what are the polarization properties of the optical elements *actually mounted* on the telescope+instruments we are using for our campaign. We asked the TNG staff for the polarization specifications of all the reflecting and transmitting optical elements of the telescope and DOLoRes. In spite of a thorough search, it turned out that such documentation does not exist or it is not available anymore; hence the only viable approach to quantify the impact of polarization on spectrophotometric observations is through on-sky tests.

²³V=9.20, spectral type: A0, V band polarization: $4.38\% \pm 0.030$, see Turnshek et al. (1990)

²⁴V=8.00, spectral type: F8V, B band polarization: $0.050\% \pm 0.030$, see Turnshek et al. (1990).

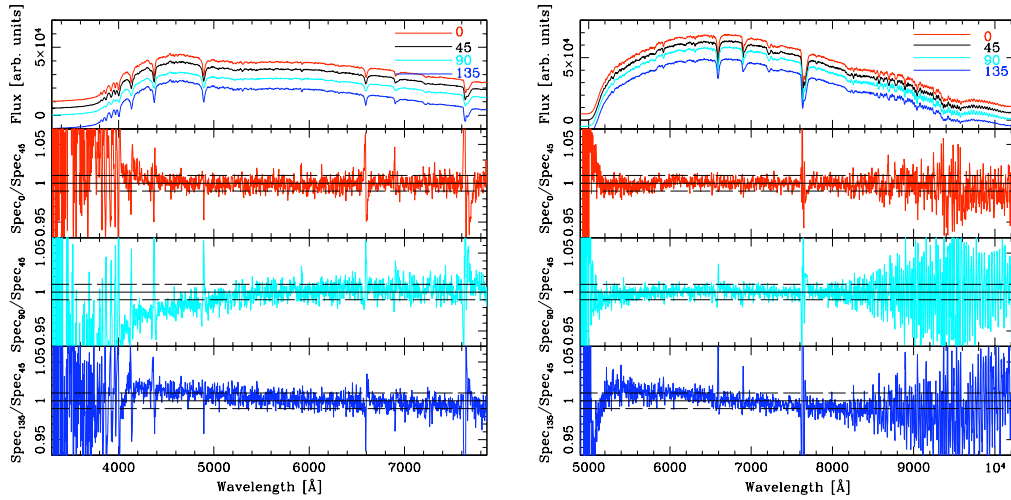


Figure 5.25: Results for the polarized star HD 155197. *Upper panels:* LR-B and LR-R spectra with an arbitrary offset. *Lower panels:* LR-B and LR-R normalized ratio of the spectra taken with the 5" slit at angles 0° , 90° and 135° with respect to the spectrum taken at 45° . The dashed lines show the $\pm 1\%$ limits. Ratios were normalized to 1 using the approximate levels at $\lambda > 4500$ in the blue and $5500 < \lambda < 8500$ in the red.

ence spectrum. Since the faint deviating spectra corresponds to the worst observing conditions²⁵ images and to different position angles (90° in the blue grism and to 135° in the red grism) we suspect that the reason of their anomaly is not due to polarization. In conclusion, the analyzed spectra of the polarized star do not show a clear dependence on the instrumental polarization and additional observations of the same star or of other polarized stars would be useful to check if the deviating spectra (see Fig. 5.25) are an artifact or if the combined effect of the source and instrumental polarization can produce deviations above 1%.

The analysis of the non polarized star spectra observed at different position angles (and better observing conditions) does not show any significant correlation of the spectral shape with the angle. The overall shape of the spectra agree with one another within 1% but at the blue edge (below 4000 \AA), which is always a noisy spectral range, and above 8000 \AA , as expected because of fringing. In conclusion, the good overall match of the spectra suggests that the instrumental polarization effects are negligible with respect to the position angle and wavelength (i.e. the instrumental

²⁵The FWHM was 1.5–2.5 times larger than other images.

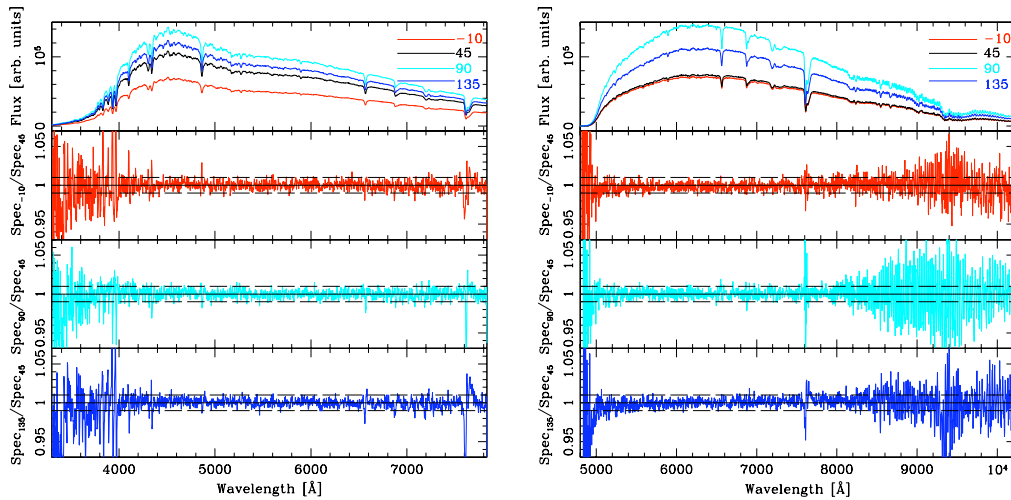


Figure 5.26: Results for the non polarized star HD 154892.. *Upper panels:* LR-B and LR-R spectra, no arbitrary offset applied, the spectra do not overlap because of variable sky transparency (clouds). *Lower panels:* LR-B and LRR normalized ratio of the spectra taken with the 5 arcsec slit at angles -10° , 90° and 135° with respect to the spectrum taken at 45° . The dashed lines show the $\pm 1\%$ limits. Ratios have been normalized to 1 using the approximate levels at $4200 < \lambda < 7400$ in the blue and $5200 < \lambda < 10000$ in the red.

polarization, if any, is quite constant). However, we plan to repeat the test on the polarized star in better observing conditions to be certain of this suspicion.

5.8 Photometricity and Extinction

Up to now we focused on relative photometry and spectroscopy procedures so the protocol for the absolute spectrophotometry has not yet been defined in details. Nevertheless, the methodologies involved in determining the photometricity of one night are already well known (see, for example, Bellazzini 2007b and references therein). Summarizing:

- for photometry: the observation of standard star fields (for example Landolt fields, Landolt 1992) acquired at different air masses and spanning the whole night allows us to compute the extinction coefficient of the night (see Fig. 5.27) and also the color terms and zero points which, in case of photometric nights, are always the same for each telescope/instrument/CCD combination;

- for spectroscopy: the observation of the same star at different air masses during the night allows us to compute the extinction curve of the night (see Fig. 5.28).

A night can be considered *photometric* if the extinction coefficients (or the extinction curve) do not vary significantly (less than 1%) along the night.

As an example, in Fig. 5.28 we show an extinction curve computed using spectroscopic data acquired in a non-photometric (but relatively stable) night at Calar Alto, in comparison with the extinction curves for summer and winter provided by Sánchez et al. (2007). Our result agrees with Sánchez et al. (2007) summer red curve if shifted by 0.27 mag. This example shows that, provided that we apply an appropriate shift to account for the non-photometric conditions of the night, the overall shape of our extinction curve is quite similar to the reference one except at the blue edge, below 3500 Å (that can be probably reduced with illumination correction) and at the red edge (affected by noise, fringing, telluric absorptions). We point out that if a rigid shift of the curve is enough to account for the non photometric conditions it means that transparency variations are grey (not color dependent) and hence one photometric band is enough to scale the spectra through synthetic photometry.

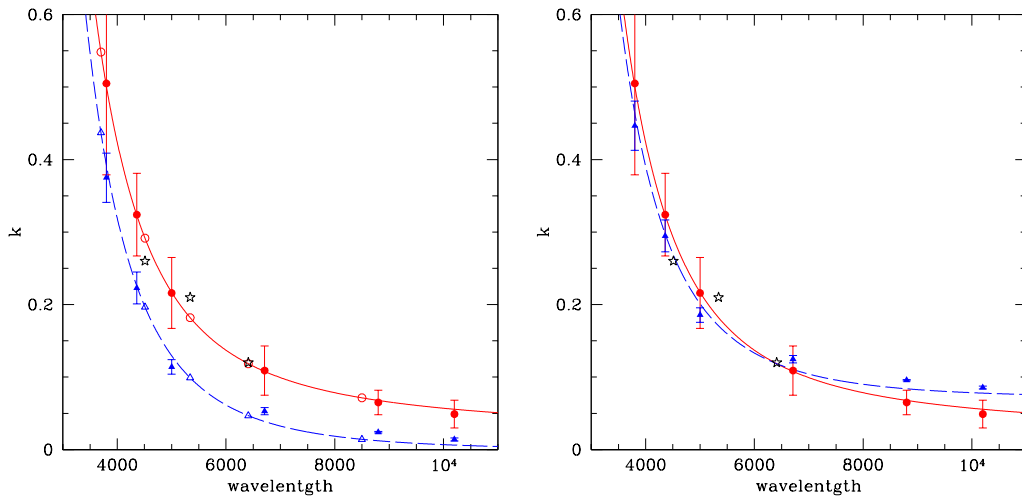


Figure 5.27: *Left panel:* Calar Alto extinction curve for summer (solid line) and winter (dashed line) and extinction coefficients by Sánchez et al. (2007). Filled dots are the values for the 8 narrow-band filters mounted at EXCALIBUR (a robotic extinction monitor able to perform quasi-simultaneous photometric observations covering the wavelength range between 3400 Å and 10200 Å). Empty dots are the extinction coefficient interpolated to U, B, V, R, I filters. Starred dots are the preliminary extinction coefficients measured from our data. *Right panel:* as left panel but, now the winter extinction curve has been shifted to better show the different shape with respect to the summer extinction curve.

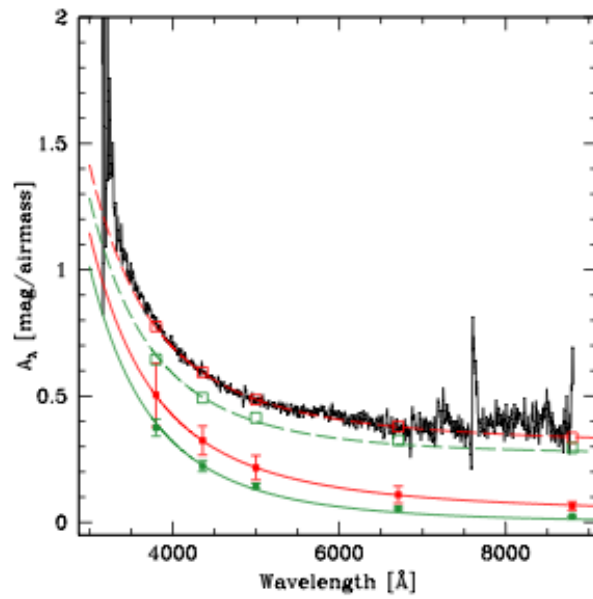


Figure 5.28: Comparison between the extinction curve computed in a relatively stable night at Calar Alto (black solid line) and the curves provided by Sánchez et al. (2007) (green and red solid lines). The data from Sánchez et al. (2007) are shown with filled dots. Our result agrees with Sánchez et al. (2007) summer curve if shifted by 0.27 mag (red dashed line, empty dots). The winter green curve requires a larger shift and does not fit as well our curve.

6

The Pre-reduction Protocol for photometric observations

In order to maintain the maximum homogeneity possible in the data quality and treatment, I built a protocol dedicated to the pre-reduction of photometric data obtained during both the auxiliary (absolute and relative photometry) and main (mainly spectroscopy, but also absolute photometry) campaigns. With the term “pre-reduction” I mean, in this context, the removal of the instrument characteristics (dark, bias, flat-field, bad-pixel mask, fringing) from the 2-d scientific photometric frames. While the data reduction methods are fairly standard, care must be taken in considering the characteristics of each instrument as determined during the Instrument Familiarization Plan (see Chapter 5), to extract the highest possible quality from each observation, since our goal is to perform spectrophotometry with a very high precision and accuracy (a few percent in flux at most, relative to Vega).

I describe here the procedure to be followed for the data pre-reduction of our imaging campaigns (see Chapter 4). The *imaging pre-reduction protocol* is centered around one checklist (Table 6.1) which summarize the procedure on a step by step basis. Since we have to handle a huge number of frames¹ in a homogeneous manner, I have built semi-automated pipelines for each pre-reduction step which allow to quicken the whole procedure and to monitor the quality of the images involved in order to meet the precision required. These pipelines² and the definition of all the Quality Control (QC) parameters used during the pre-reduction procedure are available in Wiki-Bo³.

Even if the reduction steps are similar for all the instruments used in our campaigns,

¹We expect $\simeq 400$ observing nights and of the order of 100 000 frames to complete the survey.

²And all macros called by the pipeline.

³http://yoda.bo.astro.it/wiki/index.php/IFP_QC_Parameters

The Pre-reduction Protocol for photometric observations

in some cases particular attention or special instructions are required. These cases are extensively described in details in Marinoni et al. (2011a).

Table 6.1: Imaging pre-reduction steps

Operation	Description	Sections
Pre-Reduction		6.1
	Overscan and Bias Frames	6.2
	Dark Frames	6.3
	Flat Field Frames	6.4
	Bad pixel mask	6.5
	Fringing mask	6.6
	2d pre-reductions	6.7
Single Frames Quality Assessment	Bias	6.2.1
	Flat-field	6.4.1
Master Frames Quality Assessment	Bias	6.2.2
	Dark	6.3.1
	Flat-field	6.4.2
Imaging Quality Assessment	2D pre-reduced frames	Chapter 7

6.1 Imaging Pre-reduction procedures

The primary aim of CCD data pre-reductions is to remove any effect due to the detector and the telescope, the so called “instrumental signature”. There are many instrumental patterns that appear in astronomical images. The most common are additive or multiplicative patterns and are removed from the observations using proper templates. The pattern template is generally derived from calibration frames or directly from sets of scientific data. Additive effects, such as bias or dark, are corrected by subtracting the corresponding template from the scientific images (by applying, where necessary, a numerical scaling derived from the exposure times). Multiplicative effects, such as flat field, are removed dividing the scientific frames by an appropriate template. However, some patterns vary in amplitude from exposure to exposure. The variation is caused by differences in the field of view. An example is CCD fringing because the fringing varies with the strength of the atmospheric emission lines. Patterns like this are removed by scaling the pattern amplitude to

match a data image and then subtracting it from the data image. The cosmetic defects of CCDs can be easily removed with the application of an appropriate bad-pixel mask. Bad pixels are replaced by linear interpolation along lines or columns using the nearest good pixels.

The main concepts involved in removing the instrumental signature are listed below:

- overscan (if possible) and bias subtraction;
- dark correction (if needed);
- flat field correction;
- bad pixel mask (if needed);
- fringing correction (if needed).

For each type of calibration frame, a set of QC parameters are defined in order to extract the highest possible quality from our data. All procedures are based on the Image Reduction and Analysis Facility (IRAF⁴).

6.2 Bias Frames

One of the best ways to know the condition of a CCD is to carefully examine the bias frames. While reading a CCD, the Analogue-to-Digital Converter (ADC) samples the charge accumulated in each pixel and returns a digital value. This value is proportional to the actual number of electrons detected in the pixel and is measured in Analogue-to-Digital Units (ADUs). The relation between ADU and the number of detected photons (charge) is a scale factor known as the gain (measured in e^-/ADU). The bias is an offset, preset electronically, to ensure that the Analogue-to-Digital Converter (ADC) always receives a positive value and that it is operating in a linear regime as much as possible. The offset for each exposure given by the bias level has to be subtracted before further reduction.

The bias frame may be modelled as $A+F(x_i, y_i)$, where:

- F , the pixel-to-pixel structure of the frame, is time-invariant (if there are no particular problems). F can be determined by acquiring many exposures of zero seconds without opening the shutter, i.e., by simply reading out the CCD.

⁴<http://iraf.noao.edu/>: IRAF is distributed by the National Optical Astronomy Observatories (NOAO), which are operated by the Association of Universities for Research in Astronomy (AURA), Inc., under cooperative agreement with the National Science Foundation.

$F(x_i, y_i)$ is the so-called “2-d structure of the *masterbias*”. The *masterbias* takes into account the possible dependence of the bias on the pixel position and it can be defined by building a median stack of these frames, with intrinsic uncertainties due to RON. We usually acquire at least 10 bias frames per night in order to build the *masterbias*. This allows us to get a better statistics and to exclude other spurious effects (as, for example, cosmic rays).

- A , the overall bias level, can slightly change during the night because of external factors (for example, temperature variations). The level of the bias for each exposure is best determined by the *overscan* region, when available (it is not always the case). The *overscan* data are acquired by continuing to readout the CCD past its real physical extent: the result is an oversized array with a strip of signal free pixels (because the *overscan* provides a measure of the electronic bias level that physically indicates zero photon counted) from which A can be measured for a particular exposure. If the *overscan* strip is not present, the *masterbias* implicitly contains also A .

When an *overscan* section is available, all images can be first corrected for *overscan*: this way, if the bias level of a scientific imaged has varied with respect to the *masterbias*⁵ built with frames taken hours before or after, the images can be more accurately corrected. The *overscan* correction only will follow the bias level variation with time but it will not account for possible 2-d structures of the bias. In fact when correcting for *overscan*, the *overscan* region is fitted along a row (or a column, depending on the readout direction of the CCD) and the fit is subtracted from each row (column) in the frame. In case of a zero order fit, the correction is a simple constant. In the other cases it will be a one-dimensional array. Usually a low order cubic spline (order 3-5) is sufficient.

By careful examination of the bias frames, *overscan* sections⁶, best fitting order of the *overscan*, and “good data” sections were determined for all the instrument used, which will ensure homogeneous data treatment (see Table 6.2).

If present, the *overscan* section will appear as a section of a few tens of pixels at the edge of the frame and it will have less counts with respect to the rest of the image (see right panel of Fig. 6.1). In addition, often in a frame, the first (or last) lines

⁵Obviously, also the single bias frames have to be corrected for *overscan* before creating the *masterbias*.

⁶If the *overscan* region does not appear so evident in bias frames, also a flat field frame can be used to check for the *overscan* region. In addition, if vignetting is present, a better determination of trim section is allowed using one flat.

and the first (or last) columns are deviant (see left panel of Fig. 6.1) and must be removed: this allows us to define the “good data” sections” for each CCD.

Table 6.2: CCD sections for imaging pre-reduction

Instrument	Overscan Section	Best fitting order for the overscan	Good Data Section for imaging
BFOSC@Cassini	no overscan	-	[1:1335,1:1300] (EEV old)
			[7:1340,1:1300] (EEV new)
CAFOS@CAHA2.2	no overscan	-	[10:1120,10:1120] for run P003
			[10:1014,10:1014] for all runs M (*)
DoLoRes@TNG	[15:2085,2065:2085]	5	[25:2089,25:2045] until M009a
			[55:2085,25:2045] from M009b
EFOSC2@NTT	no overscan	-	[20:2000,10:2000]
LaRuca@SPM	[1020:1070,1:1024] (SITE1)	3	[15:1013,15:1024] (SITE1)
	[2110:2150,1:2048](Marconi e2vm)	5	[60:2095, 5:2045] (Marconi e2vm)
ROSS@REM	no overscan	-	[*,*]

Because, for some instruments, we use different CCD sections (or CCD binning) for imaging (for example a square, bin1x1) and spectroscopy (for example a rectangle, bin2x2), the trimming values corresponding to the “good data” sections will change accordingly. In the pipeline, the fits headers are altered by adding the bias and trim sections with command lines similar to:

```
hedit @bias.list trimsec [15:1013,15:1024] add+ verify-
hedit @bias.list biassec [1020:1070,1:1024] add+ verify-
```

This way, the `ccdproc` command lines are independent of the specific instrument being processed because the correct sections are embedded in the fits header, and one single `ccdproc` command specifying `biassec="image"` and `trimsec="image"` can be used for all frames.

6.2.1 Single frame Quality Assessment

Image statistics (median and standard deviation) can be obtained with the IRAF task `imstat` for all raw bias frames in the regions defined by the TRIMSEC and BIASSEC values. This allows us to compute the median level and sigma of both the overscan (if present) and the good region of the CCD. The median and sigma of the bias and overscan regions of the CCD are the four basic QC parameters for bias frames. Three of these are used in the basic QC plot for single bias frames (see,

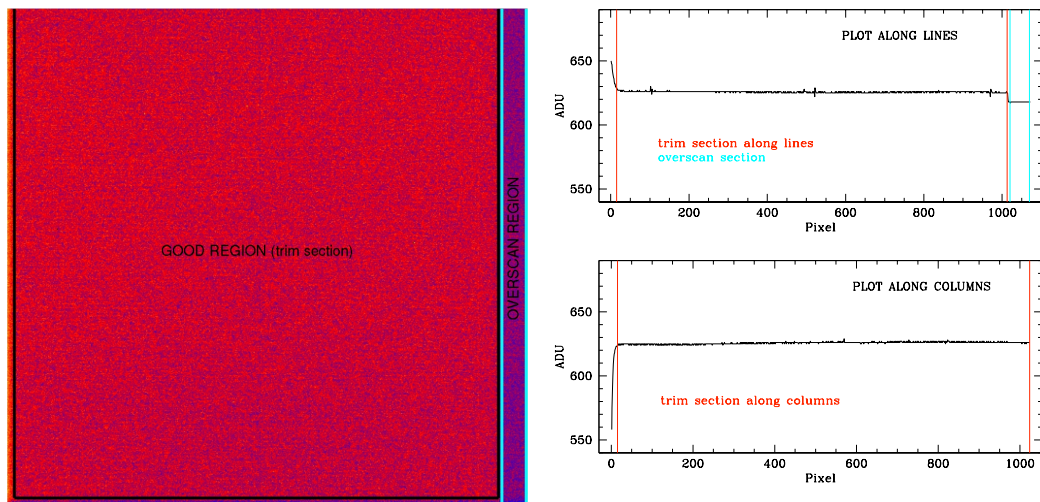


Figure 6.1: *Left panel:* raw bias taken with LaRuca@SPM on April 22 2008 . The overscan region (area contained within cyan lines) and the good part of CCD (red area contained within black lines) are shown. *Right panel:* Structure plots. The X direction structure is obtained by collapsing and averaging the raw bias along rows (*top panel*). The Y structure is obtained in the same way along columns (*bottom panel*). The bias “good section” has virtually no structure in both X and Y, but the first 15 rows and columns show an opposite structure: the first 15 rows decrease below the average level value of about 75 ADU while the first 15 columns increase above the average level value of about 25 ADU, so they have to be trimmed. In the top panel the small structures at pixel 103, 520 and 970 are due to bad columns.

for example, Fig. 6.2). In a set of consecutive bias we can suppose that the CCD temperature remains constant and the possible deviant behavior of one bias can be easily recognized. Obviously, this “bad” bias shall not be used for the construction of masterbias (see, for example, figure 6.3).

When the overscan strip is present, each “good” bias is corrected for the overscan and trimmed in order to remove the edges of the frames. The IRAF task `ccdproc` can be used to perform the correction. For example:

```
ccdproc images=@bias.list output=@bias2.list ccdtype="" noproc-
overscan+ trim+ zerocor- darkcor- flatcor- fixpix-
fringec- illumcor- interac- readaxi="line"
biassec="image" trimsec="image"
function=spline3 order=3
```

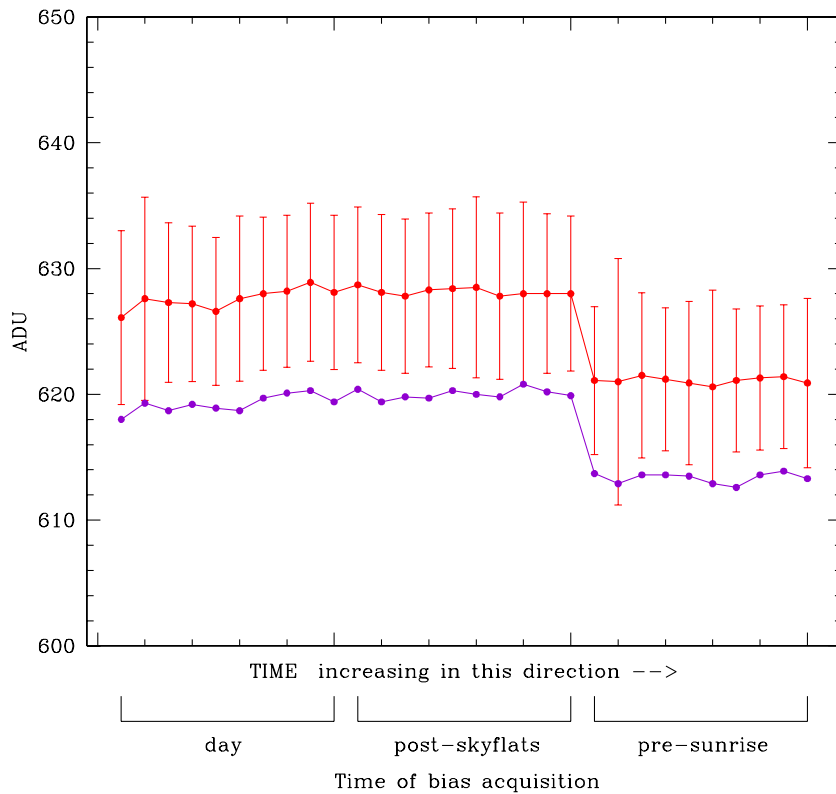


Figure 6.2: Statistics for the three sets of bias acquired with LaRuca@SPM on April 22 2008. Red dots and lines correspond to the median value and standard deviation of the “good region” of CCD. Violet dots and lines are the median of the overscan section. The bottom labels show the time of acquisition of the bias frames. Differences in counts between bias frames acquired immediately after twilight and before sunrise are due to temperature variations of CCD during the night.

Similar command line instructions are included in my pipeline, allowing for a homogeneous data reduction. The `biassec` and `trimsec` values are specified in the image header, but the user can also specify the section using `[x1:x2,y1:y2]`. The actual overscan and trimming sections and best order fit for each instrument we use are specified in Table 6.2.

Once each bias is corrected for overscan and trimmed, my pipeline again performs the Quality Assessment (QA) step on all these frames in order to investigate if the

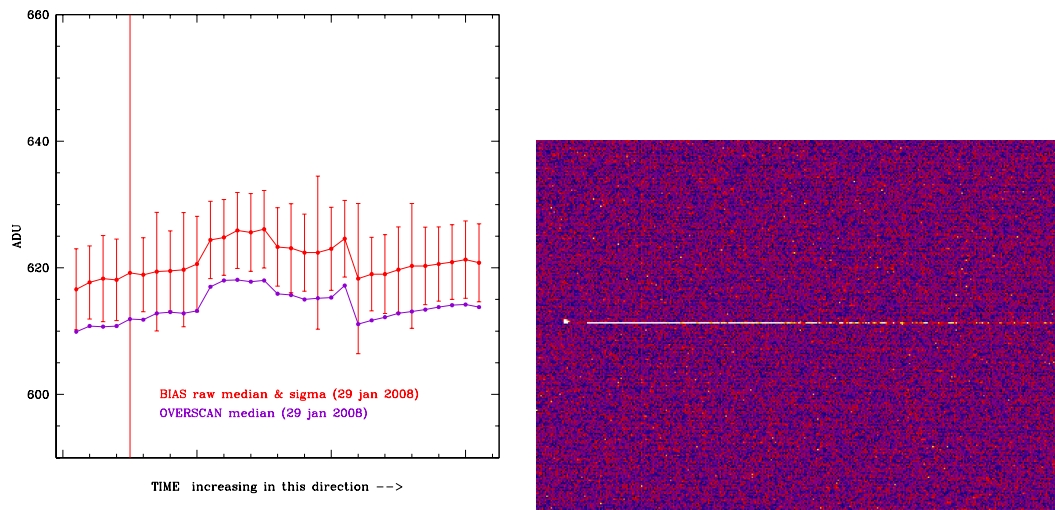


Figure 6.3: *Left panel* Statistics for the bias frames acquired with LaRuca@SPM on January 29 2008. Red dots and lines correspond to the median value and standard deviation of the “good region” of CCD. Violet dots and lines are the median of the overscan section. We can note the deviant point with a huge error bar corresponding to frame bias 4005b.fits and we can say immediately that this bias must have some problem. *Right panel* Section [460:822,672:927] of the bias 4005b.fits shows part of the cause of its high standard deviation: obviously this bias must be excluded from the procedure for building the masterbias.

correction for overscan worked properly. If there are deviant points the corresponding biases have to be excluded from the next steps of reduction. Obviously, this step can not be performed if the overscan section is not present (for example, for BFOSC@Cassini data). In this case, after performing the quality check on all raw biases and excluding those with some problems, the masterbias can be created.

6.2.2 Masterbias production and Quality Assessment

Once each single bias frame are quality checked, trimmed and overscan corrected (if possible), it can be used to create a *masterbias*. This can be done with the IRAF task `zerocombine`, setting "median" as combine mode and "minmax" as reject mode⁷. For example:

⁷The parameters for tuning the "minmax" rejection mode are set to the default values.

```
zerocombine input=@bias2.list
             output=masterbias.fits
             combine=median reject=minmax ccdtype="" process-
             rdnoise="" gain="" snoise=""
```

When masterbias frames for all nights in one run are built, their stability can be checked using the IRAF task `imstat` to make statistics (median and standard deviation) for all masterbias frames. Similarly to the QA of single bias frames, the median and standard deviation of the masterbias frames are the two main QC parameters used to produce a QC plot similar to the one shown in Fig. 6.4. This plot allows to visually assess if the nightly masterbias frames were sufficiently stable during the whole run.

The stability of the two-dimensional structure of masterbias produced during one run can be visually checked with another automatically produced QC plot, shown in Fig. 6.5. To produce the plot, five areas on the surface of each masterbias were defined for each instrument, one for each corner and one for the center of each image. The ratio between the median value of each corner and the median value of the center (measured using `imstat`) is the QC parameter which allows us to perform this check (see Fig. 6.5). The surface shape of the masterbias can be easily examined also by making a 3D plot (see, for example, Fig. 6.6).

It is important to know the stability of the masterbias frames, especially when no overscan strip is available to correct each scientific images for the appropriate bias level. In fact, if the masterbias stability is good, the lack of bias during a specific night is not a big problem, and the masterbias produced in the previous or the following night can be used in the pre-reduction process. On the other hand, if the masterbias stability is not good (within 1%), then the daily acquisition of bias frames becomes mandatory, because the masterbias produced using bias acquired in a specific night can not be used to reduce data acquired in other nights of the same run.

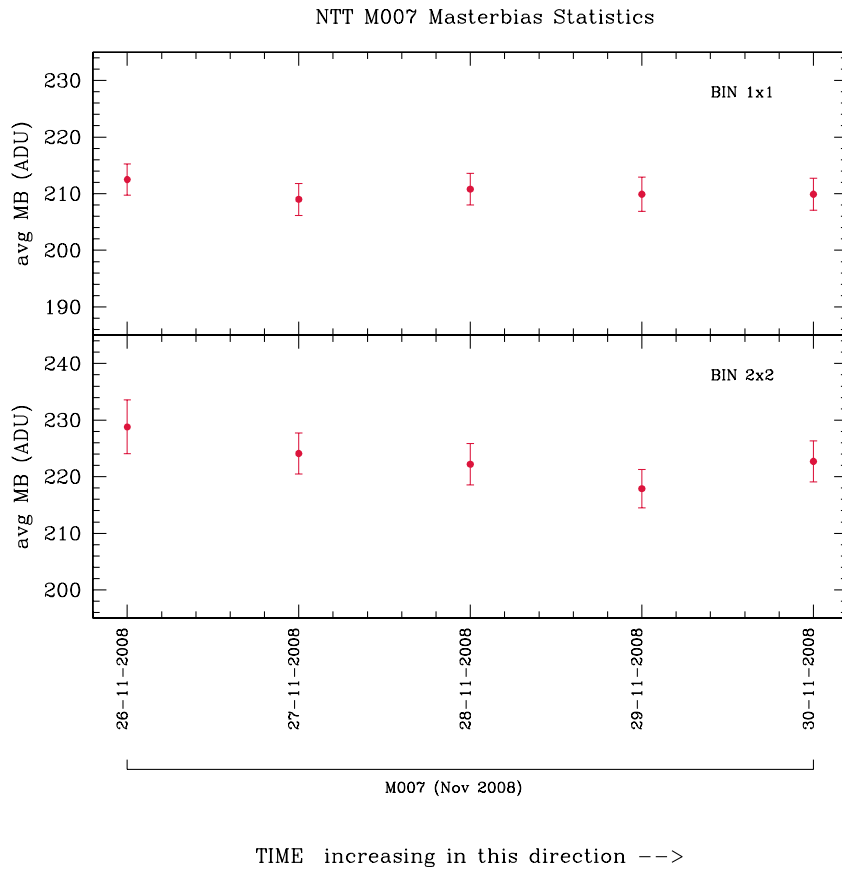


Figure 6.4: Statistics of all masterbias frames produced using the data acquired with EFOSC2@NTT during the run M007. The overscan is defined “inadequate for bias subtraction” in the ESO instrument manual. This is confirmed by our tests (see Marinoni et al. 2011a), hence the overscan correction is not performed for EFOSC2 data.

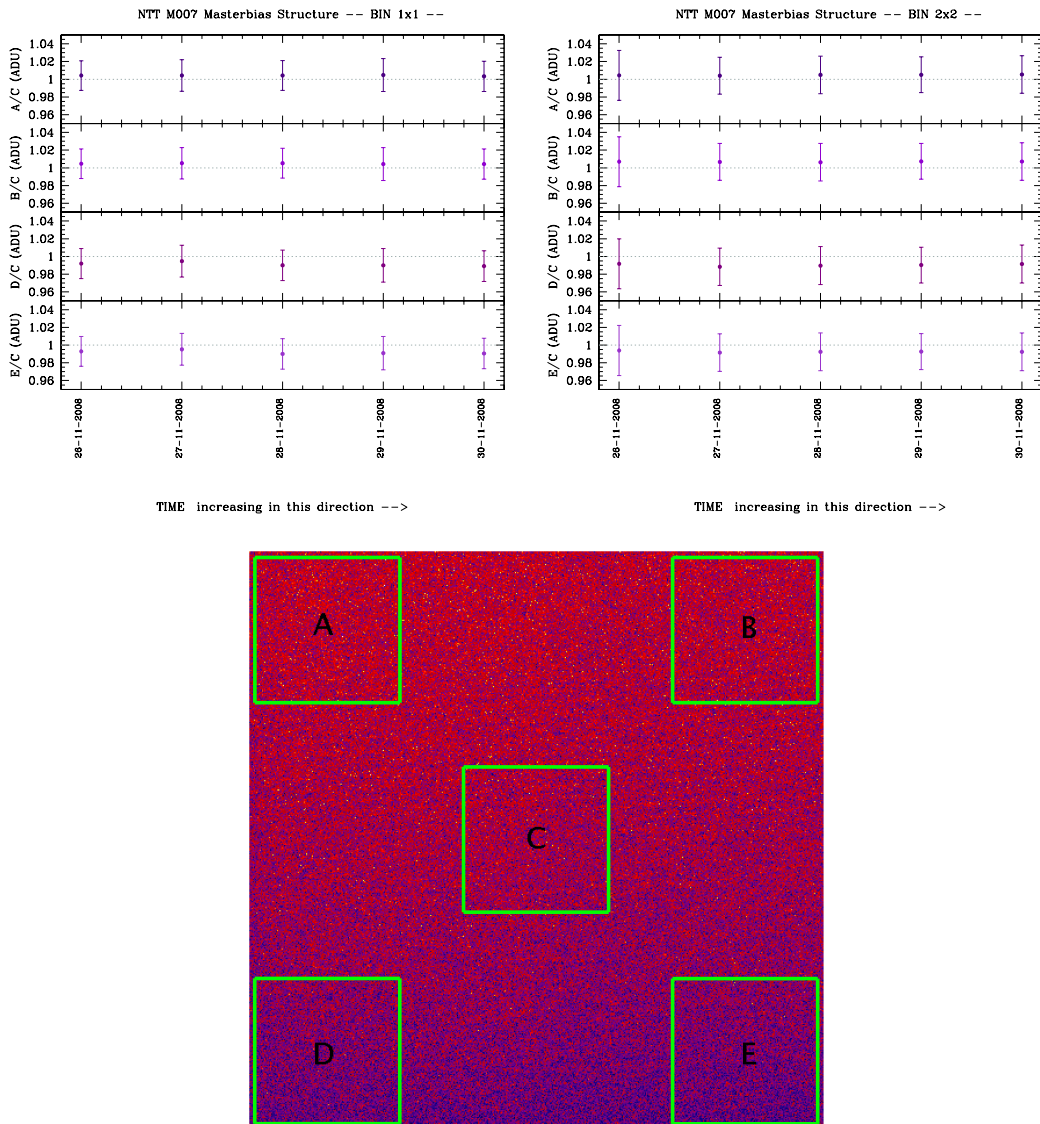


Figure 6.5: In the *upper panels*, check of the two-dimensional structure for the masterbias produced using the data acquired with EFOSC2@NTT during run M007. In the *lower panel*: location of the areas A, B, C, D and E involved in the structure stability test.

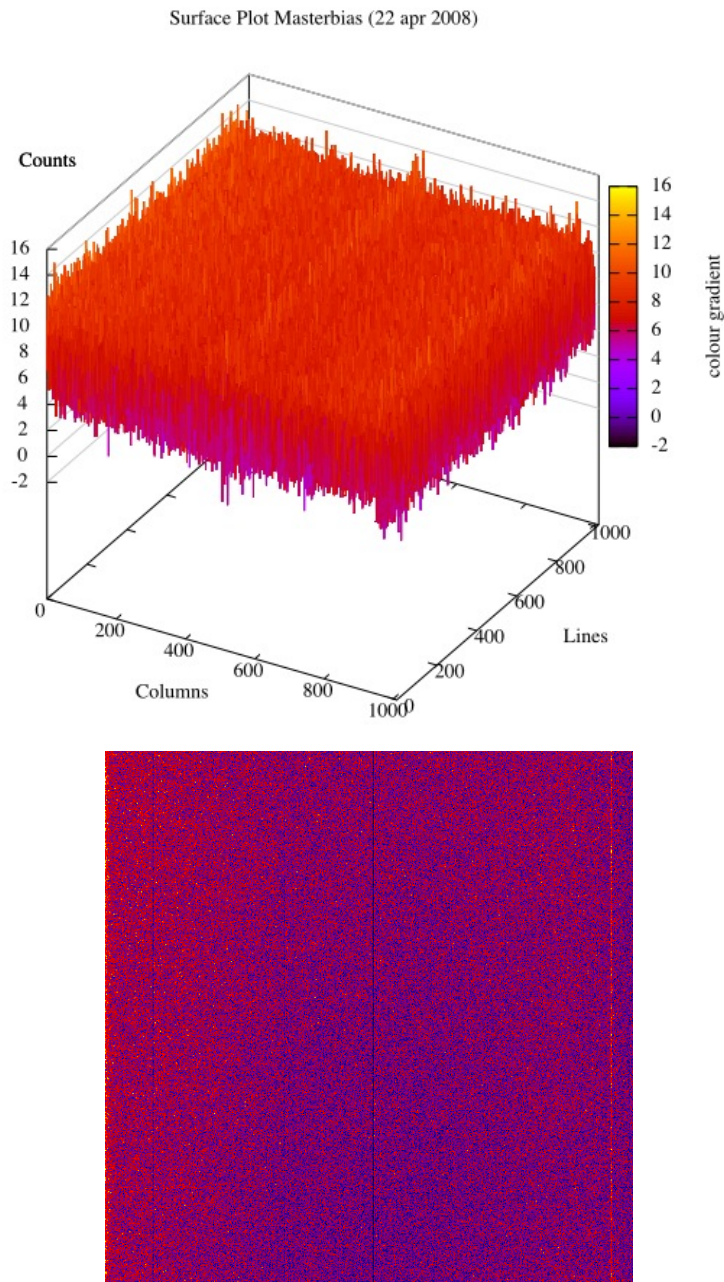


Figure 6.6: 3D plot (*upper panel*) and 2D plot (*bottom panel*) of the masterbias produced using the bias frames acquired with LaRuca@SPM on April 22 2008 . The surface of the masterbias appears very smooth and regular and no pattern is present. We can see again the dead and hot columns at pixels 103, 520 and 970 as in Fig.6.3.

6.3 Dark Frames

Dark correction is the subtraction of the electron counts which accumulate in each pixel due to thermal noise. The reduction of dark current is the main reason why all astronomical CCDs are cooled to liquid nitrogen temperatures. Most modern CCDs only produce a few ADU counts per pixel per hour, so this effect can generally be ignored⁸. In our case, since our goal is a very high precision, we checked if a dark correction was needed in the pre-reduction procedure for our instruments. If a dark correction is needed, it can be applied with `ccdproc` by setting `darkcor+` and providing the name of the masterdark frame with `dark=masterdark.fits` in the `ccdproc` command. The masterdark frame is the result of several dark frames acquired with the same exposure time and combined using the IRAF task `darkcombine`, similarly to bias frames. Before combining, dark frames must be overscan (if possible) and bias corrected and trimmed, as all images.

For example:

```
ccdproc images=@dark.list output=@dark2.list ccdtype="" noproc-
overscan+ trim+ fixpix- zerocor+ darkcor- flatcor-
illumcor- interac- readaxi="line" biassec="image"
trimsec="image" function=spline3 order=3
zero=masterbias.fits
```

```
darkcombine input=@dark2.list
output=m.V006-SPM-LaRuca_20081109_DARK_XXX.fits
combine=median reject=minmax ccdtype="" process-
rdnoise="" gain="" snoise=""
```

When applied, the masterdark is automatically scaled to the correct exposure time by `ccdproc`.

6.3.1 Masterdark Quality Assessment

To check how the dark currents grow with time, the mean value of each masterdark frame is plotted against exposure time (see. for example, Fig. 6.7). In this case, each masterdark frame is built without correcting for masterbias: this way, a linear fit can

⁸This is not the case of ROSS@REM: the CCD is cooled by a Peltier system, therefore dark frames are taken periodically by the REM team and they of course already include the bias level and pattern (bias frames are not acquired).

The Pre-reduction Protocol for photometric observations

be performed, extrapolated at zero exposure time, and this value can be compared with the measured bias level from masterbias.

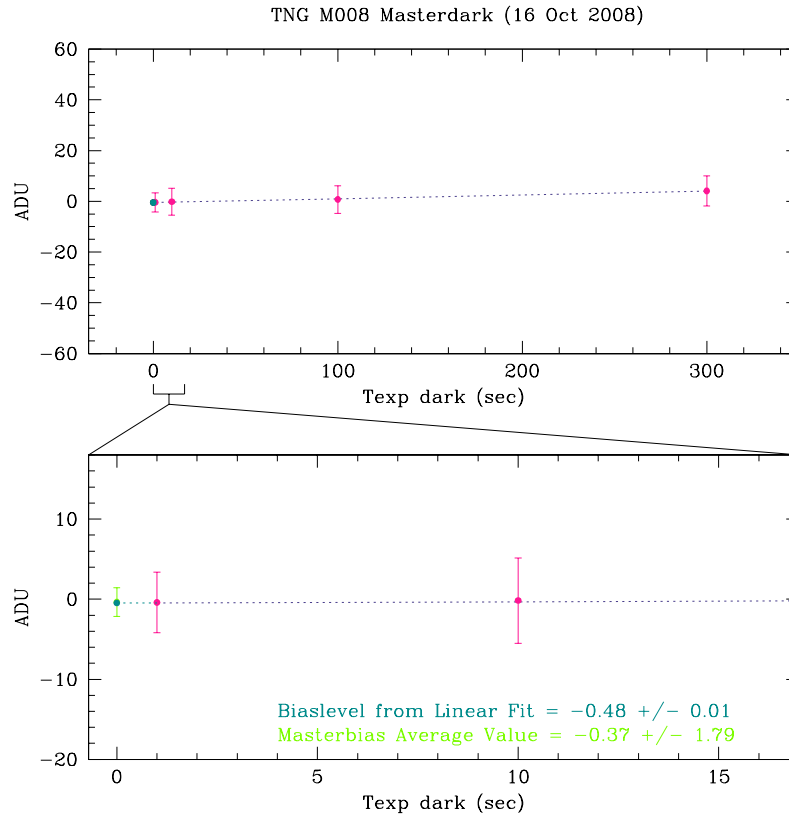


Figure 6.7: Quality Control on masterdark frames of run M-008@TNG. The mean value of each masterdark is plotted against the exposure time. In the *bottom panel* a zoom is shown in order to compare the bias level extrapolated from the linear fit with that measured directly from the masterbias.

The masterbias has to be subtracted from the masterdark with the longest exposure time in order to see if the dark correction is required. If the mean of the resulting image is negligible compared to its standard deviation, we can avoid the dark correction⁹. Our tests indicates that a dark corrections is not needed in our data, except for data acquired with ROSS@REM.

⁹If the dark correction is negligible for the longest exposure time, it will be negligible also for lower exposure times.

6.4 Flat Fielding

After bias subtraction (and dark correction, if necessary) the data values are directly related to the number of photons detected by each CCD pixel. But different pixel can be characterized by a different sensitivity. The flat field correction accounts for the non uniform CCD response to the incident light that can show variations on all scales, from the whole CCD to pixel-to-pixel scale.

The basic idea of flat field correction is to divide the data by a *sensitivity map* (called *masterflat*) created from calibration exposures. The effect of dust on the filters or on the detector, the vignetting and other variations in the throughput of the instrument optics are also corrected by flat fielding. In imaging, an evenly illuminated image is used as the flat field. It can be obtained using a uniformly illuminated screen inside the telescope dome (domeflat) or, better, the sky at twilight or sunrise (skyflat). Skyflats are usually preferred to domeflats. This is because they ensure both a much uniform illuminated field of view and, most important, the solar SED is more similar to the star light than an artificial lamp¹⁰.

Since the detector efficiency changes with wavelength, flats are needed in all the bands used for scientific frames. *Masterflats* are built by averaging (or making a median of) a number of flats in order to have better statistics, to reduce the noise and to get rid of cosmic ray hits. Flat fields are always acquired using the same instrumental setup adopted for observing scientific objects.

6.4.1 Single frame Quality Assessment

First of all, my pipeline trims and corrects both dome and skyflats for bias¹¹ and overscan (if possible), using the IRAF task `ccdproc`:

```
ccdproc images=@flat.list output=@flat2.list ccdtype="" noproc-
      overscan+ trim+ fixpix- zerocor+ darkcor- flatcor-
      illumcor- interac- readaxi="line" biassec="image"
      trimsec="image" function=spline3 order=3
      zero=masterbias.fits
```

Obviously, also for flats, each image header has to be previously updated with the correct values for `BIASSEC` and `TRIMSEC` using `hedit` (see Section 6.2).

¹⁰Another important characteristic of skyflats is that they are focused at infinity, as the scientific frames.

¹¹see Section 6.2.2 for the masterbias production

Once all single flat is bias and overscan (if possible) corrected and trimmed, the pipeline automatically check if there is some anomalous flat which must not be used in the masterflat creation using the IRAF task `imstat` in order to calculate the median level, the standard deviation and the maximum value of each flat. These three QC parameters are used to automatically build a QC plot similar to the one shown in Fig. 6.8, which allow us to visually check if the available photometric flat fields have suitable count levels. Only flats with median between 15 000 and 50 000 ADU are used to build masterflats¹², and this is valid for all our chosen instruments.

6.4.2 Masterflat Production and Quality Assessment

Once each single flat field has passed the QA, it can be used to produce the masterflat of the corresponding filter. Domeflats and skyflats (when available) are combined separately by the pipeline to produce a dome-masterflat and a sky-masterflat respectively, using the IRAF task `flatcombine`. For example:

```
flatcombine input=@domeSKYB.list
             output=m.V011-Cassini-BFOSC_20090525_SKY_B.fits
             combine=median reject=minmax ccdtype="" process-
             rdnoise="" gain="" snoise=""
```

An outlier rejection is necessary to get rid of cosmics and spurious structures (domeflats) but also stars and galaxies (skyflats). A median type of combination with `minmax`¹³ rejection was found to give the best results for all instruments.

When masterflats (dome or sky) for all nights of one run are built, their stability can be checked. Three stability QC tests can be automatically performed on masterflat frames for each run, using template macros, appropriate for each telescope/instrument combination:

- *outside VS center* plot: provides information on the shape of each masterflat.
- *Large Scale Variability* plot: provides information on the “global” variation of the masterflats shape assuming the variation uniformly distributed all over the pixels (in comparison with a reference flat)
- *9 areas* plot: provides information on “where” and “how much” is the variation of the flat shape in comparison with a reference flat

¹²this way, I can avoid all possible non-linearity effects, see Section 5.3)

¹³The parameters for tuning the "minmax" rejection mode are set to the default values

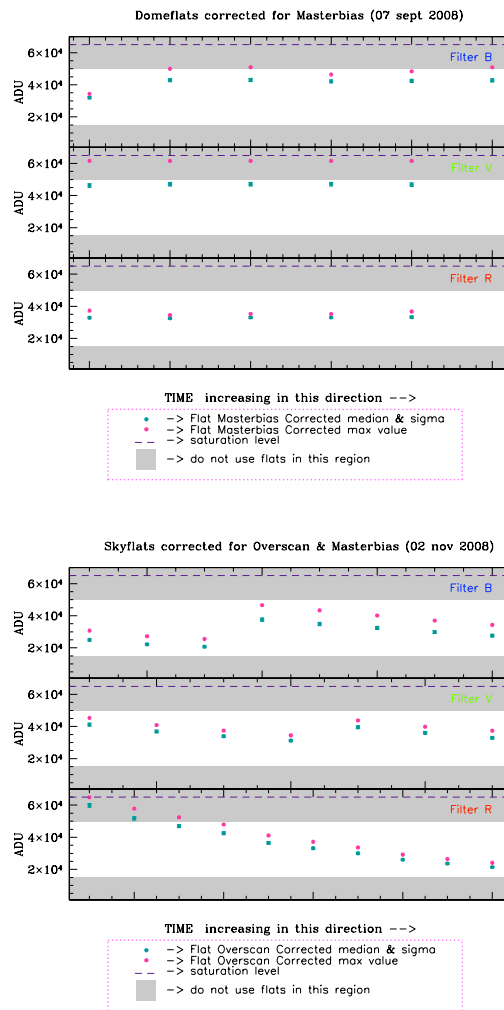


Figure 6.8: Example of QC on dome and sky flats. The QC is performed on domeflats acquired with CAFOS@CAHA on September 07 2008 (*left panel*) and on skyflats acquired with LaRuca@SPM on November 02 2008 (*right panel*). The gray shaded areas represent regions of too high (close to saturation) or too low (noisy) median counts for flat fields.

The first test is called *outside VS center* because, for each filter, each masterflat (dome or sky) is divided in 9 areas and the value of the mode is evaluated for each area. The two-dimensional structure of each masterflat can be checked by calculating the ratio between the value of each outer areas and the value of the central area: this provides information on the shape of each masterflat. For example, if we have a flat

The Pre-reduction Protocol for photometric observations

shape each ratio will be 1; if we have a “cup-like” shape each ratio will be greater than 1; if we have a “hat-like” shape each ratio will be lower than 1 and so on. When the shape is reconstructed for each masterflat, we can build the plot in Fig. 6.9 and check the stability of this two-dimensional structure during the run. If the structure does not vary significantly, we should have the same behavior for all points in each quadrant of the *outside VS center* plot.

The second test, called *large scale variability* (see Fig.6.10), is devoted to study the “global” variation of the large scale structure of masterflats. First, the masterflat are normalized by their mode value (calculated on the same area) to remove any zero-point offset; then, they are smoothed¹⁴ using the `boxcar` algorithm in IRAF; finally, one is chosen as the reference frame. The reference frame is subtracted from all the smoothed masterframes in order to obtain a “difference frame” (one for each masterflat). For each of them, the macro compute the sum of the square of each pixel value or, in other word, the value of the K_{stab} function:

$$K_{stab} = \sum_{pix=1}^n (F - F_{ref})^2 \quad (6.1)$$

Let us suppose for now that *all* pixels scale of the same quantity. In this case, if all pixels scale by 1%, the value of K_{stab} will be:

$$K_{stab}(1\%) = (0.01)^2 * (\text{number of pixels}) \quad (6.2)$$

Under this hipotesys, we can define a parameter $\Delta S/S$, called *shape variation*, which measures the “global” variation of the shape in comparison with $K_{stab}(1\%)$:

$$\frac{\Delta S}{S}(\%) = \sqrt{\frac{K_{stab}}{K_{stab}(1\%)}} \quad (6.3)$$

This parameter provides an “average behavior” of the large scale structure variations, taking into account that the underlying hipotesys (i.e., that all pixels scale of the same factor) is not totally realistic. Therefore, the large scale variability plot provides information on the “global” variation of the masterflats shape (assuming the variation uniformly distributed all over the pixels) but it is not able to point out “where” and

¹⁴Because we are interested in *large scale* variations only.

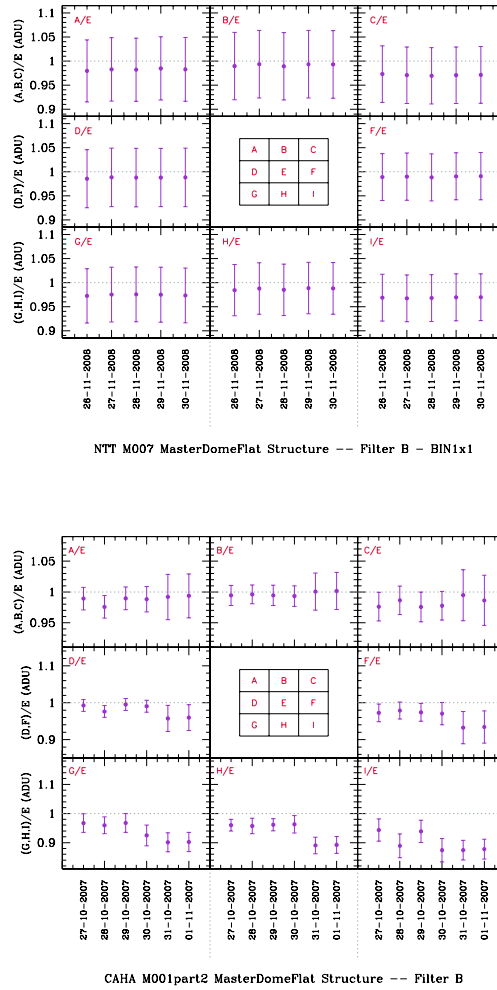


Figure 6.9: Examples of *outsideVS center* plot. In the *left panel*, the plot is built in order to check the shape of dome-masterflat frames (filter B) obtained during the run M-007@NTT (26-30 November 2008). This is a particularly good case because the shape of each masterflat is always the same during the whole run. In the *right panel* the same plot is built using the dome-masterflats (filter B) obtained during the run M-001@CAHA (27 October - 01 November 2007). In this case is easy to see the variation of masterflat shapes during the run: this is a particularly bad case, because the shape of the masterflat is changing almost every night and by almost 10%.

“how large” the variation is. This is the task of the third test, called *9 areas*. In order to perform it, the appropriate macro starts considering the normalized masterflat frames built during the previous test for each filter. The same masterflat (normalized but not smoothed) used to study the global variation of the large scale structure is used as reference frame for the 9 areas test as well. Each normalized masterflat is divided by the reference frame in order to obtain a “ratio frame”. Each of them is divided in 9 areas (the same areas used to perform the *outside VS center* test) and both the mode and standard deviation of each area are computed and used to obtain a plot like Fig.6.11.

The stability of the masterflats along an observing run is of fundamental importance because it affects both the observational and data reduction strategies. If the masterflats stability is not good as, for example, in the case of the run M-001@CAHA (see right panel of Fig. 6.10), the nightly acquisition of flat frames becomes mandatory, because the masterflat produced using flats acquired in a specific night can not be used to reduce data acquired in other nights. On the other hand, if the masterflat stability is good as, for example, in the case of M-007@NTT (see left panel of Fig. 6.10), the lack of flat fields during a specific night is not a big problem, and the masterflat produced in the previous or the next night can be used in the reduction process.

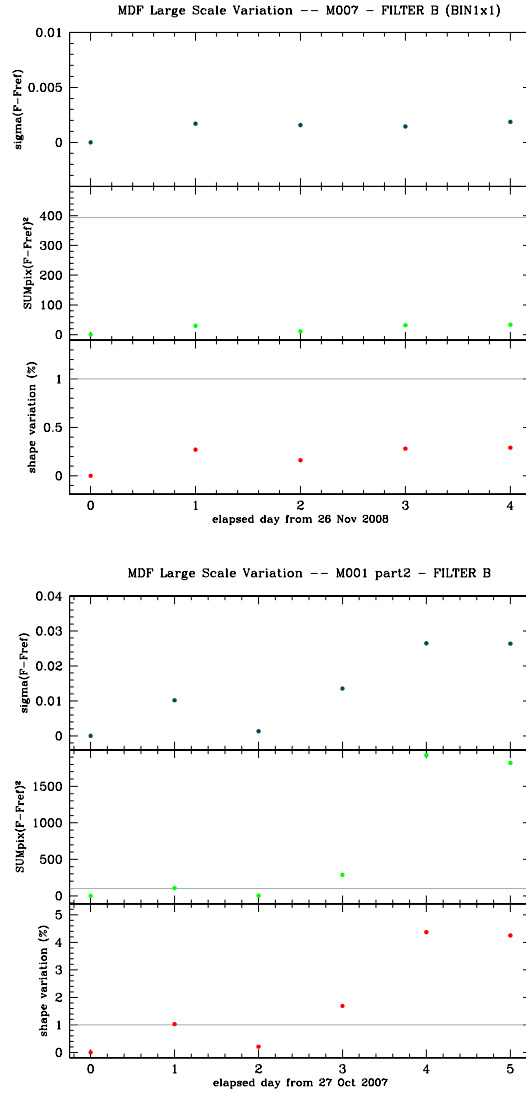


Figure 6.10: Examples of *large scale variability* plot. In both panels, the plot is built considering the same data used in Fig. 6.9. The *large scale variability* plot is divided in 3 windows reporting respectively the parameter $\Delta S/S$ (in the bottom panel), the function K_{stab} (in the middle panel) and the sigma of each “difference frame” (in the upper panel). The *upper panel* shows the very good case of M-007@NTT: the global shape variation for all masterflats is always lower than 0.3%. In the *bottom panel* the situation is not so good: the shape of the masterflats obtained during the run M-001@CAHA is changing every night and also the global shape variation is high, reaching about 4.5% in the worst case.

The Pre-reduction Protocol for photometric observations

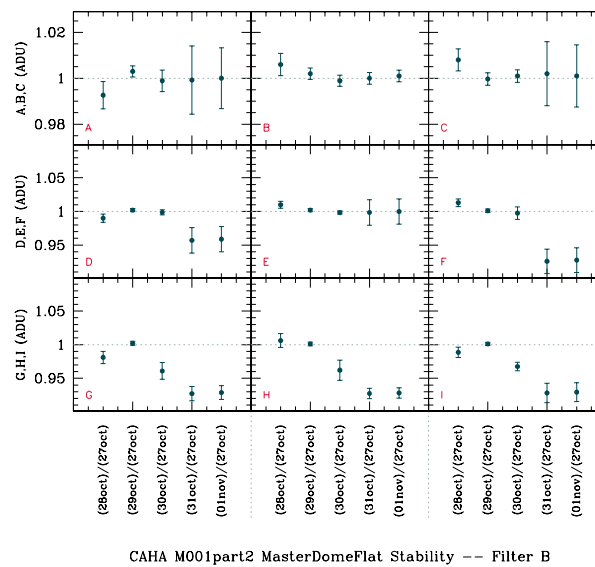
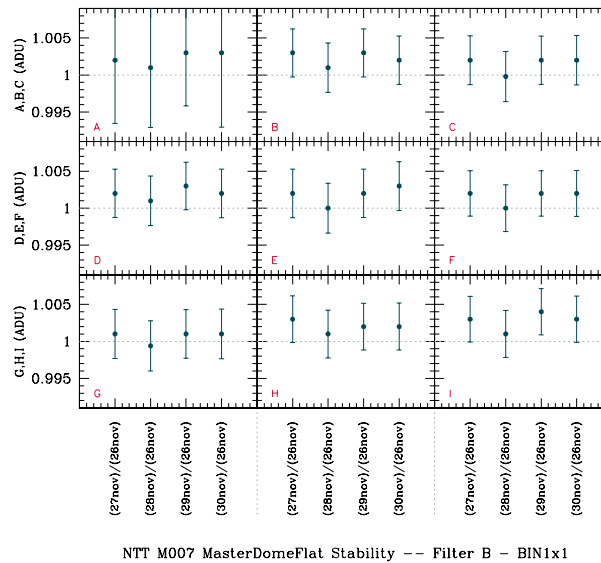


Figure 6.11: Examples of *9 areas* plot. In both panels, the plot is built considering the same data used in Fig. 6.9. The plot is divided in 9 windows in which the mode and standard deviation of each “ratio frame” are shown. The *upper panel* shows the very good example of M-007@NTT. The *bottom panel* shows the less good case of M-001@CAHA: the most important variation of the masterflat shape occurs in the bottom part of the frames.

6.5 Bad Pixel Mask

It is not uncommon that a CCD, made up of millions of pixels, contains faulty single pixels or columns. These defects can be easily identified in a flat field image as bright “hot” pixels or columns, with counts much higher than average, or black “dead” pixel or columns, with counts much lower than average.

In high quality CCDs there are few faulty pixels or columns and scientific frames are not significantly affected by them, especially if the target is placed in a clean portion of the CCD. This can be effectively done for single stars and spectra while it can be more difficult if we are interested in a “crowded” stellar field rather than in single objects, as when we are performing relative photometry or we are observing standard fields. Multiple exposures with a suitable dithering¹⁵ are a good technique to correct for this problem, as well as for the cosmic rays contamination or other spurious defects. In the case of bad pixels or columns, a better result can be obtained by means of a *bad-pixel mask*. A bad-pixel mask (hereafter BPM) is an image of the same dimension of the CCD to which it is associated, where good pixels are identified by zero values and bad pixels by non-zero values. When applied to scientific frames, the bad pixels are replaced by linear interpolation along lines or columns using the nearest good pixels.

I used the IRAF task `ccdmask` to create the BPM for each CCD/instrument combination: some examples are shown in Fig. 6.12. The input images could be of any type but this task was designed primarily for detecting column oriented CCD defects such as charge traps that cause bad columns and non-linear sensitivities. The ideal input is therefore a ratio of two flat fields¹⁶ having different exposure levels (bright and faint) so that all features which would normally be properly flat-fielded are removed: only pixels which are not corrected by flat-fielding are used to create the BPM.

I produced BPMs using the following procedure:

- correct domeflats for overscan (when possible) and bias (using the IRAF tasks `zerocombine` and `ccdproc` (see Section 6.2.2 and Section 6.4.1))
- create a masterflat with low counts using the IRAF task `flatcombine` (see Section 6.4.2)

¹⁵The *dithering* technique consists in small telescope shifts (a few arcsec) between multiple exposures. In this way a given object is imaged onto different parts of the detector.

¹⁶A single flat field can also be used but pixels of low or high sensitivity could be included as well as true bad pixels.

- create a masterflat with high counts using the IRAF task `flatcombine` (see Section 6.4.2)
- divide the masterflat with high counts for the masterflat with low counts and create a “flat-ratio” frame using the IRAF task `imarith`
- create the bad pixel mask using the IRAF task `ccdmask`

6.6 Fringing

Fringing is caused by the multiple reflections and interferences of the night-sky emission line wavelengths in the CCD substrate. This usually has the appearance of a series of “ripples” in the images. The fringe pattern is an additive effect.

The effect is particularly strong in the red due to strong sky emission lines at long wavelengths, both in imaging (especially in the I band, while in the R band it is much fainter or negligible, depending on the single CCD) and in spectroscopy¹⁷.

The *fringing mask* for the filter R (or for the filter I) can be obtained using all scientific images acquired during one night with the R filter (or the I filter, if any) and following this simple procedure:

- correct all R frames for overscan and/or masterbias (using `zerocombine` and `ccdproc` to correct images, see Sec. 6.2.2);
- combine the processed images to obtain a median final image containing only the fringing and the flat field structures (using `imcombine` with `scale="mode"`). It is very important that no stars are present in the final median image;
- correct this image for the masterskyflat R (see Sec. 6.4.2) and for the Bad-Pixel Mask (see Sec. 6.5) using `ccdproc` to obtain an image containing only the flat-scaled fringe and a flat sky;
- get the average sky level (mode) of this frame (using `imstat`);

¹⁷For the spectroscopic case, fringing is one of the major problems in data reduction because no fringing mask can be produced and no specific correction performed. Both spectroscopic masterflats and scientific frames acquired using red grisms are strongly contaminated by fringing. At least when the wide slit is adopted to acquire spectra, the corresponding masterflat seems to present a stable and almost constant fringing pattern. Nevertheless, the result in the correction for the fringing in the scientific spectra (when the masterflat correction is performed) will depend on the star position in the slit. A detailed discussion on the effects which the flat correction produce on scientific frames is presented in Coccozza et al. (2011).

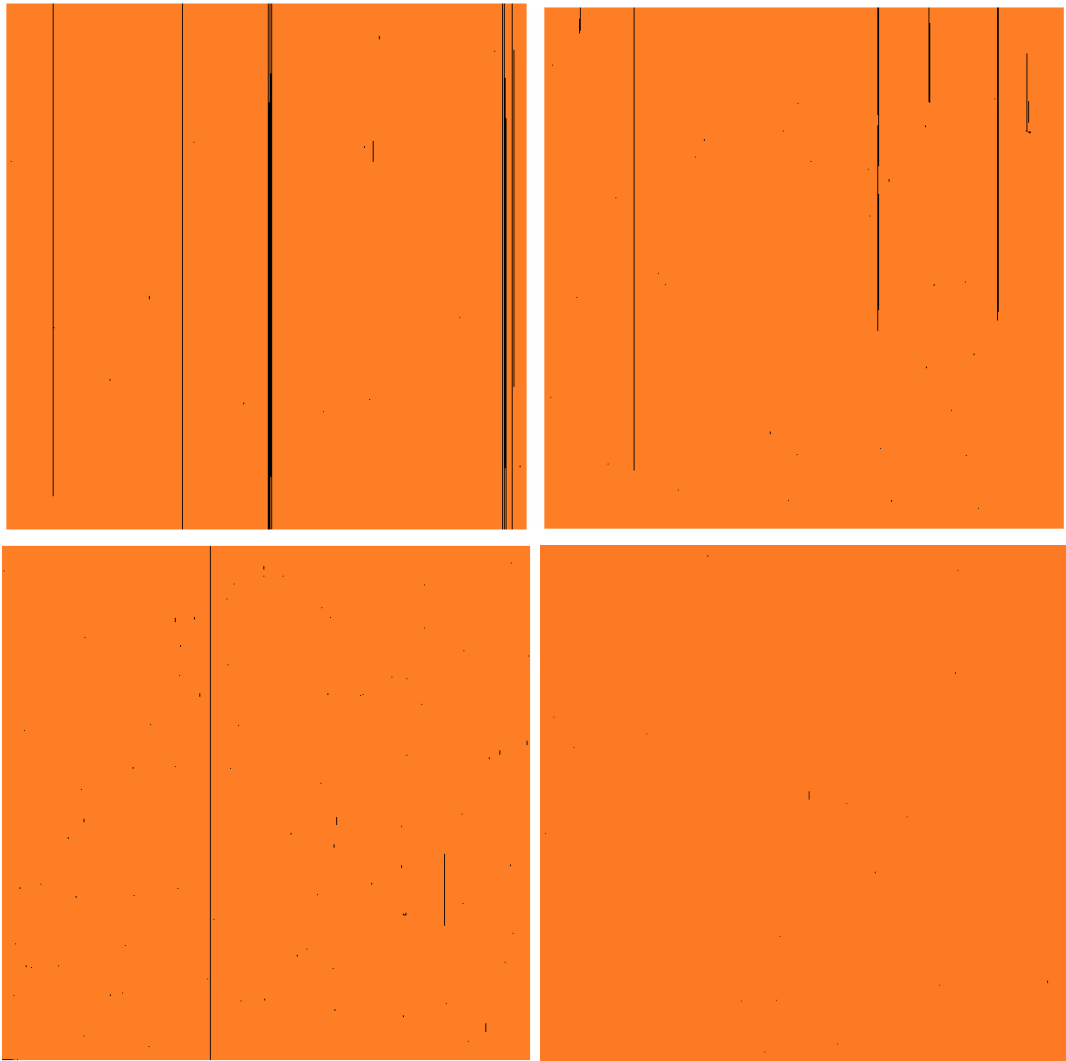


Figure 6.12: BPM examples. *Upper panels*: BPM for LaRuca SITE1 CCD (on the left) and for EFOSC2 CCD (on the right) read in 1x1 binning factor. For both CCDs, the cosmetic is not particularly good. *Bottom panels*: BFOSC BPM for the old CCD (left panel) and the new CCD (right panel): the improvement in cosmetic quality is evident.

- subtract this value from the previous frame using `imarith` (you want to have an image with a mode near to zero). You are left with an image containing the flatfielded fringes alone.
- multiply the result by the normalized (mode) `masterskyflat R` using `imarith`.

The Pre-reduction Protocol for photometric observations

This image is your *masterfringe template*, containing the original (non-flatfielded) fringing pattern.

Then, it is necessary to have a look at the masterfringe template. If some significant fringing pattern is present, it means that a fringing correction is needed since we are looking for a very high precision in our relative and absolute photometry.

I produced fringing masks for each CCD/instrument combination used in our campaigns by applying the procedure described above. In our case, our exposure times are always quite short with all the used instruments: the sky is not so strong to produce a clear fringe pattern (at least in the R filter). For this reason, usually the fringing correction is not performed in my pre-reduction pipeline.

6.7 2-d Imaging Pre-reductions

Once all calibration master frames are available, all scientific images must be corrected for overscan (if possible), trimmed, bias and flat field corrected and, if necessary, also corrected for dark, a bad pixel mask and a fringing mask. This is done simultaneously in my pipeline using `ccdproc`. For example¹⁸:

```
ccdproc images=@obj.list output=@obj2.list ccdtype="" noproc-
overscan+ trim+ zerocor+ darkcor- flatcor+ fixpix+
fringec- illumcor- readaxi="line/column" biassec="image"
trimsec="image" function="spline3" order=3
zero=masterbias.fits
flat=masterdome.fits/masterskyflat.fits
fixfile=BPM.pl
```

All pre-reduced photometric frames are now ready to be submitted to the *quality control and photometric catalogue production* procedure, described in detail in Chapter 7.

Depending on the results of quality control, a pre-reduced frame is archived or rejected (see Appendix A.2).

¹⁸In this example we suppose that no dark and fringing correction is necessary, so we set `darkcor-` and `fringec-`

7

Quality Control on SPSS Photometric Frames and Photometric Catalogues Production

Our survey contains a huge number of frames, and the precision and accuracy in reducing them is of fundamental importance to achieve our desired accuracy (a few % in flux at most, relative to Vega). For this reason, one of my main tasks was to build semi-automated procedures of quality control in order to produce check files useful to retain only data suitable for our purposes. My procedure produces aperture photometry catalogues ready to be used for further analysis (see Chapter 8) and, simultaneously, performs the quality control on the SPSS pre-reduced imaging frames¹. I used SExtractor Bertin & Arnouts 1996 , see Section 7.1) to produce aperture photometry catalogues because it can return as output a series of useful information, flags and parameters which are excellent to perform the quality control. The whole procedure can be treated as separated and consecutive steps: it starts to work on each SPSS pre-reduced photometric frame and performs aperture photometry using SExtractor and other tools (see below); as a last step, the pipeline performs the QC on each catalogue and finally, depending on the result of QC, the pre-reduced frames and the corresponding catalogues should be retained and archived for further use, or rejected.

My pipeline works using different softwares: IRAF², SExtractor³, SM⁴, CataXcorr and CataComb⁵.

¹For imaging, we term “data pre-reduction” the removal of the instrument characteristics (dark, bias, flat-field, bad-pixel mask and, if needed, fringing) as described in Chapter 6.

²IRAF is available at: <http://iraf.noao.edu/>

³SExtractor is available at: <http://www.astromatic.net/software/sextractor>

⁴SM is available at: <http://www.supermongo.net/>

⁵The CataPack is available upon request contacting its author Paolo Montegriffo (paolo.montegriffo@oabo.inaf.it).

7.1 SExtractor

SExtractor is a powerful tool to perform reliable aperture and PSF photometry. In our case, since we are working with not particularly crowded images and we are looking for the highest possible precision, we have to perform aperture photometry by setting a radius large enough to ensure no light losses. After various tests, I decided to use an aperture diameter of 6 times the stars FWHM (i.e., supposing a gaussian PSF, an aperture radius that contains almost the total flux emitted by the stars).

As mentioned before, SExtractor is a fast and robust algorithm, also useful to perform the automatic inspection and quality control of fits frames. When SExtractor works on a fits frame, first of all it estimates the background, then it looks for counts excess in order to find sources, it determines their properties (as required by the user in a parameter file) and writes them into the output catalogue. Each catalogue is composed by a list of objects reporting the measured properties for each detected source. In order to work properly, SExtractor needs a configuration file and an output catalogue parameters file. They are usually suffixed with *.sex* and *.param* respectively. SExtractor is controllable (most steps can be influenced by the user) but it is strongly dependent on some settings that are crucial for both the source detection and photometry. Therefore, it is very important to carefully choose the most appropriate value of parameters for the configuration file *.sex*. Depending on which telescope/instrument configuration we are working with, I prepared template *.sex* configuration files with a standard naming convention. These templates can be found on Wiki-Bo⁶ and ensure the maximum homogeneity in the aperture photometry measurement procedure. I report in Table 7.1 the correct values of each Telescope/CCD configuration used in the *.sex* templates. Further information about the parameters in the configuration file can be found in the SExtractor manual⁷.

The *.param* file contains the list of parameters that will be listed in the output catalogue for every detected source. This allows the software to compute only catalogue parameters that are needed by the user. A list of the parameters of use for our imaging campaigns is shown in Table 7.2 (actually, we are not interested in the value of MAG_AUTO parameter but in a value of FLAGS parameter that can appear only if MAG_AUTO magnitude is requested, as explained in Section 7.3.1). Presently, two kinds of keywords are recognized by SExtractor: scalars and vectors. Scalars, like X_IMAGE, yield single numbers in the output catalogue. Vectors, like

⁶All the *.sex* templates at:

http://yoda.bo.astro.it/wiki/index.php/QC_for_Photometry_2D

⁷<http://www.astromatic.net/software/sextractor>

Telescope	Instrument	CCD	<i>work.sex</i> file name	gain	pixel scale
				e^-/ADU	arcsec/pix
Cassini	BFOSC	EEV (before Jul 2008)	workLOIold.sex	2.13	0.58
Cassini	BFOSC	EEV (after Jul 2008)	workLOInew.sex	2.22	0.58
SPM1.5	LaRuca	SITE1 (before Oct 2009)	workSPMold.sex	1.20	0.24
SPM1.5	LaRuca	E2V-4240 (after Oct 2009)	workSPMnew.sex	1.80	0.12
REM	ROSS	Apogee Alta	workREM.sex	2.0	0.575
TNG	DoLoRes	E2V-4240 (before Dec 2007)	workTNGold.sex	1.0	0.252
TNG	DoLoRes	E2V-4240 (after Dec 2007)	workTNGnew.sex	1.0	0.252
CAHA2.2	CAFOS	SITE1	workCAHA.sex	2.3	0.53
NTT	EFOSC2	Loral	workNTT.sex	1.22	0.12

Table 7.1: Gain and pixel scale values for all Telescope+CCD configurations we use in our campaigns.

Output Parameter name	what is it?	unit
NUMBER	Running object number	-
FLUX_APER	Flux vector within fixed circular aperture(s)	count
FLUXERR_APER	RMS error vector for aperture flux(es)	count
MAG_APER	Fixed aperture magnitude vector	mag
MAGERR_APER	RMS error vector for fixed aperture mag.	mag
MAG_AUTO	Kron-like elliptical aperture magnitude	[mag]
BACKGROUND	Background at centroid position	count
X_IMAGE	Object position along x	pixel
Y_IMAGE	Object position along y	pixel
FWHM_IMAGE	FWHM assuming a gaussian core	pixel
FLAGS	Extraction flags	-

Table 7.2: The SExtractor output parameters needed for our imaging campaigns.

MAG_APER(4)⁸ or VIGNET(15,15), yield arrays of numbers. The order in which the parameters will be listed in the catalogue are the same as that of the keywords in the parameter list.

⁸SExtractor can perform aperture photometry calculation on many apertures at the same time. Therefore, in the *.param* file, (n) indicates how many apertures we are working with. For our purposes, n is always one.

7.2 The Quality Control strategy

The Quality Control procedure on SPSS pre-reduced photometric frames is designed with a multiple level approach. The fundamental QC level is performed on each single star present in each catalogue produced by SExtractor on each frame. It is named *STAR LEVEL QC*, and all next levels are related with it: its results depend only on failure of the QC-steps a-b-c-d (see Sections 7.3.1, 7.3.2, 7.3.3, and 7.3.4) and are totally independent on the scientific goal pursued.

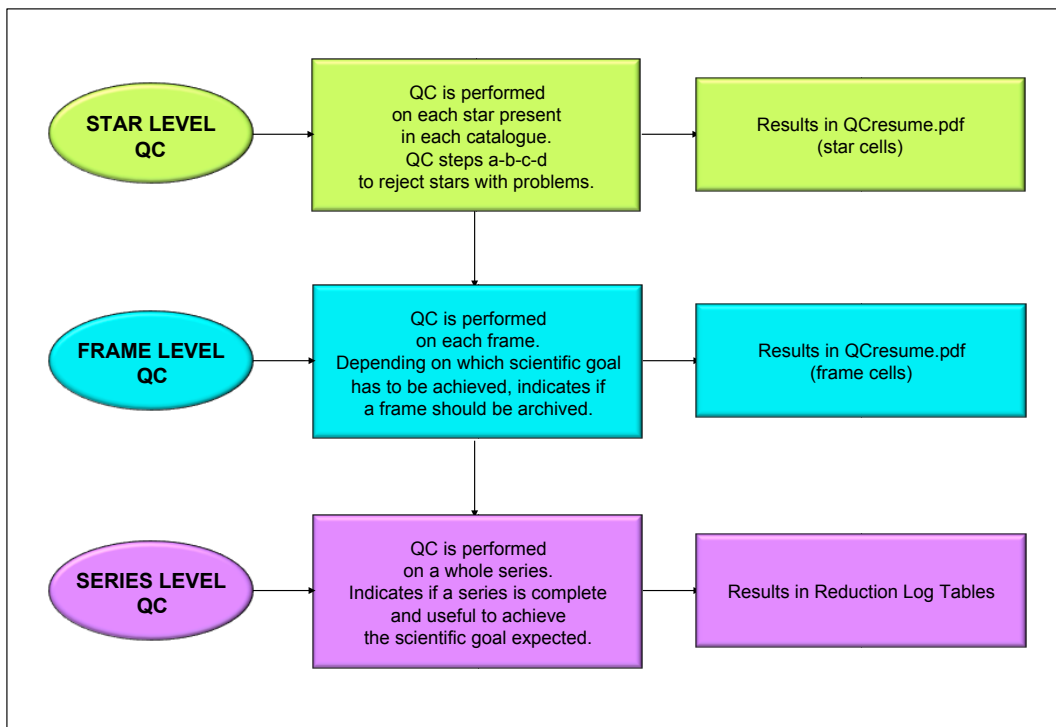


Figure 7.1: Schematic description of the QC structure.

The second and third QC levels are performed on each single frame (*FRAME LEVEL QC*) and on a whole frame series (*SERIES LEVEL QC*), respectively. One observation of a SPSS in one night, formed by 9 frames acquired in the BVR filters (3 for each filter) is called a *night point*. When the night is clear and Landolt standard star fields are observed, the *relative* night point becomes an *absolute* night point. The 9 frames belonging to a night point, absolute or relative, form a *night point series*. When an SPSS is observed for short-term variability monitoring in one filter for approximately 1-2 hours, the observation is called short-term *time series*. As described in the observing protocol, a time series should be formed by at least 30

frames. The result of the second and third level of QC depends on which scientific goal we want to achieve (i.e. absolute photometry, short or long variability study on the SPSS). The *FRAME LEVEL* results basically indicate which frames shall be archived in the SPSS Reduced Data Archive, while the *SERIES LEVEL* results provide a grade of "goodness" of the whole series. Fig. 7.1 shows the basic way in which the three levels work and are related.

7.3 The *Star Level* QC

This QC level consists of two logical steps. The first step concerns the target star (the SPSS), the second one concerns all reference stars detected by SExtractor, which are present in all catalogues (if one star is missing in one catalogue, it is rejected from the pipeline). These two steps are further divided into four QC procedures, which can be summarized as follows:

- **step a:** the SPSS and reference stars are not saturated and not affected by other problems (Section 7.3.1);
- **step b:** the SPSS and reference stars have signal-to-noise ratio larger than 100 (Section 7.3.2);
- **step c:** the SPSS and reference stars have seeing lower than 5 arcsec (Section 7.3.3);
- **step d:** no bad pixels are present in the aperture used to measure the magnitude of both SPSS and reference stars (Section 7.3.4).

I prepared template macros (stored in Wiki-Bo) to perform the QC according to the above scheme and automatically prepare check files that can be consulted whenever a QC step fails. Fig. 7.2 shows the logical flow of the *star level* QC.

7.3.1 Step *a*: SExtractor FLAGS

The first star level QC step makes heavy use of the values which the SExtractor parameter FLAGS can assume. It is worth having a look in detail at how the SExtractor flags are defined, to give an idea on their potentialities. They are decimal numbers which are the sum of all the extraction flags expressed as power of 2:

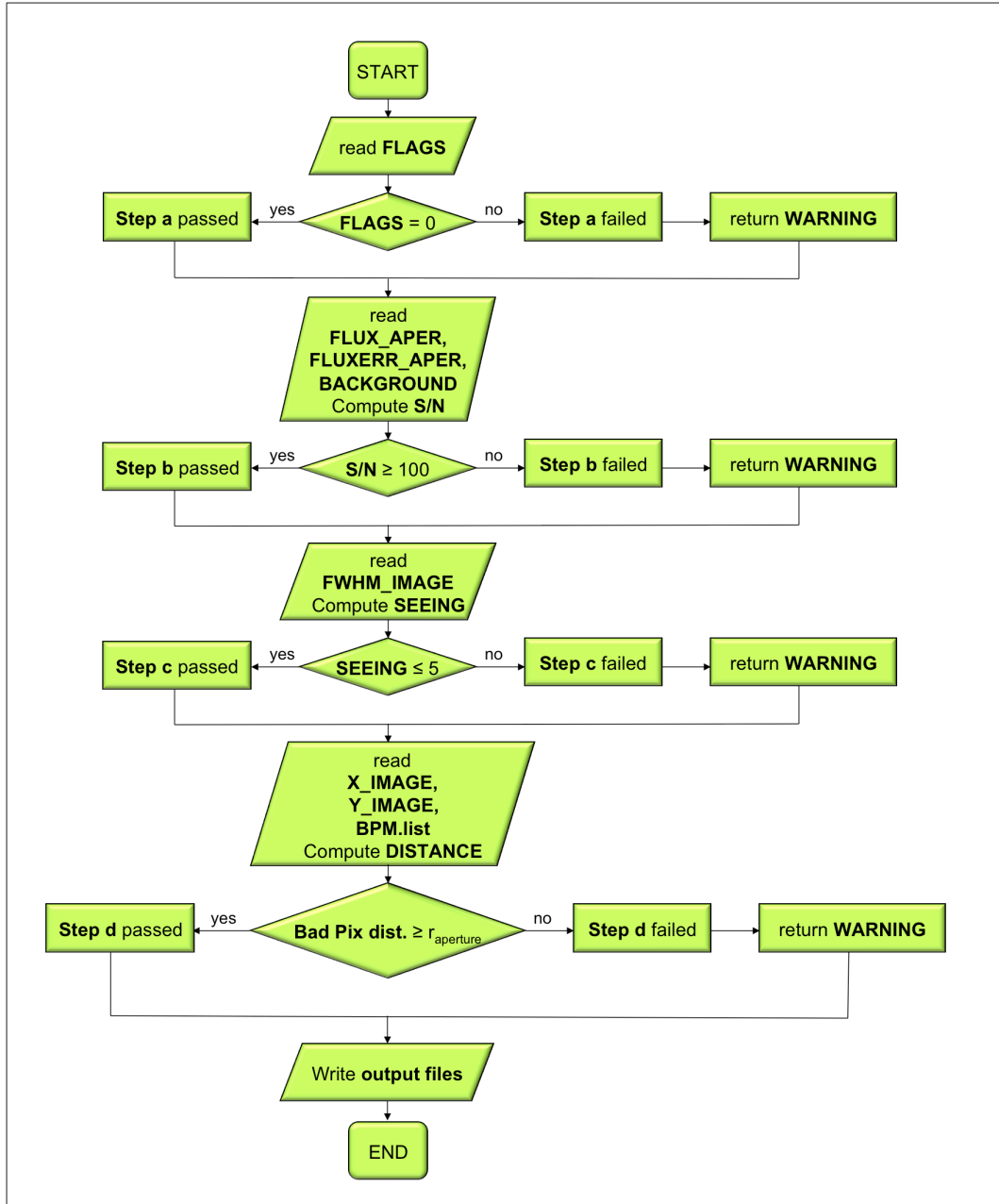


Figure 7.2: Schematic description of the STAR LEVEL QC.

- 1 = the object has neighbours (bright and close enough to significantly bias the MAG_AUTO photometry) or bad pixels (more than 10% of the integrated area affected).
- 2 = the object is blended with another one
- 4 = at least one pixel of the object is saturated (or very close to saturation)
- 8 = the object is truncated (too close to an image boundary)
- 16 = the object aperture data are incomplete or corrupted
- 32 = the object isophotal data are incomplete or corrupted
- 64 = a memory overflow occurred during deblending
- 128 = a memory overflow occurred during extraction

For example, an object close to an image border may have $FLAGS = 16$, or $FLAGS = 8+16+32 = 56$ if it is truncated by the image border .

$FLAGS$ equal to 0 means that the star examined does not have any problems and this step is successfully passed: only stars associated with this $FLAGS$ value are considered useful in order to perform photometric analysis. If the SPSS fails this QC step, the corresponding photometric catalogue shall not be used and the frame shall not be archived. If one of the reference stars fail this QC step, it shall not be used as a reference star (i.e. it is rejected when relative photometry analysis is performed). The special case of $FLAGS = 1$ may indicate the presence of bright and close neighbours or bad pixel clusters. In order to disentangle which is the case, we need to wait for the end of the whole star level QC procedure. The presence of bad pixel clusters will be pointed out even by the QC step d alone (Section 7.3.4): if step d fails as well it means that more than 10% of the star is affected by bad pixel; otherwise, if step d is successfully passed this indicates the presence of neighbours. In this case, all frames must be investigated by eye in order to estimate the distance of neighbours: for our purposes, we do not want any neighbour closer than 10 arcsec to the SPSS, with its flux larger than 1% of the SPSS flux.

The case of $FLAGS = 2$ provides a warning and not a failure. This $FLAGS$ value is generated when there is a saddle point in the intensity distribution (i.e., there are two separate peaks in the light distribution). In this case, SExtractor splits the object into two different entries in the catalogue and photometry is performed on both, by dividing up the intensity of shared pixels. In order to avoid the saturation of bright

stars we often have to defocus during the observations. The resulting image could be double peaked and SExtractor could consider it as two blended objects. Therefore the image must be examined by eye in order to determine if there are actually two close objects blended or a single one out of focus. In the last case, SExtractor photometry must be repeated with more appropriate configuration parameters.

7.3.2 Step *b*: Signal to Noise Ratio

The S/N ratio can be easily computed using some parameters provided by SExtractor and expressed in ADU. Assuming that the local background is the same throughout the star and that the read-out noise and dark currents contribution to S/N are negligible, the S/N ratio in the used aperture can be estimated whit:

$$S/N = \frac{F_*}{\sqrt{\sigma_*^2 + \sigma_{sky}^2}} \quad (7.1)$$

where F_* is the star flux, σ_* and σ_{sky} is the error on the flux of the star and the background, respectively. Using the SExtractor parameters FLUX_APER, FLUXERR_APER and BACKGROUND, and the proper value for the CCD gain g , they are obtained as follows:

$$F_* = g(\text{FLUX_APER}) \quad (7.2)$$

$$\sigma_* = \sqrt{g(\text{FLUXERR_APER})^2} \quad (7.3)$$

$$\sigma_{sky} = \sqrt{\pi r^2 g(\text{BACKGROUND})} \quad (7.4)$$

If the S/N ratio value is lower than 100, the star fails this QC step: if this star is the SPSS, the corresponding photometric catalogue shall not be used and the corresponding frame shall not be archived. Otherwise, if it is one of the reference stars, it shall be rejected.

7.3.3 Step *c*: Seeing and focus

We need to ensure that the observational conditions were good enough to allow for good quality data analysis. Therefore, if the seeing is too high or the focus of the

image too bad, the frame (and all the stars therein) has to be rejected. To do that, the SExtractor output parameter FWHM_IMAGE (in pixels, it is the FWHM of each star calculated assuming a gaussian core) turns out to be a very good indicator. Since we know the pixel scale of our CCDs, the seeing θ can be easily estimated by:

$$\theta = (\text{FWHM_IMAGE})p \quad (7.5)$$

Where p is the pixel scale in "/pix. We have set the seeing threshold at 5 arcsec: the examined star fails this QC step if the seeing calculated by SExtractor is worse than 5".

This step of the QC procedure allows us to check the quality of the night but also to reject objects that are not stars. In the examined frame, all stars will have roughly the same FWHM whereas a galaxy will have a higher value. So, every object showing a size in arcsecond larger than 5" shall be rejected. One frame in which the SPSS star fails this QC step will not be loaded in the archive and the corresponding catalogue will not be used for photometry. If a reference star fails this QC step, this star shall not be used as a reference star anymore.

7.3.4 Step *d*: Bad pixels

This is the only QC step that produces a frame warning and not a rejection. It is used to ascertain if a bad pixel falls into the aperture used to measure the magnitude for the SPSS and reference stars. The correction for bad-pixel mask (BPM) is performed during the photometric pre-reduction (Chapter 6) but, when the star level QC step *d* returns a warning, it is better to visually inspect the image, in order to see if the star examined is close to (or crossed by) a large cluster of bad pixels (for example, a group of bad columns). When IRAF performs the BPM correction, all the bad pixels are replaced with the average value of close good pixels so we must pay special attention to the photometry of stars affected by this problem.

7.4 The *Frame Level QC*

The aim of this QC procedure is to decide which pre-reduced frames shall be loaded in the SPSS Reduced Data Archive ⁹ (see Appendix A), in order to avoid wasting disk space with useless frames. In Fig. 7.3 we show how this QC level works, depending on both the star level QC results and the scientific goal pursued (i.e.

⁹<http://spss.bo.astro.it/red.cgi>

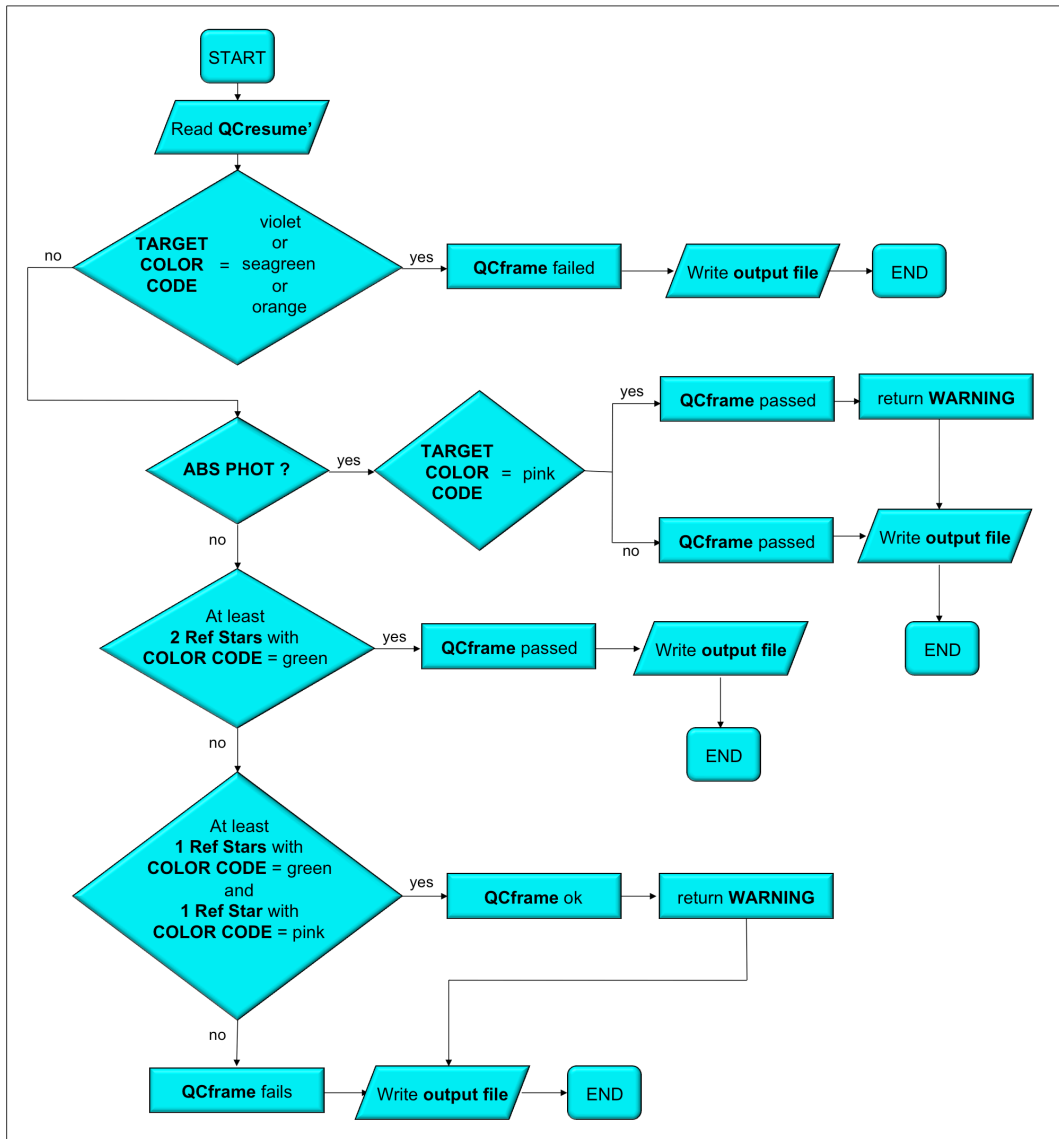


Figure 7.3: Schematic description of the FRAME LEVEL QC. For the exact meaning of color codes, please see Fig. 7.5.

absolute photometry, relative photometry performed on a night point or on short-term variability time series). The procedure first considers the star level QC results on the SPSS: if the SPSS fails either of the steps *a*, *b* or *c* (i.e., if the SPSS is saturated or too close to the edges of the frame, too faint or too much out of focus) the frame level QC fails as well. If the only star level QC step failed is step *d* (there can be some bad pixels or bad pixel cluster) or if all star level QC steps are successfully

passed, the frame level QC result changes depending on the scientific aim pursued in acquiring the data.

- In case of data acquired to perform absolute photometry, the frame level QC procedure ends successfully without considering the presence of reference stars in the frame nor the star level QC results on them.
- But, if the purpose is to perform relative photometry it is necessary to have at least two good reference stars in the frame, and the star level QC results on them becomes very important: if this condition is not respected, the frame level QC fails.

All frames passing the frame level QC are archived (see Appendix A.2), with a warning if the star level QC step d is failed.

7.5 The *Series Level QC*

The aim of this QC procedure is to express a global judgment on a series of exposures, such as a night point or a time series. The procedure takes into account which kind of scientific goal was pursued during the acquisition of the data: the spectra of SPSS, observed from various ground based sites, will mostly be calibrated with extremely accurate absolute photometry and all candidate SPSS will also be checked for variability (both long and short term) with relative photometry. Each type of observation has to be performed following precise protocols (i.e. filter used, minimum number of frames required, see Pancino et al. 2010a, 2011): the series level QC verifies that all the observational requirements were met and, in this case, it ends successfully (see Fig. 7.4).

7.6 QC results and logging

The results of all levels of QC are summarized by a series of files containing internal flags. For the star and frames QC levels these flags are used to produce tables (stored in pdf files) with a clear color code which provides an overlook of the QC procedures. If any of the levels or steps of this two QC procedure fails or issues a warning, inspection of these tables allows to pick out the offending step or level at a glance, and to identify which frame was the cause of it. The series level QC results

Quality Control on SPSS Photometric Frames and Photometric Catalogues Production

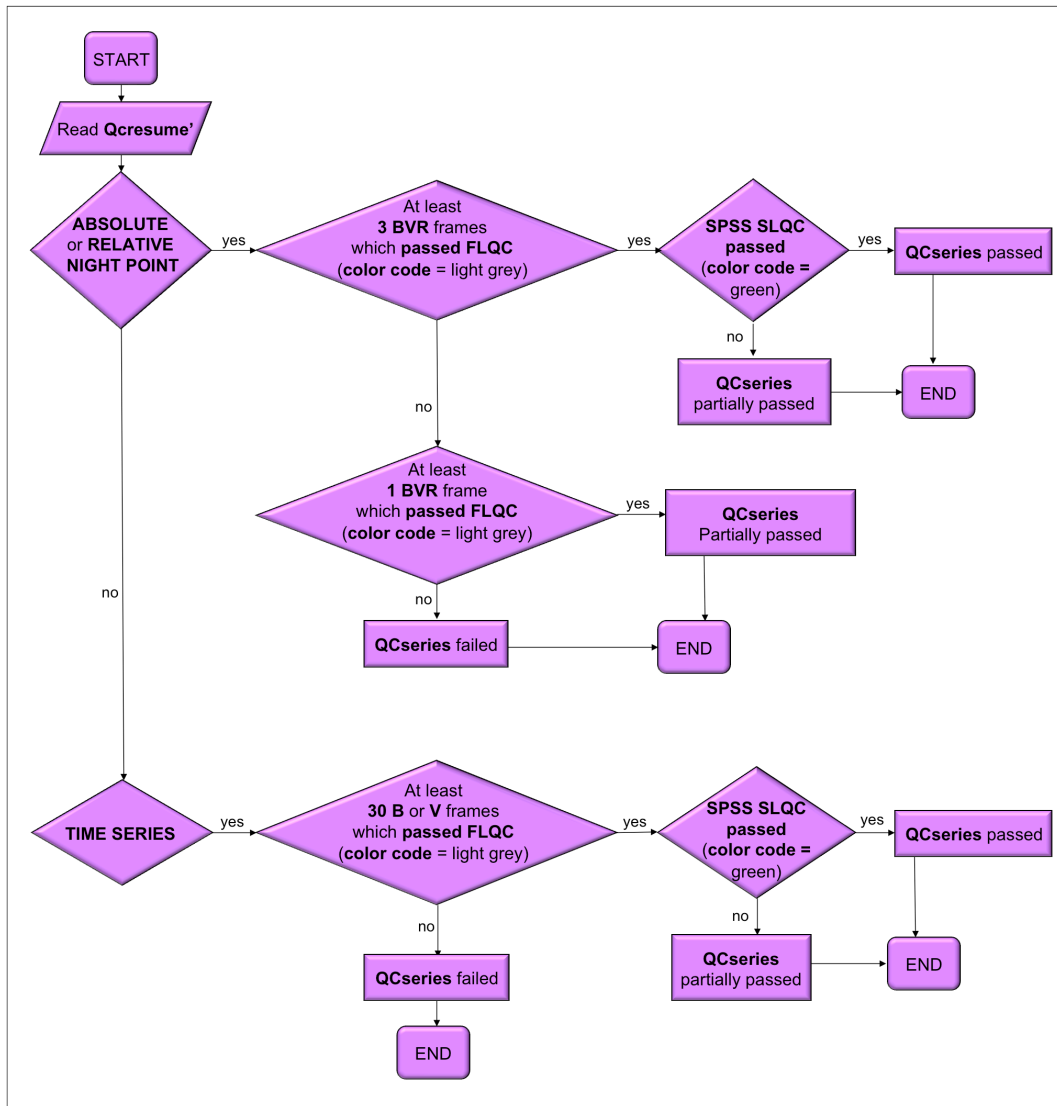


Figure 7.4: Schematic description of the Series Level QC. For the exact meaning of color codes, please see Fig. 7.5.

have a dedicated space in the various run pages hosted by Wiki-Bo (see Appendix A.1).

Quality Control on SPSS006 (run M007 - NTT) (26 nov 2008) — filter B —				
	T	R1	R2	R3
251			44	77
252		cr!	83	16
253			81	

Quality Control on SPSS006 (run M007 - NTT) (26 nov 2008) — filter V —					
	T	R1	R2	R3	R4
254				55	
255		cr!		cr!	
256					

Quality Control on SPSS005 (run M007 - NTT - 26 nov 2008) — filter R —								
	T	R1	R2	R3	R4	R5	R6	R7
257		56		36		43	83	
258	4		cr!	67		82	cr!	
259		86		57		70		

xx	QC _a failed, xx = SEx Flag
xx	QC _b failed, xx = SNR
xx	QC _c failed, xx = seeing
cx	QC _d failed
	cr(!) = crossed by bad pixels (bad columns)
	cl(!) = bad pixels (bad columns) in aperture
	vc(!) = bad pixels (bad columns) very close to the star
	all QC steps passed !!

	Frame archived
	Frame not archived
T	Target Star (SPSS)
R*	Reference Stars

Figure 7.5: An example of *QC* résumé file built for a night point observation. A table is made for each filter used: each row represents one frame and each column represents one star (T is the target SPSS, R is a Reference star: the number of columns depends on how many Reference stars are present in the catalogue). For each star in a frame, the cell color is determined by the results of star level QC: if all steps are successfully passed, the cell color will be green. A different color means that the corresponding step has failed. It is important to note that in the *QC* résumé tables only the first failed star level QC step is shown. The first cell in each row of the *QC* résumé tables is dedicated to host the frame level QC results: if this QC level fails the cell color will be dark gray and the corresponding frame shall not be loaded in the SPSS Reduced Data Archive.

Quality Control on SPSS Photometric Frames and Photometric Catalogues Production

Data Reduction

Reduction Logs

■ Meaning of colors in the progress status tables.

No	No	Not needed or not present
XX	XX	Done by person XX (QA Still Missing)
XX	XX	Assigned to person XX
TBD	TBD	To be done
XX	XX	Quality Assurance = Rejected by XX
XX	XX	Quality Assurance = Partially Accepted by XX
XX	XX	Quality Assurance = Passed by XX

Lighter Colors mean that the reduction is a pilot reduction and that will need to be revised or even redone.

First Run (6-7 August 2007)

6 August 2007										
SPSS	Name/Type	Setup	Photo PreRed	Photo AbsPhot	Photo ShortVar	Photo LongVar	Spectro PreRed	Spectro Wave/Ext	Spectro FluxCal	Notes
-	Bias	-	SMR	No	No	No	SMR	No	No	Master Bias Archived ↗
-	Phot Dome Flat	B	SMR	No	No	No	No	No	No	Master Domeflat Archived ↗
-	Phot Sky Flat	B	SMR	No	No	No	No	No	No	Master Skyflat Archived ↗
142	WD1918+725	B	SMR photQC	No	SMR	No	No	No	No	Frames Archived ↗ WARNING: only 22 frames
149	WD2047+372	B	SMR photQC	No	SMR	No	No	No	No	Frames Archived ↗
203	WD2028+390	B	SMR photQC	No	SMR	No	No	No	No	Frames Archived ↗ WARNING: only 28 frames
211	WD2140+207	B	SMR photQC	No	SMR	No	No	No	No	Frames Archived ↗ WARNING: only 22 good points in the series
300	WD2117+538	B	SMR photQC	No	SMR	No	No	No	No	Frames Archived ↗ WARNING: close companion (~9.6")
301	WD1900+705	B	SMR photQC	No	SMR	No	No	No	No	Frames Archived ↗

Figure 7.6: An example of *reduction log table* built for data acquired during the run V-002 with BFOSC@Cassini Telescope. All the observing runs performed during the pilot program, the main and the auxiliary campaigns have a dedicated page in Wiki-Bo. In all these pages a section called *Reduction Logs* hosts a series of tables, one for each observing night: an example of these tables is shown in this figure. The results of the series level QC are reported in the *Photo PreRed* column. The *QCrésumé* file which summarizes the results of both the star and frame QC levels is linked in the *photQC* link.

7.6.1 Run pages Reduction Logs Tables

All the results of the QC levels and steps procedures are logged in Wiki-Bo (see Appendix A.1) in different ways. For the star and frame QC levels and steps, pdf tables similar to the one shown in Fig. 7.5 are linked in special Wiki-Bo tables called *reduction logs*. An example of reduction logs can be found in Fig. 7.6, where the reduction log of one particular night is shown. The color code here is simpler, since it summarized three possible cases:

- QC passed (blue) and frames archived;
- QC failed (red) and frames not archived;
- QC partially passed (purple) and frames archived¹⁰, but special care must be used in further analysis.

In all these cases, the link to the detailed pdf file that summarizes the star and frame QC levels can be found.

7.6.2 Higher level logging: the Primary and Secondary observations tables

For both primary and secondary SPSS¹¹, two tables called *primary*¹² and *secondary*¹³ *observations table* summarize, for each star, the actual status of both the observing campaign and reduction process, by assigning to each cell a color code. These tables are very important because they allow to see immediately what has already been done and what instead is still left to do: in order to know if new observation are needed, the Primary and Secondary observations tables have to be regularly updated (see Appendix A.1). A portion of the secondary observation table and the meaning of color codes used are shown in Fig. 7.7, where the meaning of each color code can be found. When a series is reduced and quality checked, the color code should change in different ways depending on both the results of the series level QC and the observation type. An example of a decision tree for color coding used in the primary and secondary observation tables is shown in Fig. 7.8.

¹⁰This can happen, for example, when all the frames required for a time series are present but the SPSS fails the star level QC step *d* step, or when the minimum number of frames needed to form the series, and defined in the observing protocol, is not reached (for more details on this last case see Chapter 8).

¹¹Both primary and secondary SPSS are described in Chapter 4.

¹²http://yoda.bo.astro.it/wiki/index.php/Primary_Observations_Table

¹³http://yoda.bo.astro.it/wiki/index.php/Secondary_Observations_Table

Quality Control on SPSS Photometric Frames and Photometric Catalogues Production

Secondary Observations Table

This table contains a summary of all the Secondary SPSS observations conducted up to now. Requirements (green mark) for each type of observation:

- Absolute Photometry:** At least 3 independent night points: each 3B+3V+3R in clear sky conditions.
- Short Variability:** One hour series at least 30 exposures in one blue filter (B or V).
- Long Variability:** At least 12 independent night points on 3 years, in one band. Yellow if there is at least one image.
- Spectrophotometry:** At least three spectra (blue+red), with wide slit (6 x seeing). Narrow slit = yellow.

LAST UPDATE (19 Jan 2011) Includes:

- Pilot Observations: all 'P' runs included (P-001/P-005).
- Variability/Photometry Runs: includes runs V-001/V-015, V-017/V-018, V-020, V-021a,b.
- Main Campaigns: includes runs M-001/M-017.
- Arcell Observations Summary & without transits (last update 09/12/2010 by GA) - (Obsolete: The targets can be selected using the following commands &?).
- Literature search for Secondary SPSS Parameters &? by AB, as of 09 May 2008 [outdated at the moment].
- If the star's name is clickable, it leads to the finding chart(s).

U1090-02779214

ID	Name	RA	Dec	B	V	Type	Abs. Phot	Short Var.	Long Var.	Spectra	Done	Obs. Data	Not Yet	Rejected
101	WD0046-051	00:49:09.90	+05:23:19.01	12.92	12.36	DZ7-8	4xObs	Done	9xObs	Done	Done	-	-	-
102	WD0134+483	01:41:31.00	+83:35:00.00	13.0	-	DA	3xObs	No	5xObs	Done	Done	-	-	-
103	G72-34	01:46:03.76	+35:54:48.80	13.84	12.98	-	6xObs	Done	8xObs	Done	Done	-	-	High Proper Motion Star
104	WD0148+467	01:52:02.96	+47:00:06.67	12.50	12.44	DA8	6xObs	Done	11xData	Done	Done	-	-	Landolt phot. std.
105	WD027+050	02:30:16.62	+05:15:50.89	12.745	12.799	DA	3xObs	No	10xObs	Done	Done	-	-	magnetic WD: to be rejected?
106	WD0316-649	03:09:59.89	-84:43:21.14	11.6	10.50	DA1	Not Yet	Res	3xObs	Not Yet	Done	-	-	-
109	WD0604-203	06:06:13.39	-20:21:07.30	11.75	11.80	He-Brd	6xObs	Res	7xObs	Done	Done	-	-	-
110	WD0621-376	06:23:12.20	-37:41:29.00	11.76	12.09	DA	1xObs	Res	8xData	Done	Done	-	-	Spinning Star
112	WD0644+375	06:47:37.99	+37:30:57.99	12.00	12.08	DA8	4xObs	No	7xData	Done	Done	-	-	-
113	WD0713+484	07:17:36.26	+48:24:20.51	12.00	11.91	DA	4xObs	P Res	8xData	Done	Done	-	-	-
114	G261-54	08:11:06.24	+79:54:29.56	10.57	10.07	60	1xObs	Done	2xObs	Done	Done	-	-	CPM pair, sep. 110"
115	G114-25	08:59:03.37	-06:23:46.19	12.51	11.92	F7	4xObs	Done	12xObs	Done	Done	-	-	-
116	G43-5	09:49:51.58	+06:36:35.50	13.18	12.52	K:	4xObs	P Res	10xData	Done	Done	-	-	-
118	G265-30	10:29:48.39	+42:59:44.90	13.49	12.85	-	6xObs	Done	9xObs	Done	Done	-	-	SRT: F=6174, sep=18.7"
119	WD1031-114	10:33:42.76	-11:41:38.35	12.82	13.00	DA8	3xObs	Done	9xObs	Done	Done	-	-	-

Figure 7.7: A screenshot of the Secondary Observation Table in WikiBo.

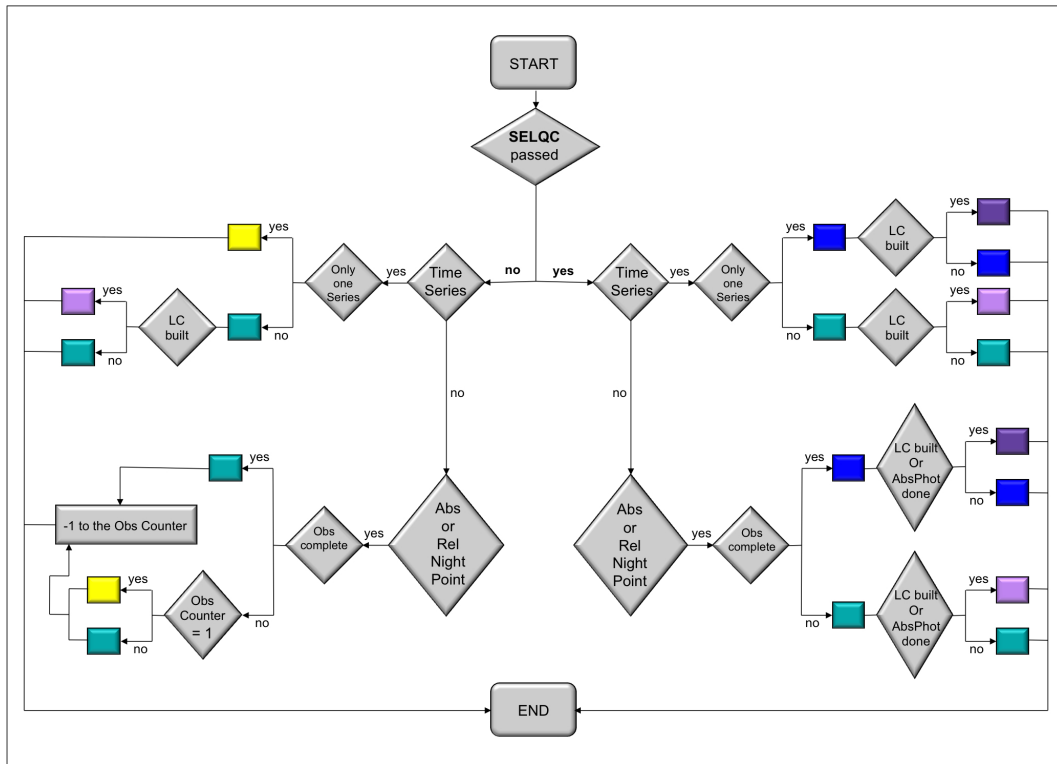


Figure 7.8: Example of a decision tree for color coding used in the Primary and Secondary Observations Tables for the imaging observation mode. In this Figure the decisional process used to assign a color code after the data analysis is shown as well, for completeness (Chapter 8).

7.6.3 The individual SPSS page

In Wiki-Bo, each SPSS has a dedicated page in order to summarize the literature information available for each star and the status of both acquisition and reduction of data (see Appendix A.1). On each individual SPSS page, a section called *Reduced Data* summarizes the status of data reduction in a table (see Fig. 7.9). When a series is reduced and all levels of QC are completed, this table is updated by adding a row (one for each observing run) in the reduction summary table. The meaning of color codes in this table is the same of the reduction logs tables (Section 7.6.1). In the *Photometric Pre-reduction & QC* subsection, for each series reduced and quality checked, the *QC résumé* file, the aperture photometry catalogues and the macro used to perform the star QC level are linked.

Quality Control on SPSS Photometric Frames and Photometric Catalogues Production

Reduced Data

Reduction Summary

Meaning of colors in the progress status tables.

No	No	Not needed or not present
XX	XX	Done by person XX (QA Still Missing)
XX	XX	Assigned to person XX
TBD	TDB	To be done
XX	XX	Quality Assurance = Rejected by XX
XX	XX	Quality Assurance = Partially Accepted by XX
XX	XX	Quality Assurance = Passed by XX

Lighter Colors mean that the reduction is a pilot reduction and that will need to be revised or even redone.

Run	Telescope	Photo PreRed	Photo AbsPhot	Photo ShortVar	Photo LongVar	Spectro PreRed	Spectro Wave/Ext	Spectro RelCal	Spectro AbsCal	Notes
V-007	La Silla	SMR	No	SMR	No	No	No	No	No	16 Sept: All Reference Stars fail QCb
		SMR	No	SMR	No	No	No	No	No	17 Sept: Heavy clouds during the series
		SMR	No	SMR	No	No	No	No	No	20 Sept: Only 24 frames the series. Low SNR in Ref Stars
		SMR	No	SMR	No	No	No	No	No	21 Sept
		SMR	No	SMR	No	No	No	No	No	22 Sept: All Reference Stars fail QCb
		SMR	No	SMR	No	No	No	No	No	23 Sept: Only 1 Red Star do not fails QCb
		SMR	No	SMR	No	No	No	No	No	24 Sept
		SMR	No	SMR	No	No	No	No	No	26 Sept

Photometric Prereduction & QC

- V-007 Service September 2008 --> 16 September : [Photometric QC resume](#) , [QCphot macro](#) and [SExtractor Catalogues](#)
- V-007 Service September 2008 --> 17 September : [Photometric QC resume](#) , [QCphot macro](#) and [SExtractor Catalogues](#)
- V-007 Service September 2008 --> 20 September : [Photometric QC resume](#) , [QCphot macro](#) and [SExtractor Catalogues](#)
- V-007 Service September 2008 --> 21 September : [Photometric QC resume](#) , [QCphot macro](#) and [SExtractor Catalogues](#)
- V-007 Service September 2008 --> 22 September : [Photometric QC resume](#) , [QCphot macro](#) and [SExtractor Catalogues](#)
- V-007 Service September 2008 --> 23 September : [Photometric QC resume](#) , [QCphot macro](#) and [SExtractor Catalogues](#)
- V-007 Service September 2008 --> 24 September : [Photometric QC resume](#) , [QCphot macro](#) and [SExtractor Catalogues](#)
- V-007 Service September 2008 --> 26 September : [Photometric QC resume](#) , [QCphot macro](#) and [SExtractor Catalogues](#)

Figure 7.9: The *Reduced Data* section from the SPSS106 individual page.

8

Short-term Constancy Monitoring of SPSS candidates

The obvious and fundamental requirement for an SPSS is that its magnitude is constant within the Gaia photometry requirements.

As explained in Chapter 4, it is mandatory that we monitor the stars that we will use as calibrators of all the Gaia spectrophotometry even for unlikely kinds of variability larger than $\simeq 0.01$ mag, i.e., larger than our best expected accuracy for the Gaia flux calibration. In addition to our study, Gaia observations themselves will further monitor variability, because each object will be observed tens of times. The candidate SPSS which will show variations larger than our requirement will be eliminated from the SPSS grid, which is built with some redundancy.

After writing the IFP protocols, performing the pre-reduction, building the aperture photometry catalogues and imaging QC pipelines, my task was to complete the semi-automated pipeline up to the production of short-term light curves. The procedure was tuned for the short-time constancy monitoring, but in principle it should be easily implemented also for the long-term constancy monitoring.

8.1 SPSS light curve production

In order to produce the light curve (LC) of an SPSS, I prepared a dedicated pipeline, which requires as input both the aperture photometry catalogues produced and quality checked with the procedures of Chapter 7 (see also Marinoni et al. 2011c), and a file containing the list of the epochs of acquisition of each frames. To build the LC plot, it is necessary to use the MJD at middle exposure, which normally is either not reported in the fits header at all, or it refers to the beginning of the exposure. Therefore, the MJD at the middle of the exposure must be derived using the obser-

vation UT date and time using, for example, the IRAF task *epoch*.

Template macros and detailed instructions to derive the MJD and to include the correct epochs in the pipeline input file can be found in Wiki-Bo¹ and in Marinoni et al. (2011d).

The LC pipeline is logically divided into two main steps. The first one takes the aperture photometry catalogues and the list of times as input. Using the reference stars chosen by the user, the difference between the magnitude of each star (including the SPSS) at that epoch and the average magnitude of the reference stars at the same epoch is computed. The first step of the pipeline assign to each magnitude measurement (both of the SPSS and the reference stars) the MJD discussed above. All these data are stored in a file used by the second step that computes some fundamental parameters for the evaluation of the light curve (see below) and produces the check plot of the SPSS light curve (see, for example, Fig. 8.1). The magnitudes of all the considered stars (the SPSS and all the reference stars) are reported to the same magnitude zero point by adding an appropriate constant, which is the difference between the median of each LC and that of one of the reference stars. This allows to plot all the LCs into a single window, which is the bottom panel of the check plot. The LC of the SPSS minus this average magnitude is plotted in the upper panel of the final plot. An output file containing the resulting (relative)LC for the SPSS is also produced. The parameters computed by the pipeline are:

- σ_{prec} : this is the average sigma of the reference stars and provides an indication on the quality of measurements (Section 8.2.1);
- σ_*/σ_{prec} : being σ_* the sigma of the SPSS light curve, this ratio is one of the fundamental indicators we use for the LC analysis (Section 8.2.2);
- $F_{\pm 1\sigma}$: this is the fraction of SPSS light curve points lying within $\pm 1\sigma_{prec}$ (Section 8.2.2). For a gaussian distribution this should be $\simeq 68.8\%$;
- $(P - N)/T$: this is the fractional asymmetry between positive and negative values in the SPSS light curve (Section 8.2.2).

¹http://yoda.bo.astro.it/wiki/index.php/Short_Term_Lightcurves

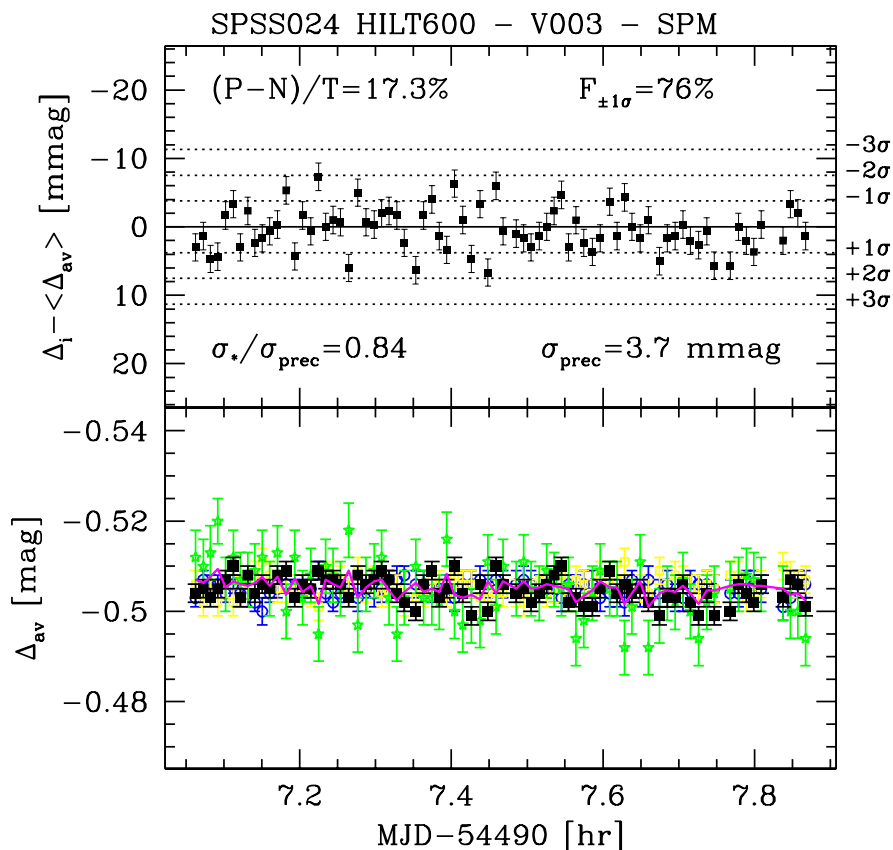


Figure 8.1: SPSS 024 light curve produced with data acquired with LaRuca@SPM1.5 during run V-003 (24 January 2008). In the *bottom panel* the LCs of the reference stars are plotted in different colors and with open circles, while the SPSS is plotted using black filled squares. The average of all reference stars LC is plotted as a magenta line. The LC of the SPSS minus this average magnitude is plotted in the *upper panel*. The ± 1 - 2 - 3σ thresholds are plotted as dotted lines: this is the average sigma of the reference stars and tracks the precision to which the magnitude of constant stars is reproduced over the whole series. This value is also reported as σ_{prec} in the bottom right corner of the panel. Top panel also reports the parameters described in the text: σ_*/σ_{prec} , $F_{\pm 1\sigma}$ and $(P-N)/T$.

An example of a LC produced using the pipeline is shown in Fig. 8.1. In both panels, points above the mean indicate a brightening of a given star, points below the mean indicate a fading of the star with respect to the average of all chosen reference stars.

8.2 Analysis of light curves

In the case of the short-term constancy monitoring data, there are two levels of the analysis which are mandatory. The first one is the QC of the LC which tells us if the LC has the capability of revealing variations of the required level (up to 0.01 magnitudes). The second level is the monitoring of the SPSS itself against short-term variability, which allows to decide if the candidate SPSS should be retained or rejected.

8.2.1 Time series and light curve QC

The first Quality Control parameter come from the series level QC performed as described in Chapter 7, which verifies that all the observational requirements (Pancino et al. 2010a) were met.

Summarizing, in the case of time series for the short-time constancy monitoring, a series is accepted if (see Chapter 7 for more details):

- the time series lasts at least one hour;
- the time series contains at least 30 good exposures;
- there are at least two comparison stars in the field which are not saturated or too faint, observed under good seeing conditions and not too much out of focus, and free of bad pixels and close neighbours;
- the SPSS is not saturated or too faint, observed under good seeing conditions and not too much out of focus, and free of bad pixels and close neighbours.

The production of light curves entails little effort, being all the photometric catalogues already produced and quality checked in a previous step (Chapter 7). So, even if the time series fails some steps of QC (for example, the S/N ratio is too low, or there are not enough frames in the time series) it may be advisable to have a look at the LC. In this case an SPSS can not be validated or rejected (new observations are needed), but its light curve can still provide some indication on the behavior of

the SPSS with respect to short-term constancy.

When the light curve is produced, it must pass a QC on its accuracy in order to assess its possibility to detect SPSS variations larger than our best expected precision and accuracy for the Gaia flux calibration. The QC parameter to be considered is σ_{prec} : the light curve is accepted only if $\sigma_{prec} \leq 10$ mmag.

The σ_{prec} tracks the precision to which the magnitude of constant stars is reproduced over the whole series. Since we want to be sure to detect all kinds of variability larger than 10 mmag, this is the minimum level of precision that we can accept in our light curves.

8.2.2 Constancy Criteria

The simplest form of variable star analysis is the inspection of the shape of the light curve, and the time and magnitude of maximum and minimum, if any. The term *range* is usually adopted to denote the difference between maximum and minimum. The term *amplitude* is often used to denote the half range, as in the coefficient of a sine or cosine function. Therefore, for our purposes:

- The SPSS is judged *constant* and is validated against short term variability if no evident pattern is present in the LC and if $\sigma_{prec} \leq 10$ mmag. In this case variations, if any, have amplitude lower than σ_* . An example of *constant* SPSS is shown in Fig. 8.3.
- The SPSS is judged *variable* and rejected if a pattern is clearly present in the light curve, if $\sigma_{prec} \leq 10$ mmag and if amplitude $A > 5$ mmag. In order to account also for asymmetric curves (see, for example, Fig. 9.5 in Chapter 9), we can define a *maximum* amplitude as $A_{max} = \max(LC_{max}, |LC_{min}|)$. An example of *variable* SPSS is shown in Fig. 8.4.

If the time series is rejected (because it lasts less than 1–2 hours or there are less than 30 frames accepted from the QC of Chapter 7) and/or the LC is rejected ($\sigma_{acc} > 10$ mmag), the SPSS can not be validated or rejected but, as mentioned before, its light curve can still provide some indication on the behavior of the SPSS with respect to variability, which can be used to interpret newer data. In these cases:

- The SPSS is judged *likely constant* if no evident pattern is present in the LC. Two examples of *likely constant* SPSS are shown in Fig. 8.5 and Fig.8.6.
- The SPSS is judged *suspect variable* if a pattern is present in the LC. An example of *suspect variable* SPSS is shown in Fig. 8.7.

Short-term Constancy Monitoring of SPSS candidates

The LC plot reports three other parameters that can be used to better understand the SPSS behavior: $F_{\pm 1\sigma}$, $(P - N)/T$ and σ_*/σ_{prec} . $F_{\pm 1\sigma}$ is the fraction of SPSS LC points lying within $\pm 1\sigma_{prec}$: this should be $\simeq 68\%$ for a gaussian scatter. That is what expected if the observed variation of the SPSS LC is just due to observational errors, not to a real variability of the source. $(P - N)/T$ is the fractional asymmetry between positive and negative values in the SPSS LC: as in the previous case, a gaussian scatter would be symmetric about zero, and this parameter should be ~ 0 as well.

In Fig. 8.2 we report the distribution of σ_*/σ_{prec} for all LCs analyzed up to 31 December 2010. The figure suggests that we can use σ_*/σ_{prec} as a robust *variability tracker*: if $\sigma_*/\sigma_{prec} \gtrsim 3$ the star can be reasonably considered variable.

The results of the analysis of all the SPSS short-term light curves are available in a dedicated page hosted in Wiki-Bo² (see Appendix A.1.1).

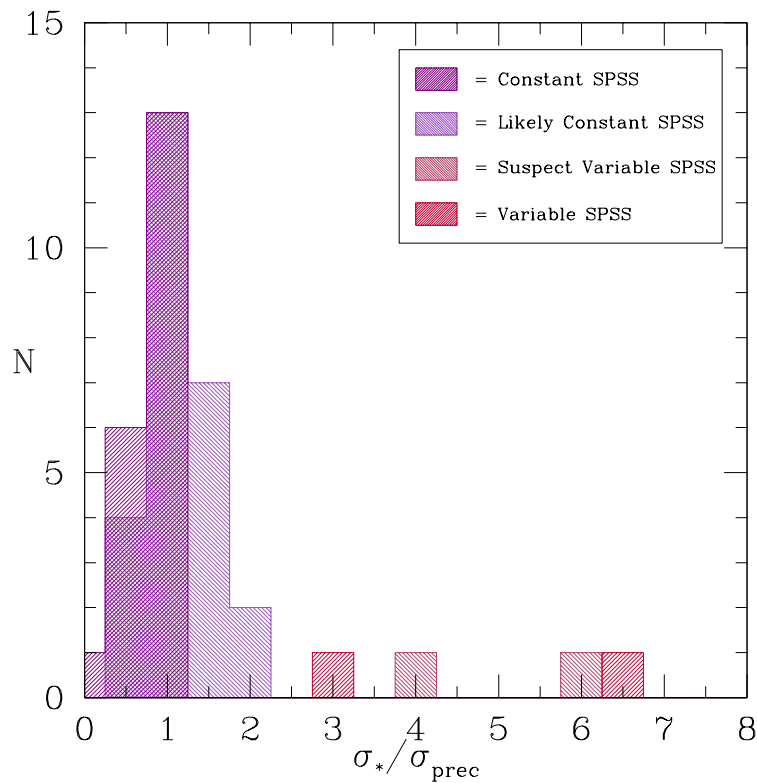


Figure 8.2: Distribution of σ_*/σ_{prec} for all LCs quality checked and analyzed at 31 December 2010.

²http://yoda.bo.astro.it/wiki/index.php/Short_Term_Lightcurves

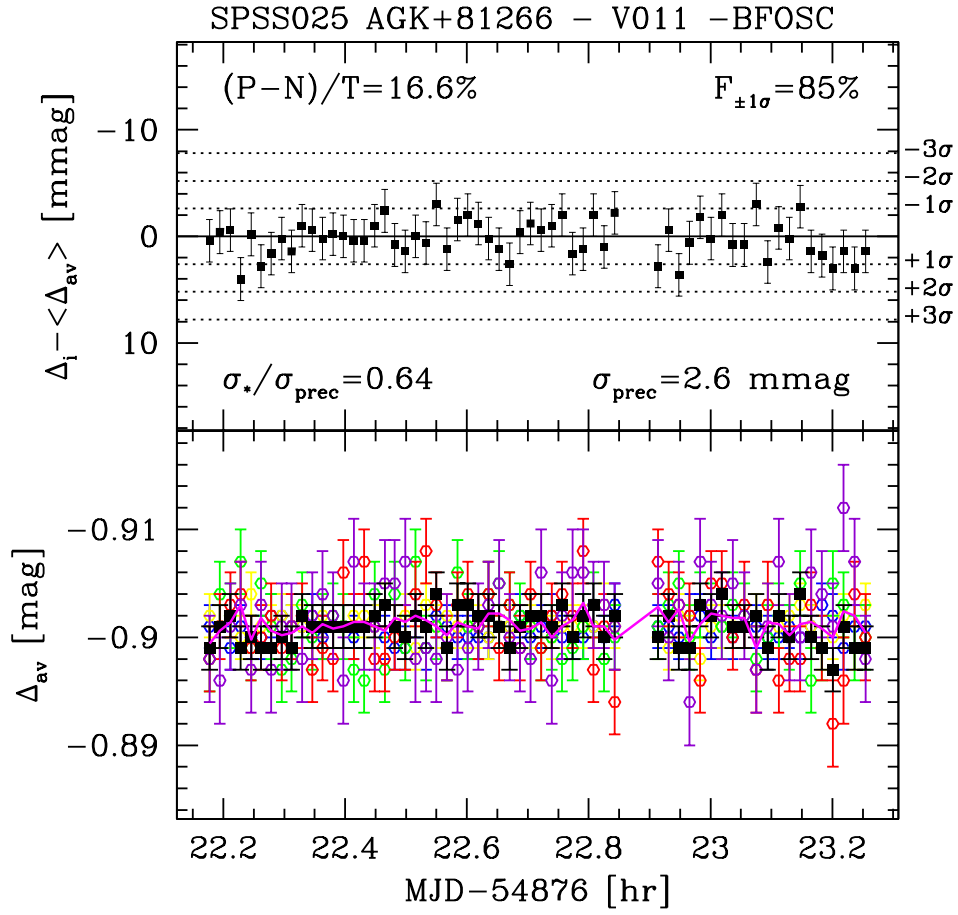


Figure 8.3: Light curve of SPSS025 produced using data acquired with BFOSC@Cassini during run V-011 (14 February 2009). The LC is accepted ($\sigma_{prec}=3.7$ mmag) and no pattern is present in the LC: SPSS 025 is judged a *constant* star and it is validated against short-term variability.

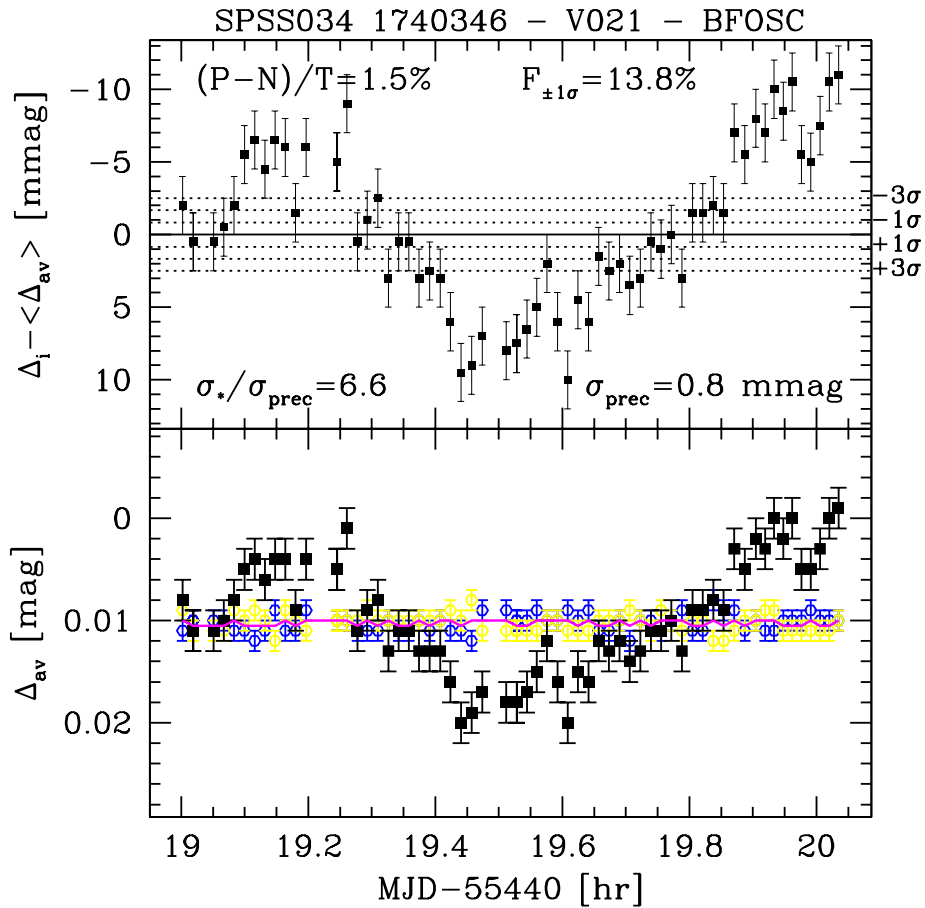


Figure 8.4: Light curve of SPSS034 produced using data acquired with BFOSC@Cassini during run V-021 (01 September 2010). The LC is accepted ($\sigma_{\text{prec}}=0.8$ mmag) and a variability pattern is clearly present: SPSS 034 is judged a *variable* star with amplitude $A \simeq 10.5$ mmag and period longer than $P \simeq 50$ minutes, and rejected.

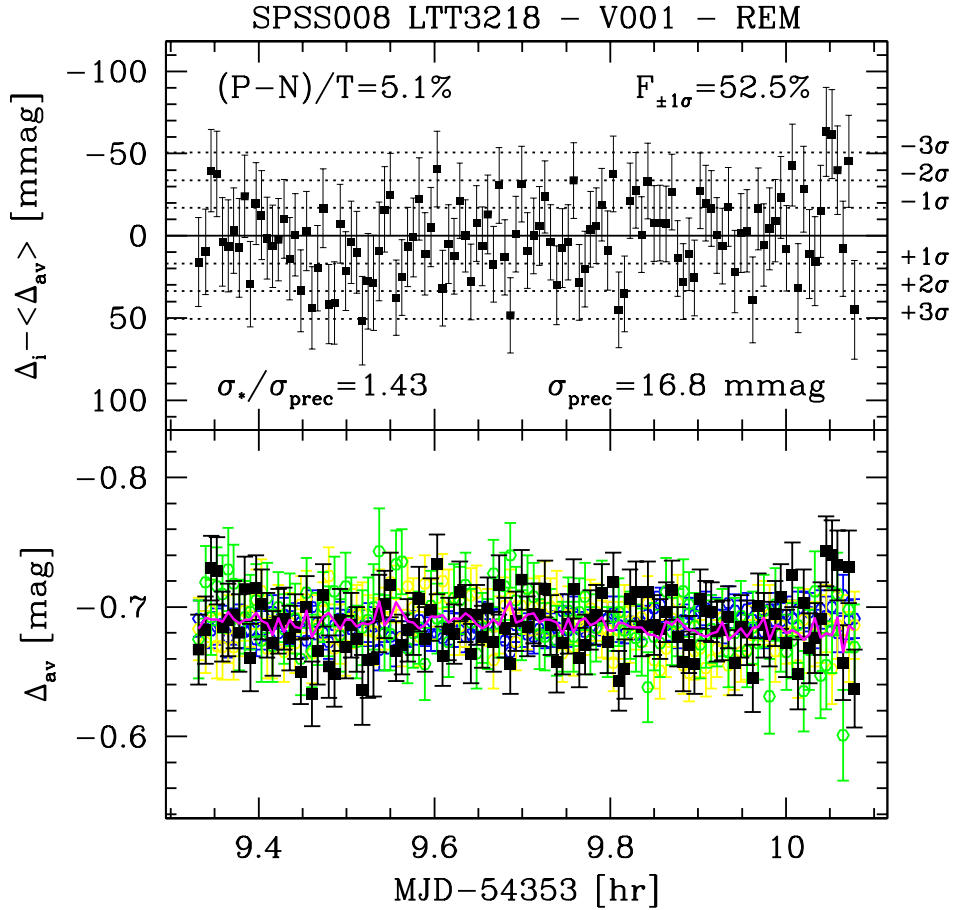


Figure 8.5: Light curve of SPSS 008 produced using data acquired with ROSS@REM during run V-001 (09 September 2007). The LC is rejected ($\sigma_{prec}=16.8$ mmag) because all stars in the time series have low S/N. However, no pattern is evident, so SPSS 008 is at the moment judged a *likely constant* star. New observations with good S/N are needed in order to validate this SPSS.

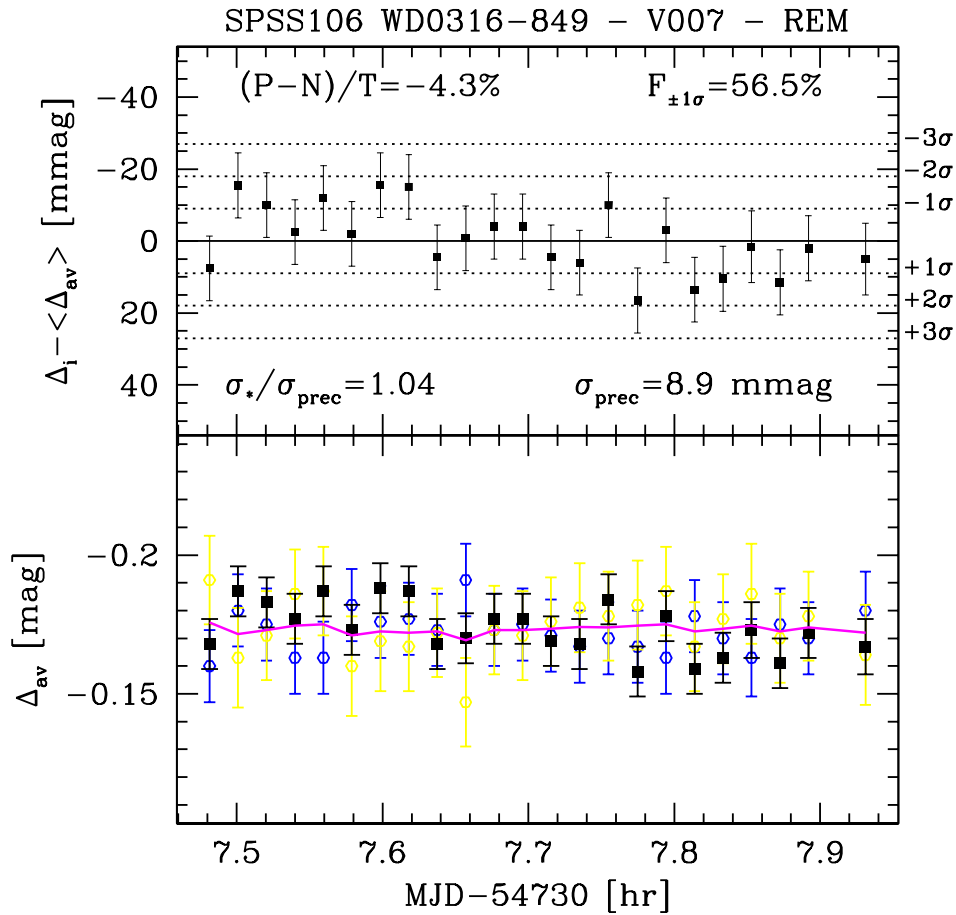


Figure 8.6: Light curve of SPSS 106 produced using data acquired with ROSS@REM during run V-007 (20 September 2008). The LC is rejected, even if $\sigma_{prec}=8.9$ mmag, for the following reasons: there are not enough points in the time series, the series lasts less than 1 hour and, in addition, the one of the reference stars (yellow circles) has too low S/N. In spite of all this, no pattern is evident, so SPSS 106 is at moment judged a *likely constant* star. New observations are needed in order to validate this SPSS.

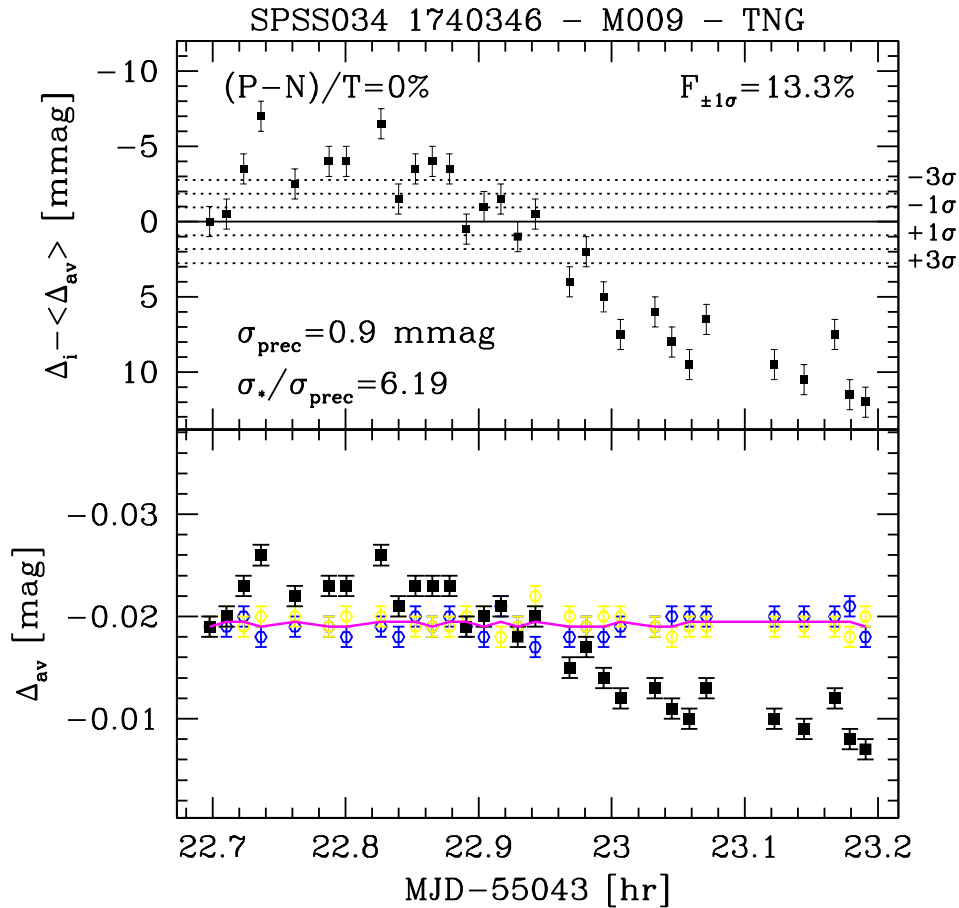


Figure 8.7: Light curve of SPSS034 produced using data acquired with DO-LoRes@TNG during run M-009 (31 July 2009). Even if σ_{prec} is very good ($\sigma_{prec}=0.9$ mmag), the LC is rejected because the first part of the time series fails the QC on S/N and seeing, and therefore only 30 minutes of good data were acquired. However, a pattern is evident in the good part of the time series, so SPSS034 was temporarily judged a *suspect variable* star. This indication was confirmed with the data acquired with BFOSC@Loiano (see Fig. 8.4).

9

Future prospects and scientific outcome

The observing campaigns for the absolute flux calibration of the Gaia spectrophotometry (described in Chapter 3) represent a huge effort: at survey completion they will amount to $\simeq 400$ observing nights at six different telescopes and instruments, and they will produce almost 100 000 frames to be reduced and analyzed. The survey started in late 2006 and the estimated completion will be around 2014.

The kind of data available at the end of the survey for each candidate SPSS are expected to be:

- the flux tables (calibrated spectra), with an uncertainty of 1-3% with respect to Vega;
- absolute B, V and R (and sometimes I) photometry, based on at least three independent night points;
- night points to monitor long-term photometric constancy in B, V and R (and sometimes I) amounting to at least 12 independent observations in 3 years;
- except for a few well known stars, a light curve in one band (usually B or V) to monitor the short-term (1-2 hrs) photometric constancy.

The main use of the SPSS grid is of course the absolute calibration of Gaia spectrophotometric data. Nevertheless, such a large grid (200–300 stars) represents an unprecedented catalogue of spectro-photometric standard stars, characterized by high precision and accuracy, full sky coverage and with stars spanning a wide range of spectral types. Most of our SPSS are WDs and hot subdwarfs, the remaining are dwarf/giant stars covering different spectral types, including cold stars of late spectral type up to M. For comparison, CALSPEC, containing the composite stellar spectra which are the fundamental flux standards for HST calibrations, consist of

about 60 stars: our SPSS grid will be more than three times larger, and it will be about two times larger than the Stritzinger et al. (2005) catalogue. Our sample will be comparable to very recent catalogues, such as the STIS Next Generation Spectral Library Version 2¹ which, in any case, do not meet as well all Gaia requirements (such as, for example, the magnitude range).

9.1 Scientific implications

9.1.1 White dwarfs atmosphere and compact pulsators

However, other scientific outcomes are foreseen. The main topics that we can explore scientifically are hot stars and stellar variability. Given the high number of WDs in our sample and the high quality of our spectra, they can be used to study the atmospheres of WDs in order to determine their atmospheric parameters. In addition, as explained in Chapter 8, when we selected our SPSS candidates, we tried to exclude stars lying within the WD instability strips. The determination of atmospherical parameters for our huge sample of WD could help to better define, from an observational point of view, both the blue and red edges of the instability strips (Fontaine & Brassard 2008).

Anyway, in many cases, the existing information was not sufficient (or sufficiently accurate) to firmly establish the constant nature of a given star². Therefore, some variable stars could be present in our sample and, in such a case, the scientific output is straightforward.

There are three distinct families of isolated pulsating white dwarfs. These are the *GW Vir* stars (He/C/O-atmosphere stars with $T_{eff} \simeq 120\,000$ K), the *V777 Her* stars (He-atmosphere, $T_{eff} \simeq 25\,000$ K), and the *ZZ Ceti* stars (H-atmosphere, $T_{eff} \simeq 12\,000$ K), all showing multiperiodic luminosity variations caused by low-order and low-degree g-mode instabilities. Fig. 9.1 shows the region of the $\log g - \log T_{eff}$ plane where the compact pulsators are found. About 80% of the white dwarfs descend from post-AGB remnants which have retained a thin hydrogen envelope. The red curve shown in Fig. 9.1 represents the evolution of such H-atmosphere white dwarfs. This channel leads to the formation of a first family of compact pulsators, the *ZZ Ceti* white dwarfs, by the time a star evolves through a narrow range of effective temperature centered around $T_{eff} \simeq 11\,800$ K, in which H recombines in the envelope

¹<http://archive.stsci.edu/prepds/stisngsl/>

²This is one of the reasons why we perform the short-term constancy monitoring.

of the star. Most of the remaining 20% of WDs descend instead from post-AGB remnants that have managed to get rid of their residual H through the born-again scenario. This second channel gives rise to two other families of compact pulsators: the extremely hot GW Vir stars, and the much cooler V777 Her stars. There is a natural evolutionary link between these two types of pulsators along the blue curve shown in Fig. 9.1, and a GW Vir star is bound to pulsate again later in its lifetime, but at that time as a DB white dwarf. Pulsating WDs show variability with periods from about 100 to 1000 seconds and amplitudes from about 1-2% up to 30% of their flux (see Fontaine & Brassard 2008 for a review).

In addition to the three classes of pulsating white dwarfs just described, two other categories of pulsators were later discovered: both belong to the class of hot B subdwarf (sdB) stars. The *short-period pulsating sdB* stars were discovered some ten years ago (Kilkenny et al. 1997). They are p-mode pulsators (officially named *V361 Hya* stars) with periods of about 2-5 minutes, though periods as long as 9 minutes are known. They can exhibit from 1 to over 40 pulsation modes and occur amongst the hotter sdB stars with $28\,000 < T_{eff} < 35\,000$ K and $5.2 < \log g < 6.1$. In the same general area of the $\log g - \log T_{eff}$ plane (see Fig. 9.1), but distinctly cooler and less compact, one finds the second family of pulsating sdB stars, the *long-period variables* (or *V1093 Her* stars) discovered more recently by Green et al. (2003). These stars are g-mode oscillators like the pulsating white dwarfs, and typically have periods of about 1-2 hours. Like the rapid sdB pulsators, they are multiperiodic but occur amongst sbB stars with $T_{eff} < 27\,000$ K and $\log g \sim 5.4$ (see Kilkenny 2007 for a review). The sbB are extreme horizontal-branch stars: low-mass stars, with a He-burning core surrounded by a H-rich shell, but whose outer H-rich layers were too thin ($0.02 M_{\odot}$ or less) for them to evolve to the asymptotic giant branch on the Hertzsprung-Russel diagram. They will eventually end their lives as low-mass WDs, as shown in Fig. 9.1.

Our light curves, covering 1–2 hours, in principle can find both WD and sdB pulsators. However, since WDs represent the 51% of our sample while sdB only the 6%, the probability of find the latter type of variable in the Gaia SPSS grid is probably very low, especially due to the care we used in the selection of the most likely constant candidates.

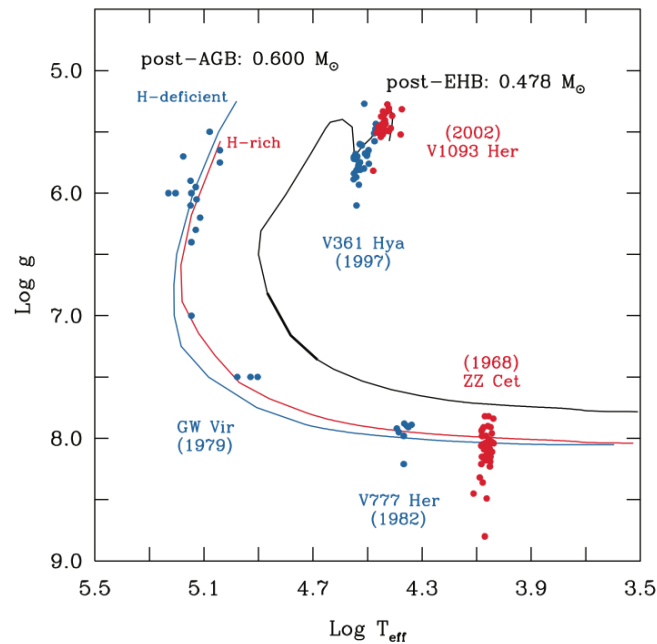


Figure 9.1: Region of the $\log g - \log T_{eff}$ plane where the compact pulsators are found. Each of the five distinct families is identified by its official IAU name, and the year of the report of the discovery of the prototype of each class is also indicated. Typical evolutionary tracks are plotted showing (1) the track followed by a $0.6 M_{\odot}$ post-AGB, H-rich star, which becomes a H-atmosphere white dwarf (red curve), (2) the path followed by a $0.6 M_{\odot}$ post-AGB, H-deficient star, which becomes a He-atmosphere white dwarf (blue curve), and (3) the path followed by a $0.478 M_{\odot}$ post-EHB model, which leads to the formation of a low-mass H-atmosphere white dwarf (black curve). Figure from Fontaine & Brassard (2008)

9.1.2 Other kinds of variables

As mentioned before, a time series of 1–2 hours is acquired for the short-term constancy monitoring of our SPSS candidates. Therefore we expect to find if any, only short-period variable stars in this particular campaign. Given the range of spectral types contained in our survey, the most common kind of variable we can expect to find are δ Scuti stars. They are pulsators of spectral types ranging from late-A to early-F, with short periods, and generally small amplitudes. They lie in the downward extension of the Cepheid instability strip (Fig. 9.2), where it crosses the densely populated main sequence. Therefore they are stars on the main sequence or

on their way from the main sequence to the giant branch. As a result, they are the most numerous and common pulsating variables among bright stars (Breger 2000, for a review). δ Scuti stars make up about a third of all A5-F2 III-V stars, therefore precision surveys of such stars are a fruitful source of new variables. The periods of δ Scuti stars range typically between 0.02 and 0.25 days: with our light curves we can expect to see at least those characterized by short period pulsations (many of these stars are multiperiodic). The amplitudes of their pulsations range typically from a few hundredths to a few tenths of magnitude, with smaller amplitudes being more common. Large amplitudes are rare: less than 1% of δ Scuti stars have amplitudes greater than 30% of their flux.

Regrettably, one should not regard the simple definition and description done above as complete. As explained in Breger (2000), we must consider two additional astrophysical situations: the evolved population II stars inside the classical instability strip with δ Scuti-like periods, and the massive stars evolving through the instability strip.

The massive ($M > 2M_{\odot}$) stars evolving from the main sequence towards the giant region cross the instability strip on nearly horizontal tracks at higher luminosities in the Hertzsprung-Russell diagram. The evolutionary state identifies them as δ Scuti stars but, due to their high mass and luminosity, the periods are longer than those of average δ Scuti star and may get as large as one day. Consequently, they overlap the RR Lyrae stars in period, which are in the post-giant stage of evolution and have low masses (below $1 M_{\odot}$). Breger (2000) proposed that these long-period δ Scuti stars can be distinguished from RR Lyrae stars by considering the size of stellar rotations: RR Lyrae stars show no detectable rotation ($v \sin i \leq 10$ Km/s), while evolved δ Scuti stars do (Petersen, 1996). Some δ Scuti stars are (pure) radial pulsators, while the majority pulsate with a large number of non-radial p-modes simultaneously. The non-radial pulsations of δ Scuti stars found photometrically are low-degree ($\ell \leq 3$) and low-order ($n = 0$ to 7) p-modes, while spectroscopic studies have confirmed the presence of high-degree non-radial modes with ℓ up to 20 (e.g., for the star τ Peg, Kennelly et al. 1998).

In addition to the vast majority of small-amplitude δ Scuti stars (pulsating mainly with non-radial p-modes), it is astrophysically reasonable to define two subgroups of δ Scuti stars:

- the *high-amplitude δ Scuti stars (HADS)* are the δ Scuti stars with amplitudes ≥ 0.30 mag. These stars are radial modes pulsators, with one or two radial modes simultaneously excited with typical amplitudes of 0.5 mag.

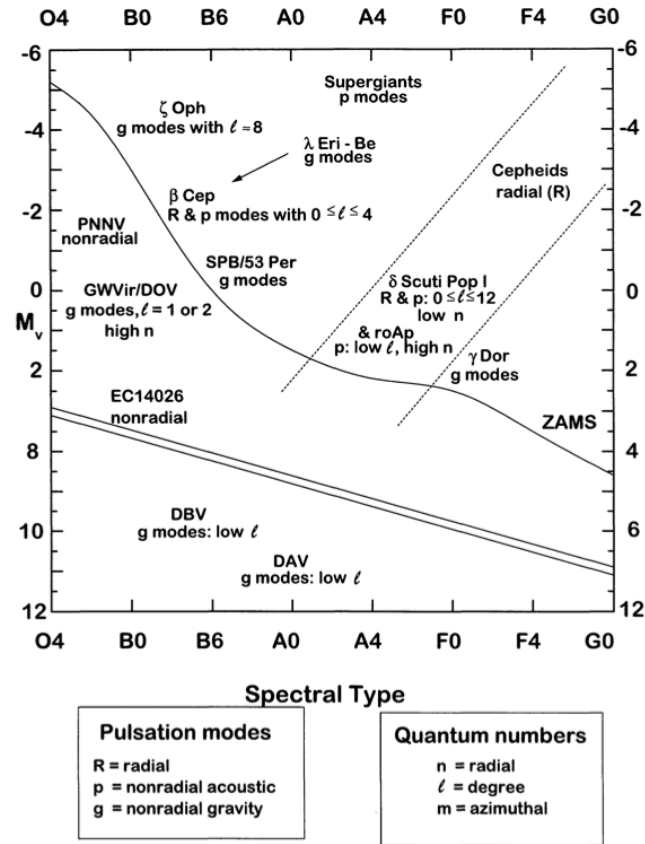


Figure 9.2: The position of δ Scuti variables in relation to other types of variable of Pop. I in the hot part of the Hertzsprung-Russel diagram. As explained in Breger (2000), from which this figure is adapted, some positions of the variables are tentative and some mode identifications may be speculative. The position of EC14026 stars (other name for the sdB pulsating stars) is taken from Koen et al. (1998).

- the *SX Phoenicis* variables are the δ Scuti stars of Pop. II and intermediate-age or old disk population. Since such stars at $\simeq 8500$ K should have already evolved away and no longer exist in this part of Hertzsprung-Russel diagram, they are also unusual from an evolutionary point of view. They probably are in a post-giant branch stage of evolution and may be merged binary stars. It is important to note that most *SX Phoenicis* stars are also HADS, but not vice versa.

There are also other kinds of short-period variable stars, which could in principle be

found in our survey, even if with a much lower probability. They are:

- β Cephei star: these variables are sometimes known as β Canis Majoris stars, because this star (like many of the class, but unlike β Cephei itself) is multiperiodic. In the General Catalogue of Variable Stars, they are classified as BCEP (with the exception of three apparently shorter-period stars which, for some reason which might not have any physical significance, are sub-classified as BCEPS). The multi-periods are often close to each other, and produce a characteristic rise and fall in the amplitude of pulsations called the *beat effect*. In the stars which are multiperiodic, there is usually one radial period and one or more non-radial periods. In a spherical non-rotating star, these non-radial periods would be degenerate (i.e., they would have the same values). But the rotation removes the degeneracy, the periods become slightly different, and they combine and interfere to produce the beat effect. These stars have spectral types of B0-B2 III-V, corresponding to temperatures of 20 000-30 000 K, and are near the top of the main sequence on the Hertzsprung-Russell diagram. Their masses are typically 10–20 times that of the sun. They have periods of 0.1 to 0.3 days and, though their radial velocity amplitudes are quite large, their visual light amplitudes are very small, typically only a few hundredths of a magnitude in visual. As expected for a hot star, in ultraviolet light, where most of the flux from these hot stars is found, their amplitudes are up to a magnitude. The small visual amplitude explains why the measurement of radial velocity variations has generally been adopted as the observational method.
- *roAp* stars: the *rapidly oscillating Ap stars* (roAp) are a subtype of the Ap star class that exhibit rapid photometric and radial velocity variations. The known periods range between 5 and 21 minutes. They lie in the δ Scuti instability strip on the main sequence, as shown in Fig. 9.2. The *peculiar A stars* (Ap) are a small group of main sequence B8 to F2 stars whose spectra are quite peculiar: the apparent abundance of certain elements is thousands of times different than in the Sun. About 5% of mid-B to mid-F stars are Ap stars. The roAp behavior is more prevalent among cooler Ap stars, those showing enhancement of strontium, chromium or europium. These stars have strong global magnetic fields, typically ranging of a few kG to tens of kG. The roAp stars oscillate in high-overtone, low-degree, non-radial pressure modes. The usual model that is used to explain the behaviour of these pulsations is the oblique pulsator model (Kurtz 1982, Shibahashi & Takata 1993). In this model the axis of pulsation is

Future prospects and scientific outcome

aligned with the magnetic axis, which can lead to modulation of the pulsation amplitude, depending on the orientation of the axis with respect to the line of sight, as it varies with rotation. The apparent link between the magnetic axis and the pulsation axis gives clues to the nature of the driving mechanism of the pulsations. As the roAp stars seem to occupy the main sequence end of the δ Scuti instability strip, it has been suggested that the driving mechanism may be similar, i.e., the opacity mechanism operating in the hydrogen ionization zone. No standard pulsation model can be made to excite oscillations of the roAp type using the opacity mechanism. As the magnetic field appears to be important, research has taken this into account in deriving non-standard pulsation models. It has been suggested that the modes are driven by the suppression of convection by the strong magnetic field near the magnetic poles of these stars (Balmforth et al. 2001) which would account for the alignment of the pulsation axis with the magnetic axis. An instability strip for the roAp stars has been calculated (Cunha 2002) which agreed with the positions on the Hertzsprung-Russell diagram of the roAp stars discovered up to that point, but predicted the existence of longer period pulsators amongst the more evolved roAp stars. Such a pulsator was indeed discovered in HD 116114, which has the longest pulsation period of any roAp star: 21 minutes (Elkin et al. 2005).

9.2 Variable SPSS examples

Up to now we reduced and analyzed about 20% of our sample in the context of the short-term constancy monitoring campaign. About 5% of the analyzed sample turned out to be variable for our criteria. Therefore, we can expect to find the same fraction of variable stars among our candidates, i.e., between a handful and a maximum of about 20 variables.

To show the scientific potential of constancy monitoring campaigns, I describe here a very preliminary analysis of the two variable SPSS found up to now (see Chapter 8 for constancy criteria). They are the most likely δ Scuti variable SPSS 034 and the puzzling case of SPSS 172.

9.2.1 SPSS 034

SPSS 034 is one of our primary SPSS, selected from CALSPEC³. The literature data available for this star are reported in Table 9.1. From our short-term variability monitoring, SPSS 034 turned out to be a variable star, as shown in Fig. 9.3. Following the criteria described in Chapter 8, SPSS 034 was rejected from our sample of candidate SPSS. Nevertheless, it is an interesting star: from the inspection of its light curve, it seems to have a short oscillation period (at least 50 minutes, but probably a little bit longer⁴) and low amplitude ($\simeq 10$ mmag). These are the typical signatures of δ Scuti type oscillations.

Table 9.1: SPSS 034 available literature data

SPSS 034 available data		
name	2MASS J17403468+6527148	from 2MASS ^a
α_{2000}	17 40 34.68	from 2MASS
δ_{2000}	+65 27 14.80	from 2MASS
l_{2000}	095.1748	from 2MASS
b_{2000}	095.1748	from 2MASS
Spectral Type	A6V	from CALSPEC ^b
	A5V	from SIMBAD ^c
V	12.48	from CALSPEC
	12.50	from SIMBAD
B	12.68	from CALSPEC
	12.90	from SIMBAD
J	12.079	from 2MASS
H	12.022	from 2MASS
K	11.996	from 2MASS

^a: Cutri et al. (2003), <http://irsa.ipac.caltech.edu/applications/Gator/>

^b: www.stsci.edu/hst/observatory/cdbs/calspec.html

^c: <http://simbad.u-strasbg.fr/simbad/>

³At present, this star is still used in CALSPEC as spectro-photometric standard star, and it will be also used for the JWST calibration (Bohlin & Cohen 2008).

⁴Unfortunately we can not see two maxima in our light curve, therefore this is only a rough estimate.

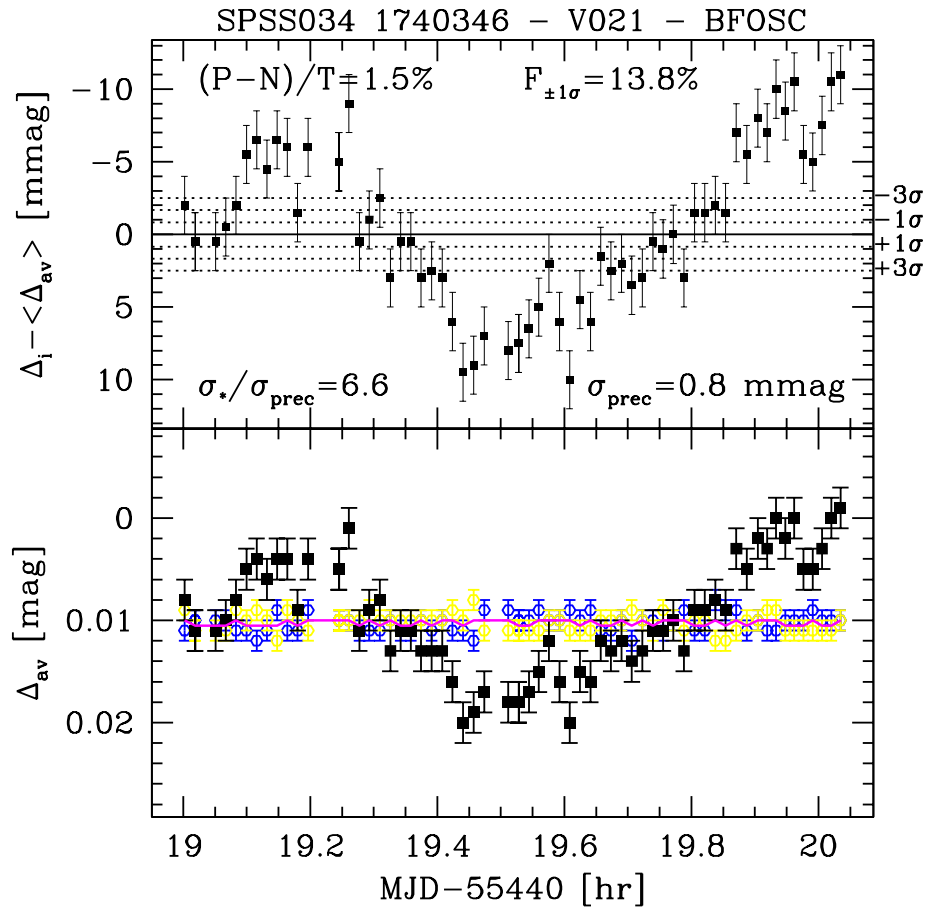


Figure 9.3: SPSS 034 light curve produced using data acquired with BFOSC@Cassini during run V-021 (01 September 2010). A variability pattern is evident in the light curve: SPSS 034 is most probably a δ Scuti star.

In order to preliminarily estimate some fundamental parameters (such as mass, T_{eff} and distance) of SPSS 034, I used appropriate theoretical isochrones from the BaSTI database⁵ (Pietrinferni et al. 2004, 2006), both scaled-solar and α -enhanced, of four different metallicity levels (solar metallicity: $[\text{Fe}/\text{H}] \simeq -0.2$, two intermediate low metallicity: $[\text{Fe}/\text{H}] \simeq -0.7$ and $[\text{Fe}/\text{H}] \simeq -1.5$, and extreme low metallicity: $[\text{Fe}/\text{H}] \simeq$

⁵<http://albione.oa-teramo.inaf.it/index.html>

2.3). The $[\text{Fe}/\text{H}]$ values used to select both the scaled-solar and α -enhanced isochrones are similar (see Fig. 9.4). I collected magnitudes of SPSS 034 from the literature and corrected them for reddening using the Schlegel maps (Schlegel et al. 1998) which provide an upper limit on the reddening correction, in order to build the color-color diagram shown in Fig. 9.4. The error bars in the plot take into account the uncertainty on the reddening correction.

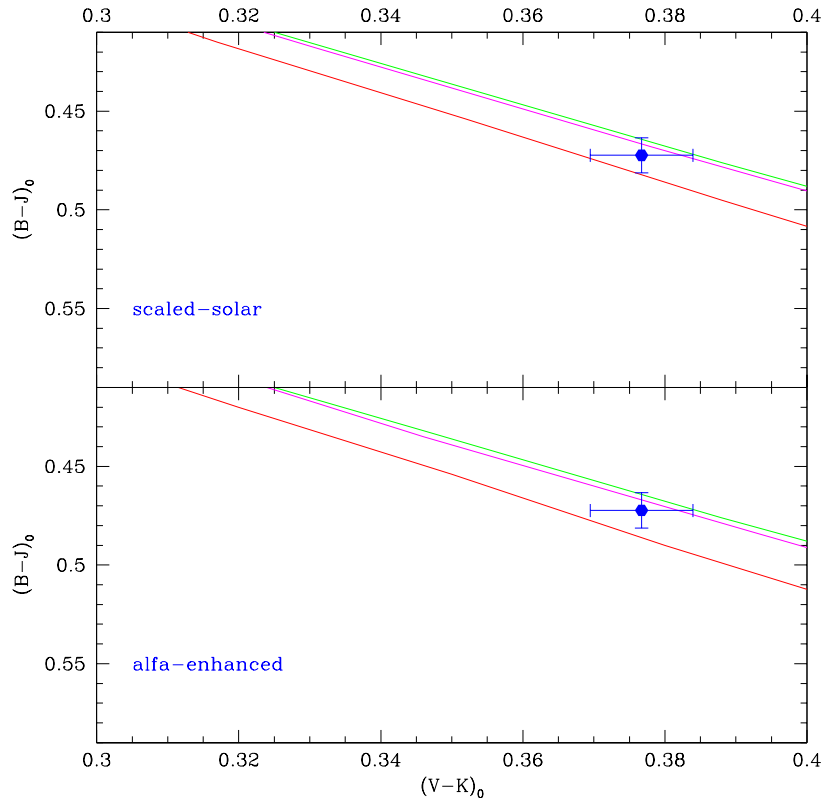


Figure 9.4: *Upper panel:* scaled-solar isochrone tracks (red: $[\text{Fe}/\text{H}] = -0.25$; violet: $[\text{Fe}/\text{H}] = -0.66$; green: $[\text{Fe}/\text{H}] = -1.49$; cyan: $[\text{Fe}/\text{H}] = -2.27$). *Bottom panel:* α -enhanced isochrone tracks (red: $[\text{Fe}/\text{H}] = -0.29$; violet: $[\text{Fe}/\text{H}] = -0.70$; green: $[\text{Fe}/\text{H}] = -1.62$; cyan: $[\text{Fe}/\text{H}] = -2.27$). In both panels, the blue point and error bars represent the colors of SPSS 034 corrected for reddening (see text).

I tried to estimate the mass, the T_{eff} , the distance and the height above the galactic plane of SPSS 034 from both scaled-solar and α -enhanced isochrones. In spite of the huge error bars, the intermediate low metallicity isochrones ($[\text{Fe}/\text{H}] = -0.66$ and $[\text{Fe}/\text{H}] = -1.49$ for the scaled-solar isochrones; $[\text{Fe}/\text{H}] = -0.7$ and $[\text{Fe}/\text{H}] = -1.62$

Future prospects and scientific outcome

for the α -enhanced isochrones) seem to better describe our data point rather than the solar or the lower metallicity ones. First of all, I derived all possible colors for SPSS 034 from the literature data, corrected for reddening. Then for each color, I derived the star parameters (mass, $\log T_{eff}$, and the absolute magnitude M_v) from each intermediate metallicity isochrone choosing the isochrone point closest in color. With the M_v and apparent dereddened V magnitude (from CALSPEC) I could obtain the dereddened distance modulus $(m-M)_0$, and therefore the distance, using $\mu = 5 (\log d - 1)$.

Knowing the distance and the Galactic latitude, I also estimated the height above the galactic plane using: $z = d \sin b$.

By averaging all the estimates derived with the different colors, I obtained the values listed in Table 9.2.

Table 9.2: Preliminary analysis of SPSS 034

SPSS 034	from scaled-solar isochrones $-1.49 < [\text{Fe}/\text{H}] < -0.66$	from α -enhanced isochrones $-1.62 < [\text{Fe}/\text{H}] < -0.70$
$\langle M \rangle$	$1.28 \pm 0.08 M_{\odot}$	$1.35 \pm 0.04 M_{\odot}$
$\langle T_{eff} \rangle$	$8338 \pm 209 \text{ K}$	$8333 \pm 239 \text{ K}$
$\langle d \rangle$	$719 \pm 47 \text{ pc}$	$768 \pm 69 \text{ pc}$
$\langle z \rangle$	$284 \pm 19 \text{ pc}$	$303 \pm 27 \text{ pc}$

The mass of SPSS 034 is about 1.2–1.3 M_{\odot} , which is typical of δ Scuti stars. This star has T_{eff} of about 8300 K and, although this analysis is preliminary, SPSS 034 seems to be a relatively metal-poor star ($[\text{Fe}/\text{H}] \simeq -0.7$). The height above the galactic plane is about 300 pc, thus locating the star in a transition zone between the thin disk and the thick disk.

Since SPSS034 appears to be a new δ Scuti candidate, at time of writing we have obtained observing time at the Loiano Cassini Telescope in order to collect a longer time series for SPSS 034. This will allow us to derive the (multi)period of the star through the accurate analysis of its light curve, and to derive the parameters of its pulsation.

9.2.2 SPSS 172

Another example of the discovery potential of our survey is the case of SPSS 172. I found in the literature four papers in which this star is studied, in the context of high proper motion stars. In particular, Carney et al. (1994) and Latham et al. (2002) derive some parameters for SPSS 172, as reported in Table 9.3.

SPSS 172 seems to be a cold, extremely metal-poor star. In order to check the temperature of SPSS 172, I derived some colors from the literature data and I used the empirical scale provided by Alonso et al. (1996) for the low main sequence stars (because $\log g=4.5$). The results are reported in Table 9.4 for each temperature/color relation used.

The temperatures computed using 2MASS colors and magnitudes from Carney et al. (1994) confirmed the value reported in Latham et al. (2002). The magnitudes from Kharchenko (2001) lead to a lower T_{eff} value. The (V-R), (V-I) and (R-I) colors could not be used because they are not compatible with the color range in which the relations by Alonso et al. (1996) can be applied.

SPSS 172 is a mysterious object: it is a cold, metal-poor star, but its light curve presents a short-period (about 40 minutes) and low-amplitude (about 15 mmag) pulsation (see Fig. 9.3). Using the distance provided by Carney et al. (1994) I could estimate the absolute magnitude using the distance modulus-magnitude relation. In Fig. 9.6, I roughly indicated the region of the T_{eff} -absolute magnitude plane corresponding to $T_{eff}=5268\pm 154$ K, and $M\approx 6$ mag. None of the well known “cold” variable types shown in Fig. 9.6 fit the characteristics of our star.

If SPSS 172 is a yellow main sequence dwarf, as indicated by its temperature and gravity, surely it can not be a RV Tauri nor a Mira-type pulsator because these stars are red supergiants characterized by high amplitudes and long period pulsations. The instability strip where Cepheids, RR Lyrae and δ Scuti stars are found is too away from our star. All these stars are much more hot and bright with respect to SPSS 172. In addition, both Cepheids and RR-Lyrae are giant and supergiant stars. On the other hand, the flare stars are too cold and faint. The pulsating stars closer to the SPSS 172 position on the diagram of Fig. 9.6 are T Tauri. However, these stars are on a different evolutionary stage: they are pre-main sequence stars, while our object is most probably a main sequence star. The brightness variations in classical T Tauri stars can be complex and irregular, with amplitudes ranging from 0.01 to many magnitudes and taking place on time scales from days, through hours, to minutes. The variation in SPSS 172 appears instead quite regular. T Tauri

Future prospects and scientific outcome

Table 9.3: SPSS 172 available literature data

SPSS 172 available data		
name	G 192–41	from Lowell PM survey Northern Hemisphere ^a
α_{2000}	06 44 26.34	from 2MASS ^b
δ_{2000}	+50 33 55.9	from 2MASS
l_{2000}	165.2940	from 2MASS
b_{2000}	+19.5676	from 2MASS
Spectral Type	?	
proper motion	-27 -396 mas/yr	from LSPM-NORTH Catalog ^c
radial velocity	126.65 \pm 0.43 km/s	from HPM star survey ^{d1}
U	14.28	from HPM star survey ^{d2}
B	13.91	from ASCC ^e
	13.89	from HPM star survey
V	13.16	from ASCC
	13.20	from HPM star survey ^{d2}
R	12.9	from USNO–B ^f
I	12.7	from USNO–B
J	11.738	from 2MASS
H	11.355	from 2MASS
K	11.280	from 2MASS
E(B–V)	0.05	from HPM star survey ^{d2}
M/M _⊙	0.58	from HPM star survey ^{d2}
distance	204 pc	from HPM star survey ^{d2}
T_{eff}	5250 K	from HPM star survey ^{d1}
	5226 K	from HPM star survey ^{d2}
logg	4.5	from HPM star survey ^{d1}
[Fe/H]	-2.5	from HPM star survey ^{d1}

^a: Giclas et al. (1971), <http://vizier.u-strasbg.fr/viz-bin/VizieR?-source=I/79>

^b: Cutri et al. (2003), <http://irsa.ipac.caltech.edu/applications/Gator/>

^c: Lépine & Shara (2005), <http://vizier.u-strasbg.fr/viz-bin/VizieR?-source=I/298>

^{d1}: Latham et al. (2002)

^{d2}: Carney et al. (1994), <http://vizier.u-strasbg.fr/viz-bin/VizieR?-source=J/AJ/124/1144>

^e: Kharchenko (2001), <http://vizier.u-strasbg.fr/viz-bin/VizieR?-source=I/280>

^f: Monet et al. (2002), <http://vizier.u-strasbg.fr/viz-bin/VizieR?-source=I/284>

stars are defined by the appearance of their spectrum. In particular they show many emission lines (usually, the Balmer, CaII H and K lines, Fe λ 4063 and 4132 lines,

Table 9.4: Temperature estimates for SPSS 172

Color	T_{eff}	notes
B-V	5072 K	using magnitudes from Carney et al. (1994)
B-V	4898 K	using magnitudes from Kharchenko (2001)
V-K	4692 K	using V from Carney et al. (1994) and K from 2MASS
J-K	5219 K	using magnitudes from 2MASS
J-H	5268 K	using magnitudes from 2MASS

forbidden SII $\lambda 4068$ and 4076 lines, strong Li $\lambda 6707$). We will obtain, in our main campaign (see Chapter 3), the spectrum of SPSS 172 with wavelength coverage from 330 nm to 1050 nm. Therefore, we will be able to verify whether emission lines are present in its spectrum.

SPSS 172 is a very interesting object and, at the moment, its nature is still a mystery, because we do not have enough data to identify what kind of variable it is. Its puzzling nature deserve further investigations: a longer time series is necessary to better understand the light curve and derive the parameters of the pulsation.

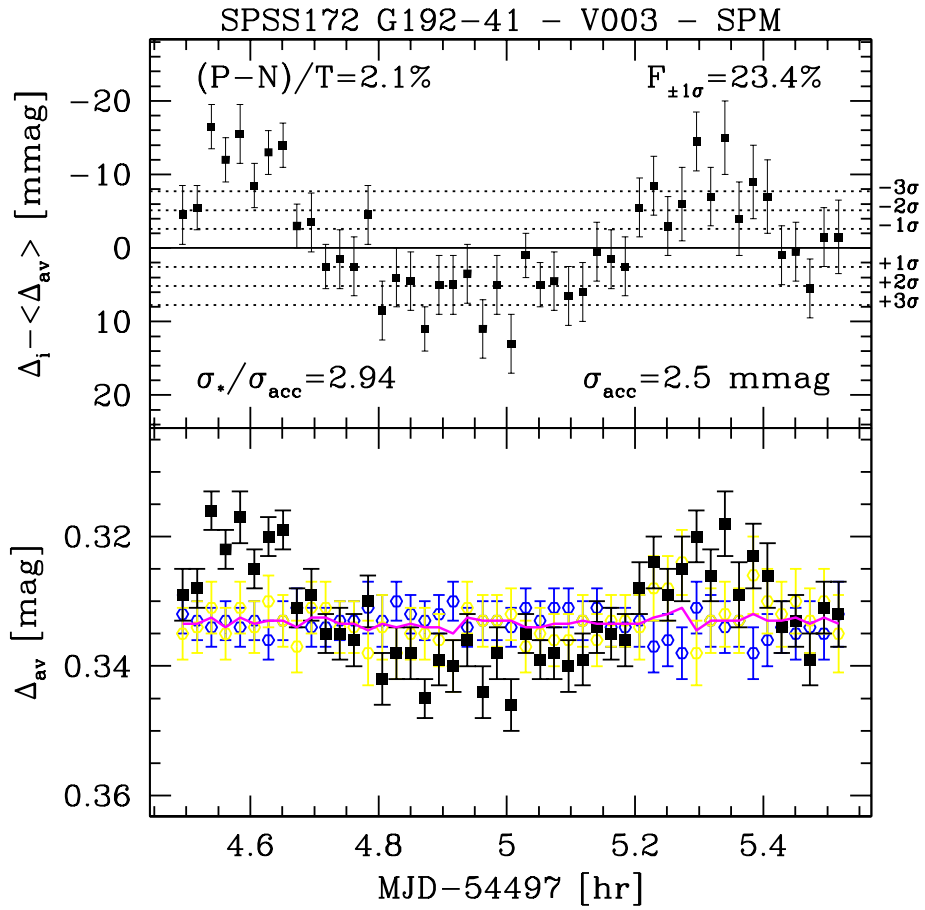


Figure 9.5: SPSS 172 LC produced using data acquired with LaRuca@SPM during run V-003 (31 January 2008). A variability pattern is clearly present in the LC.

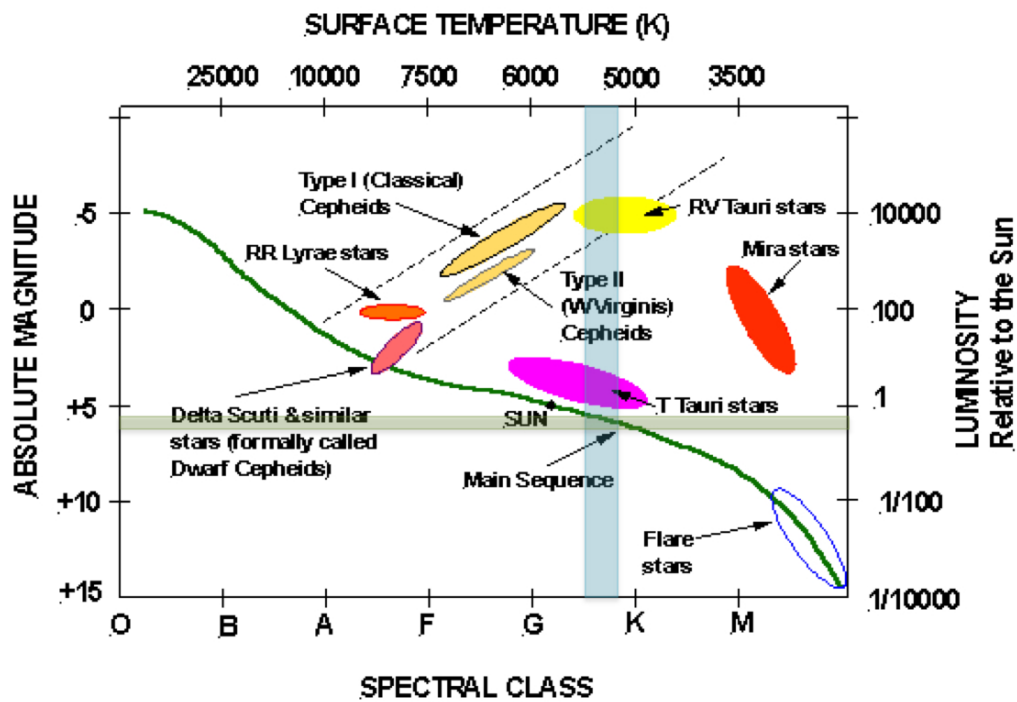


Figure 9.6: The region of the diagram around $T_{eff}=5300$ K is indicated with a light blue strip. Within this strip we can expect to find the SPSS 172, depending on its absolute magnitude. The region of the diagram around $M=6$ is indicated with a light green strip. The overlap of the light blue and light green region indicates that SPSS 172 is most probably a main sequence star.

10

Conclusions

During my PhD years, I worked at the calibration of Gaia spectrophotometry in the framework of the DPAC (Data Processing and Analysis Consortium), within the CU5-DU13 based in Bologna. I contributed to the ground-based survey of Gaia SPSS in many respects: planning and carrying out the observations (Chapter 4), establishing the instrument familiarization plan (Chapter 5), collaborating to all the data reduction and analysis activities (both photometry and spectroscopy), and to the maintenance of the data archives (Appendix A). In particular I was (and actually I am) personally responsible for the photometric data reduction and analysis, focussing my effort on the relative photometry for the production of short-term light curves.

In this context, I prepared semi-automated pipelines which allow for:

- the pre-reduction of imaging SPSS data (Chapter 6): my pre-reduction pipeline allows us to maintain the maximum homogeneity possible in the quality and treatment of photometric data obtained during both the auxiliary (constancy monitoring and relative photometry) and main (absolute photometry and spectroscopy) campaigns aimed at building the Gaia SPSS grid. In addition, since our survey contains a huge number of frames and their careful reduction is of fundamental importance to achieve our desired accuracy (a few % in flux at most, relative to Vega), my pipeline contains quality control procedures which are automatic but allow to produce check plots, useful to retain only data suitable for our purposes and to quicken the whole pre-reduction process;
- the production of quality checked aperture photometry catalogues (Chapter 7): my procedure produces aperture photometry catalogues ready to be used for further analysis and, simultaneously, performs the quality control on the SPSS pre-reduced imaging frames. This pipeline allows us to avoid wasting disk space

Conclusions

in the data reduced archive with frames which do not meet our strict quality criteria. This particular pipeline can be used on all our photometric data, from the absolute photometry to the relative one (short-term and long-term constancy monitoring);

- the production and analysis of light curves for the short-term constancy monitoring data: this allows us to validate our SPSS candidates against short-term variability or to reject them in case of variability detection (Chapter 8). The pipeline can be easily extended to the case of long-term constancy monitoring in the near future.

10.1 Gaia mission calibration

ESA's Gaia space mission is a major project for the European astronomical community. The Gaia satellite will perform a 5 year long all-sky scanning survey that will provide exquisitely accurate astrometry (> 100 times better than Hipparcos) and photometry for one billion of Galactic stars down to $V \simeq 20$, and radial velocity for several millions of stars to $V \leq 17$. Such an observational effort has been compared to the mapping of the human genome for the amount of collected data and for the impact that it will have on all branches of astronomy and astrophysics. This unprecedented wealth of data will have a significant impact on every branch of astrophysics – from asteroids to dark matter – and also on some aspects of fundamental physics (Chapter 2).

As challenging as it is, the processing and analysis of the huge data-flow incoming from Gaia is the subject of thorough study and preparatory work by the DPAC, in charge of all aspects of the Gaia data reduction. I developed my work in the context of the Gaia mission preparation working in CU5-DU13 which, together with DU14, is dedicated to the external calibration of Gaia spectrophotometric data.

On board of Gaia there will be two (spectro)photometers, the blue one (BP) and the red one (RP) covering the range 330–1050 nm, and the white light (G-band) imager dedicated to astrometry. Given the fact that the focal plane of Gaia will be constituted by 105 CCDs and the sources will cross the the focal plane at constant speed, at different positions in each of the foreseen passages (on average 70–80, but up to 250) in the mission lifetime, the “simple” problem of calibrating the integrated BP/RP and G-band magnitudes and the low resolution BP/RP spectra flux turns into a very delicate and complicated issue, including CTI effects, LSF variations across the focal plane and with time, CCD gating to avoid saturation and the like.

The calibration model (Chapter 3) developed by CU5-DU14 requires a carefully selected set of $\simeq 200$ SPSS flux tables with a nominal precision of a few %, with respect to Vega.

Gaia is usually described as a self-calibrating mission, but it also needs external data to fix the zero-point of the magnitude system and radial velocities, and to calibrate the classification/parametrization algorithms. The task of CU5-DU13 team, to which I am a member, is to build the Gaia SPSS grid with accurate flux calibrated energy distributions through ground-based observations and careful data reduction procedures, in order to allow the conversion of Gaia instrumental wide band photometry and spectrophotometry into physical units.

We started our observing campaigns in late 2006 (Chapter 4) and we estimate to eventually complete our survey around 2014. At the end of the observing campaigns, up to 400 nights¹ of data are foreseen and a huge amount of frames ($\simeq 100\,000$) is expected. In this context, my pipeline is of fundamental importance because it allows to rapidly reduce and analyze the large amount of photometric data we collected in a homogeneous way and with the maximum possible precision and accuracy. In particular, the production of light curves for the short-time constancy monitoring entails little effort, being all the photometric catalogues already produced and quality checked in a previous step of the pipeline. It is important to note that the pipeline I built for the short-term constancy analysis can be easily extended also to the analysis of the long-term constancy monitoring data.

In addition, since we are interested in accurate and precise spectrophotometry, it was mandatory, as a first step, to test the capabilities of each telescope/instrument combination and to devise methods to keep under control, and eventually to correct for, the typical instrumental effects that can affect the high precision required for the Gaia SPSS grid. The IFP (Instrument Familiarization Plan) tests (aimed at deriving shutter times, linearity, calibration frames and lamps stability, photometric distortions, 2nd order contamination of the spectra, and so on), were performed on all the instruments involved in our observing campaigns. I was deeply involved in all the IFP tests activities and, in particular, I lead the *Calibration Frames Monitoring* activities (Chapter 5).

¹Up to now we have carried out more than 300 nights of observations.

10.2 SPSS survey scientific output

The Gaia SPSS grid will be a new, unprecedented catalogue of spectrophotometric standard stars characterized by high precision and accuracy, full sky coverage and with stars spanning a wide range of spectral types. Besides the absolute calibration of Gaia spectrophotometric data, it will be useful also for the absolute calibration of ground-based observations. However, other scientific outcomes are foreseen. For example, given the high number of WDs in our sample and the high quality of our spectra, they can be used to study the atmospheres of WDs in order to determine their atmospheric parameters. The determination of atmospheric parameters for our huge sample of WD could help to better define, from an observational point of view, both the blue and red edges of the instability strips. When we selected our SPSS candidates, we tried to exclude stars lying within the WD instability strips. But, in many cases, the existing information was not sufficient (or sufficiently accurate) to firmly establish the constant nature of a given star: this is one of the reasons why we perform the short-term constancy monitoring. Therefore, some variable stars could be present in our sample and, in such case, the scientific output is straightforward (Chapter 9). Given the range of spectral types present in our catalogue, we can expect to find compact pulsators (WDs and subdwarfs represent the 57% of our sample) but also other kinds of variable as, for example, δ Scuti stars.

Up to now, we found two variable stars in our sample: SPSS 034 and SPSS 172. Obviously, both stars were rejected from the SPSS candidates list, but they are interesting new variable objects nonetheless. From the inspection of the light curve of SPSS 034, this A6V star seems to have a short oscillation period and low amplitude, a typical signature of δ Scuti type pulsations. SPSS 172 is a mysterious object: it is a cold, metal-poor star, and its light curve presents a short-period and low-amplitude pulsation. None of the well known variable types fit the characteristics of this star. A follow-up of both SPSS 034 and SPSS 172 is ongoing, in order to acquire longer light curves for better estimates of the pulsation parameters and to better understand which kind of phenomena are occurring in these stars.



Wiki-Bo pages and Data Archives

Such a large observational campaign as our SPSS survey for the absolute calibration of Gaia (see Chapter 4), where multiple observation of a large number of targets come from six different ground-based facilities, requires a big coordination effort. One example is the observation rate, involving as many as six observing runs per semester, carried out sometimes almost simultaneously. It is of fundamental importance to have a reference information on observation status and observing instruction, constantly updated, which observers can rely upon to prepare their observing runs without significant duplication of effort. Similarly, our data reduction protocols split up reduction procedures in subsequent (and also parallel steps), which require a storage place and an information control so that data analysts in the team can keep track on what was done and who did it. To fulfill these needs, we have our own local wiki pages (Wiki-Bo) and a simple but efficient archiving system.

A.1 Wiki-Bo pages

The Wiki-Bo pages are the internal CU5-DU13 wiki pages maintained in Bologna¹. The access to the Wiki-Bo is restricted, but guest credentials can be obtained contacting the team. The Wiki-Bo pages are under continuous development and contain various sections, particularly useful to make all relevant data and information easily available to all people involved in the project:

- *Documentation*: contains the Gaia official documents (where drafts and documents about the whole ground-based SPSS observation and reduction strategies are stored), and literature papers on methods and sources of SPSS candidates.

¹Wiki-Bo can be found at: http://yoda.bo.astro.it/wiki/index.php/Main_Page

- *SPSS Observations*: contains the summary table of all our observing runs (including proposals, observing logs, target summaries, links to the raw data and reduced data repositories), and the primary and secondary SPSS tables, containing the candidates lists and summary of the status of both observations and data reductions for each SPSS, and links to the individual SPSS information page with literature info and finding charts.
- *SPSS Data Reduction and Analysis*: contains the IFP section and both the photometry and spectroscopy reduction and analysis sections. In particular:
 - the IFP section contains information about the status of IFP completion, the defined calibration plan for all the instruments, the calibration frames study and the definition of our QC criteria for calibration frames. In addition, all the template macros needed to perform the QC are linked in this section;
 - the photometry reduction and analysis section contains links and information about the definition of our QC criteria for imaging pre-reduced frames, all the pipelines and template macros needed to pre-reduce and quality check our imaging data. In this section a first determination of the zero-points and extinction for selected nights and notes on Landolt stars that should be avoided in our campaigns are also reposted. In addition, a summary table contains the results of the 1–2 hours time series analysis for the short-term constancy monitoring;
 - the spectroscopy reduction and analysis section contains links and informations about the pre-reduction and the definition of our QC criteria for spectroscopic data.
- *SPSS Database and Archive*: contains the general description and the instructions for downloading/uploading data in our archives and links to both the SPSS raw data and reduced data archives.

DU13 team members, myself included, concur to the maintenance of both the Wiki-Bo pages and the data archives.

A.1.1 Short-term monitoring light curves page

The results of the analysis of all the SPSS short-term light curves are available in a dedicated page hosted in Wiki-Bo². Both the QC and analysis parameters for the light curves are summarized in this page, and LC pipeline templates built for 2 to 10 reference stars are available. A wiki table summarizes the status of the short-term constancy analysis (a portion is shown in Fig. A.1).

In the LC table, the various columns are:

- **column 1 and 2:** in the first two columns of the table are reported the ID and the name of the SPSS, linking to the individual SPSS page;
- **column 3:** ID of the observing run;
- **column 4:** series level QC color code, see Chapter 7;
- **column 5:** five files are linked in this column:
 1. Photometric QC resume, that summarize the star sevel QC results (see Chapter 7);
 2. CurvaID_RUN.sm, i.e. the macro used in order to build this particular light curve;
 3. bID_RUN.curve, i.e. the file produced by the first step of the LC pipeline, which is the input of the second step of the pipeline (see Section 8.1);
 4. SPSSID_RUN.curve, i.e. the output file produced by the second step of the LC pipeline (this file contains all the needed info to reproduce the upper panel of the LC plot);
 5. RedNotesID_RUN.txt, i.e. a file containing the main SExtractor parameters used in the catalogue production and, when needed, notes on epochs removed from the light curve;
- **column 6:** light curve plot;
- **column 7:** constancy/variability verdict as derived from the light curve (SPSS constant, variable, likely constant, suspect variable). The parameter Ivar reported is σ_*/σ_{prec} (see Section 8.2.2)
- **column 8:** notes are reported here.

Wiki-Bo pages and Data Archives

035	1742046	M-009	Photometric QC resume B Curve034_M009.am b034_M009.curve SPSS034_M009.curve RedNotes034_M009.txt		SUSPECT VARIABLE STAR Ivar = 6.19 Amax = 12.0 ± 0.9 B mmag	SUSPECT VARIABLE STAR only 30 min of good data
		V-011	Photometric QC resume V Curve034_V011.am b034_V011.curve SPSS034_V011.curve RedNotes034_V011.txt		SUSPECT VARIABLE STAR Ivar = 8.97 Amax = 10.0 ± 1.3 B mmag	SUSPECT VARIABLE STAR only 21 good point in the LC
		V-021	Photometric QC resume V Curve034_V021.am b034_V021.curve SPSS034_V021.curve RedNotes034_V021.txt		VARIABLE STAR Ivar = 6.60 Amax = 10.0 ± 0.8 B mmag	VARIABLE STAR-REJECTED
035	1742045					
036	1805292	M-006	Photometric QC resume B Curve036_M006.am b036_M006.curve SPSS036_M006.curve RedNotes036_M006.txt		Likely Constant Star ? Ivar = 2.55 A ≤ 5.9 B mmag	SUSPECT CONSTANT STAR New observations are needed
037	1812095	V-008	Photometric QC resume V Curve037_V008.am b037_V008.curve SPSS037_V008.curve RedNotes037_V008.txt		CONSTANT STAR Ivar = 1.03 A ≤ 2.1 B mmag	STAR ACCEPTED Trend: probably due to extinction effects
		V-011	Photometric QC resume V Curve037_V011.am b037_V011.curve SPSS037_V011.curve RedNotes037_V011.txt		Likely Constant star Ivar = 0.91 A ≤ 1.9 B mmag	SUSPECT CONSTANT STAR only 29 good point in the LC, bad seeing and problems with the guide during the series.

Figure A.1: Little portion of the LC Table.

Depending on the verdict reported in column 7, a color code is assigned to each SPSS (see Fig. A.2) in order to visualize in a glance if a star is accepted, rejected or if new observations are needed.

<i>CONSTANCY color codes in Light Curves Table (Wiki-Bo)</i>	
	No short-term variability monitoring needed for this SPSS All columns colored
	SPSS ACCEPTED (constant star) No further observations needed All columns colored
	SPSS SUSPECT (likely constant star or suspect variable) Further observations needed Columns colored: from 3 to 8
	SPSS REJECTED (variable star or other reasons) No further observations needed All columns colored

Figure A.2: Light Curves Table Color Codes.

²http://yoda.bo.astro.it/wiki/index.php/Short_Term_Lightcurves

Every time a new light curve is produced, it is uploaded in the Wiki-Bo LC table. The same short-term light curve and a brief summary of its analysis are reported also in the corresponding individual SPSS page, in the section called *Short-Term Variability*.

A.2 Archiving SPSS raw and reduced data

Our observing campaigns use six different telescopes, not all having public archives. Therefore, the need for some basic archiving capabilities arose. We have implemented (or are about to implement) different ways to archive our data with safely redundancies:

- all raw data are backed up on CDs or DVDs immediately after observing;
- all raw and reduced data are stored on our local archive, along with intermediate data products (the local archive is regularly backed up locally);
- an external backup space is offered by the ESAC datacenter in Madrid, managed by E. Joliet, for all GBOG data;
- professional support was offered by the ASDC in Rome, the kick-off teleconference took place in January 2011.

The local archive in Bologna is a simple system that allows us to manage our data. It is hosted on the same server of our local wiki pages. Since our web interface to the archive are quite simple, we found it more convenient to split the archive into two branches: the *raw data* branch and the *reduced data* branch.

A.2.1 The raw data archive

In the raw data archive we store all the data coming from the telescope, in fits format, with the only exception of test images and broken files which are of no particular use. The file names follow no special naming convention, the only requirement is that they end with the *.fits* extension.

Our local raw data archive can be found at <http://spss.bo.astro.it/raw.cgi>.

The main page of the raw data archive is shown in Fig. A.3.

It contains a sortable table, in which each line contains a link to a full observing night, and some basic information on the run ID, the telescope and instrument used,

SPSS Archive - INAF-OAB GAIA DU13 working group

SPSS observations: RAW data

#	Run ID	Telescope	Instrument	Date obs.
1	P001	Cassini	BFOC	19/08/2006
2	P001	Cassini	BFOC	21/08/2006
3	P002	Cassini	BFOC	25/10/2006
4	P005	Cassini	BFOC	05/02/2007
5	P003	CAHA2.2	CAFOS	30/03/2007
6	P003	CAHA2.2	CAFOS	31/03/2007
7	P003	CAHA2.2	CAFOS	01/04/2007
8	P003	CAHA2.2	CAFOS	02/04/2007
9	P003	CAHA2.2	CAFOS	03/04/2007
10	P003	CAHA2.2	CAFOS	04/04/2007
11	P003	CAHA2.2	CAFOS	06/05/2007
12	P004	TNG	DOLoRes	20/05/2007
13	P004	TNG	DOLoRes	21/05/2007
14	P004	TNG	DOLoRes	22/05/2007

Figure A.3: Portion of the main entry page of the raw data archive.

and the night date (beginning of the night). By clicking on the link appearing in the first table column, the night page can be accessed.

All raw data observed during a given observing night can be accessed from one page similar to the one in Figure A.4.

SPSS archive: **V011-Cassini-BFOC_20090214.log**

i = image preview
k = display fits header keywords

view	FILENAME	ID	OBJECT	Notes
<input type="checkbox"/> i k	spss_101.fits	0	-	Skyflat B 35000 ADU
<input type="checkbox"/> i k	spss_102.fits	0	-	" 30000 ADU
<input type="checkbox"/> i k	spss_103.fits	0	-	" 28000 ADU
<input type="checkbox"/> i k	spss_104.fits	0	-	" 22000 ADU
<input type="checkbox"/> i k	spss_105.fits	0	-	" 21000 ADU
<input type="checkbox"/> i k	spss_106.fits	0	-	Skyflat V 13000 ADU
<input type="checkbox"/> i k	spss_107.fits	0	-	" 26000ADU
<input type="checkbox"/> i k	spss_108.fits	0	-	" 25000 ADU
<input type="checkbox"/> i k	spss_109.fits	0	-	" 22000 ADU
<input type="checkbox"/> i k	spss_110.fits	0	-	Skyflat R 25000 ADU
<input type="checkbox"/> i k	spss_111.fits	0	-	" 19500 ADU
<input type="checkbox"/> i k	spss_112.fits	0	-	" 17000 ADU
<input type="checkbox"/> i k	spss_113.fits	0	-	" 15500 ADU
<input type="checkbox"/> i k	spss_114.fits	227	227_B	Tdome 4, outdoor -0.7, seeing 2"
<input type="checkbox"/> i k	spss_115.fits	227	227_B	Seeing 2", ~10000 counts

Figure A.4: Portion of the raw data archive page of one observing night.

The night pages all contain a list of archived files described by:

- **Filename.** The original filename from the telescope;
- **ID.** This is the SPSS ID, a unique number associated to each SPSS, it is 0 or 999 for calibration frames or other frames not related to a particular SPSS;

- **OBJECT.** The object keyword written in the fits header, eventually corrected according to the observer’s notes (see below);
- **Notes.** These are the notes taken by the observer at the time of observations.

There are also buttons for selecting frames and two links marked with the letters *i* and *k*, which point to a thumbnail of the fits image and to an ASCII file containing the full fits header of each archived fits file. At the very bottom of each night page there is also a section with the title “*Select additional columns to display (i.e. fits KEYWORDS)*”, listing all the fits keywords found into the fits headers, with buttons to select the ones to display in the main page table. Clicking on the button “Display selected keyword” one can refresh the page and display all the selected keywords instead of the four preset ones described above.

A.2.2 The reduced data archive

The reduced data archive contains various levels of data products (quality checked), with the naming conventions exemplified in Tables A.1 and A.2, which also give an idea of the kind of reduced data and data products we archive. The naming conventions are also reported in the Wiki-Bo pages³, where some more information on the types of data products and calibration frames can be found.

The reduced data archive can be found at <http://spss.bo.astro.it/red.cgi>.

The main page of the reduced data archive has the same structure as the raw data one (see Section A.2.1). The reduced data for each observing night are displayed in web pages very similar to those of the raw data. The main differences are:

- for reasons concerning the different data upload procedure, the log file name appearing at the top of the page is a link to the actual log file, i.e., an ASCII table containing the filename, ID, OBJECT and Notes fields which appear on the web page as well;
- besides the *i* and *k* links there are more links:
 - The number *1* links to a thumbnail of the spectrum extracted with the “*optimal*” extraction procedure, i.e., giving more weight to pixels with higher S/N;

³http://yoda.bo.astro.it/wiki/index.php/Reduced_Data_Archive_Requirements

- The number 2 links to a thumbnails of the spectrum extracted with the simple “*summation*” procedure, i.e., by giving the same wight to all pixels in the aperture;
 - The number 3 links to a thumbnail of the extracted sky spectrum;
 - The number 4 links to a thumbnail to the noise spectrum;
 - The letter *c* links to the ASCII catalogue with the SExtractor aperture magnitudes (for imaging);
- It is not possible to display additional header keywords in the reduced data night pages.

Table A.1: **Data products naming convention.**

Name	Description
r.<filename>.fits	2D pre-reduced images and spectra (bias, flats, etc.)
x.<filename>.fits	1D spectra extracted and wavelength calibrated
c.<filename>.fits	1D spectra RELATIVELY calibrated in flux
t.<filename>.fits	1D spectra corrected for telluric absorption features
f.<filename>.fits	1D spectra ABSOLUTELY calibrated in flux
c.<filename>.cat	ASCII catalogues with SExtractor aperture magnitudes

A.2.3 Downloading data

On each night page, in the archive data table (both the raw data one and the reduced data one), there are buttons that can be used to select the data to download. Below the table (Figure A.6) there are additional buttons: the usual “*select/unselect all*” button, which allows to select and de-select all files in the page, and the “*Download selected*” button, which allows to download all the selected files into a tarfile⁴. Finally, the special button: “*Download all photometry catalogues*”, only present in the reduced data night pages, allows to download all the ASCII files containing aperture magnitudes of each imaging frame.

⁴It is necessary to provide a password, which you can obtain by contacting the team.

A.2 Archiving SPSS raw and reduced data

Table A.2: Examples of master calibration frames names

Master calibration frame name	Description
m.<run-id>-<tel>-<inst>_<AAAAMMDD>_DARK_200.fits	a masterdark of 200 seconds
m.<run-id>-<tel>-<inst>_<AAAAMMDD>_BIAS_FULL.fits	a full CCD masterbias
m.<run-id>-<tel>-<inst>_<AAAAMMDD>_BIAS_SPEC.fits	a masterbias cut with the spectroscopic section, for CAHA
m.<run-id>-<tel>-<inst>_<AAAAMMDD>_BIAS_PHOT.fits	a masterbias cut with the photometric section, for CAHA
m.<run-id>-<tel>-<inst>_<AAAAMMDD>_DOME_V.fits	a photometric lamp dome-Masterflat in the V filter
m.<run-id>-<tel>-<inst>_<AAAAMMDD>_SKY_V.fits	a photometric twilight/sunrise sky-Masterflat in the V filter
m.<run-id>-<tel>-<inst>_<AAAAMMDD>_LAMP_R200_2.5.fits	a spectroscopic lamp masterflat grism R200, slit 2.5"
m.<run-id>-<tel>-<inst>_<AAAAMMDD>_LAMP_G5_5.fits	a spectroscopic lamp Masterflat grism G5, slit 5"
m.<run-id>-<tel>-<inst>_<AAAAMMDD>_LAMP_G16_10_ID212.fits	a spectroscopic lamp masterflat associated to the SPSS212, grism G16, slit 10"
m.<run-id>-<tel>-<inst>_<AAAAMMDD>_LAMP_G16_10_ID212.1.fits	a spectroscopic lamp masterflat associated to the first set of spectra of SPSS212, grism G16, slit 10", if there are multiple observations of the same star
m.<run-id>-<tel>-<inst>_<AAAAMMDD>_WAVE_LR-R_11.7.fits	a daytime reference lamp grism LR-R, slit 11.7"
m.<run-id>-<tel>-<inst>_<AAAAMMDD>_ILL_LR-B_2.fits	a twilight, spectroscopic masterflat grism LR-B, slit 2"

A.2.4 Uploading data

The detailed instructions to upload data in the raw and reduced data archives can be found in Wiki-Bo⁵. In summary, in the case of raw data, a tarball containing all the fits files and an ASCII logfile (containing filenames, SPSS ID, OBJECT, and Notes (see http://yoda.bo.astro.it/wiki/index.php/Help_Temp_Archive) is submitted to the archive server. The unpacking procedure is started through the web interface shown in Fig. A.7⁶. A new submission of the same night completely

⁵http://yoda.bo.astro.it/wiki/index.php/SPSS_Database_and_Archive

⁶<http://yoda.bo.astro.it/wiki/untar.html>

Wiki-Bo pages and Data Archives

SPSS archive: RED_M007-NTT-EFOSC2_20081126.log

i = image preview
 1 2 ... = plot preview
 k = display fits header keywords
 c = aperture photometry catalogue

view	FILENAME	ID	OBJECT	Notes
<input type="checkbox"/> i k	m.M007-NTT-EFOSC2_20081126_BIAS_BIN1x1.fits	0	BIAS_BIN1x1	bias binning 1x1 for photometry
<input type="checkbox"/> i k	m.M007-NTT-EFOSC2_20081126_BIAS_BIN2x2.fits	0	BIAS_BIN2x2	bias binning 2x2 for spectroscopy
<input type="checkbox"/> i k	m.M007-NTT-EFOSC2_20081126_DOME_B_BIN1x1.fits	0	DOMEFLAT_B_BIN1x1	
<input type="checkbox"/> i k	m.M007-NTT-EFOSC2_20081126_DOME_V_BIN1x1.fits	0	DOMEFLAT_V_BIN1x1	
<input type="checkbox"/> i k	m.M007-NTT-EFOSC2_20081126_DOME_V_BIN2x2.fits	0	DOMEFLAT_V_BIN2x2	
<input type="checkbox"/> i k	m.M007-NTT-EFOSC2_20081126_DOME_R_BIN1x1.fits	0	DOMEFLAT_R_BIN1x1	
<input type="checkbox"/> i k	m.M007-NTT-EFOSC2_20081126_DOME_R_BIN2x2.fits	0	DOMEFLAT_R_BIN2x2	
<input type="checkbox"/> i k	m.M007-NTT-EFOSC2_20081126_DOME_I_BIN2x2.fits	0	DOMEFLAT_I_BIN2x2	
<input type="checkbox"/> i k	m.M007-NTT-EFOSC2_20081126_SKY_B_BIN1x1.fits	0	SKYFLAT_B_BIN1x1	
<input type="checkbox"/> i k	m.M007-NTT-EFOSC2_20081126_SKY_V_BIN1x1.fits	0	SKYFLAT_V_BIN1x1	
<input type="checkbox"/> i k	m.M007-NTT-EFOSC2_20081126_SKY_V_BIN2x2.fits	0	SKYFLAT_V_BIN2x2	
<input type="checkbox"/> i k	m.M007-NTT-EFOSC2_20081126_SKY_R_BIN1x1.fits	0	SKYFLAT_R_BIN1x1	
<input type="checkbox"/> i k	m.M007-NTT-EFOSC2_20081126_LAMP_G11_10_BIN2x2.fits	0	SPECFLAT_G11_10_BIN2x2 i	internal reflection corrected
<input type="checkbox"/> i k	m.M007-NTT-EFOSC2_20081126_LAMP_G11_1_5_BIN2x2.fits	0	SPECFLAT_G11_1_5_BIN2x2 i	internal reflection corrected
<input type="checkbox"/> i k	m.M007-NTT-EFOSC2_20081126_LAMP_G16_10_BIN2x2.fits	0	SPECFLAT_G16_10_BIN2x2 b	built with the afternoon specflats
<input type="checkbox"/> i k	m.M007-NTT-EFOSC2_20081126_LAMP_G16_1_5_BIN2x2.fits	0	SPECFLAT_G16_1_5_BIN2x2 b	built with the afternoon specflats
<input type="checkbox"/> i k	m.M007-NTT-EFOSC2_20081126_LAMP_G3_2_BIN1x1.fits	0	SPECFLAT_G3_2_BIN1x1 b	binning 1x1, internal reflection corrected (boxcar 100x100)
<input type="checkbox"/> i k	m.M007-NTT-EFOSC2_20081126_LAMP_G16_10_ID039_1_BIN2x2.fits	0	SPECFLAT_G16_10_BIN2x2_ID039 b	built with the ID039 specflats (first set)
<input type="checkbox"/> i k	m.M007-NTT-EFOSC2_20081126_LAMP_G16_1_5_ID039_BIN2x2.fits	0	SPECFLAT_G16_1_5_BIN2x2_ID039 b	built with the ID039 specflats
<input type="checkbox"/> i k	m.M007-NTT-EFOSC2_20081126_LAMP_G16_10_ID039_2_BIN2x2.fits	0	SPECFLAT_G16_10_BIN2x2_ID039 b	built with the ID039 specflats (second set)
<input type="checkbox"/> i k	m.M007-NTT-EFOSC2_20081126_LAMP_G16_10_ID002_BIN2x2.fits	0	SPECFLAT_G16_10_BIN2x2_ID002 b	built with the ID002 specflats
<input type="checkbox"/> i k	m.M007-NTT-EFOSC2_20081126_LAMP_G16_1_5_ID002_BIN2x2.fits	0	SPECFLAT_G16_1_5_BIN2x2_ID002 b	built with the ID002 specflats
<input type="checkbox"/> i k c	r.EFOSC0314.fits	002	B BIN1x1	
<input type="checkbox"/> i k c	r.EFOSC0315.fits	002	B BIN1x1	WARNING: Target crossed by Bad Columns
<input type="checkbox"/> i k c	r.EFOSC0316.fits	002	B BIN1x1	
<input type="checkbox"/> i k c	r.EFOSC0317.fits	002	V BIN1x1	
<input type="checkbox"/> i k c	r.EFOSC0318.fits	002	V BIN1x1	WARNING: Target crossed by Bad Columns
<input type="checkbox"/> i k c	r.EFOSC0319.fits	002	V BIN1x1	
<input type="checkbox"/> i k c	r.EFOSC0320.fits	002	R BIN1x1	
<input type="checkbox"/> i k c	r.EFOSC0321.fits	002	R BIN1x1	WARNING: Target crossed by Bad Columns
<input type="checkbox"/> i k c	r.EFOSC0322.fits	002	R BIN1x1	

Figure A.5: Portion of the reduced data archive page of one observing night.

<input type="checkbox"/> 1 2 3 4 k	x.EFOSC0328.fits	00
<input type="checkbox"/> 1 2 3 4 k	x.EFOSC0329.fits	00
<input type="checkbox"/> 1 2 3 4 k	x.EFOSC0330.fits	00
<input type="checkbox"/> 1 2 3 4 k	x.EFOSC0336.fits	00
<input type="checkbox"/> 1 2 3 4 k	x.EFOSC0340.fits	00

select/unselect all fits

(password required)

Figure A.6: Download buttons in a night page of the reduced data archive.

overwrites the existing data because, generally, raw data are uploaded one night at a time, all at once.

In the case of reduced data, it is often the case that some data are reduced by one person, and later another person reduces some more data. Therefore the reduced data upload must be “*incremental*” in nature. If a new night of data is added, the

A.2 Archiving SPSS raw and reduced data

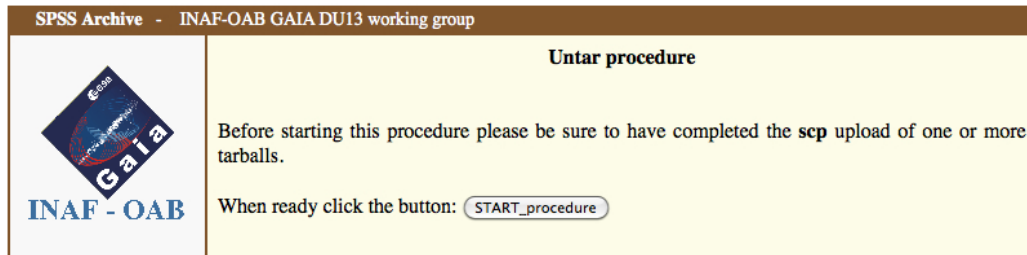


Figure A.7: Web interface with the button to start the unpacking procedure and archive the uploaded data.

procedure is very similar to the one for raw data (see http://yoda.bo.astro.it/wiki/index.php/Instructions_to_Upload_Reduced_Data). If a night that already exists in the archive needs to be updated, the new fits files are included in the tarfile together with the full logfile (which can be downloaded from the night's page and edited):

- all the new files must be listed in the logfile and will be added to the archive;
- all the existing files that should be updated or changed must be listed in the logfile and will be overwritten;
- if a line is removed from the logfile, the corresponding fits or cat files are removed from the archive interface (but are backed up in a special folder).

Bibliography

- Allen C., Poveda A., & Herrera M. A., 2000, *Wide binaries among high-velocity and metal-poor stars*, A&A, 356, 529–540
- Allende Prieto C., 2008, *Stellar Atmospheric Parameters: The Four-Step Program and Gaia's Radial Velocity Spectrometer*, in Classification and Discovery in Large Astronomical Surveys - AIP Conference Proceedings (C. A. L. Bailer-Jones editor), 1082, 47–53
- Alonso A., Arribas S. & Martinez-Roger C., 1996, *The empirical scale of temperatures of the low main sequence (F0V-K5V)*, A&A, 313, 873-890
- Altavilla G., Bellazzini M., Pancino E., Bragaglia A., Cacciari C., Diolaiti E., Federici L., Montegriffo P. & Rossetti E., 2008, *Primary standards for the establishment of the Gaia Grid of SPSS. Selection criteria and a list of candidates* Gaia Technical Report GAIA-C5-TN-OABO-GA-001, <http://www.rssd.esa.int/livelink/open/2736914>
- Altavilla G., Bragaglia A., Pancino E., Bellazzini M., Cacciari C., Federici L. & Ragaini S., 2010, *Secondary standards for the establishment of the Gaia Grid of SPSS. Selection criteria and a list of candidates* Gaia Technical Report GAIA-C5-TN-OABO-GA-003, <http://www.rssd.esa.int/livelink/open/3033479>
- Altavilla G., Pancino E., Marinoni S. & Cocozza G., 2011, *Instrument Familiarization Plan for ground based observations of SPSS. I. CCD Shutter Characterization and Linearity Evaluation* Gaia Technical Report GAIA-C5-TN-OABO-GA-004, available at moment in Wiki-Bo: http://yoda.bo.astro.it/wiki/index.php/DU13_Documents_and_Drafts
- Altmann M. & Bastian U., 2009, *Ecliptic Poles Catalogue Version 1.1* Gaia Technical Report GAIA-C3-TN-ARI-MA-002, <http://www.rssd.esa.int/livelink/open/2885828>
- Anselowitz T., Wasatonic R., Matthews K., Sion E. M. & McCook G. P., 1999, *The Parentage of Magnetic White Dwarfs: Implications from Their Space Motions*, PASP, 111, 702–708
- Aznar Cuadrado R., Jordan S., Napiwotzki R., Schmid H. M., Solanki S. K. & Mathys G., 2004, *Discovery of kilogauss magnetic fields in three DA white dwarfs*, A&A, 423, 1081–1094

BIBLIOGRAPHY

- Balmforth N. J., Cunha M. S., Dolez N., Gough D. O. & Vauclair S., 2001, *On the excitation mechanism in roAp stars*, MNRAS, 323, 362–372
- Baraffe I., Chabrier G., Allard F. & Hauschildt P. H., 2002, *Evolutionary models for low-mass stars and brown dwarfs: Uncertainties and limits at very young ages*, A&A, 382, 563–572
- Barstow M. A., Bond H. E., Burleigh M. R., & Holberg J. B., 2001, *Resolving Sirius-like binaries with the Hubble Space Telescope*, MNRAS, 322, 891–900
- Barstow M. A., Good S. A., Holberg J. B., Hubeny I., Bannister N. P., Bruhweiler F. C., Burleigh M. R. & Napiwotzki R., 2003, *Heavy-element abundance patterns in hot DA white dwarfs*, MNRAS, 341, 870–890
- Bellazzini M., Bragaglia A., Federici L., Diolaiti E., Cacciari C., Pancino E., 2006, *Absolute calibration of Gaia photometric data. I. General considerations and requirements* Gaia Technical Report GAIA-C5-TN-OABO-MBZ-001, <http://www.rssd.esa.int/livelink/open/1145146>
- Bellazzini M., Altavilla G., & Pancino E., 2007a, *Light losses due to variation of seeing with wavelength* Wiki-Bo internal report, available at: <http://yoda.bo.astro.it/wiki/index.php/File:Slit.ps>
- Bellazzini M., 2007b, *The treatment of Atmospheric Extinction in spectrophotometry. Basic concepts*. Wiki-Bo internal report, available at: <http://yoda.bo.astro.it/wiki/index.php/File:ExtinctionMBGA.ps>
- Bellazzini M., Altavilla G., & Cacciari C., 2010, *Notes on the possible use of SEGUE spectrophotometry for the absolute photometric calibration of Gaia* Gaia Technical Report GAIA-C5-TN-OABO-MBZ-002, <http://www.rssd.esa.int/livelink/open/3035273>
- Belokurov V. A. & Evans N. W., 2002, *Astrometric microlensing with the GAIA satellite*, MNRAS, 331, 649–665
- Belokurov V. A. & Evans N. W., 2003, *Supernovae with ‘super-Hipparcos’*, MNRAS, 341, 569–576
- Bergeron P., Saffer R. A. & Liebert J., 1992, *A spectroscopic determination of the mass distribution of DA white dwarfs*, ApJ, 394, 228–247

-
- Bergeron P., Wesemael F., Beauchamp A., Wood M. A., Lamontagne R., Fontaine G., & Liebert J., 1994, *A spectroscopic analysis of DAO and hot DA white dwarfs: The implications of the presence of helium and the nature of DAO stars*, ApJ, 432, 305–325
- Bergeron P., Leggett S. K. & Ruiz M. T., 2001, *Photometric and Spectroscopic Analysis of Cool White Dwarfs with Trigonometric Parallax Measurements*, ApJS, 133, 413–449
- Bertin E. & Arnouts S., 1996, *SExtractor: Software for source extraction.*, A&AS, 117, 393–404
- Bessell M. S., 1999, *Spectrophotometry: Revised Standards and Techniques*, PASP, 111, 1426–1433
- Bessell M. S., 2005, *Standard Photometric Systems*, ARA&A, 43, 293–336
- Bohlin R. C., Colina L. & Finley D. S., 1995, *White Dwarf Standard Stars: G191-B2B, GD 71, GD 153, HZ 43*, AJ, 110, 1316–1325
- Bohlin R. C., 1996, *Spectrophotometric Standards From the Far-UV to the Near-IR on the White Dwarf Flux Scale*, AJ, 111, 1743–1747
- Bohlin R. C., Dickinson M. E. & Calzetti D., 2001, *Spectrophotometric Standards from the Far-Ultraviolet to the Near-Infrared: STIS and NICMOS Fluxes*, AJ, 122, 2118–2128
- Bohlin R. C. & Gilliland R. L., 2004, *Hubble Space Telescope Absolute Spectrophotometry of Vega from the Far-Ultraviolet to the Infrared*, AJ, 127, 3508–3515
- Bohlin R. C., 2007, *HST Stellar Standards with 1% Accuracy in Absolute Flux*, in *The Future of Photometric, Spectrophotometric and Polarimetric Standardization - Astronomical Society of the Pacific Conference Series* (C. Sterken editors), 364, 315–331
- Bohlin R. C., 2008, *NICMOS Spectrophotometry and Models for A Stars*, AJ, 136, 1171–1178
- Bowyer S., Lieu R., Lampton M., Lewis J., Wu X., Drake J. J., Malina R. F., 1994, *The first Extreme Ultraviolet Explorer source catalog*, ApJS, 93, 569–587

BIBLIOGRAPHY

- Bowyer S., Lampton M., Lewis J., Wu X., Jelinsky P., Malina R. F., 1996, *The Second Extreme-Ultraviolet Explorer Source Catalog*, ApJS, 102, 129–160
- Bragaglia A., Renzini A. & Bergeron P., 1995, *Temperatures, gravities, and masses for a sample of bright DA white dwarfs and the initial-to-final mass relation*, ApJ, 443, 735–752
- Breckinridge J. B. & Oppenheimer B. R., 2004, *Polarization Effects in Reflecting Coronagraphs for White-Light Applications in Astronomy*, ApJ, 600, 1091–1098
- Breger M., 2000, *δ Scuti stars (Review)*, in Delta Scuti and Related Stars, Astronomical Society of the Pacific Conference Series (M. Breger & M. Montgomery editors), 210, 3–42
- Brown A., 2007, *Photometry with dispersed images - overview of BP/RP data processing*, Gaia Technical Report GAIA-C5-TN-LEI-AB-009, <http://www.rssd.esa.int/livelink/open/2329785>
- Brown A. & the DU11 team, 2008, *Crowded field BP/RP pre-processing: implications for the CU5 pipeline and for the CU5-CU8 interface*, Gaia Technical Report GAIA-C5-TN-LEI-AB-014, <http://www.rssd.esa.int/livelink/open/2860525>
- Brown A., Jordi C., Fabricius C. & van Leeuwen F., 2010, *Forward modelling for the BP/RP data processing: options and implications*, Gaia Technical Report GAIA-C5-TN-LEI-AB-020, <http://www.rssd.esa.int/livelink/open/3046595>
- Busonero D., Gai M., Gardiol D., Lattanzi M. G., Loreggia D., 2006 *Chromaticity in all-reflective telescopes for astrometry*, A&A, 449, 827–836
- Caballero J. A. & Solano E., 2007 *Albus 1: A Very Bright White Dwarf Candidate*, ApJL, 665, L151–L154
- Carney B. W., Latham D. W., Laird J. B. & Aguilar L. A., 1994 *A survey of proper motion stars. 12: an expanded sample*, AJ, 107, 2240–2289
- Carrasco J.M., Jordi C., Figueras F., Anglada-Escudé G. & Amores E.B., 2006, *Toward the selection of standard stars for absolute flux calibration. Signal-to-noise ratios for BP/RP spectra and crowding due to FoV overlapping*, Gaia Technical Report GAIA-C5-TN-UB-JMC-001, <http://www.rssd.esa.int/livelink/open/2703304>

-
- Carrasco J.M., Jordi C., Lopez-Marti B., Figueras F. & Anglada-Escudé G., 2007, *Revolving phase effect to FoV overlapping and its application to primary SPSS*, Gaia Technical Report GAIA-C5-TN-UB-JMC-002, <http://www.rssd.esa.int/l/llink/livellink/open/2756718>
- Carrasco J.M. & the UB&Bologna teams, 2011, *Design of the experiment to test BP/RP full forwarding model*, Gaia Technical Report GAIA-C5-TN-UB-JMC-011, in preparation
- Castanheira B. G., Kepler S. O., Handler G. & Koester D., 2006 *Analysis of IUE spectra of helium-rich white dwarf stars*, A&A, 450, 331–337
- Cocozza G., Altavilla G., Pancino E., Marinoni S., et al., 2011, *Data Reduction Protocol for Ground Based Observations of SpectroPhotometric Standard Stars. I. Spectroscopic Pre-reduction*, Gaia Technical Report GAIA-C5-TN-OABO-GCC-001, in preparation
- Cousins A. W. J. & Caldwell J. A. R., 1998 *Atmospheric extinction in the U band*, The Observatoty, 118, 85-89
- Cousins A. W. J. & Caldwell J. A. R., 2001 *Atmospheric extinction of U-B photometry*, MNRAS, 323, 380–384
- Cunha M. S., 2002 *A theoretical instability strip for rapidly oscillating Ap stars*, MNRAS, 333, 47–54
- Cutri R. M., Skrutskie M. F., van Dyk S., Beichman C. A., Carpenter J. M., et al., 2003 *2MASS All Sky Catalog of point sources*, (The IRSA 2MASS All-Sky Point Source Catalog, NASA/IPAC Infrared Science Archive <http://irsa.ipac.caltech.edu/applications/Gator/>)
- Dufour P., Bergeron P. & Fontaine G., 2005 *Detailed Spectroscopic and Photometric Analysis of DQ White Dwarfs*, ApJ, 627, 404–417
- Dupuis J., Vennes S., Chayer P., Hurwitz M., Bowyer S., 1998 *Properties of the Hot DA White Dwarf HZ 43 Based on Far-Ultraviolet (ORFEUS-SPAS). II. Observations*, ApJL, 500, L45–L49
- Dvorak S. W., 2004 *Updated Elements for Southern Eclipsing Binaries*, Information Bulletin on Variable Stars, 5542, 1–4

BIBLIOGRAPHY

- Elkin V. G., Riley J. D., Cunha M. S., Kurtz D. W. & Mathys G., 2005 *The discovery of a luminous, rapidly oscillating Ap star, HD 116114, with a 21-minute pulsation period*, MNRAS, 358, 665–670
- Eyer L. & Grenon M., 1997, *Photometric Variability in the HR Diagram*, in Hipparcos - Venice '97, ESA Special Publication (R. M. Bonnet, E. Høg, P. L. Bernacca, L. Emiliani, A. Blaauw, C. Turon, J. Kovalevsky, L. Lindegren, H. Hassan, M. Bouffard, B. Strim, D. Heger, M. A. C. Perryman, & L. Woltjer editors), 402, 467–472
- Eyer L. & Cuypers J., 2000, *Predictions on the Number of Variable Stars for the GAIA Space Mission and for Surveys such as the Ground-Based International Liquid Mirror Telescope*, in IAU Colloq. 176: The Impact of Large-Scale Surveys on Pulsating Star Research - Astronomical Society of the Pacific Conference Series (L. Szabados & D. Kurtz editors), 203, 71–72
- Fabricius C., Jordi C., van Leeuwen F., Carrasco J. M., Figueras F., Gebran M., Voss H., 2009, *Proposal for internal calibration of XP spectra*, Gaia Technical Report GAIA-C5-TN-UB-CF-012, <http://www.rssd.esa.int/llink/livelihood/open/2922510>
- Farihi J., Becklin E. E. & Zuckerman B., 2005 *Low-Luminosity Companions to White Dwarfs*, ApJS, 161, 394–428
- Filippenko, A. & Greenstein J. L., 1984 *Faint spectrophotometric standard stars for large optical telescopes. I*, PASP, 96, 530–536
- Finley D. S., Koester D. & Basri G., 1997 *The Temperature Scale and Mass Distribution of Hot DA White Dwarfs*, ApJ, 488, 375–396
- Fontaine G. & Brassard P., 2008 *The Pulsating White Dwarf Stars*, PASP, 120, 1043–1096
- Fricke W., Schwan H., Lederle T., Bastian U., Bien R., Burkhardt G., et al., 1988 *Fifth fundamental catalogue (FK5). Part 1: The basic fundamental stars*, Veröffentlichungen des Astronomischen Rechen-Instituts Heidelberg, 32, 1–106
- Gianninas A., Bergeron P. & Fontaine G., 2006, *Mapping the ZZ Ceti Instability Strip: Discovery of Six New Pulsators*, AJ, 132, 831–835
- Giclas H. L., Burnham R., & Thomas N. G., 1971, *Lowell proper motion survey Northern Hemisphere. The G numbered stars. 8991 stars fainter than magnitude 8 with motions > 0".26/year*, Flagstaff, Arizona: Lowell Observatory, 1971

-
- Giovannini O., Kepler S. O., Kanaan A., Wood A., Claver C. F., & Koester D., 1998, *Blue Edge of the ZZ Ceti Instability Strip Versus Mass*, *Baltic Astronomy*, 7, 131–140
- Giuffrida G., Troisi L., Iannicola G., Buonanno R., Pulone L., Piersimoni A., Castellani, M., 2008a, *Reconstruction of BP/RP spectra in crowded fields. I - From analytical to numerical approach*, Gaia Technical Report GAIA-C5-TN-OARM-GG-001, <http://www.rssd.esa.int/lmlink/livmlink/open/2864831>
- Giuffrida G., Troisi L., Iannicola G., Buonanno R., Pulone L., Piersimoni A., Castellani, M., 2008b, *Reconstruction of BP/RP spectra in crowded fields. II - Testing the deblending software*, Gaia Technical Report GAIA-C5-TN-OARM-GG-002, <http://www.rssd.esa.int/lmlink/livmlink/open/2864836>
- Glushneva I. N., Kharitonov A. V., Kniazeva L. N. & Shenavrin V. I., 1992, *Secondary spectrophotometric standards*, *A&APS*, 92, 1–29
- Goldberg D., Mazeh T., Latham D. W., Stefanik R. P., Carney B. W. & Laird J. B., 2002, *A Survey of Proper-Motion Stars. XV. Orbital Solutions for 34 Double-lined Spectroscopic Binaries*, *AJ*, 124, 1132–1143
- Green E. M., Fontaine G., Reed M. D., Callerame K., Seitzzahl I. R., White B. A. et al., 2003, *Discovery of A New Class of Pulsating Stars: Gravity-Mode Pulsators among Subdwarf B Stars*, *ApJL*, 583, L31–L34
- Gunn, J. E. & Stryker, L. L., 1983, *Stellar spectrophotometric atlas, wavelengths from 3130 to 10800 Å*, *ApJS*, 52, 121–153
- Hamuy M. , Walker A. R., Suntzeff N. B., Gigoux P., Heathcote S. R., Phillips, M. M., 1992, *Southern spectrophotometric standards*, *PASP*, 104, 533–552
- Hamuy M. , Suntzeff N. B., Heathcote S. R., Walker A. R., Gigoux P., Phillips, M. M., 1994, *Southern spectrophotometric standards, 2*, *PASP*, 106, 566–589
- Hardie R., 1959, *An Improved Method for Measuring Extinction*, *ApJ*, 130, 663–669
- Hartwick F. D. A., Hesser J. E. & McClure R. D., 1972, *A photometric study of the open cluster NGC 2477*, *ApJ*, 174, 557–571
- Heber U., Hamann W.-R., Hunger K., Kudritzki R. P., Simon K. P., Mendez R. H., 1984, *Non-LTE analysis of subluminescent O-stars. VI - Feige 110*, *A&A*, 136, 331–337

BIBLIOGRAPHY

- Hickson P. & Mulrooney M. K., 1998, *A Series of Faint Spectrophotometric Standard Stars at +33 deg Declination*, ApJ, 506, 191–204
- Hoard D. W., Wachter S., Sturch L. K., Widhalm A. M., Weiler K. P., Pretorius M. L., Wellhouse J. W., & Gibiansky M., 2007, *Cool Companions to White Dwarf Stars from the Two Micron All Sky Survey All Sky Data Release*, AJ, 134, 26–42
- Holberg J. B., Oswalt T. D. & Sion E. M., 2002, *A Determination of the Local Density of White Dwarf Stars*, ApJ, 571, 512–518
- Hubeny I. & Lanz T., 1995, *Non-LTE line-blanketed model atmospheres of hot stars. 1: Hybrid complete linearization/accelerated lambda iteration method*, ApJ, 439, 875–904
- Ibata R. & Gibson B., 2007, *The ghosts of galaxies past*, Scientific American, vol.296 part n. 4, 40–45
- Jenkins J. S., Ramsey L. W., Jones H. R. A., Pavlenko Y., Gallardo J., Barnes J. R. & Pinfield D. J., 2009, *Rotational Velocities for M Dwarfs*, ApJ, 704, 975–988
- Jordan S., Schmelcher P., Becken W. & Schweizer W., 1998, *Evidence for helium in the magnetic white dwarf GD 229*, A&A, 336, L33–L36
- Jordan S., Aznar Cuadrado R., Napiwotzki R., Schmid H. M., & Solanki S. K., 2007, *The fraction of DA white dwarfs with kilo-Gauss magnetic fields*, A&A, 462, 1097–1101
- Jurado Vargas M., Merchán Benítez P. & Sánchez Bajo F., 2000, *Atmospheric extinction of stellar radiation in the optical domain*, European Journal of Physics, 21, 245–252
- Kaiser M. E., Kruk J. W., McCandliss S. R., Sahnou D. J., Barkhouser R. H., Van Dixon, et al., 2010, *ACCESS: Enabling an Improved Flux Scale for Astrophysics*, ArXiv e-prints, <http://arxiv.org/abs/1001.3925>
- Kawka A., Vennes S., Schmidt G. D., Wickramasinghe D. T. & Koch R., 2007, *Spectropolarimetric Survey of Hydrogen-rich White Dwarf Stars*, ApJ, 654, 499–520
- Kepler S. O. & Nelan E. P., 1993, *IUE temperatures for white dwarf stars in and around the ZZ Ceti instability strip*, AJ, 105, 608–613

-
- Kharchenko N. V., 2001, *All-sky compiled catalogue of 2.5 million stars*, Kinematika i Fizika Nebesnykh Tel, 17, 409–423
- Kilkenny D., Koen C., O’Donoghue D. & Stobie R. S. 1997, *A new class of rapidly pulsating star - I. EC 14026-2647, the class prototype*, MNRAS, 285, 640–644
- Kilkenny D., 2007, *Pulsating Hot Subdwarfs - An Observational Review*, Communications in Asteroseismology, 150, 234–240
- Koen C., Kilkenny D., O’Donoghue D. & Stobie R. S., 1998, *The EC14026 stars - pulsating hot subdwarfs*, in *New Eyes to See Inside the Sun and Stars - IAU Symposium (F.-L. Deubner, J. Christensen-Dalsgaard, & D. Kurtz editors)*, 185, 361–366
- Koester D., Napiwotzki R., Christlieb N., Drechsel H., Hagen H.-J., Heber U., et al., 2001, *High-resolution UVES/VLT spectra of white dwarfs observed for the ESO SN Ia progenitor survey (SPY). I.*, A&A, 378, 556–568
- Kurtz D. W., 1982, *Rapidly oscillating AP stars*, MNRAS, 200, 807–859
- Lajoie C.-P. & Bergeron P., 2007, *A Comparative Study of Optical and Ultraviolet Effective Temperatures for DA White Dwarfs from the IUE Archive*, ApJ, 667, 1126–1138
- Landolt A. U., 1983, *UBVRI photometric standard stars around the celestial equator*, AJ, 88, 439–460
- Landolt A. U., 1992, *UBVRI photometric standard stars in the magnitude range 11.5-16.0 around the celestial equator*, AJ, 104, 340–371
- Landolt A. U. & Uomoto A. K., 2007, *Optical Multicolor Photometry of Spectrophotometric Standard Stars*, AJ, 133, 768–790
- Latham D. W., Mazeh T., Carney B. W., McCrosky R. E., Stefanik R. P., & Davis R. J., 1988, *A Survey of Proper-Motion Stars. VI - Orbits for 40 spectroscopic binaries*, AJ, 96, 567–587
- Latham D. W., Stefanik R. P., Torres G., Davis R. J., Mazeh T., Carney B. W., Laird J. B., & Morse J. A., 2002, *A Survey of Proper-Motion Stars. XVI. Orbital Solutions for 171 Single-lined Spectroscopic Binaries*, AJ, 124, 1144–1161

BIBLIOGRAPHY

- Lépine S. & Shara M. M., 2005, *A Catalog of Northern Stars with Annual Proper Motions Larger than 0.15" (LSPM-NORTH Catalog)*, AJ, 129, 1483-1522
- Liebert J., Bergeron P. & Holberg J. B., 2005, *The Formation Rate and Mass and Luminosity Functions of DA White Dwarfs from the Palomar Green Survey*, ApJS, 156, 47-68
- Lisker T., Heber U., Napiwotzki R., Christlieb N., Han Z., Homeier D. & Reimers D., 2005, *Hot subdwarfs from the ESO Supernova Ia Progenitor Survey. I. Atmospheric parameters and cool companions of sdB stars*, A&A, 430, 223-243
- Marinoni S., Pancino E., Altavilla G., Cocozza G., et al. 2011a, *Data Reduction Protocol for Ground Based Observations of SpectroPhotometric Standard Stars. I. Imaging Pre-reduction*, Gaia Technical Report GAIA-C5-TN-OABO-SMR-001, available at moment in Wiki-Bo:
http://yoda.bo.astro.it/wiki/index.php/DU13_Documents_and_Drafts
- Marinoni S., Cocozza G., Pancino E. & Altavilla G., 2011b, *Instrument Familiarization Plan for ground based observations of SPSS II. Calibration Frames Study and Recommendations*, Gaia Technical Report GAIA-C5-TN-OABO-SMR-002:
http://yoda.bo.astro.it/wiki/index.php/DU13_Documents_and_Drafts
- Marinoni S., Pancino E., Altavilla G., Cocozza G. et al., 2011c, *Data Reduction Protocol for Ground Based Observations of SpectroPhotometric Standard Stars. III. Quality Control on SPSS Photometric Frames and Photometric Catalogues Production*, Gaia Technical Report GAIA-C5-TN-OABO-SMR-003:
http://yoda.bo.astro.it/wiki/index.php/DU13_Documents_and_Drafts
- Marinoni S., Bellazzini M., Pancino E., Altavilla G. & Cocozza G., 2011d, *Data Reduction Protocol for Ground Based Observations of SpectroPhotometric Standard Stars. IV. Short Variability Monitoring: Light Curves production and analysis*, Gaia Technical Report GAIA-C5-TN-OABO-SMR-004:
http://yoda.bo.astro.it/wiki/index.php/DU13_Documents_and_Drafts
- Marsh M. C., Barstow M. A., Buckley D. A., Burleigh M. R., Holberg J. B., Koester D., O'Donoghue D., Penny A. J. & Sansom A. E., 1997, *An EUV-selected sample of DA white dwarfs from the ROSAT All-Sky Survey - I. Optically derived stellar parameters*, MNRAS, 286, 369-383
- Massey P., Strobel K., Barnes J. V. & Anderson E., 1988, *Spectrophotometric standards*, ApJ, 328, 315-333

-
- Massey P. & Gronwall C., 1990, *The Kitt Peak spectrophotometric standards - Extension to 1 micron*, ApJ, 358, 344–349
- Maxted P. F. L., Marsh T. R. & Moran C. K. J., 2000, *Radial velocity measurements of white dwarfs*, MNRAS, 319, 305–317
- McCook G. P. & Sion E. M., 1999, *A Catalog of Spectroscopically Identified White Dwarfs*, ApJ, 121, 1–130
- Monet D. G. , Levine S. E., Casian B., et al., 2002, *The USNO-B1.0 Catalog (Monet+ 2003)*, VizieR Online Data Catalog, <http://vizier.u-strasbg.fr/viz-bin/VizieR?-source=I/284>
- Montegriffo P., Bellazzini M., Pancino E., Altavilla G., 2007, *A model for the absolute photometric calibration of GAIA BP and RP spectra. I. Basic concepts*, Gaia Technical Report GAIA-C5-TN-OABO-PMN-001, <http://www.rssd.esa.int/livelink/open/2803061>
- Montegriffo P., 2009a, *A model for the absolute photometric calibration of GAIA BP and RP spectra. II. Removing the LSF smearing*, Gaia Technical Report GAIA-C5-TN-OABO-PMN-002, <http://www.rssd.esa.int/livelink/open/2885090>
- Montegriffo P. & Bellazzini M., 2009b, *A model for the absolute photometric calibration of GAIA BP and RP spectra. II. A full in-flight calibration of the Model Parameters*, Gaia Technical Report GAIA-C5-TN-OABO-PMN-003, <http://www.rssd.esa.int/livelink/open/2940357>
- Montegriffo P. & Bellazzini M., 2009c, *Quantitative estimate of the uncertainty on the wavelength calibration as derived from the Absolute Flux Calibration process*, Gaia Technical Report GAIA-C5-TN-OABO-PMN-004, <http://www.rssd.esa.int/livelink/open/2935860>
- Montegriffo P., Carrasco, J. M., Jordi C., Fabricius C., Cacciari C., 2011, *Planning an experiment on source and instrument update XP processing*, Gaia Technical Report GAIA-C5-TN-OABO-PMN-005, in preparation
- Oke J. B. & Gunn J. E., 1983, *Secondary standard stars for absolute spectrophotometry*, ApJ, 266, 713–717
- Oke J. B., 1990, *Faint spectrophotometric standard stars*, AJ, 99, 1621–1631

BIBLIOGRAPHY

- Pancino E., Altavilla G., Bellazzini M., Marinoni S., Bragaglia A., Federici L. & Cacciari, C., 2008, *Protocol for Ground Based Observations of SpectroPhotometric Standard Stars. I. Instrument Familiarization Tests*, Gaia Technical Report GAIA-C5-TN-OABO-EP-001, <http://www.rssd.esa.int/lmlink/livelihood/open/2858529>
- Pancino E., Altavilla G., Carrasco J. M., Monguio M., Marinoni S., Rossetti E., Bellazzini M., Bragaglia A., Federici L. & Schuster W., 2010a, *Protocol for Ground Based Observations of SpectroPhotometric Standard Stars. II. Variability Searches and Absolute Photometry Campaigns*, Gaia Technical Report GAIA-C5-TN-OABO-EP-003, <http://www.rssd.esa.int/lmlink/livelihood/open/2908205>
- Pancino E., 2010b, *An insight into the flux calibration of Gaia G-band images and BP/RP spectrophotometry*, ArXiv e-prints, <http://arxiv.org/abs/1009.1748>
- Pancino E., Altavilla G., Carrasco J. M., Cocozza G., Marinoni S., Bellazzini M., Bragaglia A. & Federici L. 2011, *Protocol for Ground Based Observations of SpectroPhotometric Standard Stars. I. Main Spectrophotometric Campaign*, Gaia Technical Report GAIA-C5-TN-OABO-EP-006, in preparation
- Percy J. R., 2007, *Understanding variable stars*, Cambridge University Press
- Perryman M. A. C., Lindegren L. & Turon C., 1997, *The Scientific Goals of the GAIA Mission*, in *Hipparcos - Venice '97*, ESA Special Publication (R. M. Bonnet, E. Høg, P. L. Bernacca, L. Emiliani, A. Blaauw, C. Turon, J. Kovalevsky, L. Lindegren, H. Hassan, M. Bouffard, B. Strim, D. Heger, M. A. C. Perryman, & L. Woltjer editors), 402, 743–748
- Perryman M. A. C., Lindegren L., Kovalevsky J., Hoeg E., Bastian U., Bernacca P. L., et al., 1997, *The HIPPARCOS Catalogue*, A&A, 323, L49–L52
- Pickles, A. J., 1985, *Differential population synthesis of early-type galaxies. I - Spectrophotometric atlas of synthesis standard spectra*, ApJS, 59, 33–61
- Pickles, A. J., 1998, *A Stellar Spectral Flux Library: 1150-25000 Å*, PASP, 110, 863–878
- Pietrinferni A., Cassisi S., Salaris M. & Castelli F., 2004, *A Large Stellar Evolution Database for Population Synthesis Studies. I. Scaled Solar Models and Isochrones*, ApJ, 612, 168–190

-
- Pietrinferni A., Cassisi S., Salaris M. & Castelli F., 2006, *A Large Stellar Evolution Database for Population Synthesis Studies. II. Stellar Models and Isochrones for an α -enhanced Metal Distribution*, ApJ, 642, 797-812
- Pounds K. A., Allan D. J., Barber C., Barstow M. A., Bertram D., Branduardi-Raymont G., et al., 1993, *The ROSAT Wide Field Camera all-sky survey of extreme-ultraviolet sources. I - The Bright Source Catalogue*, MNRAS, 260, 77-102
- Ragaini S., Bellazzini M., Montegriffo P. & Cacciari C., 2009a, *Absolute calibration of G and integrated G_{BP} and G_{RP} fluxes*, Gaia Technical Report GAIA-C5-TN-OABO-SR-001, <http://www.rssd.esa.int/l/llink/livelink/open/2872522>
- Ragaini S., Montegriffo P., Bellazzini M. & Cacciari C., 2009b, *Absolute calibration of G and integrated G_{BP} and G_{RP} fluxes: test and limits of a simple model*, Gaia Technical Report GAIA-C5-TN-OABO-SR-002, <http://www.rssd.esa.int/l/llink/livelink/open/2975172>
- Ragaini S., blabla., 2011, *Absolute calibration of G and integrated G_{BP} and G_{RP} fluxes: a new model*, Gaia Technical Report GAIA-C5-TN-OABO-SR-003, in preparation
- Rauch T., Kerber F. & Pauli E.-M., 2004, *On the discovery of an enormous ionized halo around the hot DO white dwarf PG 1034+001*, A&A, 417, 647-650
- Robichon N., 2002, *Detection of Transits of Extrasolar Planets with GAIA*, in EAS Publications Series (O. Bienayme & C. Turon editors), 2, 215-221
- Saffer R. A., Livio M. & Yungelson L. R., 1998, *Close Binary White Dwarf Systems: Numerous New Detections and Their Interpretation*, ApJ, 502, 394-407
- Sánchez S. F., Aceituno J., Thiele U., Pérez-Ramírez D. & Alves J., 2007, *The Night Sky at the Calar Alto Observatory*, PASP, 119, 1186-1200
- Sánchez-Blázquez P., Peletier R. F., Jiménez-Vicente J., Cardiel N., Cenarro A. J., Falcón-Barroso J., et al., 2006, *Medium-resolution Isaac Newton Telescope library of empirical spectra*, MNRAS, 371, 703-718
- Schlegel D. J., Finkbeiner D. P. & Davis M., 1998, *Maps of Dust Infrared Emission for Use in Estimation of Reddening and Cosmic Microwave Background Radiation Foregrounds*, ApJ, 500, 525-553

BIBLIOGRAPHY

- Schroeder D. J., 2000, *Astronomical optics*, San Diego : Academic Press
(D. J. Schroeder editor)
- Shibahashi H. & Takata M., 1993, *Theory for the distorted dipole modes of the rapidly oscillating AP stars: A refinement of the oblique pulsator model*, PASJ, 45, 617–641
- Silvestri N. M., Oswalt T. D., Woo M. A., Smith J. A., Reid I. N. & Sion E. M., 2001, *White Dwarfs in Common Proper Motion Binary Systems: Mass Distribution and Kinematics*, ApJ, 121, 503–516
- Smalley B., Gulliver A. F. & Adelman S. J., 2007, *The ASTRA Spectrophotometer: Reduction and Flux Calibrations*, in *The Future of Photometric, Spectrophotometric and Polarimetric Standardization – Astronomical Society of the Pacific Conference Series* (C. Sterken editor), 364, 265–274
- Soffel M. H., 1989, *Relativity in Astrometry, Celestial Mechanics and Geodesy*, Springer-Verlag
- Stello D., Arentoft T., Bedding T. R., Bouzid M. Y., Bruntt H., Csubry Z., Dall T. H., et al., 2006, *Multisite campaign on the open cluster M67 - I. Observations and photometric reductions*, MNRAS, 373, 1141–1150
- Stone R. P. S., 1977, *Spectral energy distributions of standard stars of intermediate brightness. II.*, ApJ, 218, 767–769
- Stone R. P. S. & Baldwin J. A., 1983, *Southern spectrophotometric standards for large telescopes*, MNRAS, 203, 347–353
- Sterken C. & Jaschek C., 1996, *Light Curves of Variable Stars, A Pictorial Atlas*, (-Sterken, C. & Jaschek, C. editors)
- Straižys V., Lazauskaitė R., Brown A. & Zdanavičius K., 2006, *Star Classification possibilities with the Gaia Spectrophotometers. I. Simulated spectra*, Gaia Technical Report GAIA-C8-TN-ITPA-VS-001, <http://www.rssd.esa.int/llink/livlink/open/2705313>
- Stritzinger M., Suntzeff N. B., Hamuy M., Challis P., Demarco, R., Germany L. & Soderberg A. M., 2005, *An Atlas of Spectrophotometric Landolt Standard Stars*, PASP, 117, 810–822

-
- Stroeer A., Heber U., Lisker T., Napiwotzki R., Dreizler S., Christlieb N., & Reimers D., 2007, *Hot subdwarfs from the ESO supernova Ia progenitor survey. II. Atmospheric parameters of subdwarf O stars*, A&A, 462, 269–280
- Szokoly G. P., Bergeron J., Hasinger G., Lehmann I., Kewley L., Mainieri V., et al. , 2004, *The Chandra Deep Field-South: Optical Spectroscopy. I.*, ApJS, 155, 271–349
- Taylor B. J., 1984, *An augmented system of secondary standards for bright-star spectrophotometry*, ApJS, 54, 259–270
- Trager S. C., 2010, *Spectrophotometric Calibration of RVS using CU5-DU13 flux calibration tables*, Gaia Technical Report GAIA-C5-TN-UG-ST-002, <http://www.rssd.esa.int/livelink/open/3027880>
- Turnshek D. A., Bohlin R. C., Williamson II R. L., Lupie O. L., Koornneef J., Morgan D. H., 1990, *An atlas of Hubble Space Telescope photometric, spectrophotometric, and polarimetric calibration objects*, AJ, 99, 1243–1261
- van Leeuwen F., 2010, *CU5 Software Requirements Specification*, Gaia Technical Report GAIA-C5-SP-IOA-FVL-014, <http://www.rssd.esa.int/livelink/open/2785868>
- Vennes S., Kawka A. & Smith J. A., 2007, *CPD -20 1123 (Albus 1) Is a Bright He-B Subdwarf*, ApJ, 668, L59–L61
- Wegner G. & Nelan E. P., 1987, *Ultraviolet and visual spectroscopy of DB white dwarfs*, ApJ, 319, 916–929
- Yanny B., Rockosi C., Newberg H. J., Knapp G. R., Adelman-McCarthy J. K., Alcorn B., et al. 2009, *SEGUE: A Spectroscopic Survey of 240,000 Stars with $g = 14-20$* , AJ, 137, 4377–4399
- Young A. T., 1974, *Seeing: its Cause and Cure*, ApJ, 189, 587–604
- Zapatero Osorio M. R. & Martín E. L., 2004, *A CCD imaging search for wide metal-poor binaries*, A&A, 419, 167–180
- Zhang H. W. & Zhao G., 2005, *Chemical abundances of very metal-poor stars*, MNRAS, 364, 712–724

BIBLIOGRAPHY

- Zechmeister M., Kürster M. & Endl M., 2009, *The M dwarf planet search programme at the ESO VLT + UVES. A search for terrestrial planets in the habitable zone of M dwarfs*, A&A, 505, 859–871
- Zuckerman B., Koester D., Reid I. N. & Hüensch M., 2003, *Metal Lines in DA White Dwarfs*, ApJ, 596, 477–495
- Zwitter T., Munari U., Marrese P. M., Prša A., Milone E. F., Boschi F., Tomov T., & Siviero A., 2003, *Evaluating GAIA performances on eclipsing binaries . II. Orbits and stellar parameters for V781 Tau, UV Leo and GK Dra*, A&A, 404, 333–340